TOWARDS QUANTUM GAS MICROSCOPY OF CESIUM AND POTASSIUM ATOMS IN OPTICAL LATTICES

Dipl.-Phys. Philipp Weinmann

UNIVERSITY OF INNSBRUCK

DOCTORAL THESIS

TOWARDS QUANTUM GAS MICROSCOPY OF CESIUM AND POTASSIUM ATOMS IN OPTICAL LATTICES

Author:
DIPL.-PHYS.
PHILIPP WEINMANN

Advisors:
PROF. DR. HANNS-CHRISTOPH NÄGERL
PROF. DR. RAINER BLATT

A Thesis submitted to the Faculty of Mathematics, Computer Science, and Physics
of the University of Innsbruck, in partial fulfillment of the requirements
for the degree of Doctor of Philosophy (PhD)

Innsbruck, July 2019

Jetzt ist mein Rucksack nur noch ein Rucksack.

Abstract

Quantum simulation promises to be of assistance in studying a variety of unresolved questions in condensed matter physics. Among the condensed matter systems that are currently of particular interest are strongly-correlated electrons in solids. Strongly-correlated electrons are believed to be at the heart of many intriguing solid-state phenomena including high-temperature superconductivity and magnetism. Many of these phenomena are still lacking a theoretical and experimentally verified understanding. Gaining a theoretical understanding of the underlying processes that cause these phenomena will put researchers in a position to design materials with tailored properties. Quantum simulation of solids therefore has attracted both theoretical and experimental interest. A promising platform for quantum simulation of solids are ultracold quantum gases of neutral atoms and polar molecules trapped in optical lattices.

This Thesis reports on the technical design and experimental realization of an entirely new quantum gas apparatus that will be used for quantum simulation of solid state systems. The new quantum gas apparatus is a two-species apparatus. It allows for the production of quantum degenerate samples of ^{133}Cs atoms, the three potassium isotopes ^{39}K, ^{40}K, and ^{41}K, as well as KCs molecules. To study and image ultracold quantum gases, the apparatus embodies an ultra-high-vacuum glass cell that incorporates in-vacuo rod electrodes and a high-resolution imaging system. The rod electrodes will enable the polarization of KCs molecules and thereby allow for studying spin lattice Hamiltonians. The high-resolution imaging system is capable of resolving single atoms at single sites of an optical lattice and thus facilitates to perform fluorescence quantum gas microscopy. The Thesis furthermore presents numerical results on the electric field dependence of the induced electric dipole moment of ^{39}KCs molecules for different rotational states of the electronic-vibrational ground state. It additionally includes simulations of different electric field distributions that can be generated with the rod electrodes within the glass cell. The effect of the residual electric field inhomogeneities found in these simulations on future experiments with ultracold ^{39}KCs molecules in optical lattices is analyzed, in particular on dipolar spin exchange within the Heisenberg XXZ spin lattice model. First experimental results of the new K$-$Cs apparatus were published in three articles of peer-reviewed journals and are summarized in this work.

Future experiments of the K$-$Cs apparatus aim at employing fluorescence quantum gas microscopy of ^{39}K atoms via the $4\mathrm{S}_{1/2} \rightarrow 5\mathrm{P}_{3/2}$ transition (transition wavelength $404.4\,\mathrm{nm}$). Violet fluorescence quantum gas microscopy of alkali atoms has not been experimentally demonstrated so far. This Thesis therefore theoretically studies its feasibility with respect to ^{39}K atoms for the case that the trapped ^{39}K atoms are simultaneously laser cooled via electromagnetically-induced transparency laser cooling. The obtained results indicate that violet fluorescence quantum gas microscopy of ^{39}K atoms with parallel electromagnetically-induced transparency laser cooling in principle should be possible. The study required computation of numerical values for the frequency-dependent atomic polarizabilities of the ground and various excited states of ^{39}K and results are presented here. To image ^{39}K atoms via the $4\mathrm{S}_{1/2} \rightarrow 5\mathrm{P}_{3/2}$ transition, a home-built diode laser was set up that generates laser light at $404.4\,\mathrm{nm}$. The Thesis therefore gives a detailed description and discussion of the laser system and its optical setup.

Kurzfassung

Das Quantensimulieren von physikalischen Systemen weckt Hoffnungen, beim Erforschen ungelöster Fragen der Physik der kondensierten Materie hilfreich zu sein. Stark korrelierte Elektronen in Festkörpern gehören zu jenen Systemen kondensierter Materie, die gegenwärtig besondere Aufmerksamkeit auf sich ziehen. So wird vermutet, dass stark korrelierte Elektronen eine zentrale Rolle bei faszinierenden Festkörperphänomenen einnehmen wie zum Beispiel Hochtemperatursupraleitung und Magnetismus. Vielen dieser Festkörperphänomene fehlt es bislang an einem theoretischen und experimentell belegten Verständnis. Das Verstehen der Prozesse, die für das Auftreten jener Phänomene verantwortlich sind, würde es Forschern ermöglichen, Materialien mit individuell abgestimmten Eigenschaften zu entwickeln. Aus diesem Grund erfährt das Quantensimulieren von Festkörpern großes Interesse sowohl vonseiten der theoretischen als auch der experimentellen Physik. Eine vielversprechende Plattform für die experimentelle Durchführung von Festkörper-Quantensimulationen bieten ultrakalte, in optischen Gittern gefangene Quantengase aus neutralen Atomen und polaren Molekülen.

Die vorliegende Doktorarbeit behandelt das technische Konzept und die experimentelle Realisierung einer von Grund auf neu entwickelten Quantengasapparatur. Bei dieser Apparatur handelt es sich um ein Zwei-Spezies Quantengasexperiment, welches zukünftig dazu verwendet wird, Festkörpersysteme mit Hilfe von Quantensimulation zu untersuchen. Der neue experimentelle Aufbau ermöglicht die Erzeugung entarteter Gase aus ^{133}Cs Atomen, den drei Kaliumisotopen ^{39}K, ^{40}K und ^{41}K als auch aus KCs Molekülen. Für das Untersuchen und Abbilden dieser ultrakalten Quantengase besitzt die Apparatur eine Ultrahochvakuum-Glaszelle, welche ein hochauflösendes Abbildungssystem und Stabelektroden beinhaltet. Das Abbildungssystem ist in der Lage, einzelne Atome auf verschiedenen Gitterplätzen eines optischen Gitters aufzulösen und ebnet damit den Weg für Fluoreszenzquantengasmikroskopie. Mittels der Elektroden können KCs-Moleküle polarisiert und damit theoretische Modelle von Spingittern untersucht werden. Diese Dissertation beschäftigt sich desweiteren mit der Feldstärkeabhängigkeit des induzierten elektrischen Dipolmomentes von ^{39}KCs Molekülen in externen elektrischen Feldern. Es werden ausschließlich die induzierten elektrischen Dipolmomente der energetisch niedrigsten Rotationszustände des vibronischen und elektronischen Grundzustandes von ^{39}KCs Molekülen betrachtet. Für diese induzierten elektrischen Dipolmomente werden numerische Werte berechnet und diskutiert. Die Arbeit enthält außerdem Simulationen elektrischer Feldkonfigurationen, welche mit den Stabelektroden erzeugt werden können. Die bei den Simulationen gefundenen elektrischen Feldinhomogenitäten werden mit Blick auf ihren Einluss auf Experimente mit ^{39}KCs Molekülen in optischen Gittern analysiert. Diese Analyse geschieht im Besonderen hinsichtlich dipolaren Spinaustausches im Heisenberg XXZ Spingittermodell. Erste experimentelle Ergebnisse der neuen K$-$Cs Quantengasapparatur wurden in drei Artikeln in Fachjournalen publiziert und sind in dieser Arbeit zusammengefasst.

Für zukünftige Experimente mit der K$-$Cs Apparatur ist der Einsatz von Fluoreszenzquantengasmikroskopie von ^{39}K Atomen mittels des atomaren $4S_{1/2} \rightarrow 5P_{3/2}-$Übergangs

(Wellenlänge $404.4\,\mathrm{nm}$) geplant. Fluoreszenzquantengasmikroskopie von Alkaliatomen im violetten Spektralbereich wurde bis heute experimentell nicht realisiert. Aus diesem Grund untersucht die vorliegende Arbeit die Durchführbarkeit von Fluoreszenzquantengasmikroskopie an gefangenen ^{39}K Atomen im violetten Spektralbereich, wobei angenommen wird, dass die ^{39}K Atome gleichzeitig mittels elektromagnetisch induzierter Transparenz lasergekühlt werden. Die numerischen Ergebnisse der Analyse legen die prinzipielle Durchführbarkeit dieser Methode nahe. Die Analyse erforderte die Berechnung der frequenzabhängigen, elektrischen Polarisierbarkeit des Grundzustandes und einiger angeregter Zustände von ^{39}K Atomen. Die berechneten Resultate für die Polarisierbarkeiten werden hier präsentiert und diskutiert. Um ^{39}K Atome auf dem $4\mathrm{S}_{1/2} \rightarrow 5\mathrm{P}_{3/2}$–Übergang letztlich abbilden zu können, wurde ein Diodenlaser zur Erzeugung von Laserlicht der Wellenlänge $404.4\,\mathrm{nm}$ aufgebaut. Eine detaillierte Beschreibung und Diskussion des Laseraufbaus und des optischen Aufbaus findet sich in dieser Arbeit.

Contents

Introduction

Electronic materials are omnipresent in our daily life. They are used to manufacture electronic components (e.g. wires, chips, circuit boards, batteries,...) and can be found in any technical device ranging from mobile phones and sensing instruments to electric cars and solar cells. Due to ever increasing expectations on technical devices and the emergence of new applications, the technical requirements on electronic materials steadily grow. Searching for novel materials that meet these new specifications thus has become a hot research field [Nat]. In the past, the quest for new (electronic) materials with desired properties has been guided by educated guesses and trial and error. This statistical approach is rather time consuming and cost-intensive. It is therefore desirable to design materials with tailored properties in a controlled and predictive fashion. In order to carry out controlled material design, different strategies can be pursued. One strategy combines experimental data of material properties of known materials and scientific theory in massive material databases. The databases are evaluated to search for new patterns in the material properties and to deduce empirical rules. Based on the found empirical rules hypotheses on material properties of unknown materials can be generated, which finally can be tested pointedly. The method just outlined to design materials relies on knowledge discovery in databases and is known as *material data mining* [Raj05]. Alternatively, one can identify and understand the physical origin of material properties by studying crystals of known materials through experiments in a laboratory. In this way one gains fundamental insight into the underlying processes within the crystal that lead to the occurence of certain material properties. The insight can be used thereafter to design materials deliberately. Studying material properties, or more general solid-state phenomena, through experiments attracts more and more attention also from related research disciplines. The latter offer novel experimental methods with which open questions in solid-state physics can be investigated. Dilute gases of neutral atoms at nanokelvin temperatures, called *ultracold atoms*, constitute such an experimental method. Since dilute gases of ultracold atoms are dominated by quantum effects, these gases are also known as *ultracold quantum gases*. This Thesis describes the technical design of an experimental apparatus that will be used in future to study solid-state phenomena via ultracold quantum gases. It demonstrates the current experimental capabilities of the apparatus, presents first experimental results, and simulates the performance of crucial parts of the setup as a characterization for future studies.

Macroscopic material properties in many cases are the result of processes that take place on the atomic scale. These processes are often associated with the electrons of the solid. To design materials with desired properties, it is hence crucial to understand the electronic processes within a solid. As the electron density of a solid is roughly on the order of $\sim 10^{23}$ electrons per cubic centimeter, electrons within a solid constitute a many-body system. Examples for material properties that occur due to electrons are the electrical conductivity of semiconductors, which depends on the number of free electrons, and magnetism, which relates to the mutual alignment of the electrons' magnetic moments. The behavior of electrons in a solid is governed among others by the chemical composition of the material, the lattice structure of the crystal as well as the interplay of kinetic energy, Coulomb repulsion, and magnetic interaction of the electrons. Depending on these parameters the electrons can exhibit radically different behaviors. In many materials, like silicon and aluminum, the kinetic energy is the dominant energy contribution [Mor12]. Thus, the electrons are well described within a picture of non-interacting particles. In many other materials, however, Coulomb repulsion is of the order of the kinetic energy or even larger and causes strong correlations between the electrons [Mor12]. Since the behavior of each electron in the latter materials is influenced by the behavior of all other electrons, the electrons cannot be treated as independent particles anymore. Instead, the strongly-correlated, cooperative behavior of all electrons needs to be considered.

Strong correlations between the particles of a many-body system generally entail a collective behavior that emerges from the particles *and* their mutual interaction. The collective behavior differs qualitatively from that of the individual particles of the many-body system. Thus, this type of behavior has been termed *emergent behavior*. Emergent behavior occurs for example in strongly correlated materials at sufficiently low temperatures [Kot04]. The electrons then exhibit ground state phases, which can have exotic properties, some of which might have technological applications. Magnetite (Fe_3O_4), for instance, exhibits a charge-ordered phase below $\sim 120\,\mathrm{K}$ [Sen11] and loss of electrical resistance (*superconductivity*) has been observed in compounds of the $\mathrm{Ba-La-Cu-O}$ system below $13\,\mathrm{K}$ [Bed86]. At zero temperature, ground state phases are known as *quantum phases* and connect to each other via *quantum phase transitions* [Sac11]. In contrast to conventional phase transitions, which are induced by thermal fluctuations, quantum phase transitions are driven by quantum fluctuations due to the Heisenberg uncertainty principle [Sac11]. Even though quantum phase transitions exist solely at zero temperature and are hence physically inaccessible, they can affect the behavior of electrons in solids at temperatures well above absolute zero and even room temperature [Sac06]. Studying quantum phases, quantum phase transitions, and phase diagrams of strongly-correlated electrons in solids is thus interesting with respect to technological applications but also from the perspective of basic science to gain a complete understanding of strongly-correlated electron systems.

Strong correlations occur not only between electrons in solids but also in various other systems in nature. Further examples for strongly-correlated systems are atomic nuclei, neutron stars, and the quark-gluon plasma. The investigation of strongly-correlated quantum systems is therefore of general interest. In general, to theoretically describe a given quantum system and to predict its time evolution, it requires knowledge of the parameters that specify the quantum mechanical state of the system at any time of its evolution. The number of parameters as well as the number of differential equations to solve for this purpose increase exponentially with the number of constituent particles within the quantum system under study. Theoretical simulations of many-body systems on classical computers therefore become challenging if not impossible. Due to this computational limitation, some of today's open questions in the field of strongly-correlated systems are too complex to be solved even with presently existing and soon-to-be supercomputers [Gro17]. A solution to that limitation are experiments that use a well controllable quantum system to simulate and study another (often less controllable) quantum system. This approach has been pointed out by Richard Feynman [Fey82] and is known as *quantum simulation*. Various quantum systems have been suggested to serve as quantum simulators of strongly-correlated quantum many-body systems, for instance, neutral atoms, ions, and polar molecules [Geo14].

Neutral atoms provide favorable attributes for quantum simulation of strongly interacting many-body systems. The existence of different atomic species, for example, facilitates the experimental realization of different quantum systems (e.g. bosonic and fermionic systems, Bose-Fermi mixtures, heterospecies mixtures). This variety of different atoms therefore expands the list of quantum systems that can be experimentally simulated. Besides that, neutral atoms in ultra-high vacuum interact weakly with the environment. The weak coupling to the environment allows for a coherent evolution of atomic quantum systems and thereby the investigation of their intrinsic time evolution. If atoms are cooled to nanokelvin temperatures, one can gain experimental control of various atomic parameters through external fields. The contact interaction between ultracold atoms, for instance, can be tuned in sign and strength by means of external magnetic fields via magnetic Feshbach resonances [Chi10]. This tunability of the interaction gives a handle to realize weakly as well as strongly interacting, repulsive or attractive quantum systems along with non-interacting quantum systems if the interaction is nulled. The level structure of neutral atoms allows for the preparation and manipulation of the internal state of atoms via microwaves, radio waves, and laser light and for probing ultracold atoms. Moreover, laser light fields permit to trap ultracold atoms in optical potentials and enable one to control their motion along each spatial direction [Gri00]. Finally, by engineering appropriate laser light fields, the optical potentials can be made periodic in one or more dimensions (so-called *optical lattice potentials*). Atoms within optical lattice potentials offer the possibility to study the behavior of particles in periodic potentials such as that of electrons within the electrostatic potential of the ionic atom cores in crystals [Lew07].

Numerous ultracold atom experiments exist nowadays. Most of them work with alkali atoms, which possess advantageous properties for the formation of ultracold atomic samples, such as a relatively simple electronic structure compared to other atomic species. Ultracold atom samples of other atomic species, including earth-alkaline atoms, lanthanide atoms, and transition metals, have been experimentally demonstrated as well, and expand the scientific capabilities of ultracold atom experiments. The technical as well as experimental progress in the field of ultracold quantum gases in the continuum or in optical lattices is well documented in several review articles, see e.g. Refs. [Blo08, Gro17, Hof18]. A landmark experiment in the field of ultracold atoms in optical lattices was the observation of the phase transition from a superfluid to a Mott insulator with bosonic ^{87}Rb atoms [Gre02]. A similar type of phase transition occurs in systems that are described by the fermionic Hubbard Hamiltonian, for example in strongly-correlated electron systems of transition metals [Hub63]. The experimental observation of the superfluid to Mott insulator transition with ultracold ^{87}Rb atoms therefore was a first step towards quantum simulation of strongly-correlated many-body systems. Ultracold atoms have furthermore been used e.g. to study low-dimensional quantum systems, to realize quantum matter whose properties are characterized by topology (*topological quantum matter*), and to observe nonequilibrium dynamics in strongly-correlated many-body systems [Blo08, Gro17].

Quantum gas apparatuses for the production of ultracold single-species atom gases are built routinely nowadays. In contrast, experimental setups that aim at the production of ultracold mixtures of two different atomic species are less common due to their increased technical complexity. A two-species quantum gas apparatus, however, offers experimental capabilities beyond those of a single-species apparatus. In particular, within a two-species apparatus atoms can be combined pairwise, one atom of each atomic species, to form heteronuclear molecules. Diatomic heteronuclear molecules possess a permanent electric dipole moment and are therefore denoted as *polar molecules* [Atk17]. When exposed to an external electric field, polar molecules exhibit a tunable induced electric dipole moment and therefore interact with each other via dipole-dipole interaction. Ultracold polar molecules thus represent a platform to study quantum gases with dipolar interactions. In the case that the dipole-dipole interaction dominates over the contact interaction, the quantum gas is said to be a *dipolar quantum gas*. Dipolar quantum gases offer a rich variety of phenomena [Lah09]. They have been realized so far mainly with neutral atoms that possess a permanent magnetic moment μ_m and thereby interact via magnetic dipole-dipole interaction. The first experimental demonstration of a dipolar quantum gas involved ^{52}Cr atoms, for which μ_m equals $6\mu_\mathrm{B}$ with μ_B being *Bohr's magneton* [Koc08]. The chemical element with the largest permanent magnetic moment is dysprosium ($\mu_m = 10\mu_\mathrm{B}$). A dipolar quantum gas of dysprosium atoms was created for the first time in Ref. [Lu11]. Since the dipole-dipole interaction between polar molecules can be much stronger than for magnetic atoms [Gad16], dipolar effects in a quantum gas of polar molecules can be more pronounced. In total 10 different combinations for diatomic polar molecules exist among the alkaline elements lithium to cesium. The molecules of five of these combinations (LiCs, LiRb, LiK, KRb, and LiNa) react exoergically under pair collisions of like dimers in their rovibrational and electronic ground state [Jul11, Żuc10]. If no countermeasures are initiated, dimer-dimer collisions lead to molecular losses and thus an elimination of the molecular quantum gas. The remaining five combinations (NaCs, NaRb, NaK, KCs, and RbCs) are chemically stable and do not suffer from dimer-dimer losses in their rovibrational and electronic ground state. Ultracold quantum gases of polar molecules in their absolute ground state have been achieved in the past with various alkali dimers in free space as well as in optical lattices [Gad16].

Ultracold polar molecules, due to their permanent electric dipole moment, possess a spectrum that is purely rotational [Atk17]. This circumstance enables one to encode a spin$-1/2$ to polar molecules by assigning the two spin states 'spin up' and 'spin down' of the spin$-1/2$ to two different rotational states of the molecules. An ensemble of polar molecules that are localized to individual sites of an optical lattice and that are polarized by an external electric field can then be effectively described as an array of localized, interacting spins [Wal15]. The dipole-dipole interaction between these trapped and polarized molecules acts as a spin exchange interaction and can lead to mutual alignment of the effective spins as well as to dipolar spin exchange between them. This behavior of the polarized molecules is similar to that of electrons in strongly correlated materials, where mutual alignment of the electronic spins is caused by the exchange interaction of the electrons. Typically, the exchange interaction of electrons in correlated materials is anisotropic [Han94]. To properly describe the magnetic behavior of the electrons in different correlated materials, a multitude of spin lattice Hamiltonians has therefore been suggested. Because ultracold polar molecules in optical lattices can be mapped onto many of these spin lattice Hamiltonians, these systems represent an interesting scientific research field to study solid-state phenomena. One example for such a spin lattice Hamiltonian that can be investigated with polar molecules is the antiferromagnetic spin$-1/2$ Heisenberg XXZ Hamiltonian on a square lattice [Wal15]. It is considered to capture the physics that is essential to understand the occurence of high-temperature superconductivity in cuprate systems [Man91].[1] Further scientific goals that can be pursued with ultracold polar molecules include precision measurements, molecule spectroscopy, quantum chemistry, and quantum computing [Car09].

The investigation of ultracold atomic and molecular quantum gases in optical lattices within the past relied mainly on optical detection methods. The workhorse among these optical imaging methods makes use of the absorptive properties of the constituent atoms [Ket99] (or molecules [Wan10]) and hence is known as *absorption imaging*. Absorption imaging of ul-

---

[1] High-temperature superconductors are materials that become superconducting at temperatures well above the one for which mercury becomes superconducting.

tracold quantum gases in optical lattices is most often performed after the quantum gas has been released from the optical lattice and then yields information on bulk properties (e.g. atom number, momentum distribution, ...) [Blo13]. Sometimes, however, it is desirable to study local quantities of the trapped particles like the in-trap particle distribution or entropy. For this reason, more and more quantum gas apparatuses study ultracold quantum gases in optical lattices in-situ via fluorescence imaging. To observe and resolve single atoms while they are trapped at single sites of an optical lattice, these apparatuses employ a high-resolution imaging system.[2] Accordingly, this imaging technique is known as *fluorescence quantum gas microscopy*. Fluorescence quantum gas microscopy has been demonstrated for the first time in 2009 using ^{87}Rb atoms [Bak09, She10]. The capability to detect single atoms and to resolve single lattice sites makes fluorescence quantum gas microscopy an ideal instrument to conduct microscopic studies of model Hamiltonians and to observe spatial ordering in quantum phases.

This Thesis centers around the design of a new two-species quantum gas apparatus within the Nägerl group in Innsbruck. The new apparatus aims at studying ultracold atoms and polar molecules within optical lattices via fluorescence quantum gas microscopy. At the beginning of this Thesis none of the existing quantum gas apparatuses of the Nägerl group offered the experimental capabilities to perform fluorescence quantum gas microscopy. It was therefore initially intended to convert the existing single-species CsIII apparatus into a two-species quantum gas apparatus and to equip it with a high-resolution imaging system for fluorescence quantum gas microscopy. The CsIII apparatus has been used to perform experimental work on ultracold Cs atoms and Cs_2 molecules in the past and has been running reliably over many years. A reconstruction of it, however, would have required a temporary shut down. After several months of planning the reconstruction of the CsIII apparatus, it was therefore decided to refrain from a modification of the CsIII apparatus. Instead, it was decided to set up a completely new laboratory with an entirely new quantum gas apparatus. The new apparatus facilitates the production of quantum gases of the two atomic species cesium and potassium. Ultracold quantum gases of cesium have a long tradition in Innsbruck and much experience has been gained with this atomic species in previous experiments over the past years [Web03b, Dan10, Rei17]. Cesium has only one stable isotope, ^{133}Cs, which is a boson [San09].[3] It offers magnetic Feshbach resonances and therefore allows for tuning of the interparticle interactions. Potassium on the other side has three stable isotopes, namely ^{39}K, ^{40}K, and ^{41}K [San08]. The isotopes ^{39}K and ^{41}K are bosonic whereas the isotope ^{40}K is fermionic. The isotope ^{40}K is the only stable fermionic isotope among the alkali metal elements besides ^{6}Li. The choice of atomic species of the new K$-$Cs apparatus will enable the Nägerl group to create and study a wide range of different quantum systems ranging from atomic K and Cs quantum gases to K$-$Cs mixtures and KCs molecules with bosonic or fermionic spin statistics or mixtures of both.

The future research lines of the new K$-$Cs apparatus are twofold: one research line will focus on using ultracold atoms in optical lattices to study (strongly-correlated) many-body quantum systems. An important aspect of this research line will be the experimental realization of model Hamiltonians and the investigation of their phase diagrams as well as the properties of their quantum phases. As part of this research line, the high-resolution imaging system of the K$-$Cs apparatus will allow for imaging of the trapped atoms with single-atom and single-site resolution and therefore for in-situ detection of spatial ordering in quantum phases. A model Hamiltonian of interest will be the Fermi-Hubbard Hamiltonian for the case

---

[2] High-resolution imaging of ultracold molecules with single-molecule and single-site resolution has not been experimentally realized up to now.

[3] As ^{133}Cs is the only stable isotope of Cs, I will often use the notation Cs instead of ^{133}Cs in this Thesis.

that the number of atoms within the optical lattice equals the number of lattice nodes (one-atom commensurate filling). In this respect, it will be attractive to probe the entire phase diagram of the Fermi-Hubbard Hamiltonian and to observe and investigate spin ordering e.g. in the weakly interacting regime. The latter might be of relevance for real materials [Tar18]. Away from a one-atom commensurate filling, i.e. in the presence of an excess or defect of atoms relative to the number of lattice nodes, the Fermi-Hubbard model is referred to as being doped. The doped Fermi-Hubbard model promises to exhibit new quantum phases such as a $d-$wave superconducting phase [Tar18]. Thus, it will be also interesting to study the doped Fermi-Hubbard model for different particle and hole dopings. The second research line of the K$-$Cs apparatus will concentrate on the production of ultracold polar KCs molecules and their application to study spin lattice models. Here, the experimental realization of the spin$-1/2$ antiferromagnetic XXZ Heisenberg model on a two-dimensional square lattice will be of special interest. This spin model is assumed to describe the physics of the current-carrying atomic layers of cuprates, which are known for being high-temperature superconductors [Man91, Han94]. Finally, since the new K$-$Cs apparatus will allow for switching between the bosonic and the fermionic K isotopes, also the production of fermionic ^{40}K^{133}Cs molecules will be within reach. Fermionic ^{40}K^{133}Cs molecules are the only chemically stable fermionic molecules of two alkali atoms apart from ^{23}Na^{40}K [Jul11]. The K$-$Cs apparatus thus facilitates the investigation of quantum phenomena in ultracold gases of fermionic molecules such as the expected occurence of a molecular superfluid due to Bardeen-Cooper-Schrieffer pairing of fermionic molecules [Car09].

Thesis Overview

The work presented in this Thesis focuses on the design and realization of a new two-species quantum gas apparatus for ultracold mixtures of K and Cs atoms and KCs ground state molecules. The Thesis describes the technical design of the entire K$-$Cs vacuum apparatus and explains each of its sections in detail. To generate electric fields and thus to polarize KCs molecules, the apparatus comprises a set of electrodes. Two electric field configurations that can be generated by these electrodes are simulated as part of this Thesis. The electric field homogeneities are numerically analyzed and the influence of field inhomogeneities on future experiments on the spin$-1/2$ Heisenberg XXZ lattice model with ^{39}KCs molecules is determined. Additionally, induced electric dipole moments of ^{39}KCs molecules are computed as a function of an applied electric field. The results will be relevant for future experiments with ^{39}KCs molecules. A long term goal of the K$-$Cs apparatus is to image ^{39}K atoms in optical lattices in-situ via fluorescence imaging in the violet region of the visible spectrum at $404.4\,\mathrm{nm}$. For this reason, a home-built diode laser setup is built that generates laser light at $404.4\,\mathrm{nm}$. To predict the optical lattice potential that the trapped ^{39}K atoms experience in different atomic states during violet fluorescence imaging, the frequency-dependent atomic polarizabilities of the ground and several excited atomic states of ^{39}K are calculated. Finally, this Thesis addresses the question whether violet fluorescence imaging and simultaneous electromagnetically-induced transparency cooling will allow for the performance of violet fluorescence quantum gas microscopy of ultracold ^{39}K atoms in optical lattices.

The Thesis is structured as follows: **Chapter 1** introduces the theoretical framework to describe electrons in crystals. This mathematical formalism has great similarity to the description of ultracold atoms in optical lattices and will be helpful to understand later Chapters. **Chapter 2** summarizes general properties of ultracold atoms and discusses how optical lattices can be generated in experiments. As an example for how model Hamiltonians can be realized with ultracold atoms in optical lattices the experimental implementation of the bosonic version of the Fermi-Hubbard model, also known as Bose-Hubbard model, is discussed. **Chapter 3** explains the fundamentals of fluorescence quantum gas microscopy of ultracold atoms in optical lattices and outlines the experimental sequence that is planned to be used for fluorescence quantum gas microscopy within the new K$-$Cs apparatus. **Chapter 4** establishes the mathematical formalism to calculate static and frequency-dependent atomic polarizabilities. The obtained equations are used to numerically determine frequency-dependent atomic polarizabilities for ^{39}K. **Chapter 5** deals with violet fluorescence imaging of trapped ^{39}K atoms and simultaneous laser cooling via electromagnetically-induced transparency cooling. It addresses the question whether this technique can be used for violet fluorescence quantum gas microscopy of ultracold ^{39}K atoms in optical lattices and therefore analyzes basic quantities. **Chapter 6** describes the technical design of the main system of the K$-$Cs apparatus. **Chapter 7** summarizes the first experimental results that were obtained with the main system of the K$-$Cs apparatus and that were published in three articles of peer-reviewed journals [Grö16, Grö17c, Grö17b]. **Chapter 8** describes the design of the science chamber of the K$-$Cs apparatus. **Chapter 9** presents numerical results for the induced electric dipole moments of ^{39}KCs molecules as a function of an external electric field. It discusses electric field simulations for the electrodes within the science chamber and analyzes the impact of the found electric field inhomogeneities on future experiments. In addition, the Chapter evaluates the electric field dependency of the spin$-1/2$ Heisenberg XXZ lattice model parameters for ^{39}KCs molecules and numerically analyzes the amplitude for dipolar spin exchange between ^{39}KCs molecules within the K$-$Cs apparatus. **Chapter 10** presents the experimental work on the home-built diode laser that is used to generate violet laser light at $404.4\,\mathrm{nm}$. The Thesis concludes with a **Summary** of the presented work and an **Outlook** of the ongoing work in the K$-$Cs laboratory. Additional technical information on the vacuum apparatus is given in the **Appendix**.

1. Electrons in Solids

A core motivation of the K$-$Cs apparatus is the simulation and studying of the behavior of electrons in solids with ultracold atoms in optical lattices. Ultracold atoms in optical lattices behave similarly to electrons in solids. Because of this similarity, mathematical concepts of solid-state physics have been adopted to describe ultracold atoms in optical lattices. This Chapter therefore aims to give a general introduction to the theoretical description of electrons within solids. The mathematical concepts and nomenclature introduced in this Chapter will be useful in later Chapters.

The behavior of electrons in a solid depends critically on the ratio of their kinetic energy and Coulomb interaction energy. If the Coulomb interaction energy is small compared to the kinetic energy of the electrons (*weak interactions*), the electrons within a solid move independently from each other. When the Coulomb interaction energy is large compared to the kinetic energy (*strong interactions*), strong correlations arise and thus a collective behavior of the electrons emerges [Ful12]. This Chapter summarizes different theoretical approaches, which have been developed in the past, to describe independent and strongly-correlated electrons in solids. For the case of strong interactions, the Chapter focuses on two important model Hamiltonians, namely the Fermi-Hubbard Hamiltonian and the spin$-1/2$ Heisenberg XXZ lattice Hamiltonian. Both models are of interest for future experiments with the K$-$Cs apparatus. A comprehensive discussion of the subject of electrons in crystals is given in many textbooks of solid-state physics, e.g. [Ash76, Kop07, Gro14, Ful12].

1.1. Independent Electrons

A solid consists of a large number of atoms (about $\sim 10^{22}$ atoms per cubic centimeter). The ionic cores of the atoms sit on the sites of a lattice that, in the ideal case, is infinitely large and strictly periodic in all three spatial dimensions. The lattice is then also known as *Bravais lattice*. If the Bravais lattice has a simple cubic geometry with *lattice constant* a and with one ionic core per lattice site, the position vectors $\vec{R}$ of the ionic cores within the solid are defined through [Ash76]

$$\vec{R} = a\left(n_x\vec{e}_x + n_y\vec{e}_y + n_z\vec{e}_z\right), \tag{1.1}$$

where $\vec{e}_x$, $\vec{e}_y$, and $\vec{e}_z$ are *Cartesian unit vectors* in $x-$, $y-$, and $z-$direction and the coefficients n_x, n_y, and n_z are integers, i.e. $\{n_x, n_y, n_z\} \in \mathbb{Z}$. Since the mass of an ionic atom core (on the order of the *proton mass* m_p) is much larger than the *electron mass* m_e ($m_\mathrm{p}/m_\mathrm{e} \approx 1836$), the motion of the ionic atom cores in solids is much slower than that of the electrons. We therefore can neglect the motional degrees of freedom of the ionic cores in the remainder and assume a rigid crystal lattice (*adiabatic approximation*) [Ash76].

The ionic cores and the electrons outside of the ionic cores interact with each other through Coulomb interaction. The *interaction potential* V that a single electron μ' experiences depends on the positions $\vec{R}_i$ (with $i \in \mathbb{N}$) of all ionic cores and the positions $\vec{r}_\mu$ of all other electrons $\mu \in \mathbb{N}$ with $\mu \neq \mu'$, i.e. $V = V(\vec{R}_1, \vec{R}_2, \ldots, \vec{r}_1, \vec{r}_2, \ldots, \vec{r}_{\mu'}, \ldots)$. For weak interactions, electrons move independently from each other (*independent electron approximation*). In the independent electron picture the interaction potential $V = V(\vec{R}_1, \vec{R}_2, \ldots, \vec{r}_1, \vec{r}_2, \ldots, \vec{r}_{\mu'}, \ldots)$ can be replaced by an effective one-electron potential $V = V(\vec{r})$ [Ash76]. Given the discrete translational invariance of the Bravais lattice, the interaction potential $V(\vec{r})$ has the periodicity of the Bravais lattice, i.e. [Ash76]

$$V(\vec{r} + \vec{R}) = V(\vec{r}) \tag{1.2}$$

for all vectors $\vec{R}$ of the Bravais lattice. The Hamiltonian for an independent electron in a solid then reads

$$H = -\frac{\hbar^2}{2m_\mathrm{e}}\vec{\nabla}^2 + V(\vec{r}), \tag{1.3}$$

where $\hbar = h/2\pi$ is the *reduced Planck constant* with h being the *Planck constant*.

1.1.1. Bloch Waves

The three-dimensional (3D) stationary Schrödinger equation associated with the Hamiltonian H in Eq. (1.3) for a single electron within a solid with a simple cubic lattice has eigenfunctions $\Psi(\vec{r})$ and eigenenergies E with

$$H\Psi(\vec{r}) = E\Psi(\vec{r}). \tag{1.4}$$

To find the eigenfunctions $\Psi(\vec{r})$, one considers the electron to reside within the finite volume of a rectangular prism with sides L_x, L_y, and L_z and imposes the usual periodic (Born-von Karman) boundary conditions on the electron wave functions [Ash76]

$$\Psi(\vec{r} + L_x\vec{e}_x) = \Psi(\vec{r} + L_y\vec{e}_y) = \Psi(\vec{r} + L_z\vec{e}_z) = \Psi(\vec{r}), \tag{1.5}$$

where L_x, L_y, and L_z are integral multiples of the lattice constant a. The volume $L_x \cdot L_y \cdot L_z$ contains $\mathcal{N} = L_x/a \cdot L_y/a \cdot L_z/a$ atoms. The periodic boundary conditions in Eq. (1.5) put constraints on the *wave vector* $\vec{k} = \vec{\nabla}/i$ for which the Schrödinger equation in Eq. (1.4) is solvable. The allowed wave vectors $\vec{k}$ have Cartesian vector components k_x, k_y, and k_z that obey the relations [Gro14]

$$k_\nu = \frac{2\pi}{L_\nu}h_\nu, \qquad \text{with} \quad \nu = x, y, z, \tag{1.6}$$

where h_ν are positive (or negative) integers, i.e. $h_\nu \in \mathbb{Z}$. The eigenfunctions $\Psi(\vec{r})$ of the Schrödinger equation depend on the wave vector $\vec{k}$. We therefore adopt the notation for the eigenfunctions to $\Psi \rightarrow \Psi_{\vec{k}}$. The eigenfunctions $\Psi_{\vec{k}}$ are products of a plane wave and a function $u_{\vec{k}}(\vec{r})$ [Ash76]

$$\Psi_{\vec{k}}(\vec{r}) = e^{i\vec{k}\cdot\vec{r}}u_{\vec{k}}(\vec{r}). \tag{1.7}$$

The functions $u_{\vec{k}}(\vec{r})$ and the eigenfunctions $\Psi_{\vec{k}}(\vec{r})$ fulfill the relations [Ash76]

$$u_{\vec{k}}(\vec{r}+\vec{R}) = u_{\vec{k}}(\vec{r}), \tag{1.8}$$

$$\Psi_{\vec{k}}(\vec{r}+\vec{R}) = e^{i\vec{k}\cdot\vec{R}}\Psi_{\vec{k}}(\vec{r}) \tag{1.9}$$

for every lattice vector $\vec{R}$. Equation (1.7) together with Eq. (1.8) constitutes *Bloch's theorem* and the functions $\Psi_{\vec{k}}(\vec{r})$ are known as *Bloch waves*. For a given Bloch wave $\Psi_{\vec{k}}(\vec{r})$, the product $\hbar\vec{k}$ corresponds to its *quasi-momentum*.[1] The probability density $\left|\Psi_{\vec{k}}(\vec{r})\right|^2$ of a Bloch wave for all lattice sites $\vec{R}$ is non-zero and of equal magnitude. An electron that is described by a Bloch wave $\Psi_{\vec{k}}(\vec{r})$ is therefore delocalized and spreads out over the entire crystal. Defining vectors $\vec{G}$ through the relation [Ash76]

$$\vec{G} = \frac{2\pi}{a}\left(g_x\vec{e}_x + g_y\vec{e}_y + g_z\vec{e}_z\right) \tag{1.10}$$

one obtains the *reciprocal lattice vectors* $\vec{G}$ associated with a simple cubic Bravais lattice. The coefficients g_x, g_y, and g_z are integers with $\{g_x, g_y, g_z\} \in \mathbb{Z}$. A substitution $\vec{k} \rightarrow \vec{k}+\vec{G}$ (where $\vec{G}$ can be any vector given by Eq. (1.10)) leaves the eigenfunctions $\Psi_{\vec{k}}(\vec{r})$ unchanged, i.e. [Gro14]

$$\Psi_{\vec{k}+\vec{G}}(\vec{r}) = \Psi_{\vec{k}}(\vec{r}). \tag{1.11}$$

Equation (1.11) shows that the wave vector $\vec{k}$ of a Bloch wave $\Psi_{\vec{k}}(\vec{r})$ is not unambiguously defined. One therefore limits the wave vector of a Bloch wave to lie within a certain region of $\vec{k}-$space and then denotes it as $\vec{q}$. This $\vec{k}-$space region is defined by the following conditions for the Cartesian vector components q_x, q_y, and q_z of $\vec{q}$ [Ash76]:

$$-\pi/a \leq q_x, q_y, q_z < \pi/a. \tag{1.12}$$

Equation (1.12) defines the *first Brillouin zone* (1. *BZ*) of the reciprocal lattice of a simple cubic Bravais lattice. If the wave vector $\vec{k}$ lies without the 1. Brillouin zone, it can be transfered into it by a reciprocal lattice vector $\vec{G}$ with

$$\vec{k} = \vec{q}+\vec{G}. \tag{1.13}$$

Owing to the reduction of the Bloch wave vectors to the 1. Brillouin zone, for each wave vector $\vec{q}$ Eq. (1.4) has in principle infinitely many solutions $\Psi_{\vec{q}}(\vec{r})$, which have different eigenenergies [Ash76, Gro14]. To distinguish the solutions for a given wave vector $\vec{q}$, they are labeled with the *band index* $n \in \{0, 1, 2, \dots\}$ in order of increasing energy ($E \rightarrow E_{\vec{q}}^{(n)}$).

Eigenenergies $E_{\vec{q}}^{(n)}$ that belong to the same band index n form an *energy band* of the solid. Since the eigenenergies $E_{\vec{q}}^{(n)}$ for a given $\vec{q}$ are discrete and increase with band index n, energy bands with different band indices are shifted in energy. All energy bands together constitute

---

[1] Bloch waves $\Psi_{\vec{k}}(\vec{r})$ are not eigenstates of the momentum operator $\frac{\hbar}{i}\vec{\nabla}$ as can be verified by evaluation of the derivative [Sin01]. The quantity $\hbar\vec{k}$ therefore does not correspond to the classical electron momentum.

the *band structure* of the solid. The ground state of the electrons within a solid is found by filling up the single-electron levels with electrons. To account for Pauli's exclusion principle, electrons in the same level must have opposite spins. Among the energy bands that are completely filled with electrons at zero temperature the energetically highest band is denoted as *valence band*. The band next higher in energy may be only partially filled with electrons or entirely empty. This latter energy band is denoted as *conduction band*.

An alternative representation of Bloch waves can be obtained through expansion in plane waves according to

$$\Psi(\vec{r}) = \sum_{\vec{k}} C_{\vec{k}} e^{i\vec{k}\cdot\vec{r}}. \tag{1.14}$$

Here, the $C_{\vec{k}}$ are expansion coefficients and the sum is over all vectors $\vec{k}$ that satisfy Eq. (1.6). As the plane wave expansion of $\Psi^{(n)}_{\vec{q}}(\vec{r})$ contains solely wave vectors $\vec{k}$ that differ from $\vec{q}$ by reciprocal lattice vectors $\vec{G}$, it simplifies to [Ash76]

$$\Psi^{(n)}_{\vec{q}}(\vec{r}) = \sum_{\vec{G}} C^{(n)}_{\vec{q}-\vec{G}} e^{i(\vec{q}-\vec{G})\cdot\vec{r}} \tag{1.15}$$

with the sum taken over all reciprocal lattice vectors $\vec{G}$.

1.1.2. Wannier Functions

Another common description of independent electrons in solids is attained through Fourier series expansion of the Bloch waves in Eq. (1.15). With this expansion a Bloch wave $\Psi^{(n)}_{\vec{q}}(\vec{r})$ can be expressed as [Gro14, Kop07, Mar12]

$$\Psi^{(n)}_{\vec{q}}(\vec{r}) = \frac{1}{\sqrt{\mathcal{N}}} \sum_{\vec{R}} \tilde{w}_n(\vec{r}-\vec{R}) e^{i\vec{q}\cdot\vec{R}}. \tag{1.16}$$

Equation (1.16) shows that a Bloch wave $\Psi^{(n)}_{\vec{q}}(\vec{r})$ can be regarded as a sum of functions $\tilde{w}_n(\vec{r})$ that are translated to all lattice sites $\vec{R}$, multiplied by a phase factor. Since the functions $\tilde{w}_n(\vec{r}-\vec{R})$ are Fourier coefficients of $\Psi^{(n)}_{\vec{q}}(\vec{r})$, they are given through [Gro14, Kop07, Mar12]

$$\tilde{w}_n(\vec{r}-\vec{R}) = \frac{1}{\sqrt{\mathcal{N}}} \sum_{\vec{q}} e^{-i\vec{q}\cdot\vec{R}} \Psi^{(n)}_{\vec{q}}(\vec{r}). \tag{1.17}$$

The functions $\tilde{w}_n(\vec{r}-\vec{R})$ are superpositions of Bloch waves $\Psi^{(n)}_{\vec{q}}(\vec{r})$ of the first Brillouin zone of band n. The functions $\tilde{w}_n(\vec{r}-\vec{R})$ describe an electron that is localized to a lattice site at position $\vec{R}$ and are known as *Wannier functions*.[2] The set of Wannier functions $\tilde{w}_n(\vec{r}-\vec{R})$ of

---

[2] Due to the periodic boundary conditions for the electron wave functions in Eq. (1.5), the set of $\vec{k}$ vectors for which Eq. (1.4) is solvable is discrete (see Eq. (1.6)). The original publication on Wannier functions (Ref. [Wan62]) as well as Ref. [Ash76] (much cited in this Chapter) are based, however, on formulas for continuous $\vec{k}$. As a result, the mathematical expressions for $\Psi^{(n)}_{\vec{q}}(\vec{r})$ and $\tilde{w}_n(\vec{r})$ given in Refs. [Wan62, Ash76] differ from those presented in this Thesis. The differences between the two representations are discussed in Ref. [Mar12].

all bands n and for all lattice sites $\vec{R}$ constitutes an orthonormal basis of functions [Ash76]. Wannier functions depend on the relative distance $\vec{r} - \vec{R}$ and decay exponentially at large relative distances [Nen83]. The probability density $\left|\tilde{w}_n(\vec{r} - \vec{R})\right|^2$ of Wannier functions thus can be seen as concentrated near the lattice sites $\vec{R}$. Since Wannier functions $\tilde{w}_n(\vec{r} - \vec{R})$ have contributions from Bloch waves $\Psi_{\vec{q}}^{(n)}(\vec{r})$ with different wave vectors $\vec{q}$, they are delocalized in momentum space. For the same reason, Wannier functions are no eigenfunctions of the Schrödinger equation in Eq. (1.4).

Bloch waves $\Psi_{\vec{q}}^{(n)}(\vec{r})$ and Wannier functions $\tilde{w}_n(\vec{r} - \vec{R})$ allow one to describe electrons in materials in which the electrons interact weakly with each other. This condition is fulfilled in insulators as well as in metals [Ash76]. We now discuss two approximations to Bloch waves that lead to a simplified description of electrons in these material classes.

1.1.3. Tight-Binding Approximation

We first consider a lattice of atoms in which the wave function overlap of adjacent atoms is much smaller than unity. An electron in the vicinity of an ionic atom core at distances small compared to the lattice constant a can then be thought of as being barely affected by other ions and electrons of the lattice. In this case, near each lattice site $\vec{R}$ the full Hamiltonian of the lattice can be approximated by the Hamiltonian of an isolated atom, H_{atom} [Ash76]. An isolated atom has electronic orbital eigenfunctions $\varphi_n(\vec{r})$ and eigenenergies E_n^{atom} given through

$$H_{\text{atom}}\varphi_n(\vec{r}) = E_n^{\text{atom}}\varphi_n(\vec{r}). \tag{1.18}$$

The subscript n in Eq. (1.18) denotes the atomic level from which the nth energy band originates when atoms of the same kind are put together to form a lattice.

If the Bloch energies $E_{\vec{q}}^{(n)}$ of the nth energy band are approximate to the eigenenergy E_n^{atom} of a free atom ($E_{\vec{q}}^{(n)} \approx E_n^{\text{atom}}$) across the entire 1. Brillouin zone, the electrons of that band can be considered as being localized to the individual atoms (*tight-binding approximation*) [Ash76]. The Wannier functions $\tilde{w}_n(\vec{r} - \vec{R})$ in Eq. (1.16) can then be approximated by localized atomic eigenfunctions $\varphi_n(\vec{r} - \vec{R})$ or a linear combination of such with [Ash76]

$$\tilde{w}_n(\vec{r} - \vec{R}) \approx \sum_m b_m \varphi_m(\vec{r} - \vec{R}), \tag{1.19}$$

where the b_m are expansion coefficients. If we substitute the Wannier functions $\tilde{w}_n(\vec{r} - \vec{R})$ in Eq. (1.16) with the approximation of Eq. (1.19), we obtain

$$\Psi_{\vec{q}}^{(n)}(\vec{r}) \approx \frac{1}{\sqrt{\mathcal{N}}} \sum_{\vec{R}} \sum_m b_m \varphi_m(\vec{r} - \vec{R}) e^{i\vec{q}\cdot\vec{R}}. \tag{1.20}$$

Equation (1.20) represents the wavefunction of an electron in the tight-binding approximation. The tight-binding approximation provides a good description of the electrons in insulators. Owing to the small but finite overlap of atomic orbitals of neighboring atoms, an electron that is described in the tight-binding approximation can be found at any lattice site $\vec{R}$ of the solid with equal probability as can be seen from Eq. (1.20). Taking as an example the case that the expansion in Eq. (1.19) contains only a single, non-degenerate orbital, namely an $s-$orbital, the resulting Bloch waves form an $s-$band of the lattice.

1.1.4. Nearly Free Electron Approximation

The tight-binding approximation yields a good description of electrons in insulators, as discussed previously. It, however, fails for conduction band electrons in metals. In the latter case, the orbital overlap of adjacent atoms is larger than for insulators. The conduction electrons cannot be considered as localized anymore and hence the electron wavefunctions cannot be constructed from undisturbed atom orbitals. Conduction electrons in metals, instead, must be seen as mobile. Due to their mobility, they experience an attenuated Coulomb interaction in many metals and behave as if they move within an almost constant potential $V(\vec{r})$ [Ash76].[3] For completeness, we summarize how nearly free electrons within a lattice can be described.

A convenient starting point is the plane wave expansion of the electron wavefunction according to Eq. (1.14). If the interaction potential $V(\vec{r})$ in Eq. (1.3) is expanded into plane waves as well, it takes the form [Gro14]

$$V(\vec{r}) = \sum_{\vec{G}} V_{\vec{G}} e^{i\vec{G}\cdot\vec{r}} \tag{1.21}$$

with the sum taken over all reciprocal lattice vectors $\vec{G}$ and the coefficients $V_{\vec{G}}$ being the associated expansion coefficients. Inserting Eqs. (1.21) and (1.14) into Eq. (1.4) and rewriting the resulting equation yields [Gro14]

$$\left[\frac{\hbar^2}{2m_\mathrm{e}}(\vec{q}-\vec{G})^2 - E(\vec{q})\right] C_{\vec{q}-\vec{G}} + \sum_{\vec{G}'} V_{\vec{G}'} C_{\vec{q}-\vec{G}-\vec{G}'} = 0. \tag{1.22}$$

The set of linear equations in Eq. (1.22) determines the Bloch wave coefficients $C_{\vec{q}-\vec{G}}$ for an electron with wave vector $\vec{q}$. Since conduction electrons in metals experience a quasi-constant potential $V(\vec{r})$, they behave like quasi-free particles. Thus the eigenenergy $E(\vec{q})$ in Eq. (1.22) can be approximated by $E(\vec{q}) \approx V_{\vec{G}=\vec{0}} + (\hbar\vec{q})^2/2m_e$. For $\vec{G} \neq \vec{0}$ and considering only the two dominant terms of the sum over $\vec{G}'$ in Eq. (1.22), one obtains [Gro14]

$$C_{\vec{q}-\vec{G}} = \frac{V_{-\vec{G}} C_{\vec{q}}}{\frac{\hbar^2}{2m_\mathrm{e}}\left[\vec{q}^2 - (\vec{q}-\vec{G})^2\right]}. \tag{1.23}$$

For a quasi-constant potential $V(\vec{r})$, the coefficients $V_{\vec{G}\neq\vec{0}}$ are small compared to $V_{\vec{G}=\vec{0}}$. A second coefficient besides $C_{\vec{q}}$, namely $C_{\vec{q}-\vec{G}}$ in Eq. (1.23), therefore becomes significant only if the relation [Gro14]

$$\vec{q}^2 \approx (\vec{q}-\vec{G})^2 \tag{1.24}$$

---

[3] A second reason that leads to an attenuated Coulomb interaction for the conduction electrons in metals relates to Pauli blocking due to the electrons of the ionic cores [Ash76].

for Bragg reflection is fulfilled. A conduction electron with wave vector $\vec{q}$ away from the Brillouin zone boundary does not fulfill Eq. (1.24). In this case, the plane wave expansion in Eq. (1.14) is governed by a single plane wave with expansion coefficient $C_{\vec{q}}$. The electron thus can be approximately described by a single plane wave (*nearly free electron approximation*). The nearly free electron approximation cannot be employed to describe electrons in real solids. However, it produces results that are similar to those of more elaborate models of electrons [Ash76].

1.2. Correlated Electrons

Electrons in insulators and metals are generally well described within the independent electron picture, which was outlined in Sec. 1.1. The same, however, is not true for electrons in transition metals. Transition metals possess a (hybridized) conduction band and in addition an incompletely filled $d-$band [Ash76, Mot64]. It is mostly because of the $d-$band electrons that transition metals exhibit their characteristic properties [Hub63]. Due to the narrow confinement of electrons in $d-$orbitals, two electrons that occupy the same $d-$orbital with opposite spins experience an enhanced Coulomb repulsion [Vol12]. As a consequence, the motion of the $d-$electrons within a lattice is not independent anymore but rather governed by correlations. Transition metals, like any other material with strongly-correlated electrons, are therefore often termed *strongly-correlated materials*. This Section introduces two commonly used models to describe electrons in strongly-correlated materials. These two models are the Fermi-Hubbard model [Hub63] and the spin$-1/2$ Heisenberg XXZ lattice model [Bis17].

1.2.1. The Fermi-Hubbard Model

We consider a solid with a simple cubic lattice geometry and with one atom per lattice site. Each atom contributes an atomic $s-$orbital, which carries up to two electrons of opposite spins. The solid that is formed by the atoms thus possesses a single energy band, namely an $s-$band. Two electrons of the $s-$band interact strongest with each other when they share a common lattice site. We thus consider only on-site interaction in the following. This approximation ignores the long-range character of the Coulomb interaction and thereby neglects intersite interactions. Hence, it represents a crucial simplification of the real state of affairs. The interaction energy of two electrons on the same lattice site is denoted as *on-site interaction energy U*. If U is positive ($U > 0$), the on-site interaction corresponds to repulsive Coulomb interaction. In the opposite case with $U < 0$ the on-site interaction is attractive.

Since the atomic $s-$orbitals overlap with each other and form an energy band, electrons can tunnel from one lattice site to another site. Tunneling between two sites i and j is specified by the *hopping matrix element t_{ij}*. In the simplest case, tunneling of electrons takes place only between nearest-neighbor lattice sites. If the hopping matrix element t_{ij} is equal for all six nearest neighbors j of each site i, all matrix elements t_{ij} take the same value $t_{ij} = -t$ with $t \geq 0$.

The Hamiltonian that describes the behavior of the $s-$band electrons, considering only on-site interaction and only nearest-neighbor tunneling, reads [Hub63]

$$\hat{H}_{\mathrm{FH}} = -t \sum_{\langle i,j \rangle} \sum_{\sigma} \left(\hat{c}^{\dagger}_{i\sigma} \hat{c}_{j\sigma} + \mathrm{h.c.} \right) + U \sum_{i} \hat{n}_{i\uparrow} \hat{n}_{i\downarrow}. \tag{1.25}$$

The operator $\hat{c}_{i\sigma}$ ($\hat{c}_{i\sigma}^{\dagger}$) in Eq. (1.25) annihilates (creates) an electron with spin $\sigma \in \{\uparrow, \downarrow\}$ at site i and therefore is called *annihilation* (*creation*) *operator*. The product of the two operators $\hat{c}_{i\sigma}$ and $\hat{c}_{i\sigma}^{\dagger}$ is equivalent to the *number operator* $\hat{n}_{i\sigma}$, which counts the electrons in spin state σ on site i and which is given by [Tar18]

$$\hat{n}_{i\sigma} = \hat{c}_{i\sigma}^{\dagger}\hat{c}_{i\sigma}. \tag{1.26}$$

The first sum in Eq. (1.25) is taken over all nearest-neighbor pairs $\langle i, j \rangle$ and spin states σ and represents the kinetic energy of the electrons. The second term corresponds to the interaction energy of the electrons and arises due to multiply occupied lattice sites. It is proportional to the on-site interaction energy U. By setting t to zero, the Hamiltonian $\hat{H}_{\mathrm{FH}}$ reproduces the atomic limit in which electrons are fully localized to the lattice sites. For $U = 0$, the electrons enter the regime of a non-interacting electron gas.

The Hamiltonian $\hat{H}_{\mathrm{FH}}$ in Eq. (1.25) is the *Fermi-Hubbard Hamiltonian*. It is one of the simplest extensions of the independent electron approximation and yet is exactly solvable only in certain cases as for example in one dimension [Tar18, Lie68]. The Fermi-Hubbard Hamiltonian was first derived for strongly-correlated electrons in a non-degenerate $s-$band [Hub63, Hub64b] and was then generalized to electrons in degenerate $d-$bands [Hub64a]. It describes the competition between kinetic energy and on-site interaction energy of $s-$band electrons on a lattice.

If the number of $s-$band electrons equals the number of lattice sites, each lattice site is occupied on average by one electron and the $s-$band is half-filled. At half filling and for strong repulsive interactions ($U \gg |t|$) the energy penalty U for double occupation of a lattice site is larger than the gain t in kinetic energy due to tunneling. Consequently, double occupancy is suppressed and each lattice site contains precisely one electron. Since in this situation the motion of the electrons is essentially frozen, the electrons are in an insulating state (*Mott-insulating state*).[4] The Fermi-Hubbard model predicts several other phases to occur at finite temperatures ($T > 0$). As the temperature is increased, the Mott-insulator state, for instance, connects to a metallic state via an insulator-to-metal transition. An overview of the different phases of the Fermi-Hubbard model can be found in Ref. [Tar18].

1.2.2. The Spin$-1/2$ Heisenberg XXZ Lattice Model

The Fermi-Hubbard model at half-filling, strong repulsive interactions ($U \gg |t|$), and temperature T with $k_{\mathrm{B}}T \ll U$, where k_{B} is the *Boltzmann constant*, exhibits a Mott-insulator ground state with precisely one electron per lattice site, similar to the case for $T = 0$ [Tar18]. In the Mott-insulator state the motional degrees of freedom of the electrons (sometimes also named *charge degree of freedom*) are essentially frozen out, however, the spin degree of freedom of the electrons ($\sigma \in \{\uparrow, \downarrow\}$) is still active. The Fermi-Hubbard Hamiltonian $\hat{H}_{\mathrm{FH}}$ in Eq. (1.25) under the previous conditions can be transformed into an effective Hamiltonian that contains only spin operators. Introducing the *vector spin operator* $\hat{S}_i$ that acts on the spin state of an electron at

---

[4] Band theory predicts that all materials with a partially filled conduction band (here the $s-$band) are metals. The occurence of the Mott-insulator state therefore cannot be understood within band theory, which is based on independent electrons and thus not applicable here.

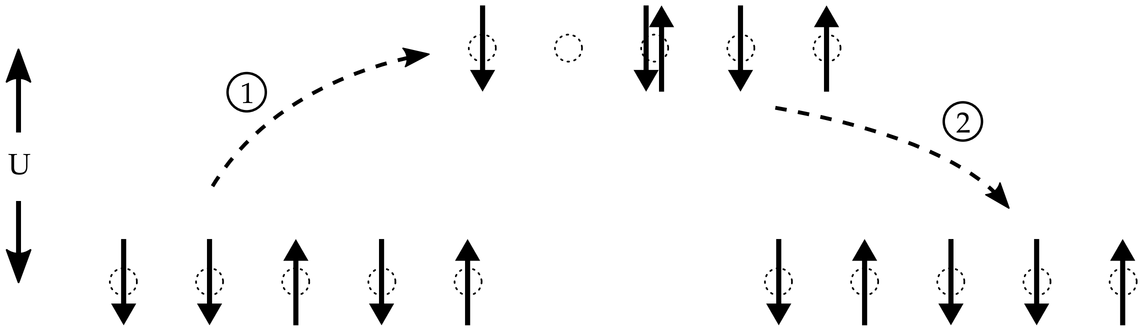

Figure 1.1.: Spin exchange. Two electrons with opposite spins (black arrows) at different lattice sites (dashed circles) can undergo exchange processes. (1) In the course of an exchange process, one of the two involved electrons tunnels to the lattice site of the other electron, resulting in an empty site and a doubly occupied site. This intermediate state is a virtual state whose energy is increased by the on-site interaction U. (2) Subsequently, the second electron tunnels to the original lattice site of the first electron. In the final state (lower right part of the figure), the two electrons appear to have exchanged their spins.

lattice site i, the effective Hamiltonian can be written, apart from a constant, as [Tar18, Aue94]

$$\hat{H}_{\text{HB}} = J_{\text{ex}} \sum_{\langle i,j \rangle} \hat{S}_i \cdot \hat{S}_j, \tag{1.27}$$

where the summation is over all pairs $\langle i, j \rangle$ of nearest-neighbor lattice sites. Mathematically, the Hamiltonian $\hat{H}_{\text{HB}}$ describes a lattice of spins that interact with each other. The strength of the effective spin-spin interaction is given by the coupling constant J_{ex}. If J_{ex} is negative ($J_{\text{ex}} < 0$), adjacent spins can minimize their energy by aligning themselves parallel to each other (*ferromagnetic spin order*). If J_{ex} is positive ($J_{\text{ex}} > 0$), antiparallel alignment of the spins (*antiferromagnetic spin order*) is energetically favorable. The Hamiltonian $\hat{H}_{\text{HB}}$ in Eq. (1.27) is known as the *Heisenberg Hamiltonian*.

Physically, the effective spin-spin interaction is a result of processes in which pairs of electrons swap their positions [Tar18, Aue94]. For $t \ll U$, an electron at lattice site i can tunnel to a nearest-neighbor lattice site j if the spins of the electrons at the two lattice sites are antiparallel. The tunneling electrons leaves behind an empty site and leads to an intermediate (virtual) state with double occupancy on the other site [Tar18]. Otherwise, if the two electrons have parallel spins, Pauli's exclusion principle forbids tunneling. The electron that originally occupied lattice site j subsequently tunnels to lattice site i, leading to a spin configuration with two swapped spins. This process is thus denoted as *spin exchange*.[5] Figure 1.1 illustrates the process of spin exchange between two electrons on a lattice. Since only electrons with opposite spins can lower their energy through spin exchange, spin exchange influences the mutual alignment of the electron spins and leads to an antiferromagnetic ordering [Aue94].

In the present Section, the Heisenberg Hamiltonian $\hat{H}_{\text{HB}}$ in Eq. (1.27) arose as an effective Hamiltonian from the Fermi-Hubbard Hamiltonian $\hat{H}_{\text{FH}}$. It is therefore possible to express the coupling constant J_{ex} through the parameters of the Fermi-Hubbard Hamiltonian. The

---

[5] In some materials tunneling of electrons takes place via an intermediate atom (*superexchange*), which can be treated in a similar fashion [Aue94].

coupling constant J_{ex} in terms of the hopping matrix element t and on-site interaction U reads [Tar18, Aue94]

$$J_{\text{ex}} = \frac{4t^2}{U}. \tag{1.28}$$

For half-filling and strong repulsive interactions, J_{ex} is positive and hence adjacent spins prefer antiferromagnetic spin order. Since the alternation of spin direction continues across the lattice, the ground state of the Hamiltonian $\hat{H}_{\text{HB}}$ for $J_{\text{ex}} > 0$ exhibits an antiferromagnetic and long-range spin order (*Néel order*). The Néel order is preserved for temperatures T well below some critical temperature T_{N} given by [Tar18]

$$T_{\text{N}} \sim \frac{J_{\text{ex}}}{k_{\text{B}}}. \tag{1.29}$$

For temperatures much higher than T_{N}, $T \gg T_{\text{N}}$, thermal fluctuations destroy the Néel order, leading to a state of uncorrelated spins with no spin order (*paramagnetic state*) [Tar18]. The temperature T_{N} is known as the *Néel temperature*. Unlike the 3D Heisenberg model, the Heisenberg model in 2D cannot exhibit long-range spin order for any temperature except for $T = 0$ as stated by the Mermin-Wagner-Hohenberg theorem [Mer66].

We now consider the Heisenberg model for spin$-1/2$ particles with antiferromagnetic spin interaction on a 2D square lattice. The lattice plane is assumed to coincide with the $xy-$plane. The dot product in Eq. (1.27) can be written in terms of the Cartesian vector components of the vector spin operator $\hat{S}_i$, namely $\hat{S}_i^x$, $\hat{S}_i^y$, and $\hat{S}_i^z$. The vector components obey the usual commutation relations [Mes65b]

$$[\hat{S}^k, \hat{S}^l] = i\hbar\epsilon_{klm}\hat{S}^m, \tag{1.30}$$

with $k, l, m \in \{x, y, z\}$ and ϵ_{klm} being the *Levi-Civita symbol*. We then obtain the expression

$$\hat{H}_{\text{HB}} = J_{\text{ex}} \sum_{\langle i,j \rangle} \left(\hat{S}_i^x \hat{S}_j^x + \hat{S}_i^y \hat{S}_j^y + \hat{S}_i^z \hat{S}_j^z \right). \tag{1.31}$$

From Eq. (1.31) it becomes apparent that J_{ex} is chosen to be identical for all three spin components (*isotropic Heisenberg Hamiltonian*). A more general treatment has to take into account unequal couplings between the spin components. In the most general case, spin coupling is characterized by three different coupling constants J_x, J_y, and J_z. Equation (1.31) must then be replaced by

$$\hat{H}_{\text{XYZ}} = \sum_{\langle i,j \rangle} \left(J_x \hat{S}_i^x \hat{S}_j^x + J_y \hat{S}_i^y \hat{S}_j^y + J_z \hat{S}_i^z \hat{S}_j^z \right). \tag{1.32}$$

The Hamiltonian $\hat{H}_{\text{XYZ}}$ is known as the *Heisenberg XYZ Hamiltonian*. For $J_x{=}J_y{=}J_\perp$ and $J_\perp{\neq}J_z$, Eq. (1.32) becomes

$$\hat{H}_{\text{XXZ}} = \sum_{\langle i,j \rangle} \left(J_\perp \left(\hat{S}_i^x \hat{S}_j^x + \hat{S}_i^y \hat{S}_j^y \right) + J_z \hat{S}_i^z \hat{S}_j^z \right) \tag{1.33}$$

and the *Heisenberg XXZ Hamiltonian* is obtained [Man91]. When $J_\perp$ and J_z are varied in magnitude, the Hamiltonian $\hat{H}_{\text{XXZ}}$ exhibits distinct ground states that give rise to different phases. In order to indicate the parameter ranges for these phases, we define the parameter $\lambda_{\text{aniso}} = J_z/J_\perp$ and rewrite the Hamiltonian $\hat{H}_{\text{XXZ}}$ as [Al 04]

$$\hat{H}_{\text{XXZ}} = J_\perp \sum_{\langle i,j\rangle} \left(\hat{S}_i^x \hat{S}_j^x + \hat{S}_i^y \hat{S}_j^y + \lambda_{\text{aniso}} \hat{S}_i^z \hat{S}_j^z\right). \tag{1.34}$$

The parameter λ_{aniso} describes the anisotropy of the spin-spin coupling. If $\lambda_{\text{aniso}} > 1$, the spins are predicted to align in $z-$direction with antiferromagnetic order (*Ising-like phase*). When λ_{aniso} is within the range $-1 < \lambda_{\text{aniso}} < 1$, the spins are expected to lie within the $xy-$plane (*planar-like phase*). For $\lambda_{\text{aniso}} < -1$, the spins are believed to align parallel to each other forming a ferromagnetic phase [Al 04, Bis17, Bis98].

One gains further insight into the spin$-1/2$ Heisenberg XXZ Hamiltonian by defining the *raising* and *lowering spin operators* $\hat{S}^+$ and $\hat{S}^-$, respectively, as [Mes65b]

$$\hat{S}^+ = \hat{S}^x + i\hat{S}^y, \tag{1.35}$$

$$\hat{S}^- = \hat{S}^x - i\hat{S}^y. \tag{1.36}$$

The raising and lowering spin operators, $\hat{S}^+$ and $\hat{S}^-$, allow one to rewrite Eq. (1.33) in the form [Wal15]

$$\hat{H}_{\text{XXZ}} = \sum_{\langle i,j\rangle} \left(\frac{J_\perp}{2}\left(\hat{S}_i^+ \hat{S}_j^- + \hat{S}_i^- \hat{S}_j^+\right) + J_z \hat{S}_i^z \hat{S}_j^z\right). \tag{1.37}$$

The first term in Eq. (1.37) is proportional to $J_\perp$. It causes combined spin flipping of opposite spins$-1/2$ at lattice sites i and j and thus leads to spin exchange. Spin-exchange processes preserve the total magnetization of the lattice spins. In contrast, the last term maintains the orientation of the individual spins.

The antiferromagnetic spin$-1/2$ Heisenberg XXZ Hamiltonian on a 2D square lattice is assumed to describe the electrons of the CuO_2 planes in cuprate high-temperature superconductors [Man91]. It has no exact solutions [Bis98]. Quantum simulation with ultracold quantum gases is an ideal tool to compute solutions for the antiferromagnetic spin$-1/2$ Heisenberg XXZ Hamiltonian on a 2D square lattice.

2. Ultracold Atoms in Optical Lattices

The K–Cs apparatus will employ ultracold atoms and molecules in optical lattices to study model Hamiltonians of solid state physics in future experiments. In this Thesis, we are concerned with bosonic quantum gases of atoms and molecules. To form the basis for the following Chapters, we review the basics of ultracold, bosonic atoms and their interactions in the present Chapter. Moreover, we introduce the fundamentals of optical lattices and discuss the implementation of a paradigm Hamiltonian, the Bose-Hubbard Hamiltonian, in ultracold, bosonic atom systems in optical lattices. A review of the physics of ultracold atoms in optical lattices is given e.g. in Refs. [Mor06, Blo08].

2.1. Ultracold Atoms and Interactions

A gas of $\mathcal{N}_{\text{atom}}$ atoms with *atom mass* m within a volume V_{gas} has an *average particle density* n_{atom} of

$$n_{\text{atom}} = \frac{\mathcal{N}_{\text{atom}}}{V_{\text{gas}}} \tag{2.1}$$

and thus a *mean interparticle separation* $\bar{d}$ of [Ket99]

$$\bar{d} = \frac{1}{\sqrt[3]{n_{\text{atom}}}}. \tag{2.2}$$

If the mean interparticle separation $\bar{d}$ is on the same order of magnitude or shorter than the thermal *de Broglie wavelength* λ_{dB} of the atoms with [Ket99]

$$\lambda_{\text{dB}} = \sqrt{\frac{2\pi\hbar^2}{mk_{\text{B}}T}}, \tag{2.3}$$

the atom gas is dominated by quantum effects (*quantum gas regime*). Atom gases that are created in typical quantum gas experiments have particle densities on the order of $n_{\text{atom}} \approx 10^{12}$ cm^{-3}. Hence, to enter the quantum gas regime, these gases need to be cooled down to temperatures in the nanokelvin regime and are then called *ultracold quantum gases*. At these temperatures and particle densities the *phase-space density* $\mathcal{D}$ of the atomic gas with [Met99]

$$\mathcal{D} = n_{\text{atom}}\lambda_{\text{dB}}^3 \tag{2.4}$$

is on the order of 1 or larger [Ket99].

A single cooling technique is usually incapable of reaching the desired low temperatures for ultracold atomic quantum gases. Instead, a sequence of different cooling and evaporation steps has to be applied to the atoms [Ket99]. These steps make use of well-established experimental techniques for trapping and cooling or evaporation of atoms. Many of these techniques require laser beams, often prepared in particular configurations, and magnetic fields. An overview of the experimental techniques for trapping and cooling of atoms is given in Ref. [Met99].

In the past decades, quantum gases of ultracold atoms have been achieved with bosonic atoms [And95] as well as with fermionic atoms [DeM99]. When cooled into the quantum gas regime, a gas of bosonic atoms undergoes a phase transition from a classical gas into a *Bose-Einstein condensate* (BEC) [Ket99]. The physics of Bose-Einstein condensation in atomic gases is discussed in Ref. [Pet08]. In contrast, fermionic atoms at ultracold temperatures form a *degenerate Fermi gas* [Ing07]. To shield ultracold quantum gases from the atmospheric environment, experiments with ultracold atoms are performed inside of an ultra-high vacuum (UHV) apparatus.

The thermodynamically stable configuration of most known atoms (and molecules) at nanokelvin temperatures is a solid [Pet08].[1] Hence, ultracold quantum gases are thermodynamically not stable and suffer from relaxation processes. The relaxation processes are caused by collisions of three atoms, where two atoms form a molecule after the collision and the third atom carries away the released binding energy [Fed96]. These collisions are known as *inelastic three-body collisions* and lead to solidification. As long as the experiment on the quantum gas is performed on a shorter timescale than the three-body collisions occur, three-body collisions are typically of no concern.

Besides inelastic three-body collisions, atoms in ultracold gases can also interact via pairwise collisions. Two-body collisions in which the total kinetic energy is conserved are denoted as *elastic two-body collisions*. At ultralow temperatures, elastic two-body collisions within a bosonic quantum gas can occur only for atoms that have zero relative angular momentum (*s-wave collisions*) [Jer14]. The cross-section for elastic s-wave collisions is then determined through a single parameter, the so-called *s-wave scattering length* a_{scatt} [Lah09, Jer14]. If the interparticle interaction of the atoms within the gas is dominated by two-body collisions and if scattering is limited to s-wave scattering, the effective interparticle interaction potential can be written as [Lah09, Jer14]

$$V_{\text{contact}}(\vec{R}) = \frac{4\pi\hbar^2 a_{\text{scatt}}}{m}\delta(\vec{R}), \tag{2.5}$$

where $\delta(\vec{R})$ is the *Dirac delta function* and $\vec{R}$ is the relative position vector of the atoms. The *contact interaction potential* $V_{\text{contact}}(\vec{R})$ is isotropic and, since it depends only on the particle density, short-range [Jer14, Lah09]. The s-wave scattering length a_{scatt} can be controlled through an external magnetic field and depends on the *magnetic field strength* B as [Chi10]

$$a_{\text{scatt}}(B) = a_{\text{bg}}\left(1 - \frac{\Delta_{\text{res}}}{B - B_{\text{res}}}\right). \tag{2.6}$$

For $B \to B_{\text{res}}$ the scattering length a_{scatt} diverges ($a_{\text{scatt}} \to \pm\infty$). The divergence of the scattering length a_{scatt} arises due to a *magnetic Feshbach resonance* [Chi10]. The center of the Feshbach resonance is at $B = B_{\text{res}}$ and the resonance width is Δ_{res}. The off-resonant value of a_{scatt} is given by the *background scattering length* a_{bg}, which can be positive as well as negative. For

---

[1] The only exception is helium, which forms a liquid at temperatures down to zero kelvin [Pet08, Cor02, Ket99].

$B = B_{\text{res}} + \Delta_{\text{res}}$, the scattering length a_{scatt} has a zero-crossing. By tuning the scattering length a_{scatt} close to a magnetic Feshbach resonance, the sign as well as the strength of the contact interaction in Eq. (2.5) can be controlled. This tunability of the scattering length a_{scatt} enables the realization and study of non-interacting ($a_{\text{scatt}} = 0$), weakly interacting as well as strongly interacting quantum gases in both the attractive ($a_{\text{scatt}} < 0$) and repulsive ($a_{\text{scatt}} > 0$) regime.

2.2. Optical Lattices

In order to create optical lattices for ultracold atoms and molecules, the K−Cs apparatus will employ interfering laser beams. This Section therefore recaps basic characteristics of Gaussian laser beams and sums up fundamentals of optical lattices.

2.2.1. Gaussian Beams and Optical Potentials

Laser beams in their simplest form can be approximated by Gaussian beams [Sie86]. A Gaussian laser beam with laser wavelength λ that propagates in $z-$direction and has a focus at the position $z = 0$ has an intensity distribution $I_{\text{L}}(x, y, z)$, which is given by [Sie86]

$$I_{\text{L}}(x, y, z) = \frac{2P}{\pi w^2(z)} \exp\left[-\frac{2(x^2 + y^2)}{w^2(z)}\right]. \tag{2.7}$$

Here, P is the total laser power and $w(z)$ is the transverse distance from the optical axis at axial position z at which the laser intensity has decreased to $1/e^2 \approx 0.135$ times the value $I_{\text{L}}(0, 0, z)$ on the optical axis. Thus, $w(z)$ characterizes the radial width (*beam width*) of the Gaussian beam at axial position z and is given by [Sie86]

$$w(z) = w_0 \sqrt{1 + \left(\frac{z}{z_{\text{R}}}\right)^2}. \tag{2.8}$$

The beam width varies along the propagation axis and is smallest in the focal plane of the Gaussian beam, where it is denoted as *beam waist* w_0. Propagation of a Gaussian laser beam is fully determined by the beam waist w_0 and the parameter z_{R} defined as [Sie86]

$$z_{\text{R}} = \frac{\pi w_0^2}{\lambda}. \tag{2.9}$$

The parameter z_{R} is also known as *Rayleigh length.*

An atom placed at position $\vec{r}$ within a Gaussian laser beam interacts with the local electric field $\vec{F}(\vec{r}, t) = \vec{\mathcal{E}} F_0(\vec{r}) \cdot (\exp(-i\omega_{\text{L}} t) + c.c.)/2$ of the laser, where $\vec{\mathcal{E}}$ is the unit field vector, $F_0(\vec{r})$ is the local electric field amplitude, and ω_{L} is the laser angular frequency. The interaction of the atom with the laser field gives rise to an oscillating induced electric dipole moment $\vec{p}$ of the atom. The induced dipole moment $\vec{p}$ has potential energy $-\vec{p} \cdot \vec{F}/2$ within the laser electric field. For this reason and because of the rapid laser oscillation the atom experiences a position-dependent, time-averaged *optical dipole potential* $V_{\text{dip}}(\vec{r})$ with [Gri00]

$$V_{\text{dip}}(\vec{r}) = -\frac{1}{2}\langle \vec{p} \cdot \vec{F} \rangle = -\frac{1}{c\epsilon_0} \operatorname{Re}(\alpha) I_{\text{L}}(\vec{r}). \tag{2.10}$$

The angular brackets $\langle\cdot\rangle$ in Eq. (2.10) symbolize averaging over the oscillation of the laser field. The constants c and ϵ_0 in Eq. (2.10) denote the *vacuum speed of light* and the *permittivity of free space* and α is the *atomic polarizability*, of which only the real part $\mathrm{Re}(\alpha)$ finds entrance into Eq. (2.10). Here, α is assumed to be a scalar for the sake of simplicity.[2] In arriving at the right side of Eq. (2.10) we made use of the relation between the *time-averaged laser intensity* $I_\mathrm{L}(\vec{r})$ and the laser field amplitude $F_0(\vec{r})$ [Gri00]

$$I_\mathrm{L}(\vec{r}) = \frac{1}{2}c\epsilon_0 \left|F_0(\vec{r})\right|^2 . \tag{2.11}$$

From Eq. (2.10) we see that the optical dipole potential $V_\mathrm{dip}(\vec{r})$ depends linearly on the intensity of the laser light. For $\mathrm{Re}(\alpha) > 0$, the potential energy of the atom in regions with higher laser intensity $I_\mathrm{L}(x, y, z)$ is less and thus the atom is attracted towards regions with maximum intensity. In the opposite case, $\mathrm{Re}(\alpha) < 0$, the atom is pulled towards regions with minimum intensity.

The optical dipole potential $V_\mathrm{dip}(\vec{r})$ that an atom in its internal ground state experiences within a Gaussian laser beam is obtained by inserting Eq. (2.7) into Eq. (2.10). When the laser frequency ω_L is tuned above the transition frequency ω_A of the strongest ground-state transition of the atom, i.e. $\omega_\mathrm{L} > \omega_\mathrm{A}$, the *detuning* $\Delta = \omega_\mathrm{L} - \omega_\mathrm{A}$ is positive (*blue detuning*). In the opposite case, $\omega_\mathrm{L} < \omega_\mathrm{A}$ and $\Delta < 0$, the laser light is said to be *red detuned*. In the remainder of this Thesis, we consider only optical dipole potentials that originate from red-detuned lasers. For a ground-state atom within a red-detuned Gaussian laser beam, $\mathrm{Re}(\alpha)$ is positive and thus the focus of the Gaussian laser beam acts as an *optical dipole trap* [Gri00, Met99].

Optical dipole traps are a commonly used experimental tool in ultracold atom experiments to trap atoms. In order to reduce spontaneous scattering of photons from the dipole trap laser beam by the trapped atoms, the frequency ω_L of the dipole trap laser beam is typically chosen many line widths off resonance (*far-off-resonance optical dipole trap*). The trap potential is then nearly conservative and gives rise to a *dipole force* $\vec{F}_\mathrm{dip}(\vec{r})$ that can be derived through [Gri00]

$$\vec{F}_\mathrm{dip}(\vec{r}) = -\vec{\nabla}V_\mathrm{dip}(\vec{r}). \tag{2.12}$$

Nowadays, far-off-resonance optical dipole traps (FORTs) in alkali quantum gas experiments have beam waists w_0 of tens to hundreds micrometers. To trap ultracold alkali atoms in FORTs of these sizes, the laser beam is focused down either by a single lens or a combination of lenses and a laser output power of up to several hundreds of watts is required. Since commercial high power lasers exist only at specific wavelengths, laser light at $1064\,\mathrm{nm}$ is typically used to realize FORTs.[3] Laser light at this wavelength is hundreds of nanometers away from the energetically lowest ground-state transitions in alkali atoms. The resulting dipole potential $V_\mathrm{dip}(\vec{r})$ can therefore be seen as quasi-static.

2.2.2. Periodic Optical Potentials

The spatial dependence of an optical potential $V_\mathrm{dip}(\vec{r})$ experienced by an atom is determined by the intensity distribution $I_\mathrm{L}(\vec{r})$ of the underlying laser field as can be seen from Eq. (2.10).

---

[2] A more thorough treatment of the subject of atomic polarizabilities follows in Ch. 4.

[3] In the early days of optical dipole traps for neutral atoms, FORTs for alkali atoms were realized at laser wavelengths other than $1064\,\mathrm{nm}$. See e.g. Refs. [Mil93, Tak96].

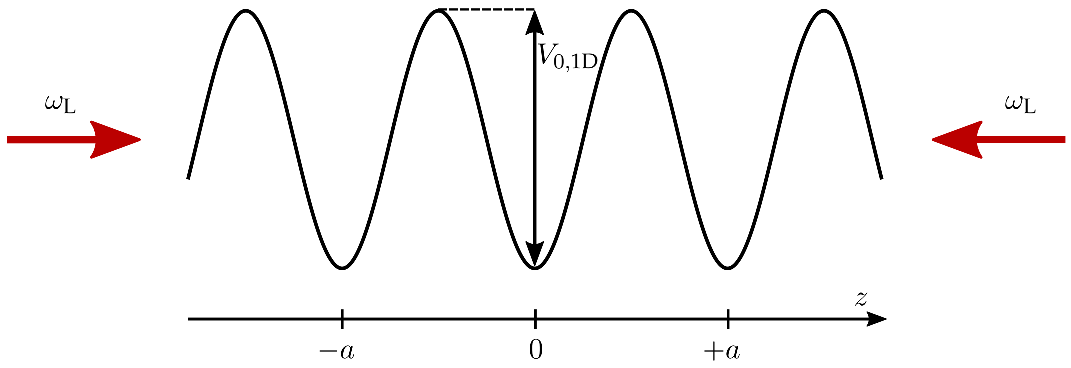

Figure 2.1.: One-dimensional optical lattice potential. A stationary 1D optical lattice can be created by two collinear, counter-propagating laser beams (red arrows), which have frequencies ω_L. The resulting optical potential (black line) has a squared cosinusoidal profile along the optical axis. The potential minima are equidistant with lattice constant a as their mutual spacing. Adjacent potential minima are separated from each other by a potential barrier of height $V_{0,1D}$.

By producing light fields with tailored intensity distributions it is thus possible to create optical potentials of different geometries and in particular optical lattice potentials. The simplest form of an optical lattice potential is realized by two counter-propagating, collinear laser beams. If both laser beams are linearly polarized and have the same polarization axis, the electric fields of the two overlapping laser beams interfere. The interference leads to a modulation of the laser intensity along the common optical axis of the two lasers.

To obtain an analytical expression for the resulting optical lattice potential, we assume that the two laser beams are Gaussian beams with intensity distributions $I_L(x, y, z)$ of the form given in Eq. (2.7). The Gaussian beams have laser frequencies $\omega_{L,1} = ck_{L,1}$ and $\omega_{L,2} = ck_{L,2}$ with $\omega_{L,1} \approx \omega_{L,2}$, where $k_{L,1} = 2\pi/\lambda_{L,1}$ and $k_{L,2} = 2\pi/\lambda_{L,2}$ are the corresponding *wave numbers*. We consider the case that the foci of the two Gaussian beams coincide at $z = 0$, that the beam waists $w_{0,L1}$ and $w_{0,L2}$ are of equal size ($w_{0,L1} = w_{0,L2} = w_0$), and that the laser beam powers $P_{L,1}$ and $P_{L,2}$ are identical ($P_{L,1} = P_{L,2} = P$). The optical lattice potential around the common focus ($|z| \ll w_0$) can then be approximated by

$$V_{1D}(x, y, z, t) \approx -V_{0,1D} \cdot \exp\left[-\frac{2\left(x^2 + y^2\right)}{w^2(z)}\right] \cdot \cos^2\left[\frac{(k_{L,1} + k_{L,2})}{2} z + \frac{(\omega_{L,2} - \omega_{L,1})}{2} t\right], \quad (2.13)$$

where the constant $V_{0,1D}$ is an abbreviation of the following conglomeration of constant parameters

$$V_{0,1D} = \frac{8P}{c\epsilon_0 \pi w_0^2} \cdot \mathrm{Re}(\alpha). \quad (2.14)$$

In the case that the two laser beams differ in their frequencies by $\Delta\omega_L = \omega_{L,1} - \omega_{L,2}$ such that $\lambda_{L,1} \approx \lambda_{L,2} \approx \lambda_L$, the optical lattice potential $V_{1D}(x, y, z, t)$ is time-dependent and moves along the $z-$axis at a velocity v given through [Sch06]

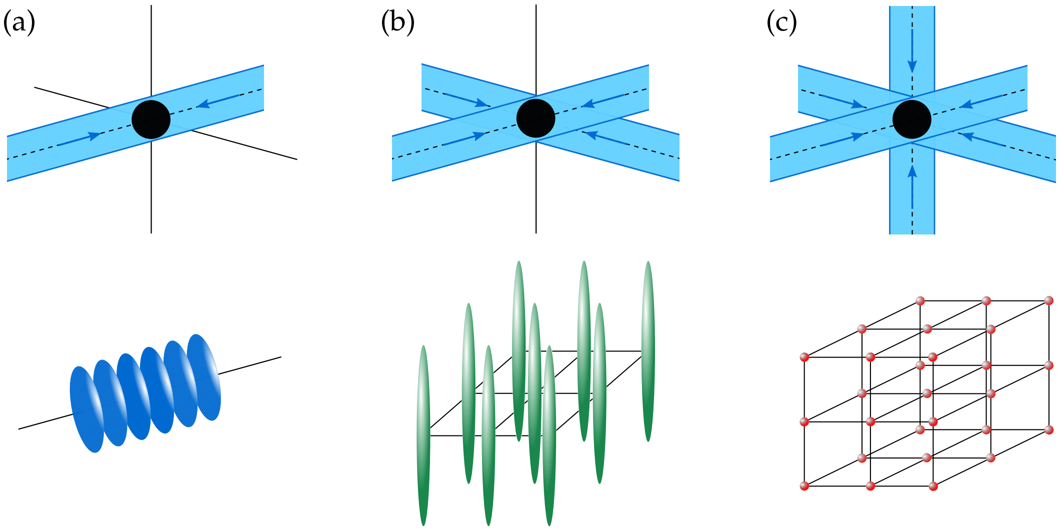

Figure 2.2.: Optical lattices. Three examples for the realization of optical lattices and the equipotential surfaces of the associated lattice potentials. (a) Two collinear, counter-propagating laser beams (blue arrows) create a 1D optical lattice of pancake-shaped traps. Superimposition of (b) one or (c) two further mutually orthogonal retro-reflected laser beam(s) forms a 2D or 3D optical lattice, respectively. The 2D optical lattice corresponds to a planar lattice of cigar-shaped traps, while the 3D lattice forms a crystal of spherical traps.

$$v = \lambda_\mathrm{L} \frac{\Delta\omega_\mathrm{L}}{4\pi}. \tag{2.15}$$

If the two laser frequencies are equal, i.e. $\omega_{\mathrm{L},1} = \omega_{\mathrm{L},2} = \omega_\mathrm{L}$ and thus $k_{\mathrm{L},1} = k_{\mathrm{L},2} = k_\mathrm{L}$, the lattice potential $V_\mathrm{1D}(x, y, z, t)$ in Eq. (2.13) is stationary and simplifies to

$$V_\mathrm{1D}(x, y, z) \approx -V_\mathrm{0,1D} \cdot \exp\left[-\frac{2(x^2 + y^2)}{w^2(z)}\right] \cdot \cos^2\left[k_\mathrm{L} z\right]. \tag{2.16}$$

The lattice potential $V_\mathrm{1D}(x, y, z)$ in Eq. (2.16) is governed in transverse $x-$ and $y-$direction by the Gaussian intensity envelope of the lattice laser beams whereas it is dictated along the $z-$axis mostly by the standing wave interference pattern. Figure 2.1 depicts the lattice potential $V_\mathrm{1D}(\vec{r})$ on the $z-$axis for $|z| \ll w_0$. The potential $V_\mathrm{1D}(\vec{r})$ possesses a series of potential minima along the $z-$axis within which atoms can be trapped. The potential minima, called *lattice sites*, have a mutual distance of $\Delta z = \lambda_\mathrm{L}/2$ and thus are equidistant. In analogy to the lattice constant a of a solid in Sec. 1.1, the separation Δz of the lattice sites is denoted as *lattice spacing* and also labeled with the symbol a. The height of the potential barrier between two successive lattice sites is the *lattice depth* $V_\mathrm{0,1D}$. It is chosen to be positive here. The lattice depth $V_\mathrm{0,1D}$ depends on the laser power P as well as the detuning Δ of the laser light (through the polarizability α), as can be seen from Eq. (2.14). Because of its spatial periodicity, $V_\mathrm{1D}(\vec{r})$ is denoted as one-dimensional (1D) optical lattice potential.

Optical lattice potentials that are periodic in more than one direction can be achieved by superimposing multiple laser beams. The most straightforward approach towards higher-dimensional optical lattices is to intersect mutually orthogonal, retro-reflected laser beams. Each retro-reflected laser beam creates a 1D optical lattice. By shifting the laser frequencies of the 1D optical lattices relative to each other, interferences between the lattice laser beams are time-averaged to zero. The emerging optical lattice potential at the common intersection point of the retro-reflected laser beams is then simply the sum of 1D optical lattice potentials. Two orthogonal, retro-reflected laser beams create in this way a 2D array of anisotropic, cigar-shaped traps (2D optical lattice). In contrast, a 1D lattice corresponds to a stack of pancake-shaped traps with tight confinement in axial direction and weaker confinement in radial direction. Adding a third retro-reflected laser beam at a right angle to the 2D lattice creates a 3D crystal of spherical traps. Figure 2.2 depicts the laser configurations for the three mentioned optical lattices and shows the equipotential surfaces of the associated lattice potentials.

A 3D optical lattice with simple cubic geometry is obtained when the three retro-reflected laser beams have similar laser frequencies ($\omega_{\mathrm{L},1} \approx \omega_{\mathrm{L},2} \approx \omega_{\mathrm{L},3}$). If the beam powers and beam waists are of equal magnitude and size for all three lattice laser beams, the optical potential around the common intersection point can be approximated by

$$V_{\mathrm{3D}}(x,y,z) \approx -V_0\left[\cos^2\left(k_{\mathrm{L}}x\right)+\cos^2\left(k_{\mathrm{L}}y\right)+\cos^2\left(k_{\mathrm{L}}z\right)\right]+\frac{1}{2}m\omega_{\mathrm{ext}}^2\left(x^2+y^2+z^2\right). \tag{2.17}$$

The optical lattice potential $V_{\mathrm{3D}}(x,y,z)$ consists of two contributions. The first term in Eq. (2.17) results from the three optical standing waves in $x-, y-$, and $z-$direction and produces a uniform, squared cosinusoidal lattice potential in each of these directions. The coefficient V_0 denotes the lattice depth of the 3D optical lattice. The last term describes a 3D harmonic trapping potential, which is characterized by the *external harmonic trapping frequency* ω_{ext}. It results from the transverse intensity profile of the Gaussian beams (see Eq. (2.7)). The harmonic potential represents an external confinement and causes a site-dependent energy offset. To simplify the further discussion, we neglect the external harmonic confinement, i.e. $\omega_{\mathrm{ext}} = 0$, and thus assume a uniform lattice potential of the form

$$V_{\mathrm{3D}}^{\mathrm{u}}(\vec{r}) = -V_0\left[\cos^2\left(k_{\mathrm{L}}x\right)+\cos^2\left(k_{\mathrm{L}}y\right)+\cos^2\left(k_{\mathrm{L}}z\right)\right]. \tag{2.18}$$

Independent experimental control of the lattice laser beams that form the 3D optical lattice allows one to dynamically modify the optical lattice in experiments. By ramping down the power of one (two) lattice beam(s), a 3D optical lattice is transfered into a 2D (1D) optical lattice. Optical lattices with geometries other than 3D simple cubic geometry can be created by varying the number of intersecting lattice laser beams, by altering their spatial arrangement or wavelengths or by adjusting the polarizations and mutual phases of the lasers [Pet94, Win13]. Among the optical lattice geometries that have been realized in the past are triangular [Bec10], honeycomb [Tar12], checkerboard [Wir10], as well as Kagome, 1D stripe and decorated triangular lattice geometries [Jo12]. An overview of systems that can be studied with ultracold atoms in optical lattices can be found e.g. in Ref. [Lew07].

2.2.3. Harmonic Approximation

A natural energy scale for ultracold atoms in optical lattices is the recoil energy E_{rec} an atom gains when it scatters a photon of the lattice laser light. It is thus common practice to express the depth V_0 of an optical lattice in units of the *lattice recoil energy* E_{rec} given by [Blo08]

$$E_{\mathrm{rec}} = \frac{h^2}{2m\lambda_{\mathrm{L}}^2}. \tag{2.19}$$

For lattice depths V_0 much larger than E_{rec}, i.e. $V_0 \gg E_{\text{rec}}$, the optical lattice potential $V_{\text{3D}}^{\text{u}}(\vec{r})$ in Eq. (2.18) can be approximated around the center $\vec{R}_i$ of each lattice site i by a harmonic potential

$$V_{\text{site}}(\vec{r} - \vec{R}_i) = \frac{1}{2} m \omega_{\text{site}}^2 \left(\vec{r} - \vec{R}_i\right)^2 . \tag{2.20}$$

Equation (2.20) neglects the energy offset due to the finite depth of the lattice potential. The *on-site potential* $V_{\text{site}}(\vec{r} - \vec{R}_i)$ corresponds to that of an isotropic 3D harmonic oscillator with trapping frequency ω_{site}. The *on-site trapping frequency* ω_{site} is given by [Blo13]

$$\omega_{\text{site}} = \frac{E_{\text{rec}}}{\hbar} \sqrt{\frac{4V_0}{E_{\text{rec}}}}. \tag{2.21}$$

For increasing lattice depths V_0, the on-site confinement of a trapped atom becomes stiffer as can be seen from Eq. (2.21).

Within the harmonic approximation of deep lattices ($V_0 \gg E_{\text{rec}}$), the motion of an atom at a lattice site is well described by the motion of a quantized harmonic oscillator. The motional eigenstates $|N_x, N_y, N_z\rangle$ of the trapped atom are characterized by three *vibrational quantum numbers* N_x, N_y, and N_z for the three lattice axes with $\{N_x, N_y, N_z\} \in \mathbb{N}$. The motional eigenstates have equidistant eigenenergies [Mes65a]

$$E_{N_x,N_y,N_z} = \left(N_x + N_y + N_z + \frac{3}{2}\right) \hbar\omega_{\text{site}}. \tag{2.22}$$

Except for the vibrational ground state ($N_x = N_y = N_z = 0$), all excited harmonic oscillator states are degenerate. Due to the finite depth V_0 of optical lattice potentials, each lattice site can host only a limited number of bound vibrational states. The highest-lying, bound vibrational states of a lattice site in the harmonic approximation, for which the eigenenergy E_{N_x,N_y,N_z} is still smaller than the lattice depth V_0, have an energy

$$E_{\text{max}} = (N_{\text{max}} + 3/2)\, \hbar\omega_{\text{site}}, \tag{2.23}$$

where N_{max}, for any of these states, is the sum of all three vibrational quantum numbers N_x, N_y, and N_z. The integer N_{max} can be calculated from the lattice parameters V_0, ω_{site}, and λ_{L} through

$$N_{\text{max}} = \left\lfloor \frac{V_0}{\hbar\omega_{\text{site}}} - \frac{3}{2} \right\rfloor = \left\lfloor \frac{m\omega_{\text{site}}}{2\hbar} \left(\frac{\lambda_{\text{L}}}{2\pi}\right)^2 - \frac{3}{2} \right\rfloor . \tag{2.24}$$

The brackets $\lfloor - \rfloor$ in Eq. (2.24) denote the floor function. With larger lattice depth V_0 atoms in an optical lattice are increasingly confined to the centers of the lattice sites, where the harmonic approximation is better. Given the anharmonicity of the real on-site lattice potential, the harmonic approximation is less accurate for excited oscillator states.

2.3. Ultracold Bosonic Atoms in Optical Lattices

The mathematical expressions given in Sec. 1.1 to describe independent electrons within a solid are general solutions of the single-particle Schrödinger equation in Eq. (1.4) for a periodic potential. The same equations can be used to describe independent ultracold atoms in optical lattices. Atoms within an optical lattice therefore exhibit an energy band structure. If the energies associated with an atomic sample in an optical lattice, e.g. thermal energy and interaction energy, are much smaller than the energy gap between the lowest and first excited energy band, the atoms can be loaded solely into the lowest energy band (band index $n = 0$) [Geo13, Mor07]. For energetical reasons, excitations to higher energy bands cannot occur under these conditions and thus higher bands can be discarded [Dut15b]. In the following, we assume atoms in the energetically lowest energy band of an optical lattice. This assumption can be well fulfilled in todays quantum gas experiments. Based on the above mentioned similarities between atoms in optical lattices and electrons in solids, a bosonic version of the Fermi-Hubbard Hamiltonian in Eq. (1.25) can be derived to describe strongly-correlated, ultracold, bosonic atoms in optical lattices.

2.3.1. The Bose-Hubbard Model

We consider a 3D optical lattice with simple cubic geometry. For reasons of clarity, we assume that the lattice potential associated with the optical lattice is that given in Eq. (2.18), namely $V_{3\mathrm{D}}^{\mathrm{u}}(\vec{r})$. If tunneling of atoms within the optical lattice is restricted to nearest-neighbor lattice sites and interaction is limited to on-site interaction, the Hamiltonian that describes the atoms in tight-binding approximation takes the form [Jak98]

$$\hat{H}_{\mathrm{BH}} = -t \sum_{\langle i,j \rangle} \left(\hat{b}_i^\dagger \hat{b}_j + \mathrm{h.c.} \right) + \frac{U}{2} \sum_i \hat{n}_i \left(\hat{n}_i - 1 \right). \tag{2.25}$$

Equation (2.25) neglects a constant energy offset that arises due to the particular choice of the lattice potential $V_{3\mathrm{D}}^{\mathrm{u}}(\vec{r})$. The first sum in Eq. (2.25) is over pairs $\langle i, j \rangle$ of nearest-neighbor lattice sites and $\hat{b}_i$ ($\hat{b}_i^\dagger$) designates the *annihilation* (*creation*) *operator* of a bosonic atom at site i. The hopping matrix element t characterizes nearest-neighbor tunneling of atoms and can be calculated through [Jak98]

$$t = \int \mathrm{d}\vec{r}\, \tilde{w}_0^*(\vec{r} - \vec{R}_i) \left[-\frac{\hbar^2}{2m} \vec{\nabla}^2 + V_{3\mathrm{D}}^{\mathrm{u}}(\vec{r}) \right] \tilde{w}_0(\vec{r} - \vec{R}_j), \tag{2.26}$$

where the Wannier functions $\tilde{w}_0(\vec{r})$ now relate to atoms. The first sum in Eq. (2.25) corresponds to the kinetic energy of the atoms. The second term represents the total interaction energy of the atoms. It contains the number operator $\hat{n}_i$ for bosonic atoms at lattice site i and is defined as $\hat{n}_i = \hat{b}_i^\dagger \hat{b}_i$. The total interaction energy is proportional to the on-site interaction energy U of two atoms given by [Jak98]

$$U = \frac{4\pi a_{\mathrm{scatt}} \hbar^2}{m} \int \mathrm{d}\vec{r}\, \left| \tilde{w}_0(\vec{r}) \right|^4. \tag{2.27}$$

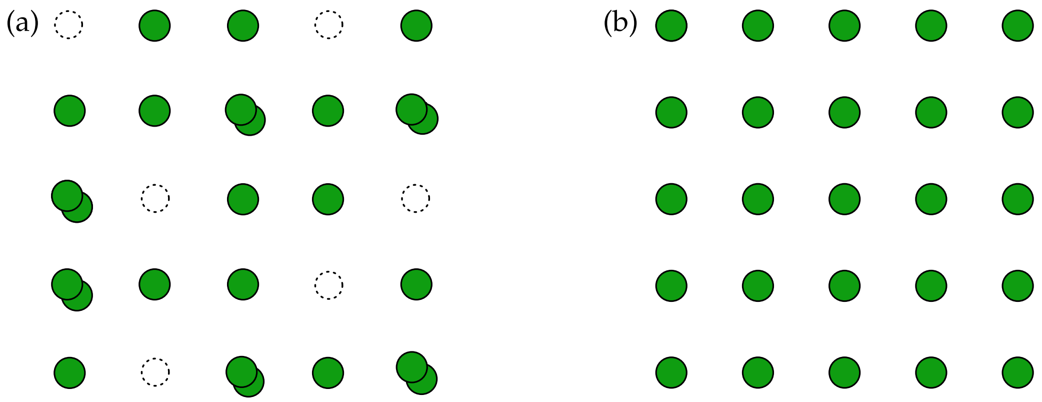

Figure 2.3.: Ground state phases of the Bose-Hubbard model. (a) In the superfluid phase the atom occupation of the lattice sites (dotted circles) follows a Poissonian distribution. (b) In the Mott-insulator phase for unit filling each lattice site is occupied with precisely one atom.

Since the on-site interaction energy U depends on the $s-$wave scattering length a_{scatt}, it can be tuned in sign and strength by means of a magnetic Feshbach resonance.

The Hamilton operator $\hat{H}_{\text{BH}}$ in Eq. (2.25) constitutes the so-called *standard Bose-Hubbard Hamiltonian*. Its mathematical structure is similar to that of the Fermi-Hubbard Hamiltonian $\hat{H}_{\text{FH}}$. The operators of the Bose-Hubbard Hamiltonian, however, do not account for the internal spin state of the atoms. Moreover, the Bose-Hubbard Hamiltonian allows for site occupation numbers that are larger than 2. The total on-site interaction of bosonic atoms at a single lattice site i is therefore given by $U\hat{n}_i\left(\hat{n}_i-1\right)/2$.

2.3.2. Ground States of the Bose-Hubbard Model

The competition between kinetic energy t and on-site interaction energy U leads to distinct ground states of the Bose-Hubbard Hamiltonian $\hat{H}_{\text{BH}}$ for different ratios U/t [Jak98]. We limit the discussion of the ground states to the case of repulsive interactions ($U > 0$). The Bose-Hubbard Hamiltonian with attractive interactions ($U < 0$) is discussed in Ref. [Jac05].

Weakly-Interacting Limit $(\mathbf{t} \gg \mathbf{U})$
If the hopping matrix element t exceeds the on-site interaction energy U ($t \gg U$), the many-body ground state of the atoms is a superfluid [Jak98]. In the superfluid phase the atoms can be described by a macroscopic wavefunction $\Psi_{\text{SF}}(\vec{r})$ with well defined phase ϕ [Win13]. Tunneling plays a dominant role in this regime. The gain t in kinetic energy that is associated with tunneling of an atom is larger than the energy cost U for double occupancy. Thus, to minimize energy, every atom aims to occupy each lattice site and spreads over the entire lattice. In the limit of a large number of atoms within the optical lattice and a large number of lattice sites (*thermodynamic limit*) and if additionally $U \to 0$, the many-body ground state $|\Psi_{\text{SF}}\rangle$ of the atoms can be approximated by a product of *coherent states* $|\zeta\rangle$ for each lattice site i [Geo13, Blo08]

$$|\Psi_{\text{SF}}\rangle \approx \prod_i |\zeta\rangle_i, \tag{2.28}$$

where the coherent states $|\zeta\rangle_i$ are given through [Geo13]

$$|\zeta\rangle_i = e^{-|\zeta_i|^2/2} \sum_{b=0}^{\infty} \frac{\zeta_i^b}{\sqrt{b!}} |b\rangle. \tag{2.29}$$

In Eq. (2.29), the states $|b\rangle$ are *Fock states*. The constant ζ_i defines the amplitude and phase of the matter wave field at site i and is given through [Blo08]

$$\zeta_i = \sqrt{\bar{b}_i} e^{i\phi_i}, \tag{2.30}$$

where $\bar{b}_i = \bar{b}$ is the average atom number per lattice site. In the superfluid phase, ϕ_i is equal for all lattice sites, i.e. $\phi_i = \phi$ [Win13]. The probability $P(b)$ to detect b atoms at a particular site of the optical lattice follows a Poissonian distribution [Geo13]

$$P(b) = |\langle b|\zeta\rangle|^2 = \frac{e^{-|\zeta|^2} |\zeta|^{2b}}{b!}. \tag{2.31}$$

Measurements of site atom numbers within the superfluid phase thus are subject to fluctuations.

Strongly-Interacting Limit $(\mathbf{U} \gg \mathbf{t})$
To understand the behavior of the atoms in the strongly-interacting regime, it is helpful to consider the case in which the number of atoms within the optical lattice equals the number of sites of the optical lattice, i.e. unit filling. For increasing U, atoms more and more repel each other and therefore seek to minimize their wavefunction overlap. Tunneling to lattice sites that contain already an atom is penalized with an energy cost U that is larger than the gain t in kinetic energy. In a lattice with unit filling, atoms are thus homogeneously distributed across the lattice with precisely one atom on every lattice site. Under these conditions, the atoms are insulating. The ground state of the Bose-Hubbard Hamiltonian for $U \gg t$ is therefore called *Mott-insulator*. In the limit $t \to 0$, the Mott-insulator many-body ground state for unit filling can be approximately written as a product state of Fock states $|b\rangle$ for each lattice site i [Geo13]

$$|\Psi_{\mathrm{MI}}\rangle \approx \prod_i |b\rangle_i \tag{2.32}$$

with $|b\rangle_i = |b{=}1\rangle_i$. Since Fock states are eigenstates of the number operator $\hat{n} = \hat{b}^\dagger \hat{b}$, the atom number at each site i is well-defined and integer. Because of quantum fluctuations, the phase ϕ_i of each site evolves randomly and hence the Mott-insulator ground state has no phase coherence [Win13]. Figure 2.3 visualizes the number statistics of the site occupation for both ground states of the Bose-Hubbard model.

2.3.3. Superfluid to Mott-Insulator Transition

The two ground states, superfluid and Mott-insulator, of the repulsive Bose-Hubbard Hamiltonian are connected to each other via a quantum-phase transition. The transition takes place at a critical ratio $(U/t)_{\mathrm{c}}$. For a uniform, simple cubic 3D lattice potential with unit filling, this critical value is $(U/t)_\mathrm{c} \approx 35$ [Jak98]. To access both ground states experimentally, it is necessary to tune the ratio U/t. In experiments, one therefore varies U and t. By increasing the lattice depth V_0, the spatial extent of the Wannier functions $\tilde{w}_0(\vec{r}-\vec{R}_i)$ decreases and thus the hopping matrix element t in Eq. (2.26) gets smaller. A larger lattice depth V_0 goes along with a larger two-particle probability density $\left|\tilde{w}_0(\vec{r}-\vec{R}_i)\right|^4$. This in turn causes a larger on-site interaction energy U. To tune U independently of t, magnetic Feshbach resonances can be employed to vary the scattering length a_scatt (see Sec. 2.1).

If the optical lattice potential contains an external harmonic confinement as in Eq. (2.17), a third energy contribution appears in the Bose-Hubbard Hamiltonian $\hat{H}_\mathrm{BH}$ in Eq. (2.25). The new energy contribution accounts for the site-dependent energy offset due to the external harmonic potential and participates in the competition between kinetic energy t and interaction energy U. It is then possible that Mott-insulator and superfluid phases can coexist [Jak98].

The superfluid to Mott-insulator transition predicted by the Bose-Hubbard model was observed with ultracold atoms in optical lattices first in 2002 [Gre02]. In this experiment, ultracold ^{87}Rb atoms were loaded into a simple cubic 3D optical lattice, which was generated by $852\,\mathrm{nm}$-lattice laser light (lattice spacing $a = 426\,\mathrm{nm}$). In a series of experiments with increasing lattice depth V_0, the atoms were brought from a superfluid into a Mott-insulating state. To observe the quantum phase transition, the atoms were released from the optical lattice and the resulting matter wave interference pattern of the atoms was recorded. The transition from a superfluid to a Mott-insulator became apparent through phase coherence loss, which led to the destruction of the matter wave interference pattern.

3. Fluorescence Quantum Gas Microscopy

In order to detect and study ultracold atoms in optical lattices within the K$-$Cs apparatus, we will use fluorescence quantum gas microscopy. This imaging technique was first experimentally demonstrated in 2009 [Bak09, She10]. It yields information on the trapped atoms that is complementary to the information obtained from the previously employed and still widely used absorption imaging technique [Ket99]. We summarize central aspects of absorption imaging of ultracold atoms in optical lattices in this Chapter and contrast those to the experimental capabilities of fluorescence quantum gas microscopy. The main purpose of this Chapter, however, is to explain the experimental fundamentals of fluorescence quantum gas microscopy and to give an overview of currently existing quantum gas apparatuses that employ this imaging technique. We furthermore point out experimental requirements for the implementation of fluorescence quantum gas microscopy into a quantum gas apparatus. Finally, we explain the envisioned experimental sequence for performing fluorescence quantum gas microscopy with the K$-$Cs apparatus. As our imaging system for fluorescence quantum gas microscopy imposes constraints on the design of the K$-$Cs apparatus, we also summarize its optical design.

3.1. Imaging Methods for Ultracold Atoms

Based on the point of time, at which a quantum gas within an optical lattice is imaged during the experimental sequence, two imaging methods can be distinguished: imaging the quantum gas while it is still confined within the optical lattice is known as *in-situ imaging* whereas probing the quantum gas after it has been released from the lattice is called *time-of-flight imaging*. Within the past, the main imaging technique to study atoms in optical lattices has been absorption imaging, which can be performed as in-situ imaging or as time-of-flight imaging.

3.1.1. Absorption Imaging

Absorptive imaging of ultracold atoms utilizes a collimated laser beam that illuminates the atom cloud under investigation. The imaging laser light is resonant with an optical transition of the atoms and thus absorption through the atoms attenuates the incident beam intensity. If the imaging beam propagates along the $z-$direction and has an incident intensity $I_0(x, y)$, the transmitted intensity $I_\mathrm{T}(x, y)$ behind the atom cloud is given by [Ket99]

$$I_\mathrm{T}(x, y) = I_0(x, y) \cdot e^{-\mathrm{OD}(x,y)}. \tag{3.1}$$

The function $\mathrm{OD}(x, y)$ in Eq. (3.1) is the *optical density* of the atom cloud and depends on the atom density $n_\text{atom}(x, y, z)$. If the intensity I_0 of the imaging beam is much lower than

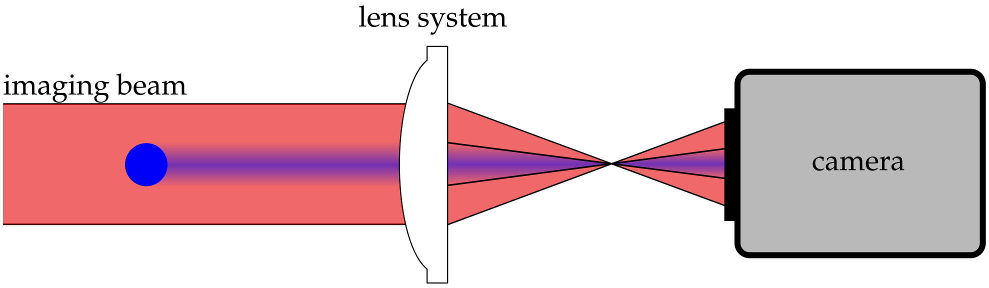

Figure 3.1.: Absorption imaging. A collimated, resonant laser beam (red) illuminates the atomic cloud (blue circle). Through absorption the column-integrated density $\bar{n}_{\text{atom}}(x, y)$ of the cloud is imprinted on the intensity $I_{\text{T}}(x, y)$ of the transmitted laser beam. A lens system projects the transmitted light onto a camera.

the *saturation intensity* I_{sat} of the atomic imaging transition, the optical density $\text{OD}(x, y)$ is proportional to the *resonant absorption cross-section* σ_0 of the imaged atoms. The optical density can then be calculated through [Ket99, Jer14]

$$\text{OD}(x, y) = \sigma_0 \int n_{\text{atom}}(x, y, z)\, dz. \tag{3.2}$$

Equation (3.1) together with Eq. (3.2) corresponds to *Beer's law*. A charge-coupled device (CCD) camera records the transmitted laser light. If $I_0(x, y)$ and σ_0 are known, it is possible to extract the *column-integrated density* $\bar{n}_{\text{atom}}(x, y) = \int n_{\text{atom}}(x, y, z)\, dz$ from the absorption images [Jer14]. The described detection technique is known as *absorption imaging* [Ket99]. Figure 3.1 depicts the conceptual optical setup for absorption imaging. The obtained column-integrated density $\bar{n}_{\text{atom}}(x, y)$ allows one to determine experimental parameters of the atomic sample, e.g. its temperature or atom number. For that purpose a bimodal distribution is fitted to the recorded column-integrated density $\bar{n}_{\text{atom}}(x, y)$. The bimodal distribution is commonly chosen to be the sum of a Gaussian distribution and a parabolic distribution. The former describes the thermal fraction of the atoms within the imaged density profile and the latter captures the fraction of the atoms that stems from a BEC [Ket99].

Absorption imaging of ultracold lattice gases is commonly executed after the quantum gas has been released from the optical lattice. After being released, the atom cloud expands freely for a variable time of flight t_{TOF}, during which the atomic density $n_{\text{atom}}(x, y, z)$ decreases. For non-interacting gases ($a_{\text{scatt}} = 0$), the case considered in the following, the expansion during time of flight is ballistic [Jer14].

Sudden Release of Lattice Gas

If the ultracold atoms are released instantaneously out of the optical lattice, the expansion of each Bloch wave $\Psi_{\vec{q}}^{(n)}(\vec{r})$ is determined by the plane wave contributions in Eq. (1.15) [Blo13]. The expanding atom cloud contains momenta $\hbar\vec{k}$ with $\vec{k} = \vec{q}, \vec{q} \pm \vec{G}$ (for any reciprocal vector $\vec{G}$), whose relative weights depend on the initial lattice depth V_0 [Mor06]. For $t_{\text{TOF}} \to \infty$, but practically already after an expansion time of a few milliseconds to about $100\,\text{ms}$, the atom distribution $n_{\text{atom}}(\vec{r})$ displays the in-trap momentum distribution of the atoms [Ger08].[1] Atoms

---

[1] In practice, typical expansion times t_{TOF} are chosen to be a few tens of milliseconds long.

found at position $\vec{r}$ then relate to a free-particle momentum $\hbar\vec{k}$ given through [Blo13]

$$\vec{k} = \frac{m}{\hbar t_{\text{TOF}}}\vec{r}. \tag{3.3}$$

A sudden release of a lattice gas thus projects the in-trap quasi-momentum distribution onto free-particle momenta. A subsequent absorption image of the expanded atom cloud hence effectively measures the momentum density. In the case of an interacting gas ($a_{\text{scatt}} \neq 0$), the interactions can lead to deviations of the detected atom distribution from the in-trap momentum distribution [Blo13, Jer14].

Adiabatic Release of Lattice Gas

If the lattice laser power is switched off slowly, i.e. such that the quasi-momentum $\hbar\vec{q}$ of a Bloch wave $\Psi_{\vec{q}}^{(n)}(\vec{r})$ is conserved, the atoms are released adiabatically from the optical lattice [Blo13]. Each Bloch wave $\Psi_{\vec{q}}^{(n)}(\vec{r})$ then connects adiabatically to a specific free-particle state with momentum $\hbar\vec{k}$ in the nth Brillouin zone (*adiabatic band mapping*) [Blo13]. Adiabatic band mapping of a lattice gas allows one to directly detect and measure atomic populations in different bands of the lattice.

3.1.2. In-Situ Imaging

In-situ imaging of an ultracold lattice gas enables measurement of local observables, e.g. in-trap density and entropy. For in-situ measurements one therefore aims at high spatial resolution to resolve single lattice sites and high sensitivity to detect single atoms. In contrast, time-of-flight measurements of ultracold atoms in optical lattices yield information on bulk properties, e.g. momentum and quasi-momentum distribution, coherence, and correlations [Blo13]. In-situ measurements therefore complement time-of-flight measurements.

High-resolution in-situ imaging of ultracold lattice gases was demonstrated via absorption imaging of ^{133}Cs atoms in a 2D square lattice [Gem09]. However, neither single-site resolution nor single-atom sensitivity was achieved in this experiment. Single-site and single-atom resolved in-situ imaging was achieved instead via fluorescence imaging; first using ^{133}Cs atoms within an optical lattice with a lattice spacing of $4.9\,\mu\text{m}$ [Nel07], for which tunneling was negligible and the emergence of Hubbard physics therefore suppressed, and later with ^{87}Rb atoms in square lattice monolayers with lattice spacings around $a \sim 600\,\text{nm}$, for which Hubbard physics could be observed [Bak09, She10].

In-situ fluorescence imaging of ultracold lattice gases with single-atom and single-site resolution, often referred to as *fluorescence quantum gas microscopy*, is based on keeping the atoms at the lattice sites while optically exciting them to emit fluorescence photons. An imaging system collects a fraction of the fluorescence photons and forms an image on a camera chip. Given the background-free detection, the signal-to-noise ratio of fluorescence quantum gas microscopy is better than for absorption imaging [Blo13, Wei14].

Table 3.1.: Principal D line transitions in alkali atoms. The Table lists the transition wavelengths for the principal D_1 and D_2 lines in alkali atoms.

	Element				
Transition	**Li**	**Na**	**K**	**Rb**	**Cs**
$n\mathrm{S}_{1/2} \to n\mathrm{P}_{1/2}$	$671\,\mathrm{nm}$	$590\,\mathrm{nm}$	$770\,\mathrm{nm}$	$795\,\mathrm{nm}$	$895\,\mathrm{nm}$
$n\mathrm{S}_{1/2} \to n\mathrm{P}_{3/2}$	$671\,\mathrm{nm}$	$589\,\mathrm{nm}$	$767\,\mathrm{nm}$	$780\,\mathrm{nm}$	$852\,\mathrm{nm}$
Ref.	[Rad95]	[Kraa]	[Kra49]	[Kra49]	[Kra49]

3.2. Fundamentals of Fluorescence Quantum Gas Microscopy

Fluorescence quantum gas microscopy is performed in several quantum gas apparatuses worldwide nowadays.[2] These apparatuses employ fluorescence quantum gas microscopy to image atoms in a single layer of an optical lattice. Due to the different atomic species and technical peculiarities that are used in these experiments, individualized experimental strategies are used to perform fluorescence quantum gas microscopy. To understand the general concept of fluorescence quantum gas microscopy, we outline a typical experimental sequence and thereby discuss key aspects.

3.2.1. Preparation of an Atomic Lattice Monolayer

The experimental sequence begins with the preparation of a lattice monolayer of ultracold atoms. To that end, an atomic BEC is created and held within an optical dipole trap. A vertical 1D optical lattice is then superimposed onto the BEC. By ramping up the laser power of the vertical optical lattice the BEC is loaded from the dipole trap into the optical lattice. If the spatial extent of the BEC within the dipole trap is larger than the lattice spacing of the vertical lattice, atoms distribute over multiple sites. In the experiment detailed in Ref. [She10], for instance, the lattice spacing was $a = 532\,\mathrm{nm}$ and atoms populated 60 lattice sites with up to 2000 atoms per lattice site. When the lattice depth of the 1D lattice is chosen large enough, the atoms in each lattice site form independent 2D atomic systems.

To prepare a lattice monolayer of atoms, the atoms from all vertical lattice sites except for one site are removed. One strategy to empty the lattice sites is to apply a vertical magnetic field gradient and a microwave pulse with tunable frequency. The microwave sweep transfers atoms of individual lattice sites, except for one site, into a different hyperfine level, on which a resonant laser pulse acts [She10]. After the resonant laser has kicked out the atoms within the undesired lattice sites, a single lattice layer of atoms remains.

In a next step, horizontal lattice lasers are switched on and create a 2D optical lattice that is superimposed onto the isolated 2D atomic sample. In Ref. [She10] the horizontal 2D lattice is a square lattice with lattice constant $a = 532\,\mathrm{nm}$. The 2D atomic lattice monolayer created in this way is used to prepare many-body quantum states and to study Hamiltonians.

---

[2] Currently existing fluorescence quantum gas microscopy apparatuses are discussed in Sec. 3.4.

3.2.2. Fluorescence Imaging

To image the 2D atomic lattice monolayer, the atoms are illuminated with (near-) resonant laser light. The atoms thereby get excited and start to emit fluorescence photons at a wavelength λ_{image} and rate Γ_{scatt}. The fluorescence rate Γ_{scatt} of an atom during fluorescence quantum gas microscopy is found to be in the kilohertz regime in current alkali apparatuses [She10].

Presently existing alkali fluorescence quantum gas microscopy apparatuses use optical transitions from the electronic ground state to the first excited fine structure doublet ($n\text{S}_{1/2} \rightarrow n\text{P}_{1/2}$ and $n\text{S}_{1/2} \rightarrow n\text{P}_{3/2}$) for imaging the trapped atoms. Here, the symbol n denotes the *principal quantum number*. These transitions are known as *principal D_1 and D_2 transitions*. For alkali atoms, the principal D line transitions have transition wavelengths between $589\,\text{nm}$ [Kraa] for Na and $895\,\text{nm}$ [Kra49] for Cs. Table 3.1 summarizes principal D line transition wavelengths of alkali atoms. By tuning the frequency of the imaging laser to higher frequencies, other atomic transitions in principle can be used for fluorescence imaging, thereby giving control on the *imaging wavelength* λ_{image}.

A small fraction of the fluorescence photons emitted by the atoms is captured by an imaging system. The collection efficiency of the imaging system is defined through the solid angle of its acceptance cone and is commonly around $15\,\%$ [She10]. The number of detected photons per atom therefore typically ranges from around $\sim\, 100$ [Edg15] to several thousands of photons [Bak09] for exposure times between $0.4\,\text{s}$ [Yam16] and $2.6\,\text{s}$ [Edg15].[3] To obtain a perpendicular view on the atomic monolayer for the fluorescence images, the optical axis of the imaging system has to be aligned with the vertical 1D optical lattice. This requires the imaging system to be placed above or below the atomic sample.

3.2.3. Imaging System

The imaging system of a fluorescence quantum gas microscopy apparatus generally consists of a microscope objective, sometimes called *fluorescence quantum gas microscope* (FQGM), and a subsequent lens. The microscope objective collects the fluorescence photons and converts the divergent fluorescence light into a collimated beam (*infinite-conjugate*). The subsequent lens projects a magnified image of the atomic monolayer onto a CCD camera.

To resolve atoms at neighboring lattice sites, the resolution of the imaging system has to be comparable to the lattice spacing or smaller. One typically specifies the spatial resolution of an imaging system by considering its response to a point source. The image of a point source formed by an imaging system is denoted as *point spread function*. The point spread function of a diffraction-limited imaging system is an Airy disc [Hec09]. The distance d_0 from the center of the Airy disc to the first ring of zero intensity is often used to quantify the spatial resolution of an imaging system (*Rayleigh criterion*). Following this criterion, the spatial resolution d_0 is then given by [Hec09]

$$d_0 = 0.61 \cdot \frac{\lambda_{\text{image}}}{\text{NA}}. \tag{3.4}$$

Here, $\text{NA} = n_{\text{object}} \sin(\theta/2)$ is the *numerical aperture* of the imaging system with n_{object} being the object space *refractive index* and θ being the *angular aperture* of the imaging system. Because of the finite aperture of the imaging system and the finite on-site confinement of the atoms, the

---

[3] Exposure times that are four orders of magnitude smaller than those given in the main text, namely $\sim 100\,\mu\text{s}$, were reported for a fluorescence quantum gas microscopy experiment with ytterbium atoms [Mir15].

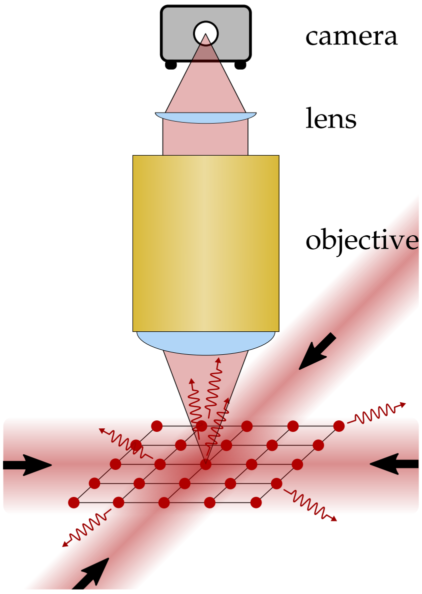

Figure 3.2.: Fluorescence quantum gas microscopy. A 2D lattice monolayer of atoms (red dots) is imaged by a FQGM. Optical molasses beams (red) aligned with the horizontal lattice laser beams (black arrows) excite the atoms, which are pinned to the sites of the optical lattice. The imaging system captures a fraction of the fluorescence photons and creates an image of the atoms on a camera. The imaging system typically consists of a microscope objective followed by a lens that forms a magnified image.

fluorescence image of a single trapped atom is a convolution of an Airy function and a Gaussian function [She10]. The convoluted intensity distribution of the image of a single trapped atom is denoted as *spot function*.

In fluorescence images obtained with a FQGM, the zero intensity ring of the Airy disc of a single atom is often buried within the wing of the Gaussian function [Bak09, She10]. The resolution of a FQGM is therefore typically characterized in terms of the *full-width at half-maximum* (FWHM) of the spot function. The spot function is determined experimentally by averaging images of single atoms in a sparsely filled lattice monolayer. Measured spot functions of imaging systems of existing FQGMs have FWHMs between $\sim 310\,\mathrm{nm}$ [Mir15] to $\sim 700\,\mathrm{nm}$ [She10]. These imaging systems have magnifications on the order of 100x [Wei11]. With such a magnification, the image of a single atom that is confined within a lattice site typically illuminates around 3x3 pixels on the camera chip.

3.2.4. Heating and Cooling of the Trapped Atoms

Fluorescence imaging causes the trapped atoms to absorb and spontaneously re-emit photons. Both processes, absorption and spontaneous emission, increase the energy of an atom on average by the *fluorescence recoil energy* E_R [Gri00, Met99]. The fluorescence recoil energy E_R is defined analogously to the lattice recoil energy in Eq. (2.19), however, depends on the wavelength λ_image of the fluorescence light. The mean energy of an atom thus grows by $2E_\mathrm{R}$ per absorption-emission cycle and increases at a rate [Gri00, Met99]

$$\Gamma_\mathrm{heat} = 2E_\mathrm{R} \cdot \Gamma_\mathrm{scatt}. \tag{3.5}$$

To illustrate the significance of the heating, we estimate the heating rate Γ_{heat} of a ^{40}K atom that is trapped at a lattice site of a 3D optical lattice during fluorescence imaging on the principal D_1 transition. As a numerical value for Γ_{scatt} we take the fluorescence rate that was calculated in Ref. [Hal15] from experimental data for ^{40}K atoms in a FQGM experiment ($\Gamma_{\text{scatt}} = 8 \times 10^3\,\text{s}^{-1}$). According to Eq. (3.5), the heating rate Γ_{heat} of the ^{40}K atom is then ($k_{\text{B}}\times 6.5$ mK)/s.

To prevent atom hopping between different lattice sites due to heating, the lattice depth V_0 during fluorescence imaging must be many times larger than the gain in energy over the exposure time [Nel07, Mir15]. For this reason, the power of the lattice lasers is increased just before fluorescence imaging starts. The increased laser power leads to a larger lattice depth V_0 and thereby enhances the confinement of the atoms to the lattice sites. To relax the requirements on the lattice depth V_0 and thereby on the lattice laser power, the imaging laser beams are typically arranged such that they provide simultaneous laser cooling of the trapped atoms. In existing FQGM experiments, simultaneous laser cooling allows one to work with lattice depths V_0 between $k_B\times\ 170\,\mu\text{K}$ [Edg15] and $k_B\times\ 2.5\,\text{mK}$ [Omr15] during fluorescence imaging without atom hopping. These lattice depths correspond to on-site trapping frequencies $\omega_{\text{site}} = 2\pi\times 275\,\text{kHz}$ for ^{40}K [Edg15] and $\omega_{\text{site}} = 2\pi\times 1.3\,\text{MHz}$ for ^{6}Li [Omr15], respectively. Such large lattice depths are more than one order of magnitude larger than those for which Bose-Hubbard physics commonly manifests in quantum gas experiments [Wei14]. Tunneling of atoms during fluorescence imaging can therefore be neglected, too.

Most alkali FQGM apparatuses use sub-Doppler laser cooling techniques acting on the principal D_1 and D_2 transitions to laser cool the confined atoms. Optical molasses cooling, for instance, has been employed in FQGM apparatuses for ^{87}Rb atoms [She10, Bak09]. In Ref. [She10], the equilibrium temperature of the trapped ^{87}Rb atoms that was reached within the optical molasses was about $22\,\mu\text{K}$ as measured in Ref. [Wei11]. While optical molasses cooling works best for atoms in free space, laser cooling schemes that are based on the presence of an optical lattice are better suited for application in fluorescence quantum gas microscopy. In that respect, Raman sideband cooling [Par15, Omr15, Che15] and electromagnetically induced transparency (EIT) cooling [Hal15, Edg15] have been demonstrated to work successfully for fluorescence quantum gas microscopy.

In the context of fluorescence quantum gas microscopy with ^{174}Yb atoms, narrow-line optical molasses cooling has been employed to cool the atoms [Yam16]. A completely different approach was pursued in the experiment detailed in Ref. [Mir15]. There the time-averaged lattice potential experienced by the trapped ^{174}Yb atoms was deep enough (effective lattice depth $V_0 = k_{\text{B}} \times 34\,\text{mK}$) to preserve the atom distribution entirely without laser cooling. Figure 3.2 illustrates the concept of fluorescence quantum gas microscopy of a 2D lattice monolayer of atoms, where the imaging system is placed above the atoms and laser cooling is performed through optical molasses.

3.2.5. Light-Assisted Atom Collisions

Atom loss during fluorescence imaging arises predominantly at multiply occupied lattice sites, where atoms can collide pairwise with each other. Two atoms, of which one is in its electronic ground state and the second one is in an excited state due to optical excitation, interact with each other through attractive dipole-dipole interaction [Fuh12]. For the time of the atomic excitation the two atoms can form a weakly bound molecule. Before the excited atom relaxes into its electronic ground state the atom pair can gain kinetic energy within the associated molecular potential [Fuh12]. The gain in kinetic energy is subsequently carried on by the dissociated atoms. If the kinetic energy of the dissociated atoms is larger than the lattice depth V_0, the two atoms are expelled from the lattice site. Collisions of this type are known as *light-assisted collisions* [Nel07, DeP99, Fuh12].

Light-assisted collisions reduce the occupation number of a lattice site by two. If the initial occupation number of a lattice site is odd, light-assisted collisions remove all atoms from that site except for a single atom. If the initial occupation number of the lattice site is even, light-assisted collisions leave an empty site. Given the enhanced lattice confinement during fluorescence imaging, the two-particle density within a lattice site is increased. Light-assisted collisions thus take place on a time scale on the order of $\sim 100\,\mu\mathrm{s}$ [Bak09, DeP99]. Within this period of time the colliding atoms do not scatter a sufficient number of photons to be discerned on the fluorescence images. Hence, fluorescence images typically display the parity projection of the initial atom occupation distribution [Bak09, She10].

3.2.6. Image Analysis

The fluorescence images obtained from a FQGM commonly have a field of view of tens of micrometers along each image axis such as in Ref. [She10]. A single fluorescence image therefore captures typically thousands of lattice sites. To extract site occupation numbers from a fluorescence image, one performs a computational analysis of the recorded image. In the course of the analysis a numerical algorithm reconstructs the recorded fluorescence image by using the experimentally measured spot function (see Sec. 3.2.3) of the imaging system. The algorithm fits copies of the spot function to a fluorescence image and thereby creates a reconstructed image. The reconstructed image allows one to identify singly occupied as well as empty lattice sites and thus to deduce site occupation numbers. The knowledge of the spot function is thus a prerequisite for the algorithm to deconvolve fluorescence images.

Depending on the ratio of the FWHM of the spot function and the lattice spacing a, the images of atoms at adjacent lattice sites overlap more or less on the camera chip. If the FWHM of the spot function is much smaller than the lattice spacing a, atoms at neighboring lattice sites are well resolved and can be directly distinguished from each other in a fluorescence image. However, if the FWHM of the spot function is larger than the lattice spacing a, adjacent atoms form a blurred spot on the camera chip and cannot be discerned anymore. In certain cases an unambiguous reconstruction of the site occupation numbers is then only possible with additional input information to the algorithm, such as the lattice geometry or the lattice spacing. Based on this supplementary information, the algorithm can exclude allegedly correct solutions of the deconvolution that are physically unrealistic within the specific experimental setting.

3.3. High-NA Microscope Objectives for FQGM Apparatuses

The microscope objective of a FQGM apparatus typically consists of a couple of lenses that are mounted within a housing. For a given imaging wavelength λ_{image}, a spatial resolution d_0 of the microscope objective that is comparable to the lattice spacing a (i.e. $d_0 \sim a$) can be achieved by adapting the numerical aperture NA of the objective. The numerical aperture increases with larger diameter of the lens aperture and shorter working distance. Since free space is often limited in a FQGM apparatus, a large lens diameter of several centimeters for the microscope objective is impractical in many cases. For this reason, one of the vital points in designing a FQGM objective and apparatus often becomes the question how close the objective can be placed to the atoms.

Common to all FQGM apparatuses is that the atoms are imaged through a window of the vacuum chamber. To withstand the pressure difference between the inside of the vacuum chamber and the outside and in order to minimize bending because of the atmospheric pressure, vacuum windows are usually a few millimeter thick. The vacuum window acts as an additional optical element and thus leads to aberrations (e.g. spherical aberrations) in the imaging system. To obtain diffraction-limited fluorescence images, the objective therefore needs to be corrected for the vacuum window. Since spherical aberrations scale with the thickness of the vacuum window [Wil96, Smi66], the vacuum window in Ref. [Edg15] was only $200\,\mu\mathrm{m}$ thick in order to reduce spherical aberrations.

Three different ways of implementing a high-resolution microscope objective to a FQGM apparatus are imaginable:

(a) Objective resides outside of the vacuum chamber
    advantages: objective is exchangeable, no in-vacuo components
    disadvantages: aberrations due to vacuum window, objective mechanically decoupled from the trapped atoms

(b) First lens of objective placed inside of the vacuum chamber
    advantages: lens can be close to the atoms, aberrations due to vacuum window can be reduced
    disadvantages: alignment of in-vacuo lens relative to objective necessary, UHV compatibility of the lens and its holders must be given

(c) First lens of objective is part of the vacuum window
    advantages: no aberrations due to vacuum window, working distance can be reduced
    disadvantages: requires alignment of objective to lens, a new lens is needed when the vacuum window is replaced and vice versa, UHV compatibility of the lens must be given

Figure 3.3 illustrates the three options (a)-(c) for implementation of a microscope objective to a vacuum chamber. The configurations (b) and (c) allow one to bring the atoms close to the first lens of the objective. These two configurations are realized in several apparatuses in which a hemispherical lens is positioned only a few micrometers away from the atoms [Par15, Che15, Bak09, Mir15]. In these setups the small working distance increases the numerical aperture of the objective by a factor that is given by the refractive index of the lens (*solid immersion effect*). As a consequence, the resolution of the objective is enhanced. A fourth possibility, namely having the entire objective placed inside of the vacuum chamber, is connected with several technical difficulties involving mechanical feasibility, vacuum compatibility, and heat resistance and has no substantial advantages over the three options described before.

3.4. State of the Art of FQGM Apparatuses

At least nine FQGM apparatuses exist presently. Table 3.2 lists currently existing FQGM apparatuses and summarizes their key specifications. These apparatuses are used to study atomic

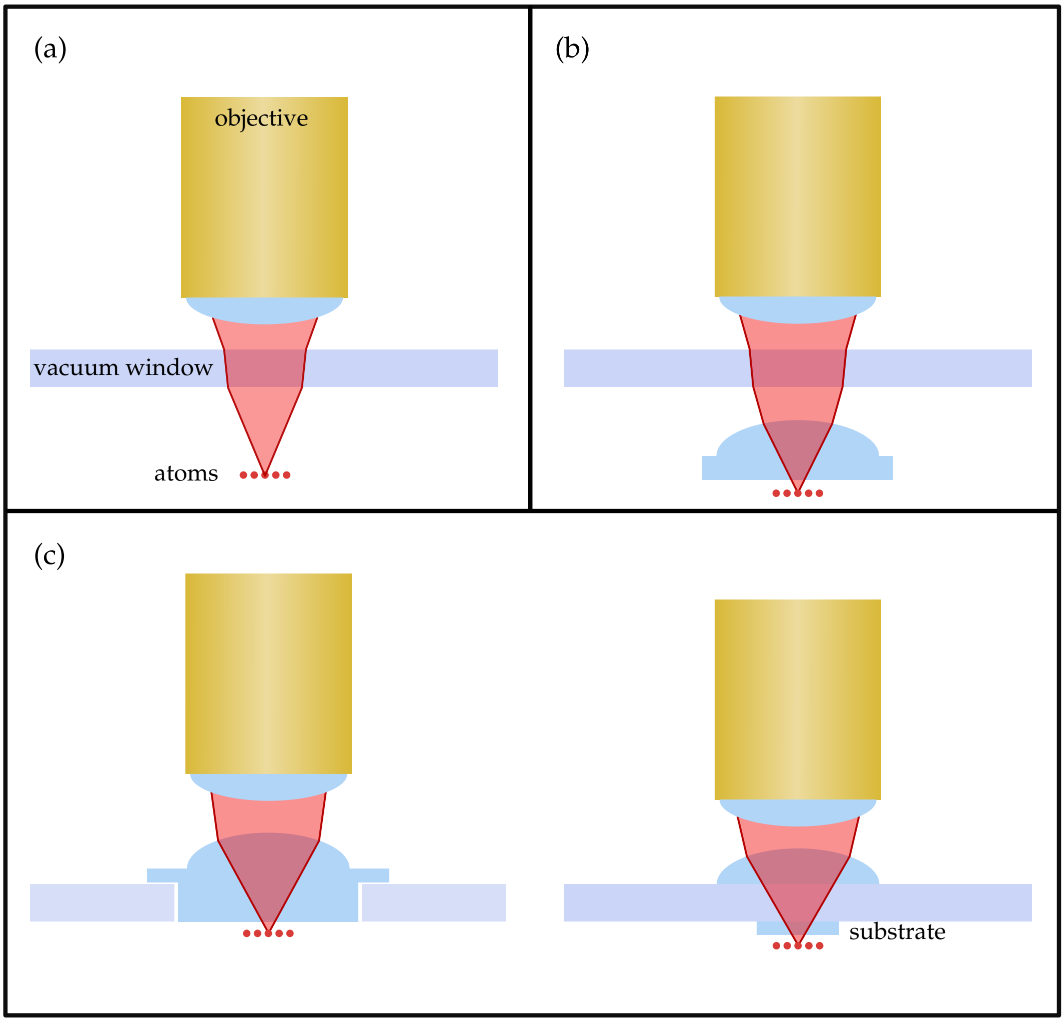

Figure 3.3.: Implementation of a FQGM objective. To implement a high-resolution microscope objective to a quantum gas apparatus, several possibilities exist. The objective might be (a) located fully outside of the vacuum chamber or (b) divided into two segments of which the front one is mounted under vacuum. (c) Another possibility involves contacting the front lens of the objective to the window of the vacuum chamber by (left) glueing or (right) optically contacting. An additional glass substrate can help to reduce the working distance.

lattice gases of the elements ^{6}Li [Par15, Omr15], ^{40}K [Hal15, Edg15, Che15], ^{87}Rb [She10, Bak09], and ^{174}Yb [Mir15, Yam16]. The apparatuses use objectives that are either custom made by companies [Omr15, Hal15, Edg17, She10, Bak11, Yam16] or make use of commercial ones [Par15, Che17, Mir15]. The objectives have numerical apertures of NA = 0.68 and larger, the only exception being the ^{6}Li FQGM objective of the Gross group, which has a numerical aperture of NA = 0.5 [Omr15]. The microscope objectives are either positioned entirely outside of the vacuum chamber (compare Fig. 3.3 (a)) [Omr15, Hal15, Edg15, She10, Yam16] or have a segmented design with optical elements that are placed inside the vacuum chamber or contacted to the vacuum window (compare Fig. 3.3 (b)+(c)) [Par15, Che15, Bak09, Mir15].

Several FQGM setups in Table 3.2 possess technical peculiarities that add more flexibility to the apparatus. Two examples in this respect concern the horizontal optical lattice for the atomic monolayer. Most setups listed in Table 3.2 superimpose pairs of counter-propagating laser beams to form an optical lattice (see Sec. 2.2.2). These lattices have a fixed lattice spacing and lattice geometry. To circumvent this inflexibility, the apparatus of Ref. [Omr15] utilizes the microscope objective besides imaging also for the generation of the horizontal optical lattice. For this, pairs of collimated, parallel laser beams are coupled in the reverse direction into the objective and are focused onto the atoms. The laser beams of each lattice beam pair intersect each other under an angle in the focal plane of the objective and thus create a standing wave within the plane of the atoms. By adding further beam pairs or by altering their spatial arrangement different lattice geometries can be obtained. Another approach towards generation of optical lattices in a FQGM apparatus has been realized in Ref. [Bak09]. There, the microscope objective has been used to focus a phase-modulated lattice laser beam onto the atoms to engineer laser light intensity patterns for optical lattices.

Another technical peculiarity realized in a FQGM apparatus of Table 3.2 relates to the process of fluorescence imaging, which is commonly intertwined with laser cooling in present FQGM experiments (see explanation in Sec. 3.2.4). This link is eliminated in Ref. [Yam16], where imaging and cooling of ^{174}Yb atoms was performed on separate atomic transitions. Narrow-line laser cooling on the $^{1}S_{0}$-$^{3}P_{1}$ transition of ^{174}Yb was applied to suppress heating due to imaging on the $^{1}S_{0}$-$^{1}P_{1}$ transition. This imaging approach permits spectral separation of imaging and cooling light and thus a reduction of background light.

3.5. Experimental Strategy for Fluorescence Quantum Gas Microscopy within the K−Cs Apparatus

In this Section, we sketch the envisioned experimental sequence for performing fluorescence quantum gas microscopy within the K−Cs apparatus. As the microscope objective provides constraints on the design of the vacuum setup of the K−Cs apparatus, we summarize its lens design here.

3.5.1. Experimental Sequence

Each experimental cycle will begin with laser and evaporative cooling of K or Cs atoms to form an atomic K or Cs BEC. All stages of BEC production will take place at the same location (*production site*) within the vacuum apparatus. Once a condensate is prepared, it will be moved to another spot (*science site*) within the apparatus along a straight, horizontal route. A detailed discussion of the vacuum setup follows in Ch. 6 and Ch. 8. Transport of the atoms from the production to the science site will be realized by optical means. The science site will be located

Table 3.2.: Overview of FQGM apparatuses. A list of presently existing FQGM apparatuses and their main technical specifications. The FQGM configurations denoted as A, B, and C refer to the configurations (a), (b), and (c) in Fig. 3.3. Following abbreviations are used: Raman sideband cooling (RSC), solid immersion effect (SIE), lattice projection with objective (LP)

	Greiner group U Harvard	**Gross group MPQ Munich**	**Kuhr group U Strathclyde**	**Thywissen group U Toronto**	**Zwierlein group MIT**	**Bloch group MPQ Munich**	**Greiner group U Harvard**	**Kozuma group TITech Tokyo**	**Takahashi group U Kyoto**
Element	^{6}Li		^{40}K			^{87}Rb		^{174}Yb	
Imaging wavelength	671 nm	671 nm	770 nm	770 nm	770 nm	780 nm	780 nm	399 nm	399 nm
NA	0.87	0.5	0.68	0.8	0.87	0.68	0.8	0.81	0.75
Objective	commercial + hemisphere	custom	custom	custom	commercial + hemisphere	custom	custom + hemisphere	commercial + hemispherical cap	custom
Resolution (FWHM)	520 nm	$\sim$750 nm	630 nm	600 nm	640 nm	$\sim$700 nm	$\sim$600 nm	$\sim$314 nm	364 nm
Lattice constant	569 nm	532 nm & 1.15 µm	532 nm	527 nm	541 nm	532 nm	640 nm	544 nm	266 nm
FQGM configuration	C	A	A	A	C	A	B	C	A
Exposure	1.9 s	1 s	1.5 s	2.6 s	1 s	0.9 s	0.2−1s	$\leq$100 µs	0.4 s
Detected photons per atom	$\sim$750	$\sim$350	$\sim$1000	$\sim$160	$\sim$1000	$\sim$5000	$\leq$ 20000	$\lesssim$2000	$\sim$200
Cooling	RSC	RSC	EIT cooling	EIT cooling	RSC	optical molasses	optical molasses	none	narrow-line optical molasses
Technical specialty	SIE for imaging	LP		200 µm-thin vacuum window	SIE for imaging		SIE for imaging & LP	SIE for imaging & fast imaging	cooling independent from imaging
Ref.	[Par15]	[Omr15, Omr16]	[Hal15]	[Edg15, Edg17]	[Che15, Che17]	[She10, Wei11]	[Bak09, Bak11]	[Mir15]	[Yam16]

right beneath a vertically oriented FQGM objective. After the atoms have been transported to the science site, they will be loaded into a vertical 1D optical lattice. The vertical lattice will be generated by retroreflecting a $1064\,\mathrm{nm}$ laser beam from the front lens of the objective. After preparation of an atomic lattice monolayer as outlined in Sec. 3.2.1, a horizontal 2D square optical lattice will be superimposed onto the atomic monolayer. The horizontal lattice will be generated by two horizontal, mutually orthogonal $1064\,\mathrm{nm}$ laser beams that will be retroreflected by mirrors mounted outside of the vacuum chamber. Following preparation of the atomic many-body quantum state to be studied the atom distribution within the optical lattice will be frozen by increasing the power of the lattice laser beams. Optical molasses beams along the lattice axes will then illuminate the trapped atoms on the principal D_2 line transitions of K and Cs. Accordingly, the imaging wavelength for K atoms will be $\lambda^{\mathrm{K}}_{\mathrm{image}} = 766\,\mathrm{nm}$ and the imaging wavelength for Cs atoms will be $\lambda^{\mathrm{Cs}}_{\mathrm{image}} = 852\,\mathrm{nm}$. The fluorescence image formed by the imaging system will be recorded by a CCD camera.

3.5.2. Optical Transport

To transport the atoms from the production site to the science site, we will combine two optical transport methods that have been successfully realized in the past [Léo14, Sch06]. The one transport method relies on a focused Gaussian laser beam that acts as an optical dipole trap for the atoms (see Sec. 2.2.1). By translating the laser focus, the atoms are dynamically displaced. Translation of a beam focus can be generally achieved by moving the focusing lens with a motorized translation stage [Gus01] or by using a focus-tunable lens. In the latter case, the lens is fixed in position and the focal length of the lens is tuned through current-control.

A focus-tunable lens dispenses from the need for a translation stage that is prone to transfer vibrations to the experimental setup. However, as the focal length of the focus-tunable lens is varied, the beam waist w_0 of the focused laser beam changes during transport. This dependence of the beam waist on the focal length comes at the expense of a varying depth and changing trapping frequencies of the optical dipole trap. To circumvent that drawback, a combination of two focus-tunable lenses and one static lens placed in series at defined mutual distances can be used. Such an optical setup enables the independent control of the focus position and beam waist w_0 and thus allows for uniform trapping conditions over the full transport distance [Léo14].

An alternative method that has been realized in the past to transport atoms is based on two collinear, counter-propagating laser beams that form a standing wave. A relative frequency shift $\Delta\omega_{\mathrm{L}}$ of the two laser beams transforms the stationary standing wave into a moving standing wave (see Eq. (2.13)). Atoms that are trapped in the minima of the optical lattice potential are then dragged in axial direction at a velocity v given in Eq. (2.15). In this way, the 1D optical lattice forms an atomic *conveyor belt* [Kuh01, Sch06]. The experiment detailed in Ref. [Sch06] uses a Bessel beam and a counter-propagating Gaussian beam to create a conveyor belt. The lattice part of the optical lattice potential yields axial confinement whereas the radial confinement due to the Bessel beam supports the atoms against gravity.

For the new K−Cs apparatus, we aim to realize the transport by two counter-propagating laser beams that form a conveyor belt. One of the laser beams will be a Gaussian beam and will be focused by focus-tunable lenses, similar to the setup described in Ref. [Léo14]. The second laser beam potentially will be a Bessel beam. Further details with respect to the optical transport can be found in the thesis of M. Gröbner [Grö17a].

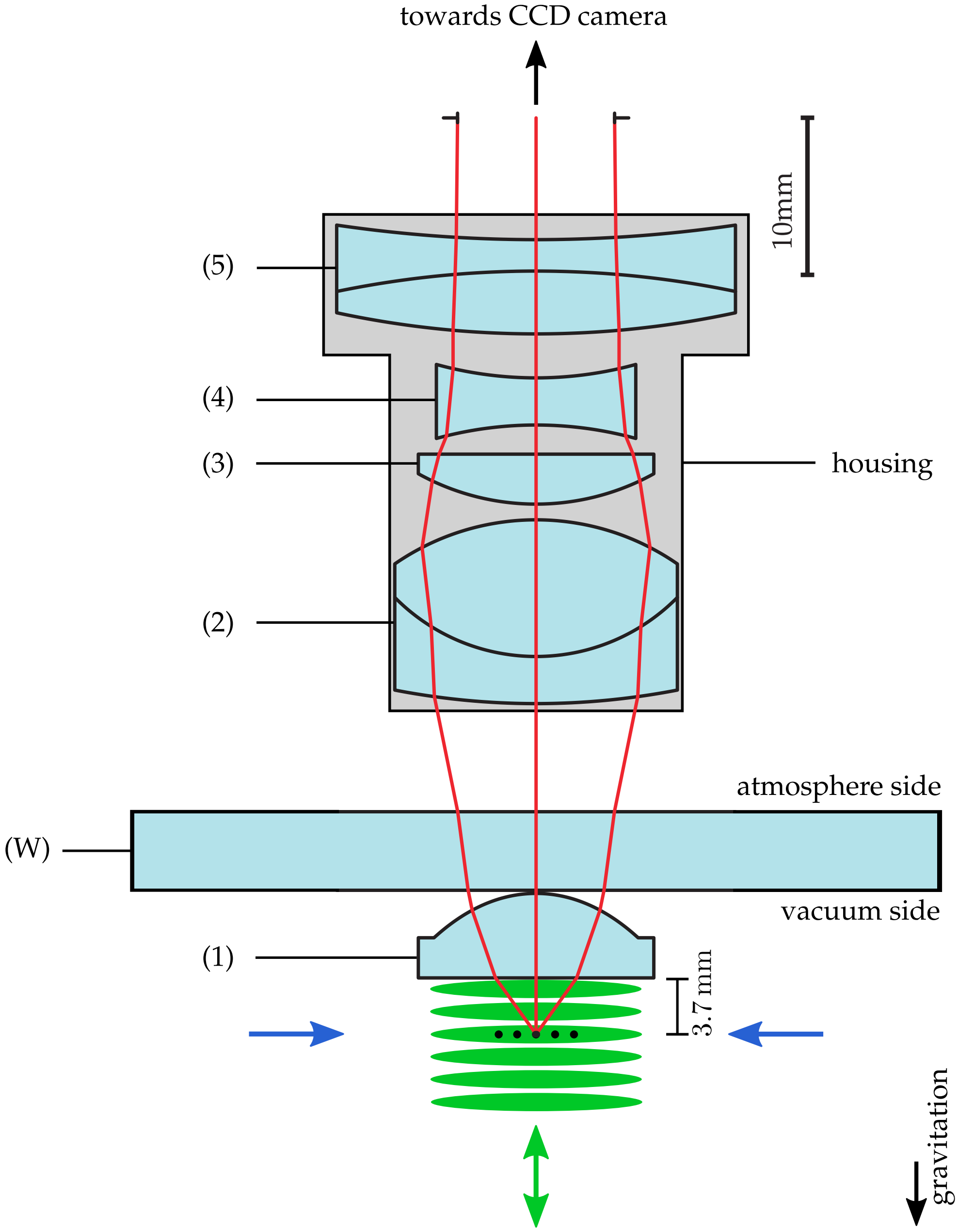

Figure 3.4.: Lens design and implementation of the FQGM imaging system. The imaging system consists of five lenses, which are labeled (1) - (5). Lenses (1) - (4) form the microscope objective and lens (5) projects the image onto a camera chip. The front lens (1) is placed inside of the vacuum chamber while lenses (2) - (5) are held within a housing outside of the vacuum chamber. Fluorescence imaging of the atoms is performed through a vacuum window, which is denoted as (W). The red lines represent ray traces to illustrate the effect of the individual lenses. The retro-reflected, vertical lattice laser beam is indicated by the green double arrow and the lattice slices of the resulting vertical 1D optical lattice are shown as green ellipses. The blue arrows indicate one of the two retro-reflected lattice laser beams that are used for the generation of the horizontal 2D optical lattice. Figure adopted from Ref. [Mar17].

3.5.3. K−Cs Imaging System

The FQGM imaging system of the K−Cs apparatus is a home-built one to avoid potential high costs for custom commercial solutions as pointed out in Ref. [Mar17]. The imaging system was designed by our Postdoc E. Kirilov and was assembled and tested by our master student M. Marszałek. For a detailed discussion of the imaging system, we refer to the thesis of M. Marszałek [Mar17]. To outline the geometrical restrictions that the imaging system imposes on the design of the K−Cs apparatus, we outline its optical design in the following.

The imaging system is designed to operate at the imaging wavelengths of potassium ($\lambda^{\mathrm{K}}_{\mathrm{image}} = 766\,\mathrm{nm}$) and cesium ($\lambda^{\mathrm{Cs}}_{\mathrm{image}} = 852\,\mathrm{nm}$). Figure 3.4 shows the lens design of the imaging system. The imaging system consists of five commercial lenses, which are labeled with (1) to (5) in Fig. 3.4. Lenses (1)[4], (2)[5], (3)[6], and (4)[7] form the microscope objective and project the image of the atoms to infinity (*infinite conjugate ratio*). The rear lens (5)[8] accepts the collimated light from the previous lenses and forms a magnified image on a camera chip.

The front lens (1) resides inside of the vacuum apparatus and is a plano-convex, aspheric lens. The asphere has an outer diameter of $15\,\mathrm{mm}$ and its flat surface points downwards towards the atoms. The distance between the asphere and the atomic sample is $3.7\,\mathrm{mm}$. We equipped the asphere with custom antireflection and high-reflectivity coatings on both sides after having purchased it. The specifications of the coatings are given in Sec. 8.3.2. The lenses (2) - (5) are positioned outside of the vacuum chamber and are mounted within a stainless steel housing. These lenses were already coated with a broadband antireflection coating on both sides upon their arrival. The imaging system is corrected for a plane-parallel, fused-silica, $5\,\mathrm{mm}$-thick vacuum window, which is denoted as (W) in Fig. 3.4.

The optical design software *Zemax* employed for the lens design predicts the imaging system to be diffraction limited and to have a spatial resolution $d_0^{766} = 793\,\mathrm{nm}$ at $766\,\mathrm{nm}$ and $d_0^{852} = 882\,\mathrm{nm}$ at $852\,\mathrm{nm}$ [Mar17]. The magnification is expected to be 55x.

To characterize the imaging system, a back-illuminated $500\,\mathrm{nm}$-diameter pinhole was imaged with the imaging system onto a CCD camera. The imaging system was tested with respect to both imaging wavelengths. To that end, the pinhole was illuminated in succession with $766\,\mathrm{nm}$ and $852\,\mathrm{nm}$ laser light. For the measurements a $5\,\mathrm{mm}$ thick fused silica substrate imitated the vacuum window (W).

When the pinhole was centered to the optical axis of the imaging system, the imaging system yielded diffraction-limited images of the pinhole for both imaging wavelengths. The spatial resolution of the imaging system was determined through wavefront reconstruction from collected pinhole images to be $d_0^{766,\mathrm{m}} = 797(1)\,\mathrm{nm}$ at $766\,\mathrm{nm}$ and was approximated to be $d_0^{852,\mathrm{m}} \approx 895\,\mathrm{nm}$ at $852\,\mathrm{nm}$ [Mar17]. The magnification of the imaging system was measured to be 56.20(8) for $766\,\mathrm{nm}$ and assumed to be identical for $852\,\mathrm{nm}$ [Mar17]. The diffraction-limited performance of the imaging system was maintained for off-axis imaging when the pinhole was moved within a field of view of approximately $\pm 40\,\mu\mathrm{m}$ in each transverse spatial direction [Mar17]. To determine the chromatic focal shift between the image planes for $766\,\mathrm{nm}$ and $852\,\mathrm{nm}$ illumination, the camera was moved along the optical axis and images were taken at several positions. The mutual distance of the focus locations revealed a focal shift of $4.15(2)\,\mathrm{mm}$ [Mar17]. With respect to future applications, the chromatic focal shift of

---

[4] LightPath, 355561.

[5] Edmund Optics, 49-955.

[6] Edmund Optics, 48-747.

[7] Thorlabs, LD2060-B.

[8] Thorlabs, AC254-500-B.

the imaging system implies that the camera needs to be translated for alternating imaging of potassium and cesium samples. The camera thus might be mounted onto a motorized translation stage.

4. Calculation of Electric-Dipole Polarizabilities of ^{39}K Atoms

A long-term goal of the K$-$Cs apparatus is to push fluorescence quantum gas microscopy of ^{39}K atoms towards higher spatial resolution. We therefore plan to image the trapped ^{39}K atoms via ground-state transitions to higher excited atomic levels. A question that arises in that regard is what optical lattice potential the ^{39}K atoms experience in the excited atomic levels. In order to calculate the optical lattice potentials for ^{39}K atoms in excited atomic levels, we numerically compute values for the atomic polarizability α for a number of excited states of ^{39}K. We begin this Chapter with a motivation of fluorescence quantum gas microscopy via higher excited atomic levels. We discuss why we cannot resort to literature values for the atomic polarizabilities for all atomic states of ^{39}K that are of interest to us. Instead, we need to calculate the atomic polarizabilities of several states of ^{39}K on our own. We provide the theoretical foundation for the calculation of atomic polarizabilities and present our numerical results for the atomic polarizabilities at the end of this Chapter. The theoretical introduction of this Chapter is partially based on Ref. [Bon97].

4.1. Motivation and Problem Statement

Conventional fluorescence quantum gas microscopy of alkali quantum gases as described in Sec. 3.2 uses the principal D line atomic transitions for imaging. Imaging on atomic transitions to higher excited levels, e.g. the $4S_{1/2} \rightarrow 5P_{3/2}$ transition for ^{39}K, shifts the fluorescence light of the atoms towards shorter wavelengths. The transition wavelength of the $4S_{1/2} \rightarrow 5P_{3/2}$ transition ($\lambda = 404.4\,\mathrm{nm}$ [Kraa]) is nearly a factor of two shorter than the transition wavelength of the principal D_1 transition that has been employed so far for imaging K atoms in FQGM apparatuses [Hal15, Edg15, Che15]. In view of the diffraction limit of an imaging system, a shorter imaging wavelength λ_{image} facilitates a higher spatial resolution d_0 (see Eq. (3.4)). An enhanced spatial resolution in fluorescence quantum gas microscopy brings single-site detection of atoms in optical lattices with reduced lattice spacings within reach of experimental realization. Optical lattices with reduced lattice spacings include for example bichromatic superlattices of overlapping $1064\,\mathrm{nm}$ and $532\,\mathrm{nm}$ lattice laser beams, where the "short lattice spacing" is $266\,\mathrm{nm}$.

Fluorescence imaging of ^{39}K atoms on the $4S_{1/2} \rightarrow 5P_{3/2}$ transition excites atoms in the $5P_{3/2}$ level. From this level the atoms decay into the $4S_{1/2}$ ground state through different decay channels. In most of the decay channels, the potassium atoms temporarily occupy intermediate atomic levels, namely the $4P_{1/2}$, $4P_{3/2}$, $5S_{1/2}$, $3D_{5/2}$, or $3D_{3/2}$ levels. This decay behavior is in contrast to conventional fluorescence quantum gas microscopy of ^{39}K atoms, where intermediate levels are absent. Since the coupling of atoms to laser light is level-dependent, the optical lattice potential experienced by the ^{39}K atoms during fluorescence imaging varies for the different excited and intermediate levels. Typically, the optical lattice potential in a

FQGM apparatus is strongly confining for atoms in their internal ground state. Within the same optical lattice the confinement for excited atomic levels, however, might be weaker or even inverted.

The optical lattice potential that an atom experiences is determined through the atomic polarizability α and the laser intensity I_L (see Eq. (2.10)). In order to calculate the lattice potential for ^{39}K atoms in excited atomic levels up to the $5\mathrm{P}_{3/2}$ level, we are interested in numerical values for the atomic polarizabilities α of the atomic levels $4\mathrm{S}_{1/2}$, $4\mathrm{P}_{1/2}$, $4\mathrm{P}_{3/2}$, $5\mathrm{S}_{1/2}$, $3\mathrm{D}_{5/2}$, $3\mathrm{D}_{3/2}$, $5\mathrm{P}_{1/2}$, and $5\mathrm{P}_{3/2}$ at $1064\,\mathrm{nm}$ lattice laser light. To our knowledge, numerical values for the atomic polarizability α of K atoms at $1064\,\mathrm{nm}$ have been reported only partially for the levels of interest in this Chapter [Saf13, Nan12]. We thus calculate the atomic polarizabilities α of ^{39}K for all missing atomic levels in this Chapter. For comparison, we determine the atomic polarizability α also for those atomic levels for which we find numerical values in literature.

4.2. Static and Dynamic Polarizability

An atom within a static and uniform electric field $\vec{F} = F \cdot \vec{\mathcal{E}}$ with *field strength F* and unit field vector $\vec{\mathcal{E}}$ experiences a deformation of its electron cloud. The energy of the rearranged charge distribution within the external field can be expressed by means of a multipole expansion [Jac99a]. The mathematical expression for the energy is thereby expanded into a sum of energy contributions that are associated with different electric multipole moments of the new charge distribution. Neutral particles do not carry a net electric charge and hence have no electric monopole moment. Thus, for a neutral atom, the lowest-order contribution to the multipole expansion is an electric dipole moment $\vec{p}$ that can be written as [Bon97]

$$\vec{p}(\vec{F}) = \vec{p}_\mathrm{perm} + \boldsymbol{\alpha} \cdot \vec{F} + \frac{1}{2!}\boldsymbol{\beta} : \vec{F}^2 + \frac{1}{3!}\boldsymbol{\gamma} \vdots \vec{F}^3 + \dots \quad . \tag{4.1}$$

The first term, $\vec{p}_\mathrm{perm}$, in Eq. (4.1) corresponds to the *permanent electric dipole moment* of the particle. Because atoms do not possess a permanent electric dipole moment [Jer14], it is zero in our treatment, i.e. $\vec{p}_\mathrm{perm} = \vec{0}$. All other terms in Eq. (4.1) represent field-induced contributions to the dipole moment $\vec{p}$. The contributions are characterized by the *atomic polarizability* $\boldsymbol{\alpha}$ and the *hyperpolarizabilities* $\boldsymbol{\beta}$ and $\boldsymbol{\gamma}$. In a mathematical sense $\boldsymbol{\alpha}$, $\boldsymbol{\beta}$, and $\boldsymbol{\gamma}$ are Cartesian tensors of rank two, three, and four [Bon97]. Since hyperpolarizabilities only become relevant for nonlinear effects in strong electric fields, we neglect them here.

In lowest order of field strength F, the atomic polarizability $\boldsymbol{\alpha}$ in Eq. (4.1) relates the induced electric dipole moment $\vec{p}$ to the electric field $\vec{F}$ that induces it according to

$$\vec{p} = \boldsymbol{\alpha} \cdot \vec{F}. \tag{4.2}$$

The polarizability tensor $\boldsymbol{\alpha}$ has tensor components $\alpha_{\mu\nu}$ with $\mu, \nu \in \{x, y, z\}$ and is in general anisotropic. The potential energy of the induced electric dipole moment $\vec{p}$ and therefore of the atom within the initially considered electric field $\vec{F}$ is [Mil78]

$$V_\mathrm{dip} = -\frac{1}{2} \cdot \vec{p} \cdot \vec{F} = -\frac{1}{2} \cdot \boldsymbol{\alpha} : \vec{F}^2. \tag{4.3}$$

For obtaining the right side of Eq. (4.3) we made use of Eq. (4.2).

An equivalent expression for the dipole moment $\vec{p}$ in Eq. (4.2) is

$$\vec{p} = \sum_i q_i \vec{r}_i, \tag{4.4}$$

where the sum runs over all constituents i that carry an *electric charge* q_i. If the nucleus of the atom with *atomic number* Z resides at the origin, Eq. (4.4) reduces to

$$\vec{p} = -\sum_{i=1}^{Z} e\vec{r}_i. \tag{4.5}$$

The sum in Eq. (4.5) now runs over all Z electrons of the atom, which have an electric charge $q_i = -e$ with e being the *elementary charge*. Equation (4.5) indicates that all Z electrons of the atom contribute to the dipole moment $\vec{p}$. Thus, numerical evaluation of the polarizability tensor components $\alpha_{\mu\nu}$ in Eq. (4.2) is generally a many-body problem.

Electrons in atoms occupy different atomic orbitals in accordance with Pauli's exclusion principle. One distinguishes between electrons in orbitals of closed shells (*core electrons*) and electrons in orbitals of open shells (*valence electrons*). Since valence electrons are more weakly bound to the atomic nucleus than core electrons, valence electrons are affected more strongly by an applied electric field than electrons of inner shells. Hence, valence electrons typically contribute most to the polarizability of an atom [Mil78].

For the cases discussed in this Thesis, we will see in the following Section that the polarizability tensor $\boldsymbol{\alpha}$ can be replaced by a scalar α_{tot}. We made use of this result already in Eq. (2.10) to calculate optical potentials, where we set $\alpha_{\text{tot}} = \alpha$. For atoms with a single valence electron (*monovalent atoms*), like alkali atoms, it is customary to write the *total atomic polarizability* α_{tot} as a sum [Mit10, Saf13, Der99]

$$\alpha_{\text{tot}} = \alpha_{\text{v}} + \alpha_{\text{c}} + \alpha_{\text{vc}}. \tag{4.6}$$

The contribution α_{v} characterizes the polarizability of the valence electrons and disregards the influence of the external electric field $\vec{F}$ on the core electrons. It is denoted as *valence polarizability*. The influence of the applied electric field $\vec{F}$ on the core electrons is described by the polarizability α_{c} of the core electrons (*core polarizability*). The effect of the polarized valence electrons on the core electrons is given by α_{vc} (*valence-core polarizability*). Since electrons of the ionic core are more strongly bound to the nucleus than valence electrons, the valence-core contribution α_{vc} is comparatively small [Dut15a]. For electric fields $\vec{F}$ that oscillate at frequency ω_{L}, each term in Eq. (4.6) becomes frequency-dependent [Dut15a]

$$\alpha_{\text{tot}}(\omega_{\text{L}}) = \alpha_{\text{v}}(\omega_{\text{L}}) + \alpha_{\text{c}}(\omega_{\text{L}}) + \alpha_{\text{vc}}(\omega_{\text{L}}). \tag{4.7}$$

4.3. Valence Scalar and Valence Tensor Polarizability

The valence polarizability α_{v} in Eq. (4.6) can be calculated within the framework of perturbation theory. It is this method that is the subject of this Section. In a semiclassical approach, one treats the electric field $\vec{F}$ classically and takes the quantum-mechanical properties of the atom into account by using the *dipole moment operator* $\hat{p}$ and the *polarizability tensor operator* $\hat{\boldsymbol{\alpha}}$.

4.3.1. Static Electric Field

A monovalent atom placed within a static and uniform electric field $\vec{F} = F \cdot \vec{\mathcal{E}}$ as considered in Sec. 4.2 is described by the Hamilton operator [Sob79]

$$\hat{H}_{\text{Stark}} = \hat{H}_{\text{atom}} - \vec{F} \cdot \hat{p}. \tag{4.8}$$

The Hamilton operator $\hat{H}_{\text{atom}}$ of the unperturbed atom has eigenstates $|\varphi_k\rangle$ with eigenenergies E_k. The dipole operator $\hat{p}$ is defined analogously to Eq. (4.4) as

$$\hat{p} = \sum_i q_i \hat{r}_i \tag{4.9}$$

with *position operator* $\hat{r}$ and the sum taken over all charged particles i. If we assume the atom to reside at the origin of an arbitrary coordinate system, Eq. (4.9) for the single valence electron of the atom becomes

$$\hat{p} = -e\hat{r}. \tag{4.10}$$

The second term in Eq. (4.8) refers to the potential energy of the induced electric dipole moment within the electric field $\vec{F}$ and is considered as perturbation. The assumption of a static electric field $\vec{F}$ simplifies the notation of the following expressions and will be dropped at the end of this Section.

In first-order perturbation theory the energy shift $\Delta E_a^{(1)}$ of an atomic eigenstate $|\varphi_a\rangle$ with eigenenergy E_a owing to the presence of the electric field $\vec{F}$ is given by the expectation value

$$\Delta E_a^{(1)} = -\langle\varphi_a|\vec{F} \cdot \hat{p}|\varphi_a\rangle. \tag{4.11}$$

For parity reasons it is zero in alkali-metal atoms, i.e. $\Delta E_a^{(1)} = 0$ [Aro07]. In second order, the energy correction $\Delta E_a^{(2)}$ to the eigenenergy E_a is [Mit10]

$$\Delta E_a^{(2)} = -\sum_{k \neq a} \frac{\left|\langle\varphi_a|\vec{\mathcal{E}} \cdot \hat{p}|\varphi_k\rangle\right|^2}{E_k - E_a} \cdot F^2, \tag{4.12}$$

where the sum is taken over all valence eigenstates $|\varphi_k\rangle$, except for $k = a$. The energy correction $\Delta E_a^{(2)}$ depends quadratically on the field strength F and can be positive or negative for different atomic states $|\varphi_a\rangle$. We can deduce an expression for the tensor components $\alpha_{\mu\nu}$ of the atomic polarizability tensor $\boldsymbol{\alpha}$ through comparison of Eq. (4.12) with Eq. (4.3). For an atom in state $|\varphi_a\rangle$ the components $\alpha_{\mu\nu}$ can be expressed as [Bon97]

$$\alpha_{\mu\nu} = 2 \sum_{k \neq a} \frac{\langle\varphi_a|\hat{p}_\mu^*|\varphi_k\rangle\langle\varphi_k|\hat{p}_\nu|\varphi_a\rangle}{E_k - E_a}. \tag{4.13}$$

Here, $\hat{p}_\mu$ and $\hat{p}_\nu$ are Cartesian components of the dipole operator $\hat{p}$. For a static electric field, the polarizability tensor $\boldsymbol{\alpha}$ is real and symmetric, i.e. $\alpha_{\mu\nu}^* = \alpha_{\nu\mu}$. The number of independent tensor components $\alpha_{\mu\nu}$ thus reduces to no more than six. These six components correspond to the three diagonal elements $\alpha_{\mu\mu}$ and the three off-diagonal elements with either $\mu < \nu$ or $\mu > \nu$.

We now assume the electric field $\vec{F}$ in $z-$direction and choose the electric field direction $\vec{\mathcal{E}}$ as the quantization axis. In experiments, the projection of the induced dipole moment $\hat{p}$ onto the $z-$axis, p_z, is measured, with $p_z = \langle\varphi_a|\hat{p}_z|\varphi_a\rangle$. With the previous choice of the electric field $\vec{F}$ the projection p_z is given by

$$p_z = \vec{\mathcal{E}} \cdot \vec{p} = \begin{pmatrix} 0 \\ 0 \\ 1 \end{pmatrix} \cdot \begin{pmatrix} \alpha_{xx} & \alpha_{xy} & \alpha_{xz} \\ \alpha_{xy} & \alpha_{yy} & \alpha_{yz} \\ \alpha_{xz} & \alpha_{yz} & \alpha_{zz} \end{pmatrix} \cdot \begin{pmatrix} 0 \\ 0 \\ F \end{pmatrix} = \alpha_{zz} F. \tag{4.14}$$

The projection p_z is proportional to the field strength F with the proportionality constant being the expectation value $\alpha_{zz} = \langle\varphi_a|\hat{\alpha}_{zz}|\varphi_a\rangle$ of the polarizability operator $zz-$component. Thus, we are left with a single quantity α_{zz} that describes the interaction of the valence electron of the atom with the external electric field $\vec{F}$. The quantity α_{zz} corresponds to the valence polarizability α_v in Eq. (4.6), i.e. $\alpha_\mathrm{v} = \alpha_{zz}$.

In a next step, we specify the atomic eigenstate $|\varphi_a\rangle$ and assume that it corresponds to a fine structure Zeeman state. A fine structure Zeeman state is determined through a set of quantum numbers, which include the principal quantum number n, the *spin angular momentum quantum number* S, the *orbital angular momentum quantum number* L, the *total electronic angular momentum quantum number* J, and the *magnetic projection quantum number* $M_J \in \{-J, -J+1, \ldots, +J\}$. For reasons of clarity, we condense n, S, and L into a single quantity γ and only notate J and M_J explicitly in the following. The eigenstate $|\varphi_a\rangle$ is then written as $|\varphi_a\rangle = |\gamma_a J_a M_{J,a}\rangle$. The valence polarizability α_v of a fine structure Zeeman state $|\varphi_a\rangle = |\gamma_a J_a M_{J,a}\rangle$ is given through [Bon97]

$$\alpha_\mathrm{v}(\gamma_a, J_a, M_{J,a}) = \langle\varphi_a|\hat{\alpha}_{zz}|\varphi_a\rangle = \langle\gamma_a J_a M_{J,a}|\hat{\alpha}_{zz}|\gamma_a J_a M_{J,a}\rangle = \alpha_0 + \alpha_2 \cdot \frac{3M_{J,a}^2 - J_a(J_a+1)}{J_a(2J_a-1)}. \tag{4.15}$$

The right side of Eq. (4.15) is a sum of two terms: the first term, α_0, is independent of $M_{J,a}$ and therefore a constant for each fine structure level. Since α_0 is constant for different orientations of the induced electric dipole moment relative to the electric field, it constitutes the isotropic part of $\alpha_\mathrm{v}(\gamma_a, J_a, M_{J,a})$. The constant α_0 is frequently denoted as *static valence scalar polarizability*. It can be understood either as the average of the expectation values $\alpha_{\mu\mu}$ of the diagonal polarizability tensor operator components for a given state $|\gamma_a J_a M_{J,a}\rangle$ or, equivalently, as the average of $\alpha_\mathrm{v}(\gamma_a, J_a, M_{J,a})$ over all $M_{J,a}$ according to [Bon97]

$$\alpha_0 = \frac{1}{3}\sum_\mu \alpha_{\mu\mu}(\gamma_a, J_a, M_{J,a}) = \frac{1}{2J_a+1}\sum_{M_{J,a}} \alpha_\mathrm{v}(\gamma_a, J_a, M_{J,a}). \tag{4.16}$$

The second term of the right side of Eq. (4.15) has an angular dependency given through $M_{J,a}$. It describes the anisotropy of $\alpha_\mathrm{v}(\gamma_a, J_a, M_{J,a})$. The factor α_2 is a constant for each fine structure level and is known as *static valence tensor polarizability*. When $J_a = 0$ or $J_a = 1/2$, the tensor polarizability contribution in Eq. (4.15) vanishes and $\alpha_\mathrm{v}(\gamma_a, J_a, M_{J,a})$ is equal to α_0 (see also discussion in Sec. 4.3.2) [Kha68, Bon97]. For $J_a = 0$, i.e. spherically symmetric states, the polarizability tensor $\boldsymbol{\alpha}$ is diagonal and the tensor components $\alpha_{\mu\mu}(\gamma_a, J_a, M_{J,a})$ are identical [Bon97]. The atomic polarizability tensor $\boldsymbol{\alpha}$ is then isotropic and reduces to a single scalar. If $J_a > 1/2$, the tensor polarizability contribution lifts the degeneracy of Zeeman states with different $|M_{J,a}|$. The tensor polarizability contribution in Eq. (4.15) is maximum for states with $M_{J,a} = \pm J_a$. The static valence polarizability $\alpha_{\mathrm{v}}(\gamma_a, J_a, M_{J,a})$ in Eq. (4.15) depends on the absolute value $|M_{J,a}|$. Zeeman states of the same fine structure level with different $|M_{J,a}|$ thus interact differently with the electric field.

4.3.2. Oscillating Electric Field

The expression for $\alpha_{\mathrm{v}}(\gamma, J, M_J)$ in Eq. (4.15) was obtained under the assumption of a static and uniform electric field $\vec{F}$ along the $z-$direction. For oscillating electric fields, e.g. laser light, with frequency ω_{L} and linear polarization parallel to the $z-$direction, Eq. (4.15) remains valid if ω_{L} is at least several line widths off from any atomic resonance [Bon97, Dut15a, Aro07]. The static valence polarizability α_{v} is then replaced by the *frequency-dependent valence polarizability* $\alpha_{\mathrm{v}}(\omega_{\mathrm{L}})$. Analogously, the static valence scalar and valence tensor polarizabilities become frequency dependent with $\alpha_0 \to \alpha_0(\omega_{\mathrm{L}})$ and $\alpha_2 \to \alpha_2(\omega_{\mathrm{L}})$. When the laser light is off-resonant, $\alpha_0(\omega_{\mathrm{L}})$, $\alpha_2(\omega_{\mathrm{L}})$, and thus $\alpha_{\mathrm{v}}(\omega_{\mathrm{L}})$ stay real [Bon97].

The *frequency-dependent valence scalar polarizability* $\alpha_0(\omega_{\mathrm{L}})$ for a fine structure level $|\gamma_a J_a\rangle$ can be expressed through [Aro07, Mit10]

$$\alpha_0(\omega_{\mathrm{L}}) = \frac{2}{3(2J_a+1)} \sum_{\substack{k\neq a \\ \text{dipole-allowed}}} \frac{(E_k - E_a)}{(E_k - E_a)^2 - (\hbar\omega_{\mathrm{L}})^2} \cdot |\langle \gamma_a J_a || \vec{p} || \gamma_k J_k \rangle|^2 \tag{4.17}$$

with the sum taken over all dipole-allowed transitions $|\gamma_a J_a\rangle \to |\gamma_k J_k\rangle$. The double-bar matrix element $\langle \cdot || \vec{p} || \cdot \rangle$ in Eq. (4.17) corresponds to the *reduced electric-dipole matrix element* (RME).

The *frequency-dependent valence tensor polarizability* $\alpha_2(\omega_{\mathrm{L}})$ for a fine structure level $|\gamma_a J_a\rangle$ can be written as [Aro07, Mit10]

$$\begin{aligned}\alpha_2(\omega_{\mathrm{L}}) = -4\mathcal{C} \sum_{\substack{k\neq a \\ \text{dipole-allowed}}} (-1)^{J_a+J_k+1} \begin{Bmatrix} J_a & 1 & J_k \\ 1 & J_a & 2 \end{Bmatrix} \frac{(E_k - E_a)}{(E_k - E_a)^2 - (\hbar\omega_{\mathrm{L}})^2} \\ \times |\langle \gamma_a J_a || \vec{p} || \gamma_k J_k \rangle|^2\end{aligned} \tag{4.18}$$

with the sum taken over all dipole-allowed transitions $|\gamma_a J_a\rangle \to |\gamma_k J_k\rangle$. The curly brackets $\{\because\}$ in Eq. (4.18) represent a *Wigner 6J-symbol*. Six-J symbols are used in angular momentum coupling of three separate systems and can be evaluated with the Racah formula given in Ref. [Mes65b]. The constant $\mathcal{C}$ in Eq. (4.18) is defined as

$$\mathcal{C} = \sqrt{\frac{5J_a(2J_a-1)}{6(J_a+1)(2J_a+1)(2J_a+3)}}. \tag{4.19}$$

For $\omega_{\mathrm{L}} = 0$, i.e. for static electric fields, Eq. (4.17) and Eq. (4.18) convert into the expressions for the static valence scalar polarizability α_0 and static valence tensor polarizability α_2 [Mit10].

Calculation of $\alpha_0(\omega_\mathrm{L})$ and $\alpha_2(\omega_\mathrm{L})$ with Eqs. (4.17) and (4.18), also known as *sum-over-states approach*, requires summation over levels $|\gamma_k J_k\rangle$ with opposite parity. Typically, for a given laser frequency ω_L, only a few atomic transitions $|\gamma_a J_a\rangle \rightarrow |\gamma_k J_k\rangle$ provide substantial contributions to the sums of $\alpha_0(\omega_\mathrm{L})$ and $\alpha_2(\omega_\mathrm{L})$. The sum-over-states method is therefore a common approach to numerically calculate the valence polarizability $\alpha_\mathrm{v}(\omega_\mathrm{L})$ of monovalent atoms.

4.4. Electric-Dipole Polarizabilities of ^{39}K Atoms

In this Section, we calculate the frequency-dependent valence scalar and tensor polarizabilities $\alpha_0(\omega_\mathrm{L})$ and $\alpha_2(\omega_\mathrm{L})$ of the fine structure levels $4S_{1/2}$, $4P_{1/2}$, $4P_{3/2}$, $5S_{1/2}$, $3D_{5/2}$, $3D_{3/2}$, $5P_{1/2}$, and $5P_{3/2}$ of ^{39}K at our lattice laser wavelength $\lambda_\mathrm{L} = 1064\,\mathrm{nm}$. We make use of the sum-over-states approach in Eqs. (4.17) and (4.18). We use the results to calculate thereafter the total polarizability $\alpha_\mathrm{tot}(\omega_\mathrm{L})$ with Eqs. (4.15) and (4.7) for individual Zeeman states of those levels.

4.4.1. Level Scheme of ^{39}K

Potassium belongs to the first group of the periodic table of elements and is therefore a monovalent atomic species. It has three naturally occuring, chemically stable isotopes, ^{39}K, ^{40}K, and ^{41}K, which are commonly used in potassium quantum gas experiments. In this Thesis, we are concerned with the most abundant isotope, ^{39}K. The isotope ^{39}K has a *nuclear spin* $\vec{I}$ with *nuclear spin quantum number* $I = 3/2$ [Ari77]. If interaction between the *total electronic angular momentum* $\vec{J}$ and the nuclear spin $\vec{I}$ is ignored, the ground state of ^{39}K is a $4S_{1/2}$ fine structure level. Figure 4.1 shows the level scheme of ^{39}K with all spectroscopic terms found in literature. We resolve the fine-structure splitting for levels up to the $5P_{3/2}$ level in Fig. 4.1. Because of the decreasing fine-structure splitting of higher-lying levels, we give only the spectroscopic term $n^{2S+1}L$ for fine structure levels beyond the $5P_{3/2}$ level. Note, in Fig. 4.1 the $3D_{5/2}$ level lies below the $3D_{3/2}$ level, which corresponds to an inverted fine structure doublet. The same behavior is observed for all n^2D terms in potassium. Doublet inversion is known for many alkali-metals and alkali-like systems and is discussed in Ref. [Luc76, Gal78, Hol76].

Dominant contributions to the valence polarizability $\alpha_\mathrm{v}(\omega_\mathrm{L})$ of an atomic state $|\varphi_a\rangle$ come from transitions $|\varphi_a\rangle \rightarrow |\varphi_k\rangle$ that are closest to resonance with the incident laser light. In Fig. 4.1, we identify the dominant transitions for the valence polarizabilities $\alpha_\mathrm{v}(\omega_\mathrm{L})$ of the $4S_{1/2}$, $4P_{1/2}$, $4P_{3/2}$, $5S_{1/2}$, $3D_{5/2}$, $3D_{3/2}$, $5P_{1/2}$, and $5P_{3/2}$ levels by indicating the energy of a photon with wavelength $1064\,\mathrm{nm}$ through vertical black arrows. The different lengths of the arrows result from the circumstance that the shown levels are not to scale. Under consideration of the selection rules for dipole transitions, we find that for the $4S_{1/2}$ ground state the transitions to the $4P_{1/2}$ and $4P_{3/2}$ levels are closest to resonance while for the $4P_{1/2}$ and $4P_{3/2}$ fine structure levels the transitions to the $3D_{5/2}$ and $3D_{3/2}$ fine structure levels are nearest. In contrast, for the $5S_{1/2}$, $3D_{5/2}$, and $3D_{3/2}$ fine structure levels the transitions to the 7^2P^o term are closest to resonance. Lastly, for the $5P_{1/2}$ and $5P_{3/2}$ levels the transitions to the highly excited 13^2S and 11^2D terms are closest. Among the dominant, dipole-allowed transitions just listed, the $5P_{1/2} \rightarrow 13S_{1/2}$ transition is closest to resonance with $1064\,\mathrm{nm}$ laser light. The detuning of the $1064\,\mathrm{nm}$ laser light relative to that atomic transition is $\Delta \approx 800\,\mathrm{GHz}$. Thus, we can use Eq. (4.17) and Eq. (4.18) to calculate atomic polarizabilities.

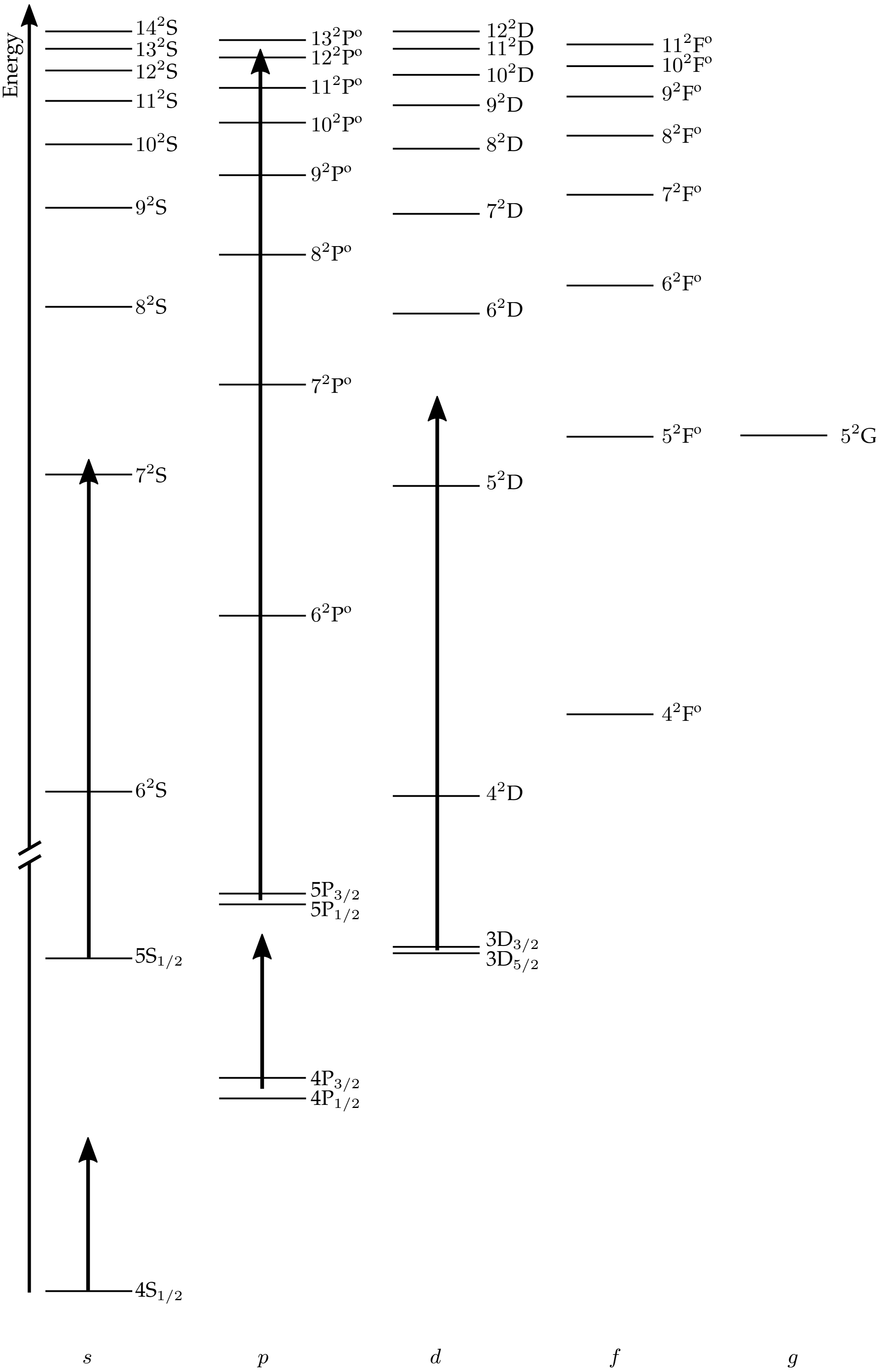

Figure 4.1.: Level scheme of ^{39}K. The level scheme shows the fine structure levels between the $4S_{1/2}$ ground state and the $5P_{3/2}$ excited level. For energetically higher levels, the associated spectroscopic terms are shown. The vertical arrows indicate the energy of a photon with wavelength $1064\,\mathrm{nm}$. Numerical values for level energies are taken from Ref. [Krab, San08]. Level energies are not to scale.

4.4.2. Calculation and Numerical Results

Atomic polarizabilities and RMEs are frequently given in atomic units (a.u.), where e, electron mass m_e, $4\pi\epsilon_0$, and $\hbar$ have values 1. We follow this common practice in the remainder of this Chapter. Polarizabilities in atomic units have dimension of volume and are given in units of a_0^3 in the following with *Bohr radius* a_0. Reduced dipole matrix elements in atomic units are given in units of ea_0 here. The conversion factors from atomic units to SI units are $4\pi\epsilon_0 a_0^3$ for polarizabilities and ea_0 for RMEs [Mit10].

Discussion of Atomic Input Data

The sum-over-states approach requires knowledge of atom-specific data including level energies E_k and numerical values of RMEs. For our calculation, we use existing atomic data for potassium from different data sets. We obtain level energies of fine structure levels relative to the $4\mathrm{S}_{1/2}$ ground state from the NIST atomic spectra database [Krab] and the atomic data compilation by J. E. Sansonetti [San08]. Our subset of atomic data contains level energies of 69 fine structure levels between the $4\mathrm{S}_{1/2}$ ground state and the $14\mathrm{S}_{1/2}$ level, as shown in Fig. 4.1. The relative uncertainties of the level energies given in the compilations vary between $\sim 1.5 \times 10^{-8}\,\%$ ($\widehat{=}\ 0.000\,002\,\mathrm{cm}^{-1}$) and $\sim 2 \times 10^{-4}\,\%$ ($\widehat{=}\ 0.06\,\mathrm{cm}^{-1}$) for different levels.

We use numerical results for RMEs listed in a theoretical study by M. S. Safronova *et al.* in Ref. [Saf13] as well as from a separate collection received from M. S. Safronova. We compare the RMEs by M. S. Safronova with those mentioned by D. K. Nandy *et al.* in Ref. [Nan12] to gain confidence in the values for RMEs for transitions to highly excited levels. Our collection of RMEs comprises in total 142 matrix elements. Among those are RMEs for all dipole-allowed transitions from the $5\mathrm{P}_{3/2}$ and lower-lying levels to levels as high as $10\mathrm{S}_{1/2}$. Reduced matrix elements for transitions to atomic levels higher than $10\mathrm{S}_{1/2}$ are partially missing in our data set. Furthermore our list contains RMEs for all dipole-allowed transitions from the $5\mathrm{P}_{1/2}$ and $5\mathrm{P}_{3/2}$ levels to levels as high as $14\mathrm{S}_{1/2}$. The RMEs have absolute values between 0.0051 a.u. (for the transition $4\mathrm{S}_{1/2} \to 13\mathrm{P}_{1/2}$) and 22.9280 a.u. (for the transition $5\mathrm{P}_{3/2} \to 4\mathrm{D}_{5/2}$). Relative errors stated for the RMEs range from $0.16\,\%$ (for the transition $5\mathrm{P}_{3/2} \to 6\mathrm{S}_{1/2}$) up to $98.29\,\%$ (for the transition $5\mathrm{P}_{3/2} \to 6\mathrm{D}_{3/2}$) and are not stated for a couple of RMEs.

Core Polarizability and Valence-Core Polarizability

The core polarizability $\alpha_\mathrm{c}(\omega_\mathrm{L})$ and valence-core polarizability $\alpha_\mathrm{vc}(\omega_\mathrm{L})$ in Eq. (4.7) take into account particle-hole excitations from core electrons and correct for core-excited states that violate Pauli's exclusion principle [Saf06, Der99]. Excitation energies of K core electrons lie in the deep ultraviolet spectral region [Krab, San08]. Since our lattice laser frequency ω_L lies within the infrared part of the spectrum, it is far off-resonant from core excitations. Core and valence-core contributions are therefore only weakly dependent on the laser frequency ω_L in this spectral region [Saf06, Saf13]. Values for $\alpha_\mathrm{c}(\omega_\mathrm{L})$ and $\alpha_\mathrm{vc}(\omega_\mathrm{L})$ can then be approximated by their static values, i.e. $\alpha_\mathrm{c}(\omega_\mathrm{L}) \approx \alpha_\mathrm{c}$ and $\alpha_\mathrm{vc}(\omega_\mathrm{L}) \approx \alpha_\mathrm{vc}$ [Saf13].

Consistency Check: Static Polarizabilities

To verify that our calculation of frequency-dependent polarizabilities $\alpha_\mathrm{tot}(\omega_\mathrm{L})$ can be seen as reliable, we perform a consistency check of our program that is used for computation. The program is a self-written MATLAB code that was developed as part of this Thesis. It incorporates the atomic input data, uses the equations given in Sec. 4.2 and Sec. 4.3, and can also be used to determine atomic polarizabilities at wavelengths other than the one considered here.

Table 4.1.: Static polarizabilities. Comparison between our numerical results α_0^c and α_2^c and reference values for static valence scalar polarizability α_0 and static valence tensor polarizability α_2 for ^{39}K given in atomic units. Numbers in brackets give uncertainties.

	Safronova *et al.* [Saf13]		Present work	
Level	$\boldsymbol{\alpha_0}$	$\boldsymbol{\alpha_2}$	$\boldsymbol{\alpha_0^c}$	$\boldsymbol{\alpha_2^c}$
$5P_{3/2}$	7230(60)	-1065(18)	7201(116)	-1058(43)
$5P_{1/2}$	7052(70)		7023(120)	
$3D_{3/2}$	1420(30)	-482(19)	1371(53)	-473(30)
$3D_{5/2}$	1412(30)	-673(23)	1346(48)	-655(34)
$5S_{1/2}$	4961(22)		4954(32)	
$4P_{3/2}$	621(4)	-109.4(1.1)	603(6)	-106(3)
$4P_{1/2}$	612(5)		593(6)	
$4S_{1/2}$	290.4(6)		287(4)	

For the consistency check, we numerically compute the static valence scalar and valence tensor polarizabilities α_0 and α_2 for the fine structure levels $4S_{1/2}$ to $5P_{3/2}$ and compare our results with existing reference data from Ref. [Saf13]. Table 4.1 lists our calculated values for α_0 and α_2, denoted as α_0^c and α_2^c, as well as the reference values. The uncertainties of α_0^c and α_2^c take into account the uncertainties of the input data, i.e. of the level energies E_k and the RMEs and are derived from propagation of uncertainties. The smallest relative uncertainty of the RMEs is several orders of magnitude larger than the largest relative uncertainty of the level energies, as discussed earlier. We therefore use the largest absolute uncertainty of the level energies to approximate the uncertainty of all level energies but consider the uncertainties for the RMEs individually.

Our results show a clear increase of the polarizabilities for higher lying levels. This behavior is in agreement with the observation that more loosely bound electrons are easier to polarize. We find that our results agree with the theoretical reference data in sign and furthermore in absolute value within $\pm 5\,\%$. Based on these findings, we conclude that our program satisfies the consistency check. We attribute the discrepancy between our results and the reference data mainly to the limited atomic data that we have.

Frequency-Dependent Polarizabilities

We now calculate the frequency-dependent valence scalar and valence tensor polarizabilities $\alpha_0(\omega_L)$ and $\alpha_2(\omega_L)$ of the $4S_{1/2}$, $4P_{1/2}$, $4P_{3/2}$, $5S_{1/2}$, $3D_{5/2}$, $3D_{3/2}$, $5P_{1/2}$, and $5P_{3/2}$ levels. Table 4.2 lists our results for $\alpha_0(\omega_L)$ and $\alpha_2(\omega_L)$, denoted as $\alpha_0^c(\omega_L)$ and $\alpha_2^c(\omega_L)$, as well as their calculated uncertainties $\Delta\alpha_0^c(\omega_L)$ and $\Delta\alpha_2^c(\omega_L)$. We calculate $\Delta\alpha_0^c(\omega_L)$ and $\Delta\alpha_2^c(\omega_L)$ in the same way as we computed the uncertainties of the static polarizabilities.

The results obtained for $\alpha_0^c(\omega_L)$ and $\alpha_2^c(\omega_L)$ allow the evaluation of the total atomic polarizability $\alpha_{\text{tot}}(\omega_L)$ for the fine structure Zeeman states. We approximate the core and valence-core contributions to the total atomic polarizability by their static values, which for K atoms correspond to $\alpha_c = 5.5$ a.u. and $\alpha_{vc} = -0.18$ a.u. [Saf13].[1] Table 4.2 summarizes our numerical results $\alpha_{\text{tot}}^c(\omega_L)$ and their uncertainties $\Delta\alpha_{\text{tot}}^c(\omega_L)$ for individual Zeeman states. The uncertainties $\Delta\alpha_{\text{tot}}^c(\omega_L)$ consider the uncertainties $\Delta\alpha_0^c(\omega_L)$ and $\Delta\alpha_2^c(\omega_L)$ and are determined

---

[1] No uncertainties are given for α_c and α_{vc} in Ref. [Saf13].

Table 4.2.: Frequency-dependent polarizabilities. Numerical results for the frequency-dependent valence scalar polarizability $\alpha_0^{\mathrm{c}}(\omega_{\mathrm{L}})$, the frequency-dependent valence tensor polarizability $\alpha_2^{\mathrm{c}}(\omega_{\mathrm{L}})$, the total atomic polarizability $\alpha_{\mathrm{tot}}^{\mathrm{c}}(\omega_{\mathrm{L}})$, and their uncertainties $\Delta\alpha_0^{\mathrm{c}}(\omega_{\mathrm{L}})$, $\Delta\alpha_2^{\mathrm{c}}(\omega_{\mathrm{L}})$, and $\Delta\alpha_{\mathrm{tot}}^{\mathrm{c}}(\omega_{\mathrm{L}})$, respectively, for ^{39}K at $1064\,\mathrm{nm}$. Reference values for $\alpha_{\mathrm{tot}}(\omega_{\mathrm{L}})$ are listed where available and are given for comparison. All values are given in atomic units.

	Present					Present		[Saf15][2]
Level	$\alpha_0^{\mathrm{c}}(\omega_{\mathrm{L}})$	$\Delta\alpha_0^{\mathrm{c}}(\omega_{\mathrm{L}})$	$\alpha_2^{\mathrm{c}}(\omega_{\mathrm{L}})$	$\Delta\alpha_2^{\mathrm{c}}(\omega_{\mathrm{L}})$	$\lvert M_J\rvert$	$\alpha_{\mathrm{tot}}^{\mathrm{c}}(\omega_{\mathrm{L}})$	$\Delta\alpha_{\mathrm{tot}}^{\mathrm{c}}(\omega_{\mathrm{L}})$	$\alpha_{\mathrm{tot}}(\omega_{\mathrm{L}})$
$5P_{3/2}$	-544	27	21	10	3/2	-518	37	-482.605
					1/2	-560	37	-484.155
$5P_{1/2}$	-587	29			1/2	-582	29	-526.372
$3D_{3/2}$	-445	53	-682	22	3/2	-1122	75	
					1/2	242	75	
$3D_{5/2}$	-528	51	-855	29	5/2	-1378	80	
					3/2	-352	57	
					1/2	161	75	
$5S_{1/2}$	94	12			1/2	99	12	
$4P_{3/2}$	-2995	21	796	9	3/2	-2194	30	
					1/2	-3786	30	
$4P_{1/2}$	-3176	22			1/2	-3171	22	
$4S_{1/2}$	598	7			1/2	603	7	603.872

through uncertainty propagation. Reference data for the total polarizability $\alpha_{\mathrm{tot}}(\omega_{\mathrm{L}})$ is given where available.

4.4.3. Discussion

We first discuss the results for the total polarizabilities $\alpha_{\mathrm{tot}}^{\mathrm{c}}(\omega_{\mathrm{L}})$ for which no reference data is available to compare with. According to Table 4.2, the Zeeman states of the $4P_{1/2}$ level have a total polarizability of -3171 a.u. and the Zeeman states of the $4P_{3/2}$ level a total polarizability of -3786 a.u. (for $|M_J| = 1/2$) and -2194 a.u. (for $|M_J| = 3/2$). The negative polarizabilities indicate that an atom in the $4P_{1/2}$ and $4P_{3/2}$ level is attracted towards locations with minimum laser intensity as discussed in Sec. 2.2.1. The $5S_{1/2}$ level with $|M_J| = 1/2$ has a total polarizability of 99 a.u., which is a factor of six smaller than the $4S_{1/2}$ ground state polarizability of 603 a.u. The total polarizabilities of the $3D_{5/2}$ level (161 a.u. for $|M_J| = 1/2$, -352 a.u. for $|M_J| = 3/2$, -1378 a.u. for $|M_J| = 5/2$) and the $3D_{3/2}$ level (242 a.u. for $|M_J| = 1/2$ and -1122 a.u. for $|M_J| = 3/2$) have positive and negative signs.

For the $4S_{1/2}$, $5P_{1/2}$, and $5P_{3/2}$ levels reference data for the total atomic polarizability exists and is presented in Ref. [Saf13]. We obtained the numerical values of the total polarizabilities in Ref. [Saf13] from M. S. Safronova [Saf15]. The calculated value for the $4S_{1/2}$ level (603 a.u.) agrees reasonably well with the reference data [Saf15] in Table 4.2.[2] On the contrary, the numerical results for the $5\mathrm{P}_{1/2}$ (-582 a.u.) and $5\mathrm{P}_{3/2}$ (-560 a.u. for $|M_J| = 1/2$ and -518 a.u. for $|M_J| = 3/2$) levels show a discrepancy with the reference data. In particular, the reference data for the $5\mathrm{P}_{1/2}$ level and the $5\mathrm{P}_{3/2}$ Zeeman states with $|M_J| = 1/2$ lie without the uncertainty boundaries of our results. We attribute this discrepancy to our limited atomic input data.

4.4.4. Upper and Lower Bounds for the Valence Polarizabilities

In order to calculate more precise values for the valence polarizability $\alpha_{\mathrm{v}}(\omega_{\mathrm{L}})$, we need to include more data of atomic transitions to higher lying atomic levels into our program. Such data, however, could not be found in literature despite an extensive research. On the other hand, computing this data on our own through atomic structure calculations is beyond the scope of this Thesis. We therefore analyze to which extent the computed results in Table 4.2 can be seen as reliable. To that end, we aim at calculating the theoretical upper and lower bounds for the valence scalar and tensor polarizability, $\alpha_0(\omega_{\mathrm{L}})$ and $\alpha_2(\omega_{\mathrm{L}})$, for each fine structure level.

Bounds on the Valence Scalar Polarizability

We first deal with the upper and lower bounds for the valence scalar polarizability $\alpha_0(\omega_{\mathrm{L}})$. For this purpose we rewrite Eq. (4.17) in terms of oscillator strengths. The *oscillator strength* f_{ak} of a transition $|\gamma_a J_a\rangle \to |\gamma_k J_k\rangle$ is given through [Sob79]

$$f_{ak} = \frac{2m_{\mathrm{e}}\omega_{ka}}{3\hbar e^2(2J_a+1)}|\langle\gamma_a J_a\|\vec{p}\|\gamma_k J_k\rangle|^2, \tag{4.20}$$

where $\omega_{ka} = (E_k - E_a)/\hbar$. Equation (4.17) then becomes

$$\alpha_0(\omega_{\mathrm{L}}) = \frac{\hbar e^2}{m_{\mathrm{e}}}\sum_{k\neq a}\frac{(E_k - E_a)}{(E_k - E_a)^2 - (\hbar\omega_{\mathrm{L}})^2}\frac{f_{ak}}{\omega_{ka}}. \tag{4.21}$$

We split the sum in Eq. (4.21) into two sums: one sum runs over all transitions to atomic levels $|\gamma_k J_k\rangle$ for which we have the level energies E_k and the associated RMEs. This sum is indicated through the notation $\sum_{k(\text{known})}\dots$. The second sum runs over all transitions to atomic levels $|\gamma_{k'} J_{k'}\rangle$ for which we possess none (or only an incomplete part) of this information. This sum is indicated through the notation $\sum_{k'(\text{unknown})}\dots$. Equation (4.21) can then be written as

$$\begin{aligned}\alpha_0(\omega_{\mathrm{L}}) =& \frac{\hbar e^2}{m_{\mathrm{e}}}\sum_{\substack{k\neq a\\ \text{(known)}}}\frac{(E_k - E_a)}{(E_k - E_a)^2 - (\hbar\omega_{\mathrm{L}})^2}\frac{f_{ak}}{\omega_{ka}} \\ &+ \frac{\hbar e^2}{m_{\mathrm{e}}}\sum_{\substack{k'\neq a\\ \text{(unknown)}}}\frac{(E_{k'} - E_a)}{(E_{k'} - E_a)^2 - (\hbar\omega_{\mathrm{L}})^2}\frac{f_{ak'}}{\omega_{k'a}}.\end{aligned} \tag{4.22}$$

Our atomic data set lacks numerical values for RMEs of transitions only to levels higher than those for which we calculate the polarizabilities ($E_{k'} > E_a$). The oscillator strengths $f_{ak'}$ and

---

[2] Uncertainties for the total atomic polarizabilities $\alpha_{\mathrm{tot}}(\omega_{\mathrm{L}})$ from Ref. [Saf15] are unknown to us. We therefore estimate the uncertainty of these atomic polarizabilities to correspond to the typical uncertainty for $\alpha_{\mathrm{tot}}(\omega_{\mathrm{L}})$ listed in Ref. [Saf13], which is $\Delta\alpha_{\mathrm{tot}}(\omega_{\mathrm{L}}) = \pm 1$.

energy differences $E_{k'} - E_a$ in Eq. (4.22) are therefore all positive, i.e. $f_{ak'} > 0$ and $(E_{k'} - E_a) > 0$. Furthermore, since the energy differences $E_{k'} - E_a$ of the missing transitions are larger than the energy $\hbar\omega_\mathrm{L}$ of a $1064\,\mathrm{nm}$ lattice photon, the denominator of the second sum in Eq. (4.22) is positive as well. Consequently, each term of the second sum in Eq. (4.22) is positive. Thus, the lower bound for the valence scalar polarizability $\alpha_0(\omega_\mathrm{L})$ of a fine structure level, denoted as $\alpha_{0,\mathrm{min}}(\omega_\mathrm{L})$, is given through the first sum in Eq. (4.22):

$$\alpha_{0,\mathrm{min}}(\omega_\mathrm{L}) = \frac{\hbar e^2}{m_\mathrm{e}} \sum_{\substack{k \neq a \\ \text{(known)}}} \frac{(E_k - E_a)}{(E_k - E_a)^2 - (\hbar\omega_\mathrm{L})^2} \frac{f_{ak}}{\omega_{ka}}. \tag{4.23}$$

The lower bound $\alpha_{0,\mathrm{min}}(\omega_\mathrm{L})$ hence just corresponds to the values $\alpha_0^\mathrm{c}(\omega_\mathrm{L})$ in Table 4.2, i.e. $\alpha_{0,\mathrm{min}}(\omega_\mathrm{L}) = \alpha_0^\mathrm{c}(\omega_\mathrm{L})$.

To determine the upper bound $\alpha_{0,\mathrm{max}}(\omega_\mathrm{L})$ for the valence scalar polarizability $\alpha_0(\omega_\mathrm{L})$, we proceed as follows [Bon97]. Strictly speaking, the summations in Eqs. (4.12), (4.13), (4.17), and (4.18) have to be replaced by a summation over all discrete, bound levels and integration over all unbound continuum states with eigenenergies larger than the ionization threshold of the atom. Equation (4.22) then changes to

$$\alpha_0(\omega_\mathrm{L}) = \alpha_{0,\mathrm{min}}(\omega_\mathrm{L}) + \frac{\hbar e^2}{m_\mathrm{e}} \sum\!\!\!\!\!\!\!\!\int_{\substack{k' \neq a \\ \text{(unknown)}}} \frac{(E_{k'} - E_a)}{(E_{k'} - E_a)^2 - (\hbar\omega_\mathrm{L})^2} \frac{f_{ak'}}{\omega_{k'a}}. \tag{4.24}$$

The symbol $\sum\!\!\!\!\!\!\int$ indicates summation over all bound levels and integration over all continuum states for which we do not possess the level energies $E_{k'}$ and RMEs. We approximate the energies $E_{k'}$ with the energy of the energetically lowest atomic state that is not included in the atomic data set, $E^\mathrm{lowest} = \min\{E_{k'}\}$. In our case, this is the $12\mathrm{F}_{1/2}$ fine structure level. This approximation leads to the inequality

$$\alpha_0(\omega_\mathrm{L}) < \alpha_{0,\mathrm{min}}(\omega_\mathrm{L}) + \frac{\hbar^2 e^2}{m_\mathrm{e}} \frac{1}{(E^\mathrm{lowest} - E_a)^2 - (\hbar\omega_\mathrm{L})^2} \sum\!\!\!\!\!\!\!\!\int_{\substack{k' \neq a \\ \text{(unknown)}}} f_{ak'}. \tag{4.25}$$

For an atom with one active electron and within an initial atomic level $|\gamma_a J_a\rangle$ the relation [Her15]

$$\sum\!\!\!\!\!\!\!\!\int_{k} f_{ak} = 1 \tag{4.26}$$

applies. Here, the summation (integration) runs over all discrete, bound levels (continuous, unbound levels) $|\gamma_k J_k\rangle$. Equation (4.26) is known as *Thomas-Reiche-Kuhn sum rule*. We divide the sum in Eq. (4.26) into two terms f_known and f_unknown that contain the known oscillator strengths of our atomic data set and the unknown oscillator strengths, respectively. The two terms f_{known} and f_{unknown} are defined through

$$f_{\text{known}} = \sum_{\substack{k \neq a \\ \text{(known)}}} f_{ak} \qquad \text{and} \qquad f_{\text{unknown}} = \mathop{\sum\!\!\!\!\!\!\!\int}_{\substack{k' \neq a \\ \text{(unknown)}}} f_{ak'} . \tag{4.27}$$

We write Eq. (4.26) in the form

$$\mathop{\sum\!\!\!\!\!\!\!\int}_{k} f_{ak} = f_{\text{known}} + f_{\text{unknown}} = 1. \tag{4.28}$$

With Eqs. (4.28) and (4.25) the upper bound $\alpha_{0,\text{max}}(\omega_{\text{L}})$ can then be calculated through

$$\alpha_{0,\text{max}}(\omega_{\text{L}}) = \alpha_{0,\text{min}}(\omega_{\text{L}}) + \frac{\hbar^2 e^2}{m_{\text{e}}} \cdot \frac{1 - f_{\text{known}}}{(E^{\text{lowest}} - E_a)^2 - (\hbar\omega_{\text{L}})^2} . \tag{4.29}$$

We obtain as upper bounds for the valence scalar polarizability 598 a.u. (for the 4S$_{1/2}$ level), -3136 a.u. (for the 4P$_{1/2}$ level), -2955 a.u. (for the 4P$_{3/2}$ level), 100 a.u. (for the 5S$_{1/2}$ level), -218 a.u. (for the 3D$_{5/2}$ level), -144 a.u. (for the 3D$_{3/2}$ level), 1408 a.u. (for the 5P$_{1/2}$ level), and 1640 a.u. (for the 5P$_{3/2}$ level). These values do not incorporate the uncertainties $\Delta\alpha_0^{\text{c}}(\omega_{\text{L}})$ from Table 4.2, which simply add up. The upper bounds for the valence scalar polarizability of the higher atomic states deviate significantly from the calculated polarizabilities $\alpha_0^{\text{c}}(\omega_{\text{L}})$. This deviation indicates that further atomic input data is needed to refine the calculated values $\alpha_0^{\text{c}}(\omega_{\text{L}})$.

Bounds on the Valence Tensor Polarizability

The factor $(-1)^{J_a+J_k+1}$ and the Wigner 6J-symbol in Eq. (4.18) lead to an alternating sign of the terms within the sum. The determination of an upper and lower bound for the valence tensor polarizability $\alpha_2(\omega_{\text{L}})$ hence requires additional approximations than those for the bounds of the valence scalar polarizability. We therefore first rewrite Eq. (4.18) as

$$\begin{aligned}\alpha_2(\omega_{\text{L}}) = \alpha_2^{\text{c}}(\omega_{\text{L}}) - 4\mathcal{C} \mathop{\sum\!\!\!\!\!\!\!\int}_{\substack{k' \neq a \\ \text{(unknown)}}} (-1)^{J_a+J_{k'}+1} \begin{Bmatrix} J_a & 1 & J_{k'} \\ 1 & J_a & 2 \end{Bmatrix} \frac{(E_{k'} - E_a)}{(E_{k'} - E_a)^2 - (\hbar\omega_{\text{L}})^2} \\ \times \left| \langle \gamma_a J_a || \vec{p} || \gamma_{k'} J_{k'} \rangle \right|^2 .\end{aligned} \tag{4.30}$$

We replace the Wigner-6J symbol by the maximum absolute value it takes for transitions between states with $J_a \in \{1/2, 3/2, 5/2\}$ and $J_{k'} \in \{1/2, 3/2, 5/2, 7/2\}$. Additionally, we substitute the factor $(-1)^{J_a+J_{k'}+1}$ with its absolute value. Through these simplifications the terms within the sum (integral) in Eq. (4.30) are all positive and thus add up. We then obtain a lower bound ($\alpha_{2,\text{min}}(\omega_{\text{L}})$) and an upper bound ($\alpha_{2,\text{max}}(\omega_{\text{L}})$) for the frequency-dependent valence tensor polarizability through

$$\alpha_{2,\text{min}}(\omega_{\text{L}}) = \alpha_2^{\text{c}}(\omega_{\text{L}}) - \mathcal{G}, \tag{4.31}$$

$$\alpha_{2,\text{max}}(\omega_{\text{L}}) = \alpha_2^{\text{c}}(\omega_{\text{L}}) + \mathcal{G} \tag{4.32}$$

with

$$\mathcal{G} = 4\mathcal{C} \cdot \left| \max \left[\begin{Bmatrix} J_a & 1 & J_{k'} \\ 1 & J_a & 2 \end{Bmatrix} \right] \right| \cdot \frac{1 - f_{\text{known}}}{\left(E^{\text{lowest}} - E_a\right)^2 - (\hbar\omega_{\text{L}})^2} \cdot \frac{3\hbar^2 e^2 (2J_a + 1)}{2m_{\text{e}}}. \tag{4.33}$$

The previous simplifications lead to the following values for $\mathcal{G}$: 40 a.u. (for the $4\text{P}_{3/2}$ level), 354 a.u. (for the $3\text{D}_{5/2}$ level), 301 a.u. (for the $3\text{D}_{3/2}$ level), and 2183 a.u. (for the $5\text{P}_{3/2}$ level). The given values for $\mathcal{G}$ do not incorporate the uncertainties $\Delta\alpha_2^{\text{c}}(\omega_{\text{L}})$ from Table 4.2, which simply add up. To obtain narrower bounds on $\alpha_2(\omega_{\text{L}})$, it might be helpful to estimate the contributions of individual atomic transitions for which we do not possess the RMEs in Eq. (4.30) to the valence tensor polarizability. Such estimations could be obtained by extrapolating values for missing RMEs from fits of analytical functions to plots that show available RMEs as a function of the associated transition frequency ω_{ka}.

5. Simulation of Violet Fluorescence Imaging and Laser Cooling of Trapped ^{39}K Atoms

Violet fluorescence quantum gas microscopy of ^{39}K atoms will allow for fluorescence images with enhanced spatial resolution in future experiments of the K−Cs apparatus. As the ^{39}K atoms are trapped within potential wells of an optical lattice during fluorescence imaging, their motional states are quantized. We intend to take advantage of the quantized motional states by cooling the atoms during imaging via EIT cooling [Mor00, Mor03]. Electromagnetically-induced transparency cooling has been first demonstrated for trapped ions [Roo00] and recently for ^{40}K atoms during fluorescence quantum gas microscopy [Hal15, Edg15]. In this Chapter, we simulate violet fluorescence imaging of trapped ^{39}K atoms within a $1064\,\mathrm{nm}$-light optical lattice on the $4\mathrm{S}_{1/2} \rightarrow 5\mathrm{P}_{3/2}$ transition and simultaneous EIT cooling on the $4\mathrm{S}_{1/2} \rightarrow 4\mathrm{P}_{3/2}$ transition. The simulation allows us to estimate the increase in energy of the trapped ^{39}K atoms during imaging. Furthermore, the expected number of scattered violet fluorescence photons can be calculated from the simulation. For the sake of simplicity, we consider only the fine structure of ^{39}K within this Chapter.

5.1. Level Scheme of ^{39}K

A ^{39}K atom that is excited into the $5\mathrm{P}_{3/2}$ level with a laser that is resonant with the $4\mathrm{S}_{1/2} \rightarrow 5\mathrm{P}_{3/2}$ transition can decay back into the $4\mathrm{S}_{1/2}$ ground state through six different decay channels. Figure 5.1 shows a reduced level scheme of ^{39}K and depicts the fine structure together with the possible decay channels from the $5\mathrm{P}_{3/2}$ level. The level scheme indicates that in five out of the six decay channels (i.e. in about $84\,\%$ of all decay events), the atom decays cascade-like from the $5\mathrm{P}_{3/2}$ level into the $4\mathrm{S}_{1/2}$ ground state via two intermediate levels. In these cases, the atom emits three photons in the red and infrared spectral range. In only one decay channel (i.e. in about $16\,\%$ of all decay events) the excited atom decays via the direct $5\mathrm{P}_{3/2} \rightarrow 4\mathrm{S}_{1/2}$ transition, which generates a single violet fluorescence photon. The $4\mathrm{S}_{1/2} \rightarrow 5\mathrm{P}_{3/2}$ transition has a line width $\Gamma_{4\mathrm{S}_{1/2}\rightarrow 5\mathrm{P}_{3/2}}/2\pi = 184.6\,\mathrm{kHz}$ and a saturation intensity $I_{\mathrm{sat}}^{4\mathrm{S}_{1/2}\rightarrow 5\mathrm{P}_{3/2}} = 57.6\,\mathrm{mW/cm^2}$ [Han15]. The maximum rate at which violet fluorescence photons can be scattered during imaging is $\Gamma_{4\mathrm{S}_{1/2}\rightarrow 5\mathrm{P}_{3/2}}/2 \approx 5.8 \times 10^5\,\mathrm{s}^{-1}$. This rate is more than thirty times smaller than the maximum fluorescence rate of the $4\mathrm{S}_{1/2} \rightarrow 4\mathrm{P}_{1/2}$ and $4\mathrm{S}_{1/2} \rightarrow 4\mathrm{P}_{3/2}$ transitions.

During the decay processes from the $5\mathrm{P}_{3/2}$ level a ^{39}K atom temporarily occupies different atomic states. Since the atom experiences different optical lattice potentials in each of these atomic states (see discussion in Ch. 4), the potential well experienced by the atom in its ground state can be more strongly or weakly confining or even inverted in excited atomic states. The state-dependent, and for the atoms thus time-dependent, optical lattice potential

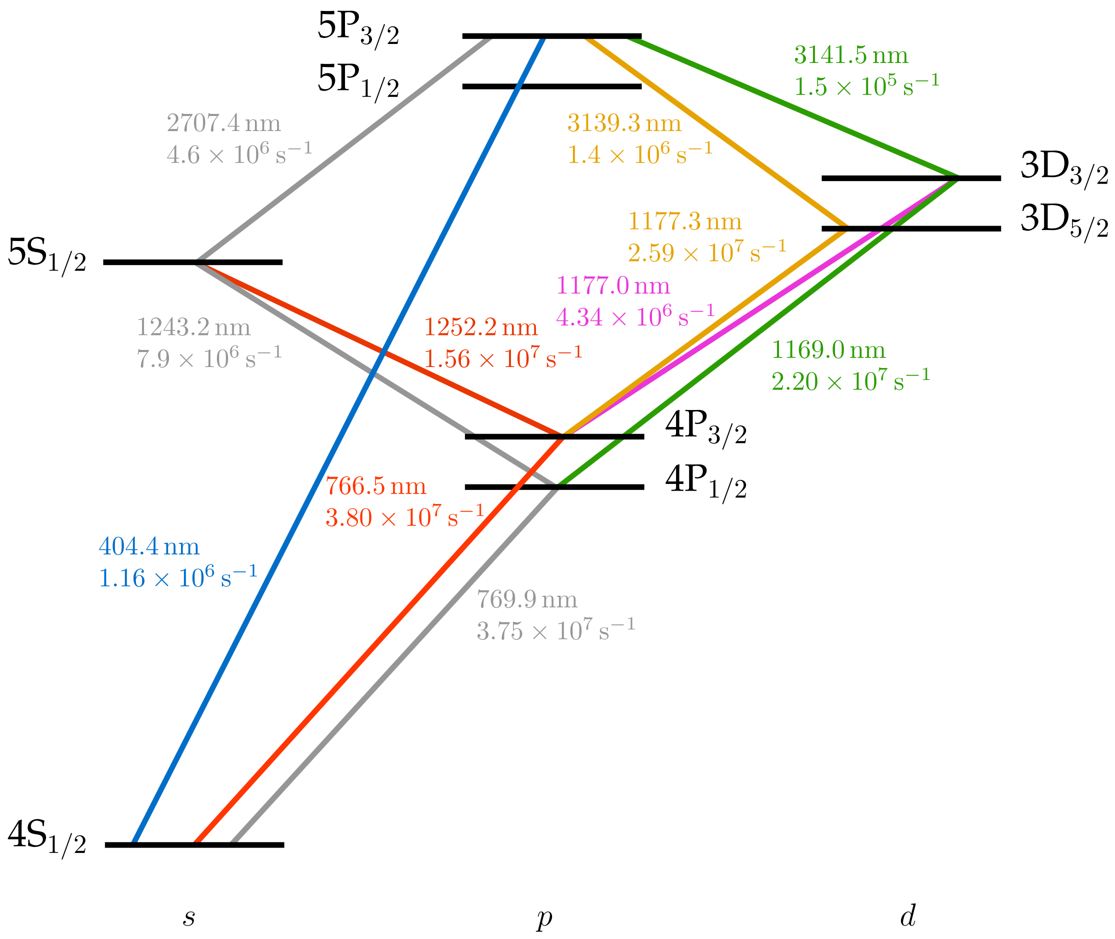

Figure 5.1.: Fine structure of ^{39}K. Shown are the fine structure levels between the $4S_{1/2}$ ground state and the $5P_{3/2}$ level. The colored lines indicate dipole-allowed transitions. Quoted values correspond to transition wavelengths and transition rates [Kraa]. Level spacings are not to scale.

possibly heats the trapped ^{39}K atoms. To mitigate heating, we plan to perform EIT cooling on the $4S_{1/2} \rightarrow 4P_{1/2}$ transition while imaging.

The nuclear spin $\vec{I}$ of ^{39}K gives rise to a hyperfine structure in the level scheme. Figure 5.2 shows the hyperfine levels of ^{39}K, which are specified through the *total angular momentum quantum number* F. The splitting of hyperfine levels becomes increasingly narrow for higher-lying fine structure levels. The splitting of the $5P_{3/2}$ hyperfine levels is between 1 and 7 MHz and thus comparable to the decay rate $\Gamma_{5P_{3/2}}$ of the $5P_{3/2}$ level, which is $\Gamma_{5P_{3/2}}/2\pi = 1.16\,\text{MHz}$ [Kraa]. Since therefore not all $5P_{3/2}$ hyperfine levels can be resolved, we neglect the hyperfine structure of ^{39}K in a first order approximation within this Chapter.

5.2. General Considerations

Prior to violet fluorescence imaging each ^{39}K atom will reside in its internal ground state and will be deeply confined to a single site of an optical lattice potential. At this stage, each atom

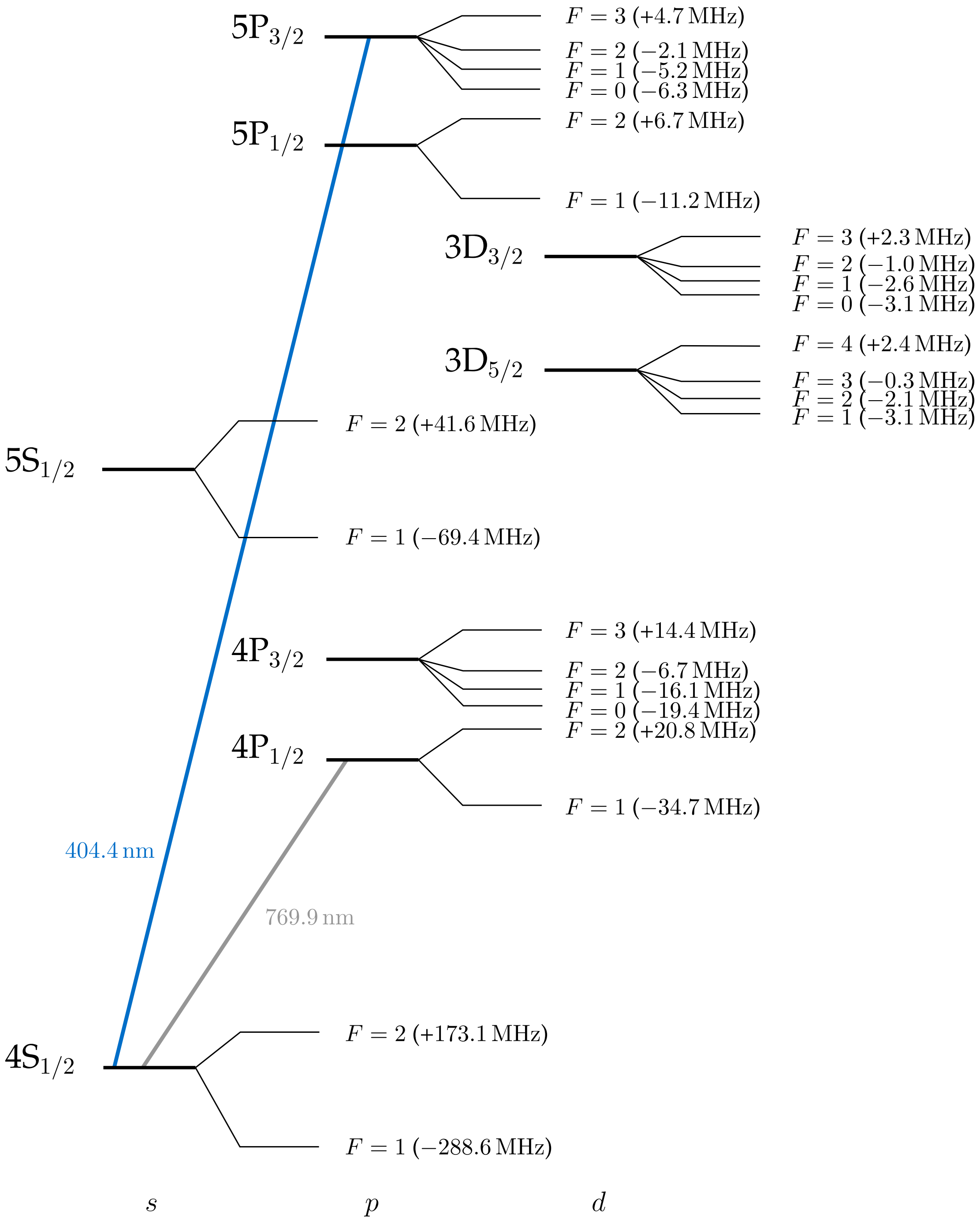

Figure 5.2.: Hyperfine structure of ^{39}K. Numbers in brackets give the frequency shift of hyperfine structure levels relative to the associated fine structure levels. Frequency shifts were calculated with data from Ref. [San08]. Level spacings are not to scale.

occupies the vibrational ground state of its harmonic on-site potential. In the course of fluorescence imaging, each time a ^{39}K atom transitions into an other internal state the atomic wavefunction is projected onto the eigenfunctions of the new lattice potential experienced by the atom. After one absorption-emission cycle the ^{39}K atom is again in its internal ground state, however, does not necessarily occupy the vibrational ground state of the on-site potential anymore. Instead, the atom might end up in a vibrational state with higher energy. We consider this transfer into higher vibrational states as heating of the atom. In this Section, we outline the model that we use to describe the dynamics of a trapped ^{39}K atom during fluorescence imaging.

5.2.1. Model for the Simulation

We consider a single ^{39}K atom that is confined to a lattice site of a 1D optical lattice potential. We restrict the discussion to one spatial dimension, namely the lattice axis along the $x-$direction. We assume that the optical lattice is generated by laser light of frequency ω_{L} and that it has a lattice depth $V_{0,\mathrm{1D}}$ for the atom in its internal ground state that is large enough to approximate the on-site lattice potential with a harmonic potential. The atom is then described by the Hamiltonian

$$\hat{H}_{\mathrm{tot}} = \hat{H}_{\mathrm{atom}} + \hat{H}_{\mathrm{motion}}, \tag{5.1}$$

where $\hat{H}_{\mathrm{atom}}$ is the Hamiltonian of the unperturbed atom and $\hat{H}_{\mathrm{motion}}$ describes the center-of-mass motion of the atom within the harmonic on-site potential. If the atomic fine structure states $|\varphi_k\rangle = |\gamma_k J_k M_{J,k}\rangle$ have eigenenergies E_k, the Hamiltonian $\hat{H}_{\mathrm{atom}}$ can be expressed as

$$\hat{H}_{\mathrm{atom}} = \sum_k E_k |\varphi_k\rangle\langle\varphi_k|. \tag{5.2}$$

The second term in Eq. (5.1), $\hat{H}_{\mathrm{motion}}$, is given by [Mes65b]

$$\hat{H}_{\mathrm{motion}} = \frac{\hat{p}_x^2}{2m} + \frac{1}{2}m\omega_{x,k}^2\hat{x}^2 - V_{0,\mathrm{1D}}^k\mathbb{1}, \tag{5.3}$$

where $\hat{p}_x$ is the *momentum operator*[1], $\hat{x}$ is the Cartesian $x-$component of the position vector operator $\hat{r}$, $\mathbb{1}$ is the *identity operator*, and $V_{0,\mathrm{1D}}^k$ is the state-dependent lattice depth. The on-site trapping frequency $\omega_{x,k}$ depends on the atomic polarizability $\alpha_{\mathrm{tot},k}(\omega_{\mathrm{L}})$ and thus on the atomic state $|\varphi_k\rangle$. It is given through

$$\omega_{x,k} = \frac{E_{\mathrm{rec}}}{\hbar}\sqrt{\frac{8\alpha_{\mathrm{tot},k}(\omega_{\mathrm{L}})P}{c\epsilon_0\pi w_0^2 E_{\mathrm{rec}}}}. \tag{5.4}$$

If the atomic polarizability $\alpha_{\mathrm{tot},k}(\omega_{\mathrm{L}})$ of the atom in state $|\varphi_k\rangle$ is positive ($\alpha_{\mathrm{tot},k}(\omega_{\mathrm{L}}) > 0$), $\omega_{x,k}$ is positive as well and the on-site lattice potential corresponds to that of a harmonic oscillator. If the polarizability $\alpha_{\mathrm{tot},k}(\omega_{\mathrm{L}})$ is negative ($\alpha_{\mathrm{tot},k}(\omega_{\mathrm{L}}) < 0$), $\omega_{x,k}$ becomes imaginary ($\omega_{x,k} \to i\omega_{x,k}$)

---

[1] Here, $\hat{p}_x$ is the momentum operator and should not be confused with the electric-dipole moment operator in Chapter 4.

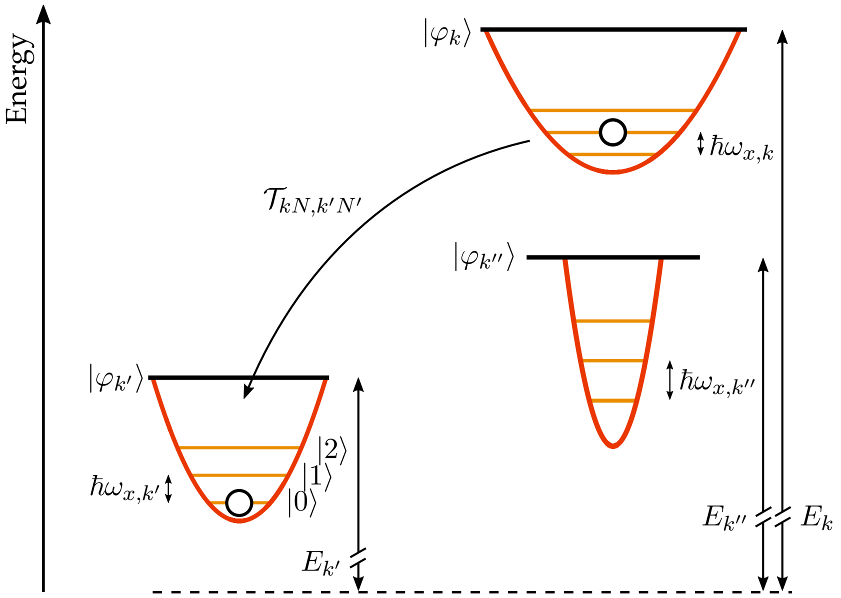

Figure 5.3.: Energy spectrum of a harmonically trapped atom with only positive atomic polarizabilities. An atom in state $|\varphi_k\rangle$ with eigenenergy E_k and positive atomic polarizability $\alpha_{\text{tot},k}(\omega_{\text{L}})$, trapped at a lattice site of an optical lattice, experiences a harmonic on-site potential with trapping frequency $\omega_{x,k}$. Transitions from a state $|\varphi_k, N\rangle$ into a state $|\varphi_{k'}, N'\rangle$ ($\alpha_{\text{tot},k'}(\omega_{\text{L}}) > 0$) take place at a rate $\mathcal{T}_{kN,k'N'}$.

and the harmonic potential is inverted. As the fine structure Zeeman states of ^{39}K have positive as well as negative atomic polarizabilities (see Table 4.2), we next discuss how we describe the dynamics of the trapped atom in these two cases.

5.2.2. Positive Atomic Polarizability (Harmonic Oscillator On-Site Potential)

If the atom is in a state $|\varphi_k\rangle$ with positive atomic polarizability $\alpha_{\text{tot},k}(\omega_{\text{L}})$, the Hamiltonian $\hat{H}_{\text{motion}}$ in Eq. (5.3) can be written as [Mes65b]

$$\hat{H}_{\text{motion}} = \hbar\omega_{x,k}\left(\hat{N} + \frac{1}{2}\right) - V_{0,\text{1D}}^{k}\mathbb{1} \tag{5.5}$$

with $\hat{N}$ being the number operator. The eigenstates of $\hat{H}_{\text{motion}}$ are Fock states $|N\rangle$ with eigenenergies [Mes65b]

$$E_{k,N} = \hbar\omega_{x,k}(N + 1/2) - V_{0,\text{1D}}^{k} \tag{5.6}$$

and N being the integer (non-negative) vibrational quantum number. With this, the eigenstates of $\hat{H}_{\text{tot}}$ in Eq. (5.1) are product states $|\varphi_k, N\rangle = |\varphi_k\rangle|N\rangle$. If we restrict ourselves to atomic states $|\varphi_k\rangle$ with positive atomic polarizabilities, the energy spectrum of that subspace corresponds to that of harmonic oscillators with trapping frequencies $\omega_{x,k}$, which are shifted in energy by $E_k - V_{0,\text{1D}}^{k}$. Figure 5.3 illustrates the resulting energy spectrum.

Transitions from an initial state $|\varphi_k, N\rangle$ to another state $|\varphi_{k'}, N'\rangle$ can take place via optical dipole transitions. The rate at which such transitions occur, $\mathcal{T}_{kN,k'N'}$, can be written as a

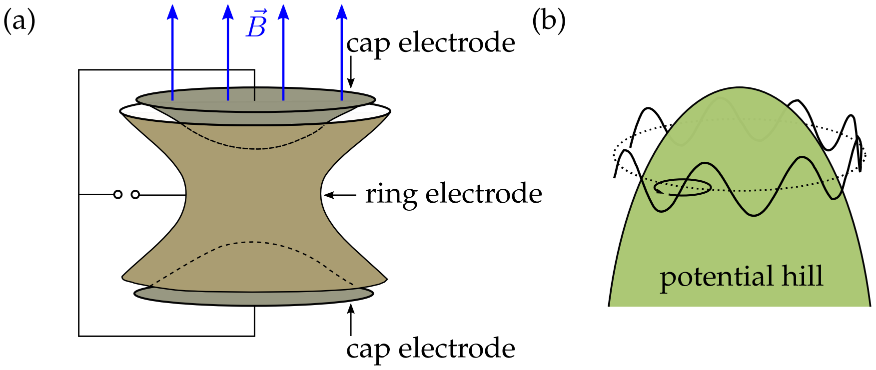

Figure 5.4.: Penning trap. (a) Schematic drawing of a Penning trap with magnetic field $\vec{B}$. (b) The motion of a charged particle within a Penning trap consists of a harmonic oscillation in axial direction (up and down), a magnetron motion (dotted line), and a cyclotron motion (circular arrow).

product of the transition rate $\mathcal{A}_{kk'}$ for the atomic transition $|\varphi_k\rangle \rightarrow |\varphi_{k'}\rangle$ and the probability $|\mathcal{F}_{N\rightarrow N'}|^2$ for the vibrational transition $|N\rangle \rightarrow |N'\rangle$ [Esc03, Lei03]:

$$\mathcal{T}_{kN,k'N'} = \mathcal{A}_{kk'} \cdot |\mathcal{F}_{N\rightarrow N'}|^2. \tag{5.7}$$

The mathematical expressions for the factors $\mathcal{A}_{kk'}$ and $\mathcal{F}_{N\rightarrow N'}$ are discussed in Sec. 5.3.

5.2.3. Negative Atomic Polarizability (Inverted Harmonic Oscillator On-Site Potential)

If the atom in state $|\varphi_k\rangle$ has a negative atomic polarizability ($\alpha_{\mathrm{tot},k}(\omega_{\mathrm{L}}) < 0$), the on-site trapping frequency $\omega_{x,k}$ in Eq. (5.3) has to be replaced according to $\omega_{x,k} \rightarrow i\omega_{x,k}$. This substitution turns the harmonic on-site potential into an inverted harmonic on-site potential. To describe the motion of the atom within an inverted harmonic oscillator potential, one has to find the associated eigenfunctions. The Schrödinger equation of the inverted oscillator is exactly solvable and has two solutions [Yuc06]. One solution is a plane wave solution whereas the second solution corresponds to a particle confined into an expanding box. The substitution $\omega_{x,k} \rightarrow i\omega_{x,k}$, however, cannot be used to find the eigenenergies of the inverted oscillator with Eq. (5.6) [Yuc06] as the Hamiltonian $\hat{H}_{\mathrm{motion}}$ in Eq. (5.3) would have imaginary eigenenergies otherwise.

An atom within an inverted harmonic oscillator potential has similarities with a charged particle within a Penning trap. Figure 5.4(a) depicts the schematic setup of a Penning trap. The motion of a charged particle within a Penning trap can be divided into a harmonic oscillation in axial direction and a combined cyclotron and magnetron motion in radial direction. The magnetron motion of the particle describes a circular orbit about an effective, radial potential hill [Bro86]. Figure 5.4(b) illustrates the horizontal motion of a charged particle within a Penning trap. Excitation of the magnetron motion increases the radius of the magnetron orbit and causes the particle to move down the potential hill. The eigenstates of the magnetron motion

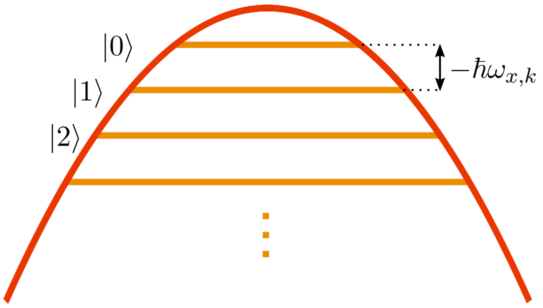

Figure 5.5.: Inverted harmonic oscillator potential. Within our approximation, the eigenstates of the 1D inverted harmonic oscillator are harmonic oscillator states $|N\rangle$. For increasing vibrational quantum number N, the energy of the oscillator states $|N\rangle$ decreases in this case.

are harmonic oscillator states with eigenenergies given by [Bro86]

$$E_{\text{magnetron}} = -\hbar\omega_{\text{magnetron}}\left(l + \frac{1}{2}\right), \tag{5.8}$$

where the quantum number l is a positive integer.

To describe the motion of a ^{39}K atom within an inverted harmonic on-site potential, we use the picture of the magnetron motion. We assume that the eigenstates of the ^{39}K atom in the 1D inverted harmonic potential are harmonic oscillator states $|N\rangle$, whose eigenenergies are obtained by replacing $\omega_{x,k}$ in Eq. (5.6) by $-\omega_{x,k}$. Figure 5.5 illustrates that within our inverted oscillator approximation the energy of the harmonic oscillator states decreases with increasing quantum number N.

We calculate the rates $\mathcal{T}_{kN,k'N'}$ for transitions between two states $|\varphi_k, N\rangle$ and $|\varphi_{k'}, N'\rangle$ of which at least one state has a negative atomic polarizability analogously to those rates in Eq. (5.7) for atomic states with positive atomic polarizability.

5.3. Transition Rates of a Trapped Atom

During violet fluorescence imaging the trapped ^{39}K atom is continuously transfered between different atomic states $|\varphi_k\rangle$ through absorption, stimulated emission, and spontaneous emission. For each transition type, the $\mathcal{A}_{kk'}$ factor in Eq. (5.7) is different. We give mathematical expressions for the $\mathcal{A}_{kk'}$ factor for all three types of dipole transitions. Furthermore, we give mathematical expressions for the $\mathcal{F}_{N\to N'}$ factor for vibrational transitions. We use the obtained expressions thereafter to set up rate equations in Sec. 5.5.

5.3.1. Absorption

In our simulation, the imaging laser leads to absorption on the $4S_{1/2} \to 5P_{3/2}$ transition. We assume that the imaging laser has a *center frequency* ω_c, an area-normalized *line shape function* $\mathcal{L}(\omega_c - \omega)$, and a *frequency-integrated intensity* I_{tot}. The factor $\mathcal{A}_{kk'}$ for absorption is then given by [Hil82]

$$\mathcal{A}_{\text{abs}} = B^{\omega}_{\text{abs}} \int_0^{+\infty} g(\omega_{kk'} - \omega)\rho(\omega_c - \omega)\mathrm{d}\omega, \tag{5.9}$$

where the factor B^{ω}_{abs} is the *Einstein B coefficient for absorption.*[2] The function $\rho(\omega_{\text{c}} - \omega)$ in Eq. (5.9) is the *energy density per unit angular frequency* given by [Hil82]

$$\rho(\omega_{\text{c}} - \omega) = \frac{I_{\text{tot}}}{c} \mathcal{L}(\omega_{\text{c}} - \omega). \tag{5.10}$$

The function $g(\omega_{kk'} - \omega)$ in Eq. (5.9) is the area-normalized *line shape function* of the atomic transition $|\varphi_k\rangle \to |\varphi_{k'}\rangle$ with transition frequency $\omega_{kk'} = (E_{k'} - E_k)/\hbar$. It is given by [Dem08]

$$g(\omega_{kk'} - \omega) = \frac{1}{\pi} \cdot \frac{\Gamma_{k'}/2}{(\omega_{kk'} - \omega)^2 + (\Gamma_{k'}/2)^2}, \tag{5.11}$$

where $\Gamma_{k'}$ is the decay rate of the excited state $|\varphi_{k'}\rangle$. If the laser line width is much smaller than the line width of the atomic transition, Eq. (5.9) can be approximately written as

$$\mathcal{A}_{\text{abs}} \approx \frac{B^{\omega}_{\text{abs}} I_{\text{tot}}}{c} \cdot \frac{1}{\pi} \cdot \frac{\Gamma_{k'}/2}{(\omega_{kk'} - \omega_{\text{c}})^2 + (\Gamma_{k'}/2)^2}. \tag{5.12}$$

The factor $\mathcal{A}_{\text{abs}}$ corresponds to the photon absorption rate.

5.3.2. Stimulated Emission

The imaging laser causes also stimulated emission on the $5\text{P}_{3/2} \to 4\text{S}_{1/2}$ transition, for which the factor $\mathcal{A}_{kk'}$ is given by [Hil82]

$$\mathcal{A}^{\text{stim}}_{\text{emi}} = B^{\omega}_{\text{emi}} \int_0^{+\infty} g(\omega_{kk'} - \omega)\rho(\omega_c - \omega)\mathrm{d}\omega, \tag{5.13}$$

where the factor B^{ω}_{emi} is the *Einstein B coefficient for stimulated emission.* Analogously to Eq. (5.12), Eq. (5.13) can be approximated by

$$\mathcal{A}^{\text{stim}}_{\text{emi}} \approx \frac{B^{\omega}_{\text{emi}} I_{\text{tot}}}{c} \cdot \frac{1}{\pi} \cdot \frac{\Gamma_{k'}/2}{(\omega_{kk'} - \omega_c)^2 + (\Gamma_{k'}/2)^2}. \tag{5.14}$$

If $|\varphi_k\rangle$ and $|\varphi_{k'}\rangle$ are not degenerate, the Einstein B coefficients for stimulated absorption and stimulated emission are identical ($B^{\omega}_{\text{abs}} = B^{\omega}_{\text{emi}}$) [Dem08] and therefore $\mathcal{A}_{\text{abs}} = \mathcal{A}^{\text{stim}}_{\text{emi}}$. The factor $\mathcal{A}^{\text{stim}}_{\text{emi}}$ corresponds to the stimulated photon emission rate.

5.3.3. Spontaneous Emission

Spontaneous emission occurs in our simulation from every excited atomic state. The factor $\mathcal{A}_{kk'}$ for spontaneous emission is given by [Axn04]

$$\mathcal{A}^{\text{sp}}_{\text{emi}} = \frac{|\omega_{kk'}|^3}{3\pi\epsilon_0\hbar c^3} \left|\langle\varphi_k|\vec{u}_\xi \cdot \vec{p}|\varphi_{k'}\rangle\right|^2, \tag{5.15}$$

---

[2] The superscript ω in the notation of the Einstein B coefficient indicates that its definition through Eq. (5.9) requires $\rho(\omega)$ to be given in units of energy density per unit angular frequency.

where $\langle\varphi_k|\vec{u}_\xi\cdot\vec{p}|\varphi_{k'}\rangle$ is the *dipole transition matrix element* and $\vec{u}_\xi$ is the *spherical polarization vector* of the emitted photon. The subscript ξ indicates the polarization of the photon. It is zero for linear polarization, $\xi = 0$, and for circular polarization $\xi = \pm 1$. The spherical vectors $\vec{u}_\xi$ are given by [Met99]

$$\vec{u}_{-1} = \frac{(\vec{e}_x - i\vec{e}_y)}{\sqrt{2}}, \tag{5.16}$$

$$\vec{u}_0 = \vec{e}_z, \tag{5.17}$$

$$\vec{u}_{+1} = -\frac{(\vec{e}_x + i\vec{e}_y)}{\sqrt{2}}. \tag{5.18}$$

Equation (5.15) corresponds to Fermi's Golden rule and $\mathcal{A}^{\mathrm{sp}}_{\mathrm{emi}}$ is the *Einstein A coefficient*. The Wigner-Eckart theorem allows us to evaluate the matrix element $\langle\gamma_k J_k M_{J,k}|\vec{u}_\xi\cdot\vec{p}|\gamma_{k'} J_{k'} M_{J,k'}\rangle$ in Eq. (5.15) according to [Jud77]

$$\langle\gamma_k J_k M_{J,k}|\vec{u}_\xi\cdot\vec{p}|\gamma_{k'} J_{k'} M_{J,k'}\rangle = (-1)^{J_k - M_{J,k}} \begin{pmatrix} J_k & 1 & J_{k'} \\ -M_{J,k} & \xi & M_{J,k'} \end{pmatrix} \langle\gamma_k J_k||\vec{p}||\gamma_{k'} J_{k'}\rangle. \tag{5.19}$$

The first two factors in Eq. (5.19) depend on $M_{J,k}$ and $M_{J,k'}$ and thus constitute the angular part of the transition dipole matrix element. The factor enclosed in round brackets (: : :) is a *Wigner 3J-symbol*. Three-J symbols are used in quantum mechanics to express Clebsch-Gordon coefficients in angular momentum coupling of two separate systems. Three-J symbols can be computed with the Racah formula [Mes65b]. The reduced matrix element $\langle\cdot||\vec{p}||\cdot\rangle$ depends neither on $M_{J,k}$, $M_{J,k'}$, and ξ and is thus identical for all dipole transitions between two fine structure levels. It represents the radial part of the transition dipole matrix element. The Einstein coefficient $\mathcal{A}^{\mathrm{sp}}_{\mathrm{emi}}$ relates to the Einstein coefficient $B^{\omega}_{\mathrm{emi}}$ through [Dem08]

$$B^{\omega}_{\mathrm{emi}} = \frac{\pi^2 c^3}{\hbar\omega^3_{kk'}}\mathcal{A}^{\mathrm{sp}}_{\mathrm{emi}}. \tag{5.20}$$

5.3.4. Vibrational Transition Probabilities

To find mathematical expressions for the factor $\mathcal{F}_{N\to N'}$ in Eq. (5.7), we define the parameter [Ste86]

$$\eta = \frac{2\pi}{\lambda_{kN,k'N'}}\sqrt{\frac{\hbar}{2m\omega_{x,k}}}, \tag{5.21}$$

where $\lambda_{kN,k'N'}$ is the transition wavelength of the transition $|\varphi_k, N\rangle \to |\varphi_{k'}, N'\rangle$. The parameter η is denoted as *Lamb-Dicke parameter*. With Eq. (5.21) the factor $\mathcal{F}_{N\to N'}$ is given by [Win79, Cah69]

$$\mathcal{F}_{N\to N'} = \exp\left[-\frac{\eta^2}{2}\right](i\eta)^{|\Delta N|} L^{|\Delta N|}_{N_<}\left(\eta^2\right)\sqrt{\frac{N_<!}{(N_< + |\Delta N|)!}}, \tag{5.22}$$

where $N_< = \min\{N, N'\}$, $\Delta N = N' - N$, and $L_{N_<}^{|\Delta N|}(\eta^2)$ denotes the associated Laguerre polynomials [Lei03, Win79]

$$L_{N_<}^{|\Delta N|}(\eta^2) = \sum_{l=0}^{N_<} (-1)^l \binom{N_< + |\Delta N|}{N_< - l} \frac{\eta^{2l}}{l!}. \tag{5.23}$$

For vibrational transitions $|N\rangle \to |N'\rangle$ with $\Delta N \in \{0, \pm 1, \pm 2\}$, Eq. (5.22) approximated to second order in η yields:

$$\mathcal{F}_{N\to N+2} \approx -\frac{1}{2}\eta^2\sqrt{(N+2)(N+1)}, \tag{5.24}$$

$$\mathcal{F}_{N\to N+1} \approx i\eta\sqrt{N+1}, \tag{5.25}$$

$$\mathcal{F}_{N\to N} \approx 1 - \eta^2\left(N + \frac{1}{2}\right), \tag{5.26}$$

$$\mathcal{F}_{N\to N-1} \approx i\eta\sqrt{N}, \tag{5.27}$$

$$\mathcal{F}_{N\to N-2} \approx -\frac{1}{2}\eta^2\sqrt{N(N-1)}. \tag{5.28}$$

5.3.5. Calculation of Transition Rates

We calculate the transition rate $\mathcal{T}_{kN,k'N'}$ for every possible transition $|\varphi_k, N\rangle \to |\varphi_{k'}, N'\rangle$ within our simulation. To that end, we determine the corresponding factors $\mathcal{A}_{kk'}$ and $\mathcal{F}_{N\to N'}$ for each transition and multiply them according to Eq. (5.7). Since the imaging laser only acts on the $4S_{1/2} \to 5P_{3/2}$ transition, absorption and stimulated emission processes have to be taken into account only for these two levels. We use the obtained transition rates $\mathcal{T}_{kN,k'N'}$ to set up rate equations for the population probabilities of the individual states $|\varphi_k, N\rangle$ in Sec. 5.5.

5.4. Electromagnetically-Induced Transparency Cooling

In this Section, we summarize EIT and how it can be used to cool trapped atoms. Furthermore, we give rate equations for the temporal evolution of the population probabilities of vibrational states during EIT cooling. Reviews on EIT and EIT cooling can be found in Ref. [Fle05, Mor00, Mor03].

5.4.1. Electromagnetically-Induced Transparency

We consider a free atom with two internal ground or meta stable states, labeled $|g_1\rangle$ and $|g_2\rangle$, and one excited state $|e\rangle$ with decay rate Γ_e. Two laser beams couple the states $|g_1\rangle$ and $|g_2\rangle$ to the excited state $|e\rangle$ leading to a Λ-scheme. Figure 5.6 shows the involved atomic levels and lasers. One intense laser, denoted as *coupling laser*, is blue detuned from the $|g_2\rangle \to |e\rangle$ transition (Rabi frequency Ω_couple, wave vector $\vec{k}_\text{couple}$, detuning $\Delta_\text{couple} > 0$). A second laser, denoted as *probe laser*, has a variable detuning Δ_probe from the $|g_1\rangle \to |e\rangle$ transition and probes the absorption of the atom (Rabi frequency Ω_probe, wave vector $\vec{k}_\text{probe}$). Dipole transitions between $|g_1\rangle$ and $|g_2\rangle$ are forbidden for parity reasons. The coupling laser induces level mixing of the bare atomic states. The new eigenstates are the dressed states $|+\rangle, |-\rangle$, and $|g\rangle$. The

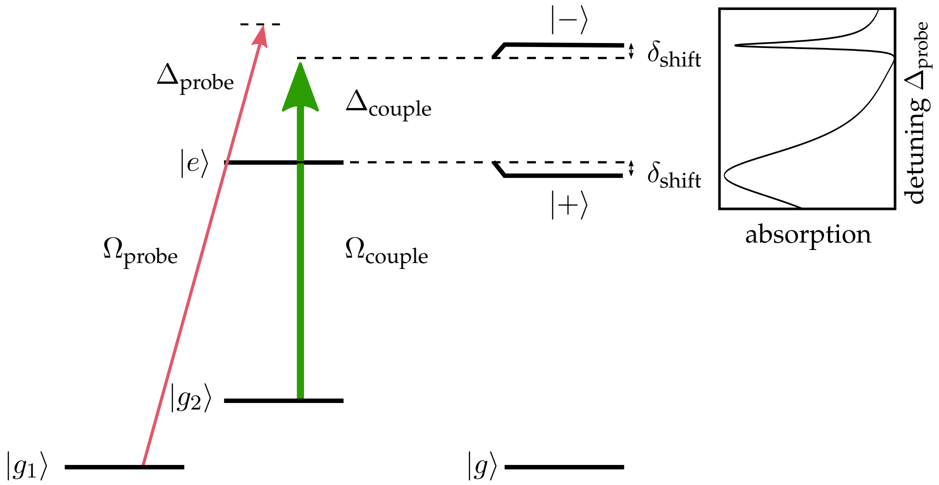

Figure 5.6.: $\Lambda-$level scheme for EIT. A coupling laser (green arrow) couples the ground state $|g_2\rangle$ to the excited state $|e\rangle$ with detuning $\Delta_{\text{couple}} > 0$ and Rabi frequency Ω_{couple}. It thus creates dressed states $|+\rangle$, $|-\rangle$, and $|g\rangle$. The dressed states $|+\rangle$ and $|-\rangle$ are shifted in frequency by $\pm\delta_{\text{shift}}$. A probe laser (pink arrow) probes the absorption of the driven atom with variable detuning Δ_{probe} and Rabi frequency Ω_{probe}. The inset shows the absorption of the probe light as a function of its detuning Δ_{probe}.

dressed state $|+\rangle$ is lowered in energy by the ac Stark shift $\hbar\delta_{\text{shift}}$ caused by the coupling laser. The light shift is given through [Mor00]

$$\delta_{\text{shift}} = \frac{\sqrt{\Delta^2_{\text{couple}} + \Omega^2_{\text{couple}}} - \Delta_{\text{couple}}}{2}. \tag{5.29}$$

In contrast, the dressed state $|-\rangle$ is lifted by $\Delta_{\text{couple}} + \delta_{\text{shift}}$ relative to $|e\rangle$. By sweeping the detuning Δ_{probe} around $\Delta_{\text{probe}} = \Delta_{\text{couple}}$ (two-photon resonance) the probe laser samples the absorption spectrum of the driven atom. The inset of Fig. 5.6 depicts the resulting absorption spectrum as a function of Δ_{probe}. The absorption spectrum has three distinct features: two absorption peaks and one absorption minimum with zero absorption. The broader peak corresponds to absorption on the transition $|g\rangle \to |+\rangle$ and has a width Γ_+ of approximately $\Gamma_+ \simeq \Gamma_{\text{e}}$. The narrow peak emerges from absorption on the transition $|g\rangle \to |-\rangle$ and has a width $\Gamma_- \ll \Gamma_{\text{e}}$ [Mor00]. For $\Delta_{\text{probe}} = \Delta_{\text{couple}}$, the two excitation paths from $|g_1\rangle$ and $|g_2\rangle$ interfere destructively and thus the absorption is zero. The atom in state $|g\rangle$ becomes transparent for the probe light and thus EIT is achieved.

5.4.2. EIT Cooling of a Trapped Atom

If the atom considered in the previous Sec. 5.4.1 is trapped within a harmonic potential with trapping frequency ω_{site}, each dressed state $|g\rangle, |+\rangle$, and $|-\rangle$ unfolds into a manifold of states with different vibrational states $|N\rangle$. Figure 5.7 shows the level scheme of the trapped atom. If $\omega_{\text{site}} \gg \Gamma_{\text{e}}$, the vibrational states of the dressed state $|-\rangle$ are well resolved. By choosing $\Delta_{\text{probe}} = \Delta_{\text{couple}}$ and tuning δ_{shift} such that $\delta_{\text{shift}} = \omega_{\text{site}}$, the transition $|g, N\rangle \to |-, N-1\rangle$ is brought into resonance with the probe laser. For this parameter setting, Fig. 5.8 indicates the absorption for transitions from state $|g, N\rangle$ to the states $|-, N-1\rangle, |-, N\rangle$, and $|-, N+1\rangle$.

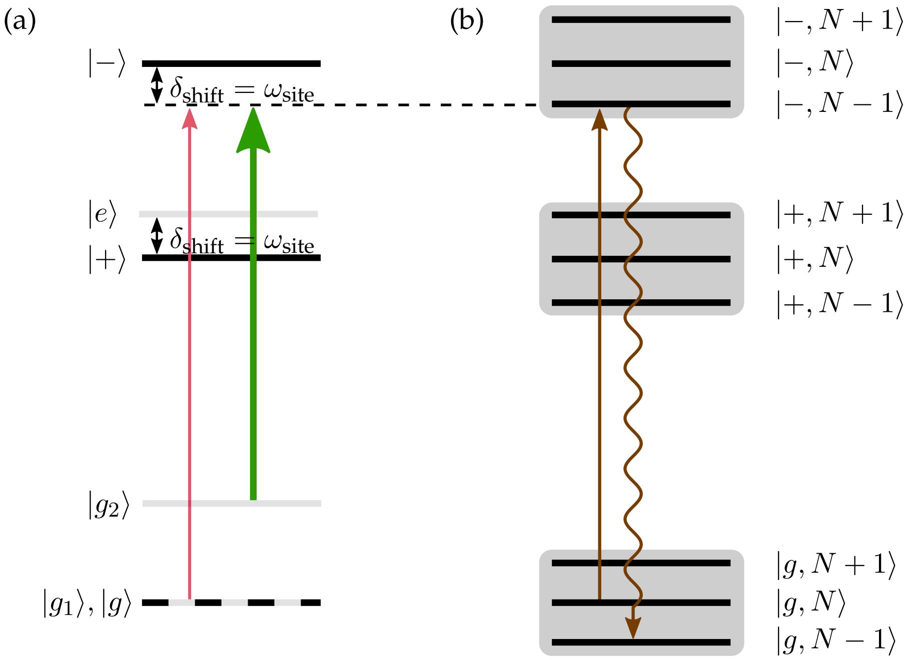

Figure 5.7.: EIT cooling of a trapped atom. (a) Level energies of bare atomic states (gray lines) and dressed states (black lines) for EIT for a free atom. The coupling laser is indicated through a green arrow, the probe laser is represented by a pink arrow. (b) Level energies for a trapped atom. Each dressed state of (a) unfolds into a manifold of equidistant states with different vibrational quantum number N. If $\delta_{\text{shift}} = \omega_{\text{site}}$, the probe laser drives transitions $|g, N\rangle \to |-, N-1\rangle$ (straight brown arrow). If $\eta \ll 1$, the atom in state $|-, N-1\rangle$ decays most likely into state $|g, N-1\rangle$ (wavy brown arrow).

The individual transitions have absorption rates that significantly differ from each other. The narrow absorption peak in Fig. 5.8 corresponds to absorption on the transition $|g, N\rangle \to |-, N-1\rangle$ (red-sideband transition). If $\eta \ll 1$ (Lamb-Dicke regime), spontaneous emission from the excited $|-, N-1\rangle$ state appears predominantly on the transition $|-, N-1\rangle \to |g, N-1\rangle$ (carrier transition). For a carrier transition, the vibrational quantum number N is preserved. A red-sideband transition followed by a carrier transition ($|g, N\rangle \to |-, N-1\rangle \to |g, N-1\rangle$) thus lowers the vibrational quantum number N of the atom by one and represents one cooling cycle. Transitions like $|g, N\rangle \to |-, N\rangle$, which lead to diffusion, or $|g, N\rangle \to |-, N+1\rangle$ (blue-sideband transition), which lead to heating, are extinguished or attenuated compared to the cooling transition [Mor00]. Since cooling events occur at a higher rate than heating events, EIT cooling allows cooling of the trapped atom close to the vibrational ground state.

Electromagnetically-induced transparency cooling redistributes the atomic population in the vibrational states towards lower vibrational states. The probability $P(N)$ to find the trapped atom within the vibrational state $|N\rangle$ of the electronic ground state $|g\rangle$ thus varies with time. In the Lamb-Dicke regime, the temporal evolution of $P(N)$ can be modeled with rate equations. If $\Omega_{\text{probe}} \ll \Omega_{\text{couple}}$ and provided that the probe laser does not saturate the transition $|g\rangle \to |-\rangle$, the rate equation for the population probability of state $|g, N\rangle$ becomes [Mor00]

$$\dot{P}(N) = \eta_2^2 \{A_- [(N+1)P(N+1) - NP(N)] + A_+ [NP(N-1) - (N+1)P(N)]\}. \tag{5.30}$$

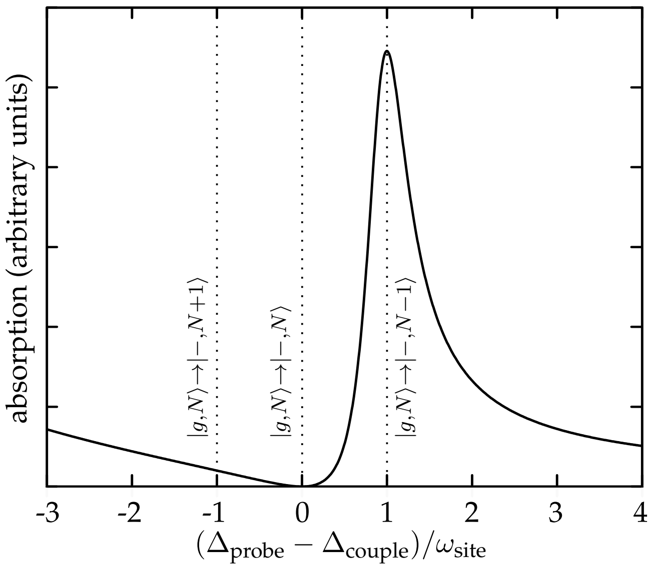

Figure 5.8.: Absorption spectrum for EIT cooling. Shown is the absorption of the probe laser. If $\delta_{\mathrm{shift}} = \omega_{\mathrm{site}}$, transitions from state $|g, N\rangle$ to the excited states $|-, N-1\rangle$, $|-, N\rangle$, and $|-, N+1\rangle$ (vertical dotted lines) have different absorption strengths. Because of EIT, absorption on the transition $|g, N\rangle \to |-, N\rangle$ is extinguished.

The parameter η_2 is defined as [Mor00]

$$\eta_2 = \left|\vec{k}_{\mathrm{probe}} - \vec{k}_{\mathrm{couple}}\right| \cdot \Upsilon, \tag{5.31}$$

where Υ denotes the root-mean-square size of the harmonic oscillator ground state wave function. The parameter η_2 is known as *two-photon Lamb-Dicke parameter*. The coefficients $A_\pm$ in Eq. (5.30) are given by [Mor00]

$$A_\pm = \frac{\Omega^2_{\mathrm{probe}}}{\Gamma_{\mathrm{e}}} \frac{\Gamma^2_{\mathrm{e}}\omega^2_{\mathrm{site}}}{\Gamma^2_{\mathrm{e}}\omega^2_{\mathrm{site}} + 4[\Omega^2_{\mathrm{couple}}/4 - \omega_{\mathrm{site}}(\omega_{\mathrm{site}} \mp \Delta_{\mathrm{couple}})]^2}. \tag{5.32}$$

Note, that even for unresolved sidebands ($\Gamma_{\mathrm{e}} \gg \omega_{\mathrm{site}}$) EIT cooling of trapped atoms works and Eq. (5.30) and Eq. (5.32) remain valid [Mor00].

5.5. Simulation

To study the dynamics of the trapped ^{39}K atoms during violet fluorescence quantum gas microscopy and simultaneous EIT cooling on the principal D$_1$ transition, we numerically compute the evolution of the *population probabilities* $\mathcal{P}_k(N,t)$ of the vibrational states $|N\rangle$ for each atomic state $|\varphi_k\rangle$. For this purpose, we consider a single trapped ^{39}K atom representative for all ^{39}K atoms within the optical lattice and take into account all fine structure Zeeman states $|\varphi_k\rangle = |\gamma_k J_k M_{J,k}\rangle$ between the 4S$_{1/2}$ and 5P$_{3/2}$ level.

5.5.1. Assumptions and Initial Conditions of the Simulation

The starting point of our simulation is a ^{39}K atom within a single well of a 1D optical lattice potential ($\lambda_{\mathrm{L}} = 1064\,\mathrm{nm}$) in one dimension. Initially, the atom is in one of its two internal ground states, namely in state $|4\mathrm{S}_{1/2}, M_J{=}1/2\rangle$. The lattice depth that the atom experiences in this state is assumed to be $V_{0,4\mathrm{S}1/2} = 1000\ E_{\mathrm{rec}}$. A similarly deep lattice was used during fluorescence imaging of EIT-cooled ^{40}K atoms in a previous experiment [Edg15]. Such a deep lattice justifies a harmonic approximation of the on-site lattice potential. The on-site trapping frequency for a ground state ^{39}K atom then equals $\omega_{x,4\mathrm{S}1/2} = 2\pi\times\ 286\,\mathrm{kHz}$. A 1D harmonic oscillator with trapping frequency $\omega_{x,4\mathrm{S}1/2}$ has sixteen vibrational states $|N\rangle$, whose energies E_N are smaller than the lattice depth $V_{0,4\mathrm{S}1/2}$. We calculate the on-site trapping frequencies $\omega_{x,k}$ of the excited atomic states $|\varphi_k\rangle$ by means of the total polarizabilities $\alpha^{\mathrm{c}}_{\mathrm{tot}}(\omega_{\mathrm{L}})$ from Ch. 4.

At the beginning of the simulation, we assume the atom within the vibrational ground state $|N{=}0\rangle$ of the lattice site, i.e. the initial state of the atom is $|4\mathrm{S}_{1/2}, M_J = 1/2, N = 0\rangle$. At $t = 0$, a violet imaging laser along the lattice axis starts to excite the ^{39}K atom from the $4\mathrm{S}_{1/2}$ level into the $5\mathrm{P}_{3/2}$ level. The laser line width Γ_{laser} is assumed to be $\Gamma_{\mathrm{laser}} = 2\pi\times 100\,\mathrm{kHz}$, which is smaller than the line width of the $5\mathrm{P}_{3/2}$ level ($\Gamma_{\mathrm{laser}}/\Gamma_{5\mathrm{P}3/2} \ll 1$). We furthermore assume that the laser light has linear polarization and that it is resonant with the transition $|4\mathrm{S}_{1/2}, M_J{=}1/2; N{=}0\rangle \rightarrow |5\mathrm{P}_{3/2}, M_J{=}1/2; N{=}0\rangle$. The laser intensity I_{tot} in our calculation corresponds to the saturation intensity of the $4\mathrm{S}_{1/2} \rightarrow 5\mathrm{P}_{3/2}$ transition, i.e. $I_{\mathrm{tot}} = I_{\mathrm{sat}}$. In our simulation, EIT cooling is assumed to take place on the principal D_1 transition. The parameters for EIT cooling considered are those with which EIT cooling of trapped ^{40}K atoms was experimentally demonstrated in Ref. [Hal15], namely $\Omega_{\mathrm{couple}} = 2\pi\times 4.8\,\mathrm{MHz}$, $\Omega_{\mathrm{probe}} = 2\pi\times 1.6\,\mathrm{MHz}$, and $\Delta = 10\Gamma_{4\mathrm{P}1/2}$. With these values the coefficients A_+ and A_- in Eq. (5.32) become $A_+ = 3.78\times 10^3\,\mathrm{s}^{-1}$ and $A_- = 1.49\times 10^4\,\mathrm{s}^{-1}$.

5.5.2. Setting Up the Rate Equations

We calculate the temporal evolution of the population probabilities $\mathcal{P}_k(N,t)$ for each state $|\varphi_k, N\rangle$ with $N \in \{0, 1, 2, \ldots, 12\}$ through rate equations. To set up the rate equation for $\mathcal{P}_k(N,t)$ of a given state, we sum up all contributions from processes that lead to population transfer out of this state or into it. These processes include fluorescence imaging, which causes absorption as well as stimulated and spontaneous emission, and EIT cooling. We therefore use the mathematical expressions for the transition rates $\mathcal{T}_{kN,k'N'}$ from Sec. 5.3.5 and Eq. (5.30). We exemplify the structure of the resulting rate equations by giving the explicit form of the rate equation for the population probability of the $|4\mathrm{S}_{1/2}, M_J{=}1/2; N{=}0\rangle$ state, i.e. $\mathcal{P}_{4\mathrm{S}1/2,1/2}(N{=}0,t)$, which reads

$$
\begin{aligned}
\dot{\mathcal{P}}_{4\mathrm{S}1/2,1/2}(N{=}0,t) = &- \mathcal{A}_{\mathrm{abs}}^{4\mathrm{S}1/2\rightarrow 5\mathrm{P}3/2} \cdot \mathcal{P}_{4\mathrm{S}1/2,1/2}(N{=}0,t) \sum_{N'} |\mathcal{F}_{N=0\rightarrow N'}|^2 \\
&+ \mathcal{A}_{\mathrm{emi}}^{\mathrm{stim},5\mathrm{P}3/2\rightarrow 4\mathrm{S}1/2} \sum_{N'} |\mathcal{F}_{N'\rightarrow N=0}|^2 \cdot \mathcal{P}_{5\mathrm{P}3/2,1/2}(N',t) \\
&+ \frac{1}{3} \sum_{k'',N''} \mathcal{A}_{\mathrm{emi}}^{\mathrm{sp},k''\rightarrow 4\mathrm{S}1/2} \cdot |\mathcal{F}_{N''\rightarrow N=0}|^2 \cdot \mathcal{P}_{k''}(N'',t) \\
&+ \eta_2^2 \{A_- \mathcal{P}_{4\mathrm{S}1/2,1/2}(N{=}1,t) - A_+ \mathcal{P}_{4\mathrm{S}1/2,1/2}(N{=}0,t)\}. \qquad (5.33)
\end{aligned}
$$

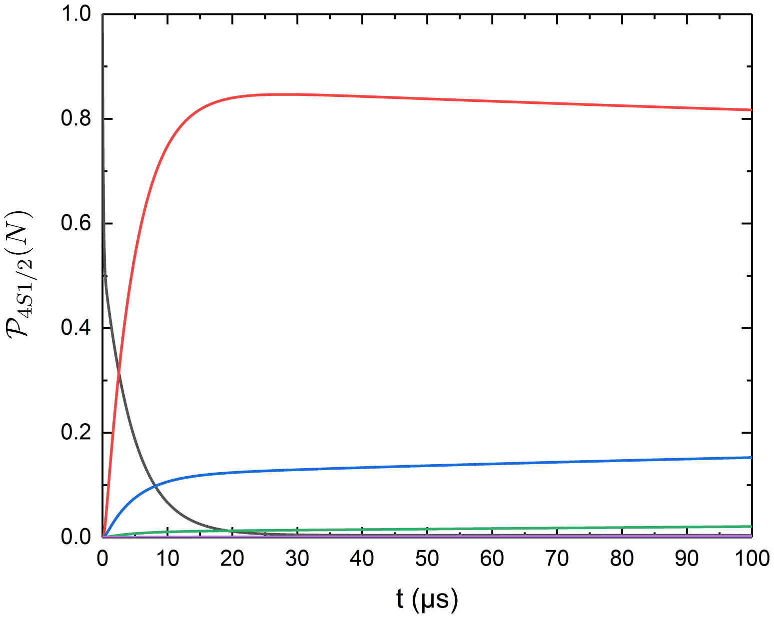

Figure 5.9.: Evolution of the vibrational state population probabilities $\mathcal{P}_{4S1/2}(N,t)$. Shown is the time evolution of the population probabilities $\mathcal{P}_{4S1/2}(N,t)$. Color code: $N = 0$ (black), $N = 1$ (red), $N = 2$ (blue), $N = 3$ (green), and $N = 4$ (purple).

The four terms in Eq. (5.33) describe population loss due to absorption of imaging light on the $4\mathrm{S}_{1/2} \rightarrow 5\mathrm{P}_{3/2}$ transition, population growth because of stimulated emission from the $5\mathrm{P}_{3/2}$ level, population growth owing to spontaneous emission from all energetically higher atomic states, and change in population because of EIT cooling.

In Eq. (5.33) we made the assumption that spontaneous emission is isotropic and thus included a factor $1/3$ to account for the one spatial dimension of our simulation. The maximum Lamb-Dicke parameter η of all transitions in our simulation has the value $\eta = 0.35$. We therefore consider only transitions with $\Delta N = \{0, \pm 1, \pm 2\}$ in all of our rate equations. Since fluorescence imaging and EIT cooling act only on the $4\mathrm{S}_{1/2}$, $4\mathrm{P}_{1/2}$, and $5\mathrm{P}_{3/2}$ levels, the rate equations for all other atomic levels include solely spontaneous emission terms.

5.5.3. Results of the Simulation

The simulation yields the population probabilities for the vibrational states $|N\rangle$ of the atomic states $|4\mathrm{S}_{1/2}, M_J{=}-1/2\rangle$ and $|4\mathrm{S}_{1/2}, M_J{=}+1/2\rangle$ for times up to $t = 4\,\mathrm{ms}$.[3] Since the two Zeeman states are degenerate in the absence of a magnetic field, we give the population probabilities for their different vibrational states $|N\rangle$ as the sum over the two atomic states, i.e.

$$\mathcal{P}_{4\mathrm{S}1/2}(N,t) = \mathcal{P}_{4\mathrm{S}1/2,1/2}(N,t) + \mathcal{P}_{4\mathrm{S}1/2,-1/2}(N,t). \tag{5.34}$$

Figure 5.9 presents the numerical results for $\mathcal{P}_{4\mathrm{S}1/2}(N,t)$ for $N \in \{0,1,2,3,4\}$. After around 30 µs the atom is nearly entirely pumped from the vibrational ground state $|N{=}0\rangle$ into excited vibrational states $|N\rangle$ of the $4\mathrm{S}_{1/2}$ level. For times $t > 30\,\mu\mathrm{s}$ the population probabilities of

---

[3] The duration of 4 ms is chosen because of limited computational power.

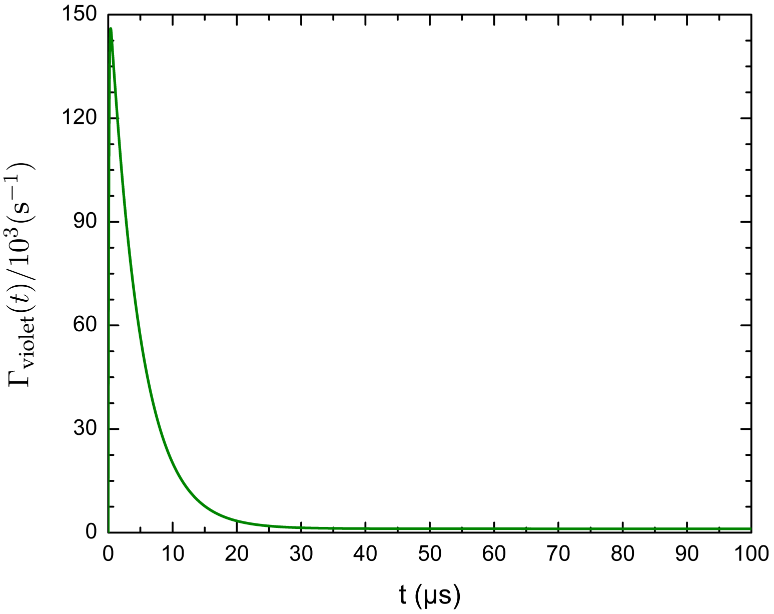

Figure 5.10.: Fluorescence rate of violet photons, Γ_{violet}, as a function of time t. The time starts with the beginning of violet fluorescence quantum gas microscopy.

the excited vibrational states $|N = 2\rangle$ and $|N = 3\rangle$ increase continuously. We explain this growth through EIT cooling being not efficient enough to cool the trapped atom during fluorescence imaging. At $t = 100\,\mu\mathrm{s}$, the population probabilities $\mathcal{P}_{4\mathrm{S}1/2}(N,t)$ of the vibrational states $|N{=}0\rangle$, $|1\rangle$, $|2\rangle$, $|3\rangle$, and $|4\rangle$ are 0.004, 0.82, 0.15, 0.02, and 0.002, respectively, with no considerable population probabilities for higher vibrational states and excited atomic states. The *average vibrational quantum number* $\overline{N}$ of the atom at that point of time is $\overline{N} = 1.2$. At $t = 4\,\mathrm{ms}$, the average vibrational quantum number has increased to $\overline{N} = 1.39$.

In a next step, we use the population probabilities $\mathcal{P}_k(N,t)$ obtained for the Zeeman states of the $5\mathrm{P}_{3/2}$ level to calculate the fluorescence rate Γ_{violet} of violet photons as a function of time. Figure 5.10 depicts the numerical results for $\Gamma_{\text{violet}}(t)$. The function $\Gamma_{\text{violet}}(t)$ flattens after a time $t \approx 10\,\mu\mathrm{s}$ and is constant for $t > 30\,\mu\mathrm{s}$. The average fluorescence rate within the first 30 microseconds is $\bar{\Gamma}_{\text{violet,30}} \approx 25700$ photons/s. For times longer than 30 μs, $\Gamma_{\text{violet}}(t)$ has decreased to around 1100 photons/s.

To determine how the average vibrational quantum number $\overline{N}$ and $\bar{\Gamma}_{\text{violet,30}}$ depend on the lattice depth $V_{0,4\mathrm{S}1/2}$, we numerically calculate both quantities for lattice depths between $600E_{\text{rec}}$ and $1200E_{\text{rec}}$. Figure 5.11 depicts $\overline{N}$ at times $t = 30\,\mu\mathrm{s}$, denoted as $\overline{N}_{30}$, as well as $\bar{\Gamma}_{\text{violet,30}}$ as a function of the lattice depth $V_{0,4\mathrm{S}1/2}$. The numerical results confirm that a stronger confinement of the ^{39}K atom leads to a smaller average vibrational quantum number $\overline{N}_{30}$ and a larger average fluorescence rate $\bar{\Gamma}_{\text{violet,30}}$. However, the lattice depth dependency is rather weak for both quantities.

5.5.4. Discussion and Conclusion

To evaluate whether violet fluorescence imaging and simultaneous EIT cooling on the principal D_1 transition of trapped ^{39}K atoms will allow for the performance of fluorescence quantum gas microscopy, it is important to know whether the ^{39}K atoms scatter a sufficient number of

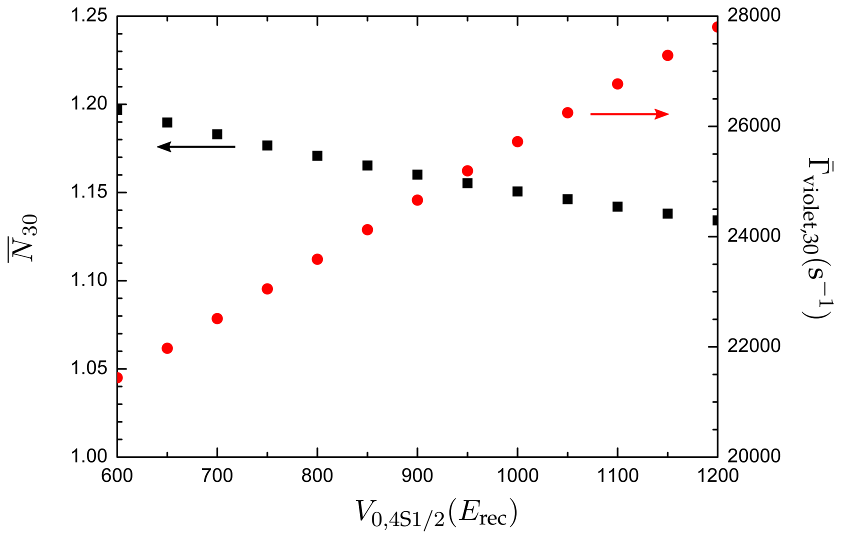

Figure 5.11.: Lattice depth dependency of $\overline{N}_{30}$ and $\bar{\Gamma}_{\text{violet,30}}$. The numerical data shows the dependence of the average vibrational quantum number $\overline{N}_{30}$ (black squares) and the average fluorescence rate $\bar{\Gamma}_{\text{violet,30}}$ of violet photons (red circles) on the lattice depth $V_{0,4S1/2}$.

violet photons during imaging. For exposure times longer than 30 µs, the fluorescence rate of a single trapped ^{39}K atom ($\Gamma_{\text{violet}} \approx 1100$ photons/s) is smaller than the scattering rates measured in most existing FQGM apparatuses, for which fluorescence rates are typically between ~ 5000 photons/s (for ^{40}K in Ref. [Che15]) and ~ 60000 photons/s (for ^{87}Rb in Ref. [She10]). It is, however, comparable to that of the ^{40}K FQGM apparatus of the Thywissen group. In this apparatus, the fluorescence rate per atom has been experimentally determined to be ~ 900 photons/s [Edg15]. We therefore conclude that violet fluorescence quantum gas microscopy and simultaneous EIT cooling of trapped ^{39}K should be in principle possible with regards to emitting a sufficient number of fluorescence photons.

In order to increase the number of detected violet fluorescence photons, it could be expedient to repeatedly pulse the violet laser. One would then switch off the imaging laser after a time $t = 30$ µs when fluorescence emission becomes less efficient. After a certain duration during which EIT cooling has acted on the atom one could switch on the imaging laser again and profit from the enhanced fluorescence rate. Bare EIT cooling leads to a *steady-state vibrational quantum number* $\langle N \rangle_{\text{st}}$ given by [Mor00]

$$\langle N \rangle_{\text{st}} = \frac{A_+}{A_- - A_+}. \tag{5.35}$$

In our simulation, $\langle N \rangle_{\text{st}} = 0.34$. Since $\langle N \rangle_{\text{st}} > 0$, EIT cooling in our simulation does not transfer the trapped ^{39}K atom entirely back into the vibrational ground state. This circumstance limits the fluorescence rate when the violet imaging laser is switched on again.

In a next step, we have to quantify the probability of atom loss during violet fluorescence quantum gas microscopy. This requires an extension of the simulation described in this Chapter. Our simulation is based on a simplified model in 1D, in which the eigenstates of an inverted harmonic oscillator are assumed to be harmonic oscillator states. As can be seen from Table 4.2, 18 out of 26 fine structure Zeeman states possess a negative atomic polarizability

$\alpha_{\mathrm{tot}}(\omega_{\mathrm{L}})$ and are therefore anti-trapping states. To improve the simulation, the true eigenstates of an inverted oscillator should be used since that provides a more realistic description of the dynamics of the trapped atom. It might then be possible to estimate the probability for loss of the ^{39}K atom from the lattice site during imaging.

In a further step, the simulation could account for the hyperfine structure of the ^{39}K atom. The refinement of the definitions of the frequency-dependent valence scalar and tensor polarizabilities $\alpha_0(\omega_{\mathrm{L}})$ and $\alpha_2(\omega_{\mathrm{L}})$ for hyperfine structure Zeeman states is straightforward [Bon97]. Lastly, the simulation can be extended to three spatial dimensions, where vibrational levels are degenerate.

Experiments on violet fluorescence imaging of K atoms in an optical lattice have been performed by G. Edge in the Thywissen group with ^{40}K atoms. In these experiments, D_1 EIT cooling was applied simultaneously to fluorescence imaging. In another set of experiments, EIT cooling was executed sequentially with cooling and imaging alternating with a period of $\sim 1\,\mathrm{ms}$ [Edg17]. When the intensity of the $404.5\,\mathrm{nm}$-imaging laser was below a certain threshold, the obtained fluorescence images suffered from a poor signal to noise ratio. For laser intensities larger than the threshold, loss of atoms out of the lattice sites was observed. It was hence concluded that EIT cooling did not cool the trapped atoms quickly enough during imaging in their experiments. It will be thus interesting to study the experimental feasibility of combined violet fluorescence imaging and D_1 EIT cooling of ^{39}K atoms in future experiments.

6. Design of the Main Vacuum System

Experiments with ultracold quantum gases are performed under UHV and hence require a UHV chamber. An important part of this Thesis was the design of the vacuum apparatus of the K−Cs experiment from scratch. To be able to adapt the K−Cs vacuum setup in future to new experimental needs, we opted for a modular design of the vacuum apparatus. The vacuum apparatus comprises two vacuum systems, which are connected to each other: one vacuum system is used to produce ultracold K and Cs quantum gases (*main vacuum system*) and a second vacuum chamber is used to implement our FQGM imaging system (*science chamber*). This Chapter outlines the overall design of the entire vacuum apparatus and focuses on the technical design of the main vacuum system. At the end of this Chapter, we discuss magnetic field coils, which are employed to generate a magnetic offset field and whose design is closely related to the main vacuum system. Chapter 8 then deals with the design of the science chamber. Both vacuum systems in combination will allow us to perform fluorescence quantum gas microscopy of K and Cs atoms according to the envisioned experimental sequence that has been detailed in Sec. 3.5.1. The main vacuum system has been implemented and enabled the experiments reported in Ch. 7.

6.1. General Considerations

In this Section, we list the experimental requirements on our vacuum apparatus and treat the question of which material is most suited for these purposes.

6.1.1. Experimental Requirements on the K−Cs Apparatus

We divide the experimental requirements on our vacuum apparatus into three categories: vacuum quality, experimental capabilities, and physical shape.

- Requirements on vacuum quality
  - The vacuum apparatus must contain two chambers that allow us to generate directed beams of slow potassium and cesium atoms. Both chambers must be designed to operate at pressures around $\sim 1 \times 10^{-6}\,\mathrm{mbar}$
  - For production and investigation of ultracold quantum gases, the vacuum system has to provide a UHV region with a pressure around $\sim 10^{-11}\,\mathrm{mbar}$
- Requirements on experimental capabilities
  - The apparatus has to facilitate the implementation of our imaging system discussed in Sec. 3.5.3
  - To polarize KCs molecules, the apparatus must offer in-vacuo electrodes

- Requirements on physical shape and material
  - To apply laser cooling, trapping, and probing techniques to the ultracold atoms, the vacuum system needs to offer optical access to the atoms from several directions
  - Because of limited lab space, the design of the apparatus must aim for a high degree of compactness
  - The possibility to install external magnetic field coils around the UHV region must be given
  - To minimize magnetization effects, the vacuum system should be non-magnetic

6.1.2. Material Choices

In today's vacuum technology, users can choose between numerous materials for vacuum chambers including stainless steel, aluminum, titanium, and glass. We summarize some advantages and disadvantages of each material in the following.

Stainless Steel
Stainless steel exists in different grades, which are grouped into four families: ferritic, martensitic, austenitic, and austenitic-ferritic [Inf]. Austenitic stainless steel is well machinable and very common in UHV technology. It offers a sufficiently high mechanical strength to make leak-free ConFlat flange joints between vacuum components, which are preserved even at bakeout temperatures of $400\,^{\circ}\mathrm{C}$. On the other side, stainless steel contains substantial amounts of hydrogen, which represent a source of continuous outgassing. Hydrogen stored in stainless steel limits the ultimate achievable pressure of a vacuum system and thus requires a thorough degassing treatment of the vacuum chamber. Austenitic steel would be non-magnetic if it was defect-free but practically always contains small magnetic (ferrite/martensite) portions [Bri]. The *relative magnetic permeability* μ_r of austenitic stainless steel is typically around $\mu_r \approx 1.05 - 1.1$ [Bri].

Aluminum
Aluminum has several advantages over stainless steel: its reduced mechanical hardness goes along with better machining. The higher thermal conductivity supports a uniform bakeout of the vacuum chamber and facilitates lower bakeout temperatures. Aluminum alloys in vacuum technology contain orders of magnitude less hydrogen than stainless steel and are less magnetic [Atl]. When aluminum is left unprotected against oxygen and water, it instantaneously builds up a porous oxide layer on its surface. As this oxide layer causes severe outgassing, it calls for special surface processing techniques. Because aluminum is too soft to compress standard copper gaskets, leak-tight ConFlat flange joints are problematic with aluminum. For this reason, flanges require special processing and come, for instance, as CrN coated aluminum flanges for increased hardness at the expense of a maximum bakeout temperature of $150\,^{\circ}\mathrm{C}$ [Kur].

Titanium
Titanium is strong enough for machining all-titanium ConFlat flanges and can be orders of magnitude less magnetic than stainless steel [Boy94]. So far, titanium is particularly used when aiming for extra-high vacuum ($\sim 10^{-12}\,\mathrm{mbar}$). For this reason, there is only a limited selection of commercially available titanium vacuum components.

Glass
One of the technically purest forms of glass is fused silica, a fully synthetic material of silicon dioxide [Her]. Vacuum chambers out of fused silica offer high optical access, electrical insulation, and a non-magnetic environment. Since glass becomes fragile in the presence of tensile stress, a vacuum chamber out of glass always carries the risk of being damaged easily and does not offer straightforward solutions for fixing internal fittings to it. Glass-metal transitions enable one to connect vacuum glass cells to stainless steel chambers.

Conclusion
Due to the broad range of commercially available stainless steel vacuum parts, we decided to use a stainless steel vacuum apparatus for the main vacuum system. We dismiss the option of titanium for reasons of lack of commercially available parts. We aim to transport the quantum gases from the main vacuum system to the science chamber. Therefore we refrain from choosing glass as it is rather fragile, especially when multiple connections to other vacuum components have to be made. A stainless steel apparatus supports riskless mounting of internal and external parts. To reduce magnetization effects due to the stainless steel bulk, we select austenitic stainless steel grades with low magnetic permeability.

6.2. The K−Cs Apparatus

The entire vacuum system of the K−Cs apparatus is located on top of an optical table[1]. Figure 6.1 shows the final design of the vacuum system of the K−Cs apparatus. In order to isolate the experimental setup from mechanical vibrations coming from nearby mechanical workshops, the table top has six internally mounted, passive precision dampers and resides on four pneumatic, vibration isolating legs[2]. Several optical bread boards hold the vacuum apparatus at a height of approximately $330\,\mathrm{mm}$ above the table top. To get optical access into the vacuum system from the top, the optical bread boards are partially stacked on top of each other. The optical bread boards are commercial as well as home-built. The commercial breadboards[3] are $61\,\mathrm{mm}$ thick and have a honeycomb core and damped working surfaces out of austenitic stainless steel of grades 316/316L. The two square bread boards shown at the left side of Fig. 6.1 are home-built, $20\,\mathrm{mm}$ thick aluminum bread boards. Vertical aluminum legs carry the bread boards and enable the installation of cross-bracings between the legs to reduce mechanical vibrations.

Typically, many optical and technical components such as mirrors and magnetic coils are mounted around the vacuum chamber of a quantum gas experiment. Because of blocked optical access to the atoms, it is therefore often not possible to implement every desired experimental technique to the apparatus. For this reason, the design of the K−Cs apparatus follows the concept of a bi-sected vacuum system. The vacuum system consists of a main unit that is permanently installed (main vacuum system) and a vacuum cell that is exchangeable (science chamber). Main vacuum system and science chamber are connected to each other and can be operated independently from each other. Figure 6.1 shows the position and the orientation of the main vacuum system (green color) and the science chamber setup (orange color). We use the main vacuum system to produce quantum gases and to perform experiments for which

---

[1] Newport Spectra-Physics GmbH, M-RS4000-58-12.
[2] Newport Spectra-Physics GmbH, S-2000A-423.5.
[3] Newport Spectra-Physics GmbH, Precision Grade Series.

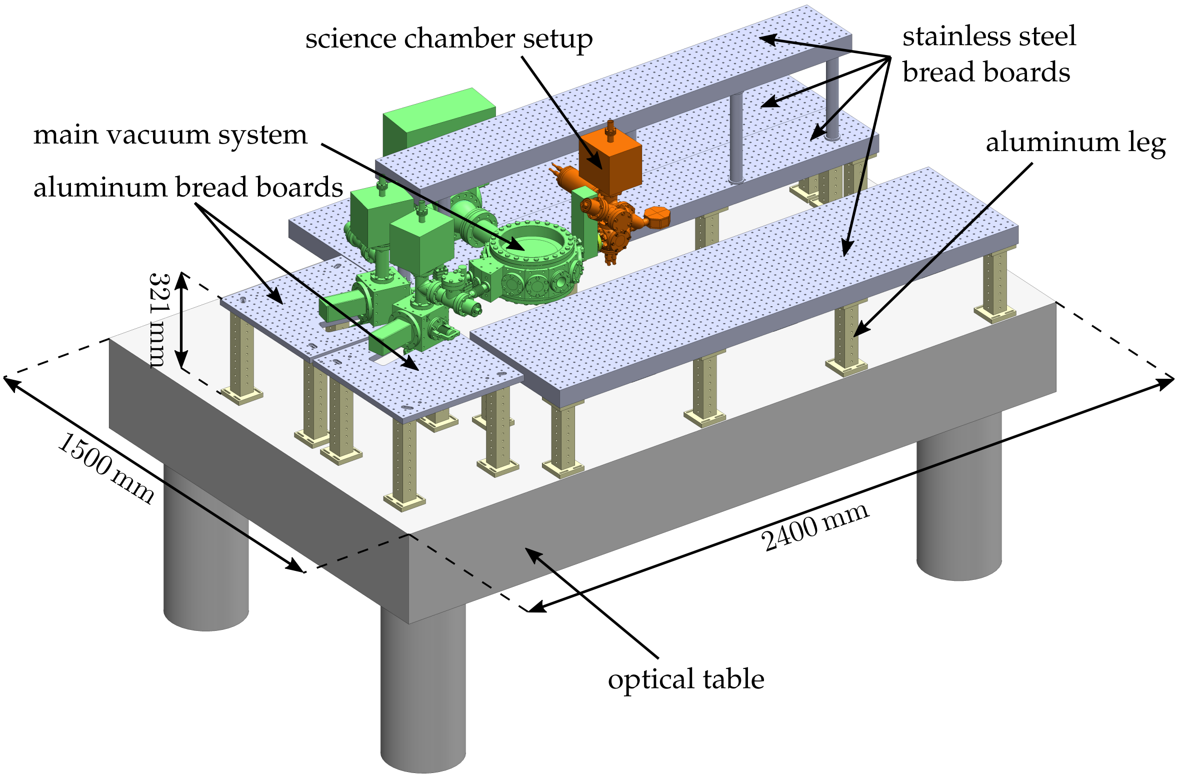

Figure 6.1.: Overview of the K−Cs apparatus. The K−Cs apparatus is built on a floating optical table. The vacuum apparatus consists of the main vacuum system (green color) and the science chamber setup (orange color). It is mounted on optical bread boards, which are held by aluminum legs.

probing via standard absorption imaging is sufficient. It has been built and led to several publications so far [Grö16, Grö17c, Grö17b]. The science chamber will be used solely to study quantum gases and thus will be free from surrounding magneto-optical trap (MOT) optics. It therefore provides the possibility to implement additional experimental tools to the apparatus. The science chamber is designed for the specific experimental needs of current research goals and can be replaced by a modified one whenever new research goals appear. At the time of this Thesis, the science chamber was mainly designed to provide the structural and experimental capabilities to implement our high-resolution imaging system (see Sec. 3.5.3) and to perform fluorescence quantum gas microscopy.

6.3. Main Vacuum System

The main vacuum system of the K−Cs apparatus centers around a stainless steel chamber, which serves as production site of ultracold potassium and cesium samples. Figure 6.2 gives an overview of the main vacuum system. The stainless steel chamber is designed to enable UHV and is denoted as *main chamber* in the following. The atoms for the ultracold samples stem from two atom sources that connect on the left side of the main chamber in Fig. 6.2. The atom sources, one for each atomic species, generate atomic beams of potassium and cesium and send them towards the main chamber. The angle between the two atom sources is chosen

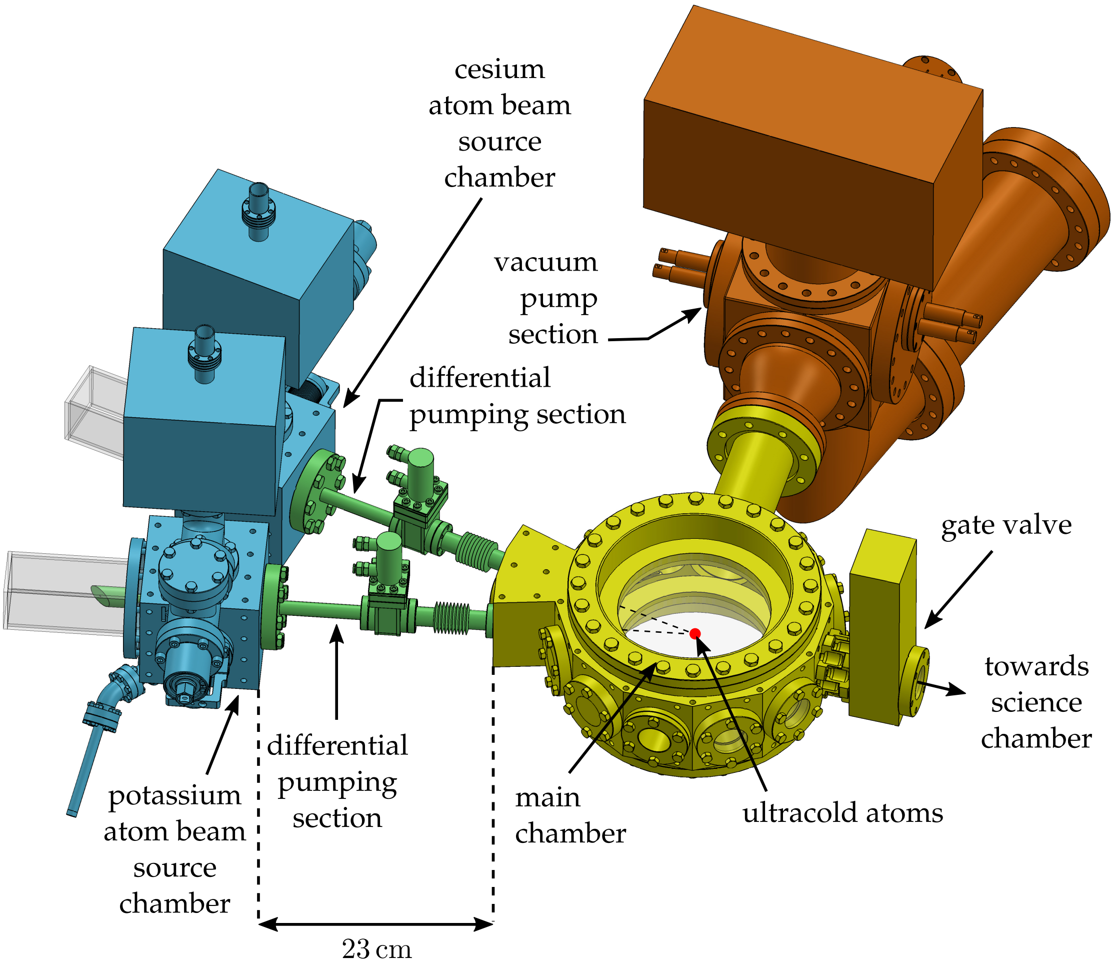

Figure 6.2.: Overview of the main vacuum system. The main vacuum system consists of four sections that are highlighted by different colors in this Figure. Two atomic beam sources (blue) generate beams (dashed lines) of potassium and cesium atoms and send them towards the main chamber (yellow) for production of ultracold quantum gases. Differential pumping sections (green) between the atom beam sources and the main chamber make the physical connections between those vacuum chambers. Simultaneously, the differential pumping sections prevent pressure equalization between the different vacuum chambers that maintain different pressures. A vacuum pump section (orange) joins to the back side of the main chamber and creates an UHV environment within the main chamber. On the right side of the main chamber, a gate valve enables the connection of the science chamber, which is not shown here.

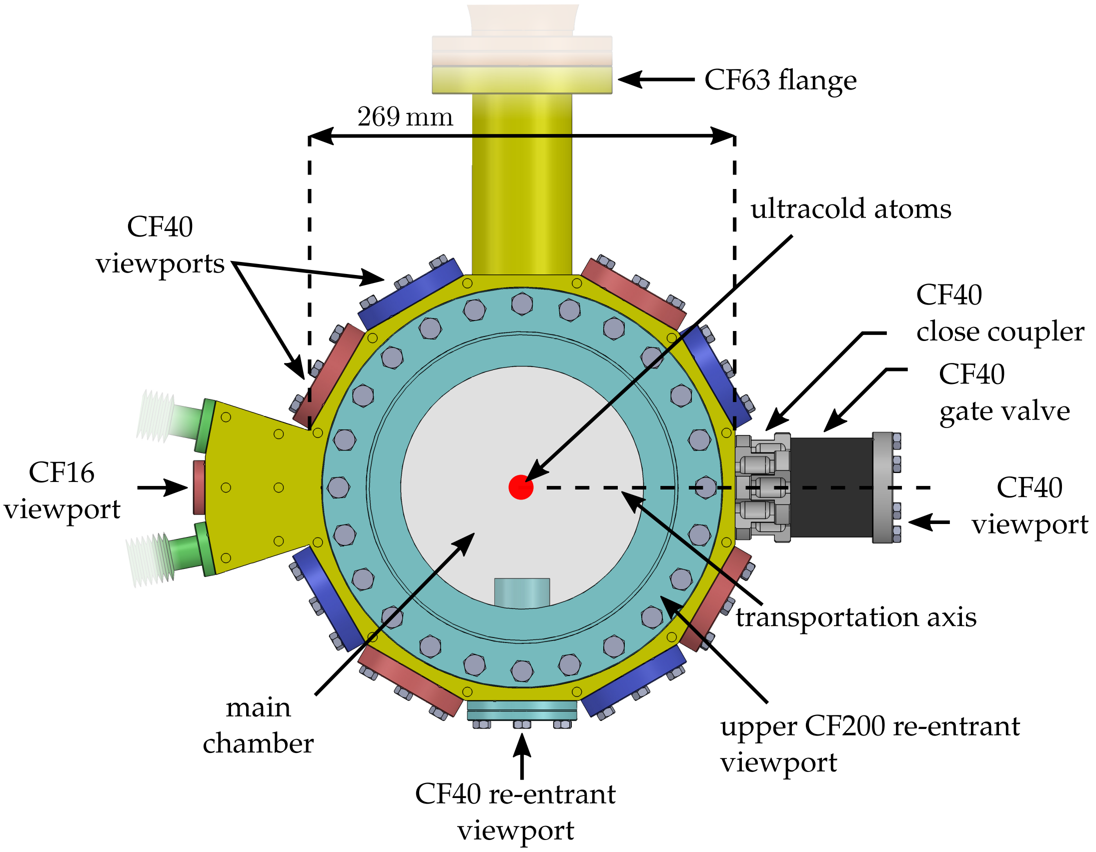

Figure 6.3.: Top view of main chamber. The main chamber is equipped with a total of twelve viewports. Four CF40 viewports (blue color) with anti-reflection coating 'A' and four CF40 viewports (red color) with anti-reflection coating 'B' are arranged crosswise in the horizontal plane. In addition, a CF40 re-entrant viewport (light blue) and a CF16 viewport are mounted to the vertical faces of the main chamber. Along the vertical axis, two CF200 re-entrant viewports (light blue) are attached on the top and bottom side of the main chamber. A CF63 flange connects to the vacuum pumps section and a CF40 straight connector of minimum length (close coupler) in combination with a CF40 gate valve make the transition towards the science chamber. The science chamber is not shown in this Figure. A CF40 viewport terminated the gate valve until the science camber was attached to the main chamber. The horizontal, dashed line marks the transportation axis along which the atoms are moved from the main chamber to the science chamber.

such that their atomic beams intersect in the geometrical center of the main chamber. At the center of the main chamber, the potassium and cesium atoms are collected in 3D-MOTs and cooled to Bose-Einstein condensation.

All previously built cesium quantum gas apparatuses in Innsbruck have used Zeeman slowers for loading 3D-MOTs [Web03a, Ryc04, Gus08, Pil09]. In those apparatuses, the distance between atom source and UHV chamber is typically on the order of one meter. To make the K$-$Cs vacuum setup more compact compared to previous quantum gas apparatuses in Innsbruck with Zeeman slowers, we employ 2D magneto-optical traps (2D-MOTs) as atomic beam sources similar to the one described in Ref. [Rid11a]. In this way, we were able to reduce the distance between the 2D-MOT and the main chamber to about $23\,\mathrm{cm}$.

In Ref. [Rid11a], efficient operation of a potassium 2D-MOT has been reported for a potassium partial pressure between $1 \times 10^{-6}\,\mathrm{mbar}$ and $1 \times 10^{-7}\,\mathrm{mbar}$. To maintain UHV in the main chamber while allowing for a higher pressure in the 2D-MOT chambers, the two 2D-MOTs are connected to the main chamber via tubes (*differential pumping sections*) with reduced gas flow conductance. In the back of the main chamber in Fig. 6.2, vacuum pumps are installed to create and maintain UHV inside the main chamber. This section is denoted as *pumping section*. On the right side of the main chamber in Fig. 6.2, a gate valve permits the connection of a science chamber to the main chamber. We discuss the sections of the main vacuum system individually in the following.

6.3.1. Main Chamber

The main chamber is at the heart of the K$-$Cs vacuum apparatus and designed to obtain pressures as low as $1 \times 10^{-11}\,\mathrm{mbar}$. Due to its central position we opted for a custom design of the chamber. Figure 6.3 shows a top view of the main chamber, while Fig. 6.4 depicts a vertical cut of the main chamber. The shape of the main chamber resembles that of a straight prism with a dodecagonal footprint. The left side of the dodecagon in Fig. 6.3 is substituted by a protrusion. The main chamber has a width of $269\,\mathrm{mm}$ and a height of $95\,\mathrm{mm}$. Our in-house mechanical workshop first wire-cut and then milled the main chamber body out of a single piece of austenitic stainless steel (material number 1.4429-ESU). This stainless steel type possesses a very homogeneous microstructure, which leads to a relative magnetic permeability of $\mu_r \leq 1.005$ [Vacb]. It has the lowest relative magnetic permeability we could find for commercially available stainless steel.

Ten viewports are mounted on the vertical faces of the main chamber. Eight CF40 viewports[4] and one CF16 viewport[5] (colored red and dark blue in Fig. 6.3), are anti-reflection coated on both sides of the glass substrates. We use two distinct anti-reflection coatings for these viewports, covering different wavelength bands:

- **Coating A** (minimum reflectivity between $750\,\mathrm{nm}$ and $1500\,\mathrm{nm}$):
  - reflectivity at $770\,\mathrm{nm}$ (potassium laser cooling light) is $0.1\,\%$
  - reflectivity at $852\,\mathrm{nm}$ (cesium laser cooling light) is $0.3\,\%$
  - reflectivity between $1100\,\mathrm{nm}$ and $1500\,\mathrm{nm}$ (laser light for driving transitions in KCs molecules) is smaller than $2.3\,\%$

---

[4] Viewports were manufactured by Larson Electronic Glass, California, U.S.A. Optical specifications: Corning HPFS 7980, homogeneity grade 0, inclusion class A. Transmitted wavefront error $< \lambda/4$ at $632\,\mathrm{nm}$, parallelism $< 10''$. Flange specifications: Stainless steel AISI 316LN, non-magnetic titanium sleeve for glass-metal transition.

[5] See footnote 4.

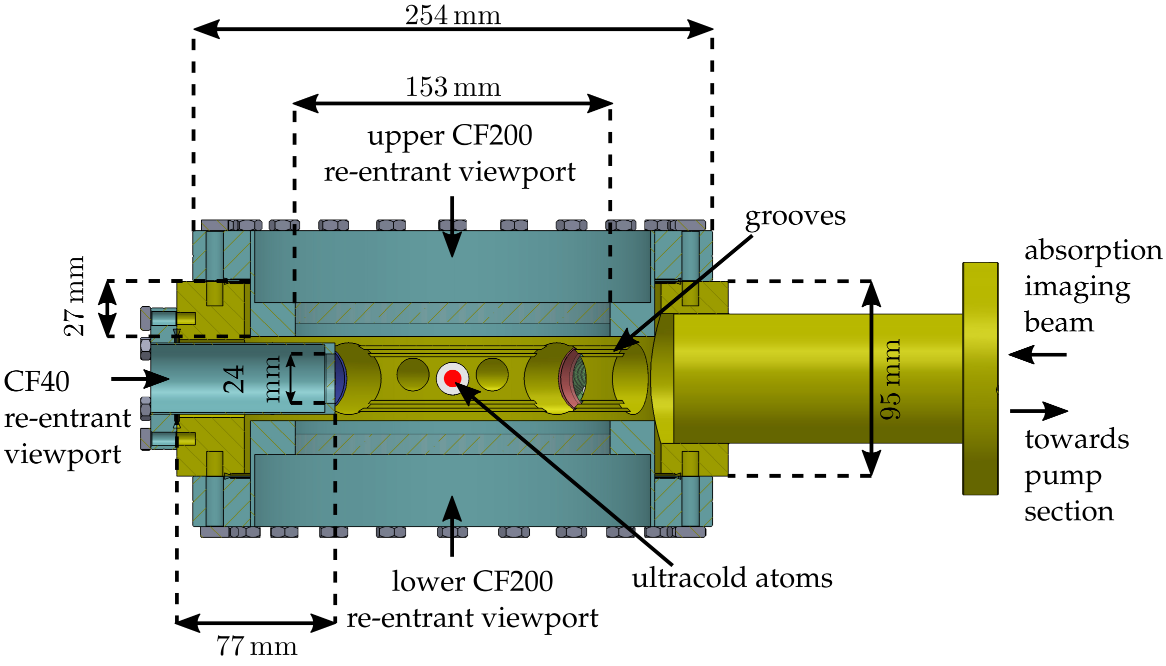

Figure 6.4.: Vertical cut of main chamber. The upper and lower CF200 re-entrant viewports extend 27 mm into the main chamber. A horizontal CF40 inverted viewport reaches between the vertical viewports. For absorption imaging of the atoms the absorption laser beam is guided through the vacuum pump section towards the atoms. Grooves at the inside wall of the main chamber are used for mounting in-vacuo electrodes.

- **Coating B** (minimum reflectivity between 400 nm and 532 nm and at 1064 nm):
  - reflectivity at 1064 nm (optical dipole traps, optical lattices, and optical transport) is 0.2 %
  - reflectivity at 405 nm (violet imaging of potassium) is 0.7 %
  - reflectivity at 532 nm (super-lattice) is 0.3 %

The experimentally measured coating charts provided by the company are shown in Appendix B.1 and Appendix B.2. The tenth viewport is a custom-made, non-magnetic, uncoated inverted CF40 viewport[6]. It extends 77 mm into the main chamber as shown in the light blue color in Fig. 6.3. The inverted CF40 viewport is used for absorption imaging. The absorption laser beam passes through the vacuum pump section and then travels through the inverted CF40 viewport towards a camera. To form an image of the atoms, a lens can be placed within the inverted CF40 viewport. Because of the inverted form of the viewport, the lens can be brought close to the atoms. Having a clear aperture of 24 mm, as detailed in Fig. 6.4, the inverted viewport allows for a numerical aperture of up to NA = 0.19 for absorption imaging. The technical drawing of the inverted CF40 viewport is given in Appendix C.1.

---

[6] Manufactured by UKAEA, Oxfordshire, United Kingdom. Optical specifications: Quartz material is Spectrosil 2000 by Heraeus, transmitted wavefront error $< \lambda/4$, thickness of 4 mm, parallelism $\leq 3'$, index of refraction homogeneity ≤ 10 ppm.

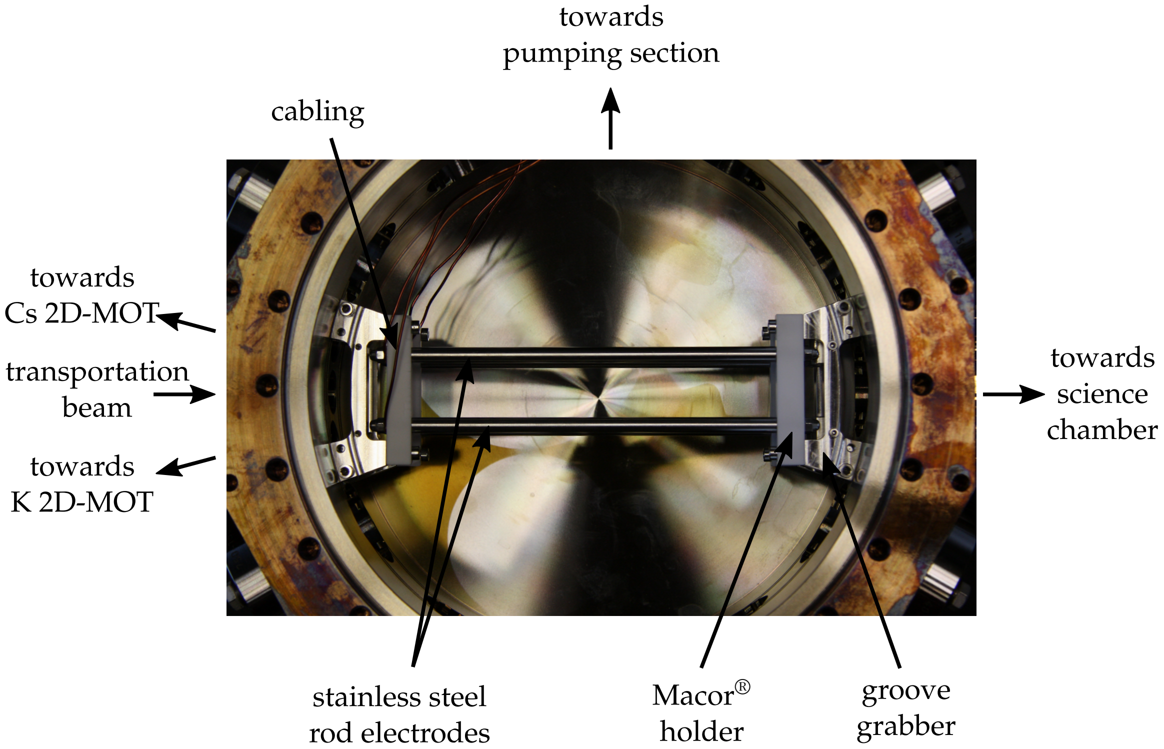

Figure 6.5.: Main chamber electrodes. Top view of the main chamber during assembly. The rod electrodes run parallel to the transportation axis and can be seen in the middle of the Figure. The electrodes are held by Macor® holders and groove grabbers. On the left side, one can see the cabling being fed from electrical feedthroughs to the electrodes.

On the left side of the main chamber in Fig. 6.3, a cornered lump protrudes and contains three CF16 flange connections. The center CF16 flange connection is occupied by the above-mentioned CF16 viewport. The CF16 viewport lies on the axis that goes through the center of the main chamber and the center of the science chamber. The viewport is thus used for inserting the optical transportation laser beam into the vacuum system. The two outer CF16 flange connections make the joints between the differential pumping sections and the main chamber. To take into acocunt the gravitational sag of the slow atom beams during their journey from the 2D-MOT chambers into the main chamber, the two flange connections are positioned $2\,\mathrm{mm}$ above the vertical midplane of the main chamber. On the right side of the main chamber in Fig. 6.3, a manual CF40 gate valve[7,8] terminates the main chamber and allows for the installation of the science chamber. At the back of the main chamber, a CF63 flange with a $132\,\mathrm{mm}$ long tube (inner diameter of $61\,\mathrm{mm}$) connects the main chamber to the pumping section.

On the top and bottom side of the main chamber, two identical uncoated CF200 re-entrant

---

[7] Lesker, CF40 manual gate valve, SG0150MCCF.

[8] The manual CF40 gate valve mounted to the main chamber relies on a fluorocarbon o-ring seal and has been chosen over an all-metal valve because of cost reasons. For future experiments, the usage of an all-metal angle valve is recommended.

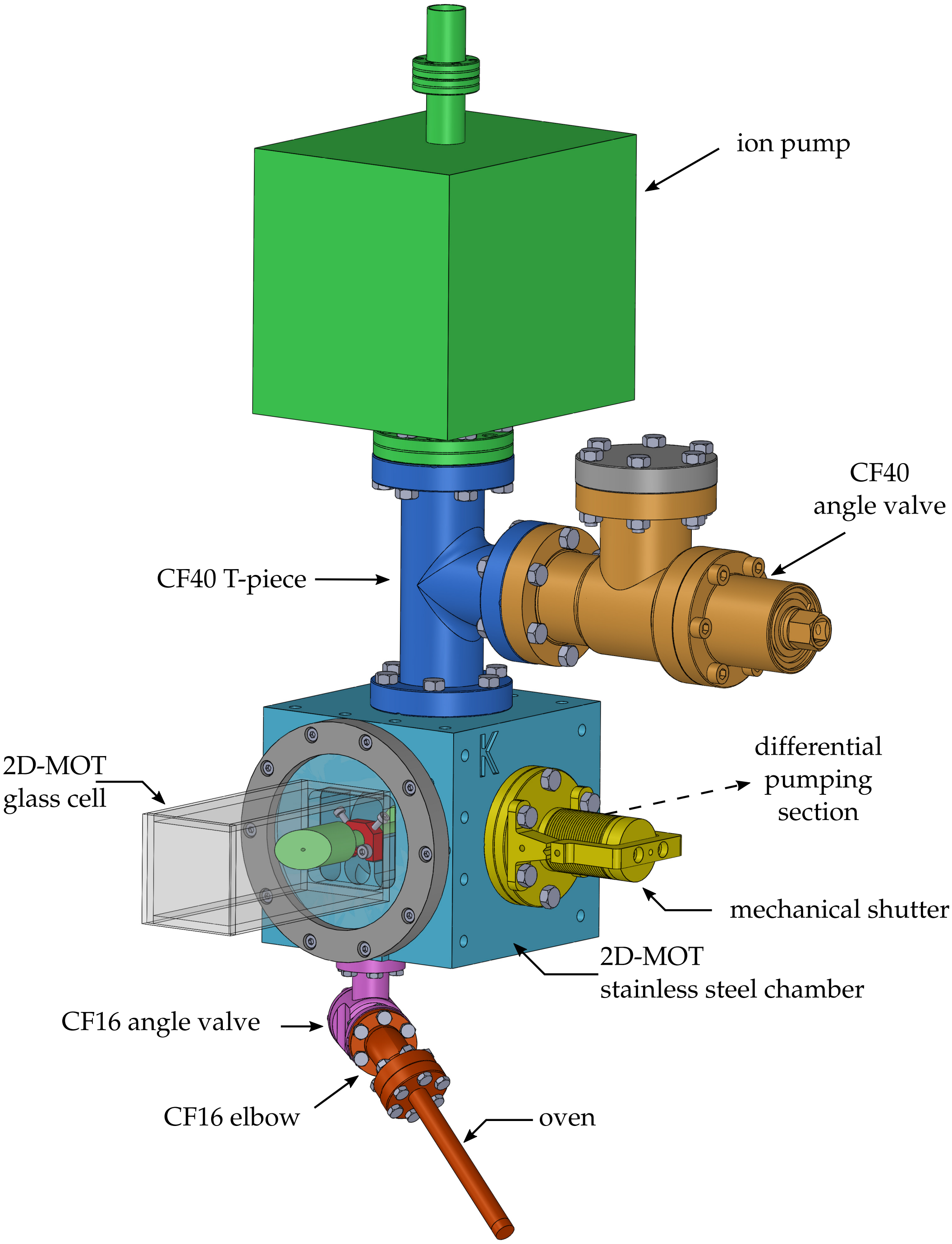

Figure 6.6.: Overview of the potassium 2D-MOT chamber setup. The glass cell of the potassium 2D-MOT chamber is oriented horizontally and mounted to the front facet of the 2D-MOT stainless steel chamber. The latter incorporates several components to maintain vacuum within the 2D-MOT chamber and to operate the potassium 2D-MOT. These components include an ion pump, a CF40 angle valve, a mechanical shutter, a CF16 angle valve, a CF16 elbow, and an oven. The 2D-MOT vacuum chamber attaches to the differential pumping section at the rear side of the stainless steel chamber.

viewports[9,10] are installed (see Fig. 6.4). The CF200 viewports have an inwards recession of $27\,\mathrm{mm}$, a clear view of $153\,\mathrm{mm}$, and are made out of AISI 316LN/316L austenitic stainless steel. The technical drawing of the CF200 viewports is given in Appendix C.2.

Inside the main chamber, four straight rod electrodes in rectangular configuration are capable of generating electric fields with field strengths of up to $20\,\mathrm{kV/cm}$ [Grö16]. The electrodes are held in place by home-built groove grabbers, which are clamped to grooves running along the inner wall of the main chamber. Figure 6.5 shows the rod electrodes within the main chamber. The grooves to which the groove grabbers are mounted are pointed out in Fig. 6.4. The rod electrodes are isolated against the groove grabbers and the main chamber by home-built Macor® isolators. Kapton-insulated copper wires connect the rod electrodes to electrical feedthroughs at the pumping section (see Sec. 6.3.5).

To generate magnetic fields with field strengths of more than 1000 G (with 1 G = 10^{-4} T), the K$-$Cs apparatus includes several magnetic coils. The design of the magnetic coils and their function within the experimental sequence is described in Ref. [Grö17a]. The magnetic coils are externally mounted to the main chamber. To reduce the spatial separation of the coils and thus the electric current needed to generate the mentioned field strengths, the coils are sunk within the inverted CF200 viewports.

6.3.2. 2D-MOT Vacuum Chambers

The 2D-MOT vacuum chambers for potassium and cesium are copies of each other and nearly identical. We therefore concentrate on the description of the potassium 2D-MOT vacuum chamber in the following and refer to the cesium 2D-MOT chamber where necessary.

Figure 6.6 shows an overview of the potassium 2D-MOT chamber setup. The central parts of the potassium 2D-MOT vacuum setup are a glass cell and a home-built stainless steel chamber. The back facet of the 2D-MOT stainless steel chamber connects to the differential pumping section via a CF50 flange. The opposing front facet accepts the 2D-MOT glass cell. While the 2D-MOT glass cell offers optical access for laser beams to create a 2D-MOT in it, the stainless steel chamber acts as a socket for the 2D-MOT glass cell. The 2D-MOT stainless steel chamber was milled out of a monolithic block of stainless steel grade AISI 304[11]. It has outer dimensions of $118 \times 118 \times 120\,\mathrm{mm}$.

To operate the 2D-MOT vacuum chamber setup, the stainless steel chamber provides several CF flanges for installing vacuum components as depicted in Fig. 6.6. On top of the stainless steel chamber, a CF40 tee includes a CF40 angle valve[12] for initial pumping with a turbo pump and an ion pump[13] for vacuum maintenance. A CF40 mechanical shutter, which is mounted horizontally to the stainless steel chamber in Fig. 6.6, can be used to control the particle flux from the 2D-MOT chamber to the main chamber. On the bottom side of the stainless steel chamber, a CF16 angle valve[14] connects to a CF16 elbow and a stainless steel tube that are mounted in series. The tube is $95\,\mathrm{mm}$ long, $10\,\mathrm{mm}$ wide, and has a wall thickness of $0.5\,\mathrm{mm}$.

---

[9] Manufactured by UKAEA, Oxfordshire, United Kingdom. Optical specifications: Quartz material is Spectrosil 2000 by Heraeus, transmitted wavefront error < $\lambda/4$, thickness of $10\,\mathrm{mm}$, parallelism $\leq 3'$, index of refraction homogeneity $\leq 10\,\mathrm{ppm}$.

[10] The inverted CF200 viewports were left uncoated in order not to be affected in future experiments by wavelength limitations resulting from the anti-reflection coating and for cost reasons.

[11] Magnetic permeability $\mu_r \leq 1.3$ [Vaca].

[12] VAT, Easy-close all-metal angle valve, CF40, Series 541.

[13] Agilent Technologies, VacIon Plus 20, StarCell.

[14] VAT, Easy-close all-metal angle valve, CF16, Series 541.

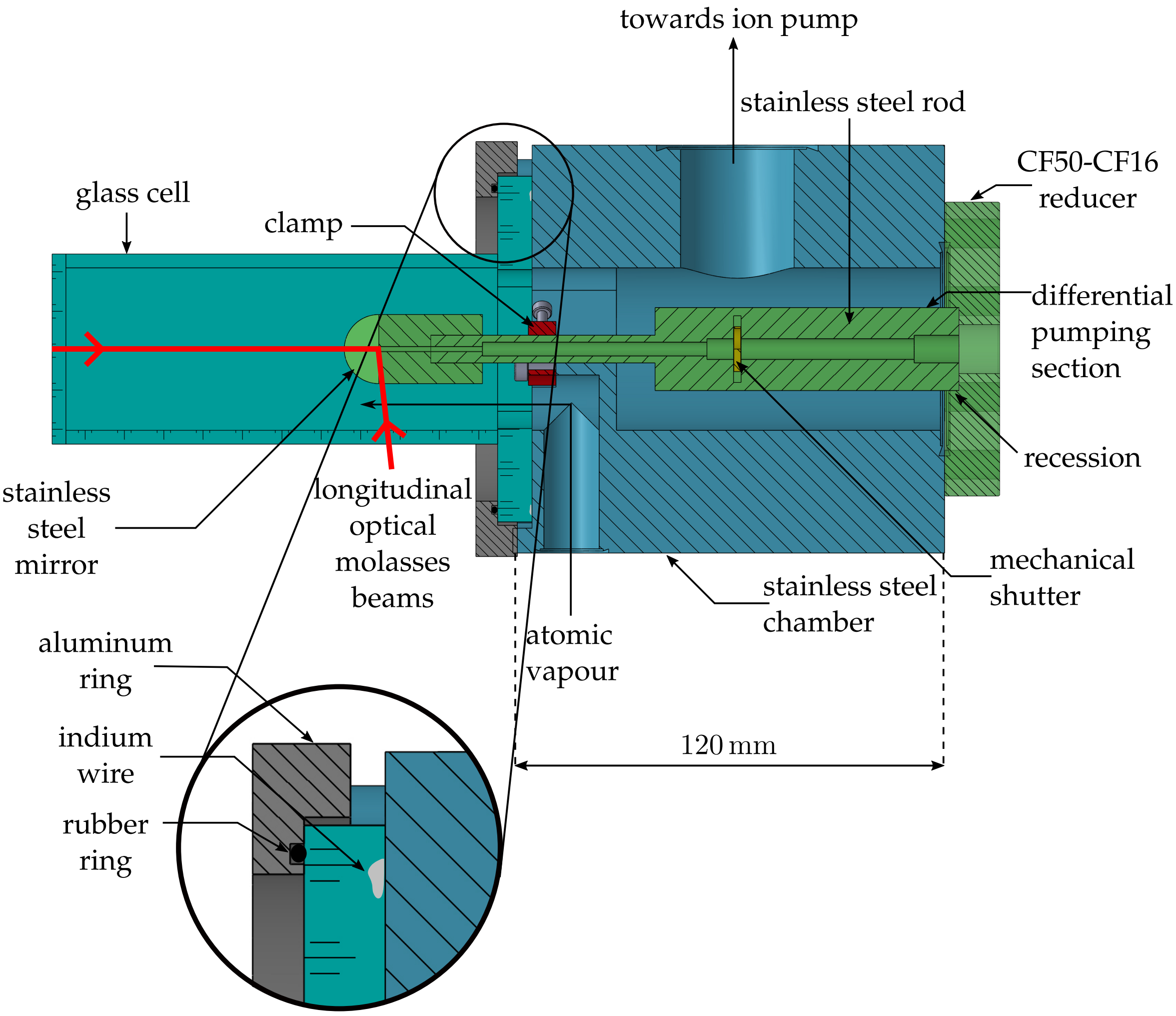

Figure 6.7.: Vertical cut of 2D-MOT chamber. The inside of the 2D-MOT chamber houses several parts: the stainless steel mirror and a subsequent stainless steel rod (both belong to the differential pumping section (green color)) are secured against slipping out of position by a clamp and a recession within the CF50 flange. The stainless steel mirror facilitates to overlap counterpropagating laser beams (red arrows) in longitudinal direction. A mechanical shutter intersects the differential pumping section and blocks the atomic beam from the 2D-MOT if in closed position and otherwise clears the passage. The sealing mechanism between the glass cell and the stainless steel chamber is illustrated in the inset: the glass cell flange sits on a circumferential indium wire layed out on the sealing surface of the stainless steel chamber. An aluminum ring encloses the glass cell flange. As the screws of the aluminum ring are tightened, the glass cell is pressed against the stainless steel chamber and the indium wire is compressed. A rubber ring reduces potential stress in the glass cell flange.

The stainless steel tube contains two commercial, vacuum sealed pyrex ampoules[15] filled with potassium. Each ampoule contains approximately 15 mg of potassium, which is enriched to $9\,\%$ of the isotope ^{40}K. We piled two ampoules on top of each other. By compressing the stainless steel tube with pliers one breaks the ampoules. After having broken the first ampoule, the solid potassium sample within the ampoule starts to sublimate and thus feeds the 2D-MOT chamber with vapour of atomic potassium. To increase the partial pressure of potassium within the 2D-MOT chamber, the stainless steel tube is heated by externally mounted heating wires and thereby acts as potassium oven. The potassium vapour is guided into the 2D-MOT glass cell through the CF16 elbow, the CF16 angle valve, and two perpendicular drillings in the stainless steel chamber. The two drillings are pointed out in Fig. 6.7 by an arrow.

Similarly, for the cesium 2D-MOT chamber, we use two vacuum sealed ampoules of cesium[16]. Here, each glass ampoule contains 1 g of cesium with a purity of $99.98\,\%$. The stainless steel tube for the cesium ampoules is $134\,\mathrm{mm}$ long and $14\,\mathrm{mm}$ wide.

Figure 6.7 shows a vertical cut of the 2D-MOT chamber and gives an overview of the components that are mounted within the chamber. A custom-made stainless steel cylinder[17] with a diameter of $20\,\mathrm{mm}$ and a length of $40\,\mathrm{mm}$ extends into the 2D-MOT glass cell. The cylinder is cut under an angle of $45°$ relative to its symmetry axis. To obtain a polished and thus reflecting cut surface, the cut surface is diamond-machined. The reflecting surface can be used to reflect and overlap laser beams that propagate parallel or antiparallel to the atomic beam generated by the 2D-MOT. In this way it is possible to add an unbalanced optical molasses in the longitudinal direction of the 2D-MOT and thereby create a so-called $2\mathrm{D}^{+}-$MOT [Die98]. Figure 6.7 depicts the two longitudinal optical molasses beams within the glass cell. A drilling along the axis of the stainless steel cylinder (stainless steel mirror) with $1.5\,\mathrm{mm}$ diameter allows the atomic beam from the 2D-MOT to enter the differential pumping section towards the main chamber. Atoms that move fast in longitudinal direction spend little time within the 2D-MOT and are therefore not cooled sufficiently in the transverse directions [Die98]. These atoms collide with the stainless steel mirror and are rejected from entering the differential pumping section. The drilling aperture of the stainless steel mirror thus acts as a filter for the transverse and longitudinal velocity of the atoms in the atomic beam [Die98, Rid11a]. The usage of stainless steel as material for the mirror within the 2D-MOT glass cell excludes the risk of potential chemical reactions with potassium and cesium. A diamond-polished stainless steel mirror, however, comes at the expense of comparatively high costs.[18] A technical drawing of the stainless steel mirror is shown in Appendix C.3.

The 2D-MOT glass cell[19] is custom-made. It consists of a glass cell body that merges into a round glass disk. Figure 6.8 shows a schematical drawing of the 2D-MOT glass cell. The glass cell body has a 55×55 mm quadratic cross-section. It is built up of five rectangular $4\,\mathrm{mm}$-thick fused silica substrates that are optically contacted to each other. The overall length of the glass cell is $139\,\mathrm{mm}$. This length is long enough to substantially vary the width of the transverse 2D-MOT laser beams for optimization of the atomic beam flux. The glass substrates are polished

---

[15] Precision Glassblowing of Colorado, U.S.A. The ampoule size is approximately $7\,\mathrm{mm}$ (outer diameter) x $25\,\mathrm{mm}$ (length).

[16] Alfa Aesar GmbH, Karlsruhe, Germany.

[17] Made out of stainless steel 1.4432 by Kugler GmbH, Salem, Germany.

[18] An alternative solution for the 2D-MOT mirror has been realized within the dysprosium-potassium experiment of the Grimm group in Innsbruck. In this experiment, a commercial, silicon dioxide protected mirror with a hole has been used and so far no complications have been reported.

[19] Manufactured by Hellma GmbH, Müllheim, Germany.

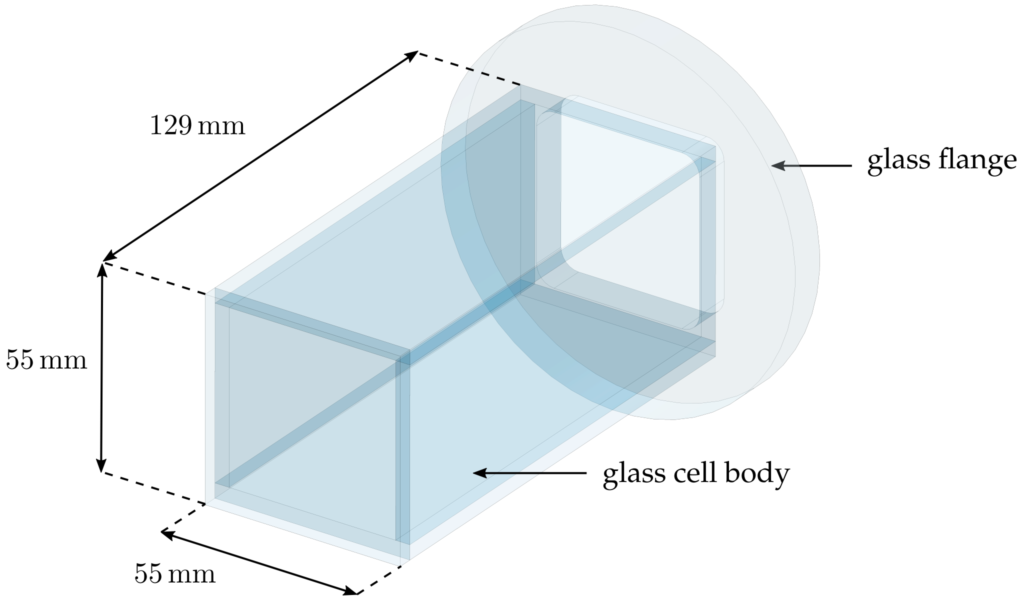

Figure 6.8.: 2D-MOT glass cell. The 2D-MOT glass cells consist of a cuboid glass cell body that merges into a round glass disk. The glass disk acts as a glass flange.

to have a transmitted wavefront error[20] of equal to or smaller than $\lambda/4$. To avoid potential complications resulting from chemical reactions of the atomic vapour and an in-vacuo coating, we opted for uncoated glass substrates. The glass disk of the glass cell has an outer diameter of $100\,\mathrm{mm}$, is $10\,\mathrm{mm}$ thick, and acts as a glass flange.

We mount the glass cell to the 2D-MOT stainless steel chamber by pressing the glass flange of the glass cell against the front facet of the stainless steel chamber. In contrast to other groups, which glue their 2D-MOT windows to a titanium 2D-MOT chamber [Cat06] or have a glass cell with welded glass-metal transition [Rid11b], we use an indium wire to achieve a vacuum compatible glass-metal transition. Indium sealings have several advantages over other sealings e.g. a comparatively small force needed for compression, being less susceptible to mechanical shock, and being more compact [ESP]. Indium as glass-metal transition has also been used in another ultracold atom experiment [Ueh08]. An indium wire[21] layed out in a circle with its two ends overlapping creates a reliable glass-metal transition[22] when compressed. To press the glass flange gently against the stainless steel chamber, an aluminum ring encloses the glass flange. By tightening ten M4 screws, the indium wire is compressed and the glass cell is fixed. To avoid stress-induced cracking of the glass flange, a rubber ring is placed in a groove between the aluminum ring and the glass flange. The inset of Fig. 6.7 depicts the mounting mechanism of the 2D-MOT glass cell. A technical drawing of the 2D-MOT glass cell is given in Appendix C.4. During the assembly of the 2D-MOT chamber leaks at the glass-metal transition occurred. It turned out that the surface roughness of the glass flange sealing surface was too large and thus undermined the sealing. To achieve a proper sealing, the sealing surface of the glass flange was manually re-polished with polyurethane foil and cerium oxide based

---

[20] Wavefront deformation measured over a circular area of $20\,\mathrm{mm}$ diameter.

[21] ESPI Metals, Oregon, U.S.A, $1.52\,\mathrm{mm}$ diameter and purity of $99.999\,\%$.

[22] Indium is widely known for creating reliable and leak-proofed seals between glass and metal. Unlike other sealants that just form a barrier, indium also seals by forming a chemical bond between itself and the surfaces to be connected [ESP].

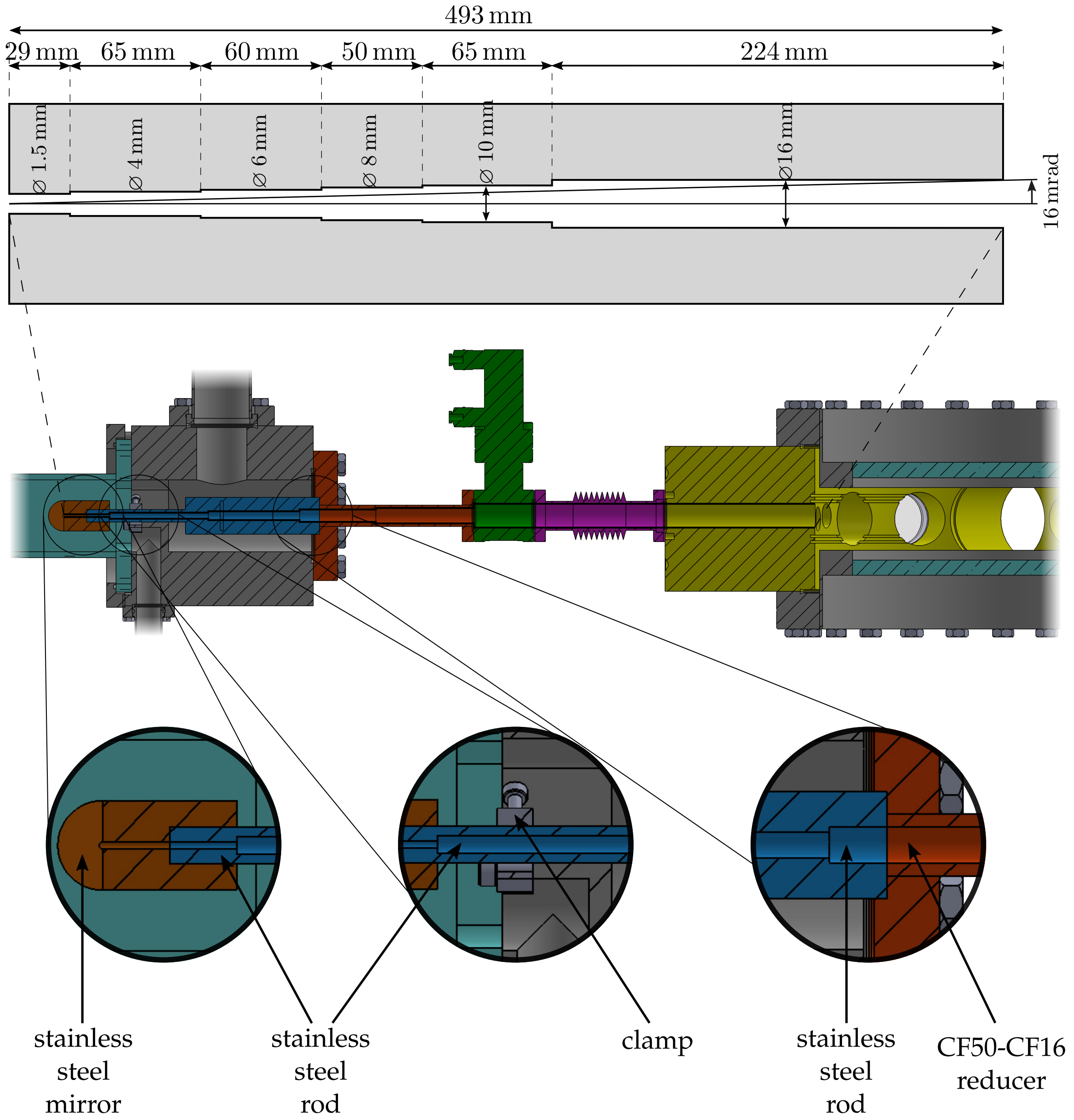

Figure 6.9.: Differential pumping section. The upper part of the Figure shows the inner profile of the DPSs. Each of the two DPSs is made up of five components, which are shown in the middle of this Figure: a stainless steel mirror (brown), a stainless steel rod (blue), a CF50-to-CF16 straight connector (orange), a CF16 gate valve (green), and a CF16 bellow (purple). The lower part of the Figure depicts the connection of the stainless steel mirror to the stainless steel rod. The stainless steel rod is clamped to the stainless steel chamber on the left side and is held by a recession in the CF50 flange on the right side.

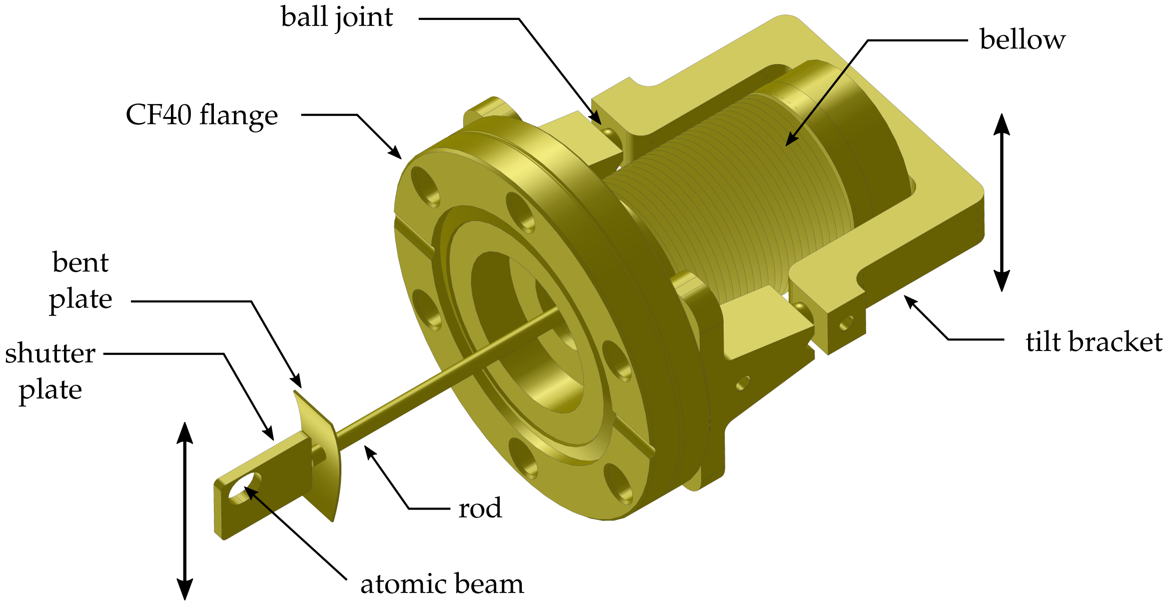

Figure 6.10.: Mechanical shutter. The mechanical shutter disrupts the atom flux between the 2D-MOT chamber and the main chamber. The shutter uses a tilting mechanism that relies on a flexible bellow and a ball joint. If the tilt bracket is moved upwards (vertical black arrow) this movement translates into a downmove of the shutter plate, which is welded to a rod. The shutter plate then frees the path towards the main chamber. In the opposite case of an downward move of the tilt bracket, the atom flux is blocked. A bent plate helps to cover the differential pumping section.

glass polishing slurry provided by Hellma.

6.3.3. Differential Pumping Sections

Two differential pumping sections (DPSs) connect the potassium and cesium 2D-MOT chambers to the main chamber. The DPSs run partially inside and partially outside the 2D-MOT chambers. Figure 6.9 depicts the inner and outer part of a DPS. The DPSs have a tubular shape through which the atomic beams from the 2D-MOTs can travel into the main chamber. In order to prevent pressure equalization between the 2D-MOT chambers and the main chamber, the DPSs are designed to maintain a pressure ratio of $\sim 10^5$ [Jou13]. The top of Fig. 6.9 shows the design of the DPSs, which is identical for the K and Cs DPSs. The total length of each DPS is $493\,\mathrm{mm}$ and the inner diameter increases stepwise from $1.5\,\mathrm{mm}$ to $16\,\mathrm{mm}$ towards the main chamber. In a previous experiment, the divergence of a potassium atomic beam emitted from a potassium 2D-MOT was measured to be $(34 \pm 6)\,\mathrm{mrad}$ [Cat06]. We therefore designed our DPSs to allow the potassium and cesium atomic beams for a comparable divergence of around $32\,\mathrm{mrad}$ $(1.86°)$.

We realize each DPS by joining five tubular vacuum parts in a row. The bottom of Fig. 6.9 shows the five vacuum parts in different colors. The first part is the stainless steel mirror (brown) within the 2D-MOT chamber. The mirror is attached to a stainless steel rod (blue) that has a drilling along its cylinder axis. The third part of the DPSs is a CF50-to-CF16 straight

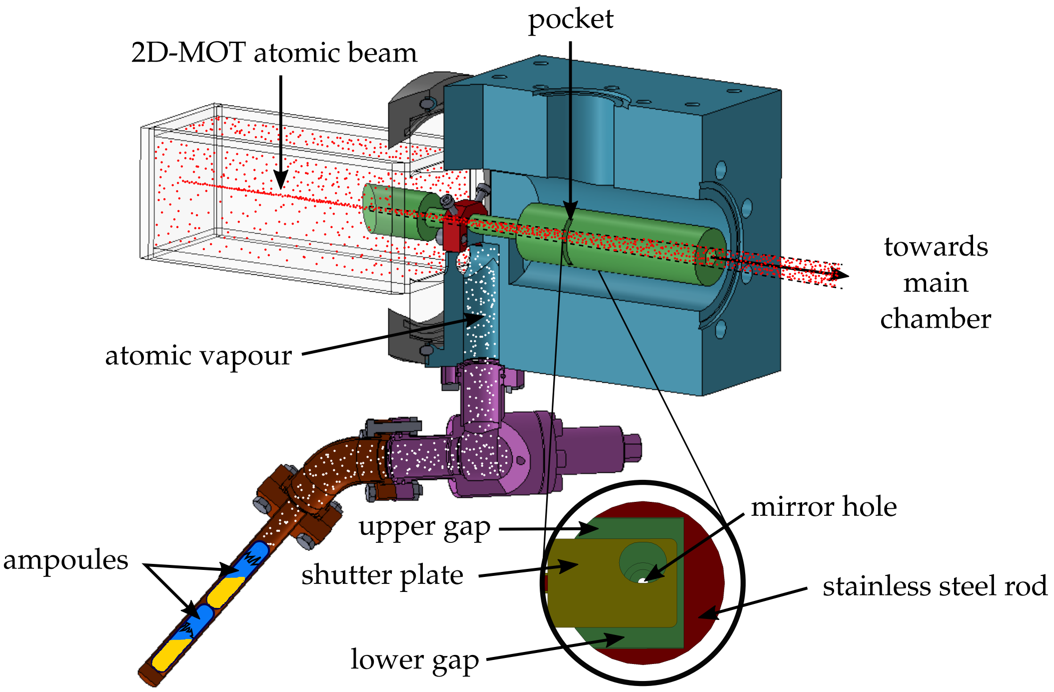

Figure 6.11.: Atomic motion within the 2D-MOT chamber. The atomic vapour (white and red circles) released from the broken glass ampoules within the oven feeds the 2D-MOT in the glass cell. Atoms that have been cooled by the 2D-MOT access the DPS and move towards the main chamber. The dashed lines indicate the divergence of the atomic beam. To control the atom flux, the mechanical shutter protrudes into the horizontal pocket of the stainless steel rod (shown in the inset in half-open half-closed position) producing an upper and a lower gap.

reducer (orange), followed by a pneumatic CF16 gate valve[23,24] (green), and a custom-made CF16 bellow[25] (purple). The connection of the stainless steel mirror to the stainless steel rod relies solely on friction. The stainless steel rod is mechanically clamped to the chamber on the left end in Fig. 6.9 and rests inside a recession of the CF50 flange on the right end. The rod has a transversal pocket that allows the mechanical shutter to block the atomic beam. The technical drawings of the stainless steel rod and the CF50-to-CF16 reducer are given in Appendix C.5 and Appendix C.6.

6.3.4. Mechanical Shutter

Figure 6.10 depicts a mechanical shutter of the 2D-MOT chambers. The shutter consists of a rod that extents into the stainless steel chamber. The rod is welded to the end cap of a flexible bellow on one side and carries a plate with a hole on the other side. By moving a tilt bracket of a ball joint with an external servo motor, the shutter can be moved up and down, i.e.

---

[23] Lesker, CF16 pneumatic gate valve, SG0063PCCF.

[24] The pneumatic CF16 gate valves rely on fluorocarbon o-ring seals and have been chosen over all-metal valves because of cost reasons. For future experiments, the exclusive usage of all-metal angle valves is recommended.

[25] Manufactured by Vacom Vakuum Komponenten & Messtechnik GmbH.

can be toggled between an open and a closed position. If the shutter is in open position, the atom beam from the 2D-MOT can leave the 2D-MOT chamber through the circular hole of the shutter plate towards the main chamber. If the shutter is in closed position, the shutter plate blocks the atomic beam towards the main chamber.[26]

Figure 6.11 shows a section view of the potassium 2D-MOT chamber and points out the working principle of the mechanical shutter. Since the atomic beam axis of the 2D-MOT is aligned with the hole of the stainless steel mirror and thus centered to the DPS, atoms can travel through the DPS. The shutter reaches into the pocket of the stainless steel rod and either blocks the atomic beam or clears the passage. To hinder background gas from entering the DPS through the gaps above and below the shutter plate shown in Fig. 6.11, the bent metal plate of the mechanical shutter (see Fig. 6.10) covers these gaps.

6.3.5. Vacuum Pumps Section

The vacuum pumps section serves to maintain the ultra-low pressure in the main chamber and thus incorporates different vacuum pumps. Figure 6.12 gives an overview of the pumping section. The vacuum pumps are centered around a standard CF100 cube[27] that joins to the back of the main chamber via a CF100-to-CF63 conical reducer. To pump non-getterable gases, we connect an ion pump[28] with $75\,\mathrm{L/s}$ pumping speed to the cube and use a titanium sublimation (TiSub) cartridge[29] to pump active gases such as hydrogen. The cartridge reaches into a CF100 straight connector[30]. When the cartridge is fired, the inner surface ($\sim 1500\,\mathrm{cm}^2$) of the straight connector and a subsequent CF100 elbow[31] is covered with titanium. Assuming a hydrogen pumping speed of $3.1\,\mathrm{L/s}$ per square centimeter for titanium [Agi], the titanium-coated surface has a pumping speed of $\sim 4650\,\mathrm{L/s}$. The effective pumping speed at the main chamber is limited by the intermediate tubing. On the left and right side of the CF100 cube in Fig. 6.12 two electrical feedthroughs[32] with in total four connectors enable the application of voltages up to $20\,\mathrm{kV}$ to the rod electrodes inside the main chamber. A CF40 cross[33] provides a CF40 angle valve[34] for initial pumping of the main chamber, a pressure ion gauge[35] as well as a CF40 viewport[36] with anti-reflection coating of type 'A' (see Sec. 6.3.1) for the absorption imaging laser beam.

6.4. Compensation Coils

We use magnetic coils to cancel dc magnetic stray fields at the position of the atoms within the main chamber. Static magnetic stray fields result from the earth magnetic field as well as

---

[26] The mechanical shutter is similar to the shutter of the erbium experiment of the Ferlaino group in Innsbruck. It was designed in cooperation with our mechanical workshop and manufactured by the latter.

[27] Home-built by our mechanical workshop.

[28] Agilent Technologies, VacIon Plus 75, StarCell.

[29] Agilent Technologies, Titanium sublimation pump filament cartridge.

[30] Vacom, CF100 straight connector, SC100R-304.

[31] Vacom, CF100 elbow, EL100R-316LNS.

[32] Lesker, SHV-20 electrical feedthrough, IFTXE021153.

[33] Vacom, CF40 cross, X40R-304.

[34] VAT, Easy-close all-metal angle valve, CF40, Series 541.

[35] Agilent Technologies, UHV-24p ion gauge with two tungsten filaments.

[36] Viewport was manufactured by Larson Electronic Glass, California, U.S.A. Optical specifications: Corning HPFS 7980, homogeneity grade 0, inclusion class A. Transmitted wavefront error $< \lambda/4$ at $632\,\mathrm{nm}$, parallelism $< 10''$. Flange specifications: Stainless steel AISI 316LN, non-magnetic titanium sleeve for glass-metal transition.

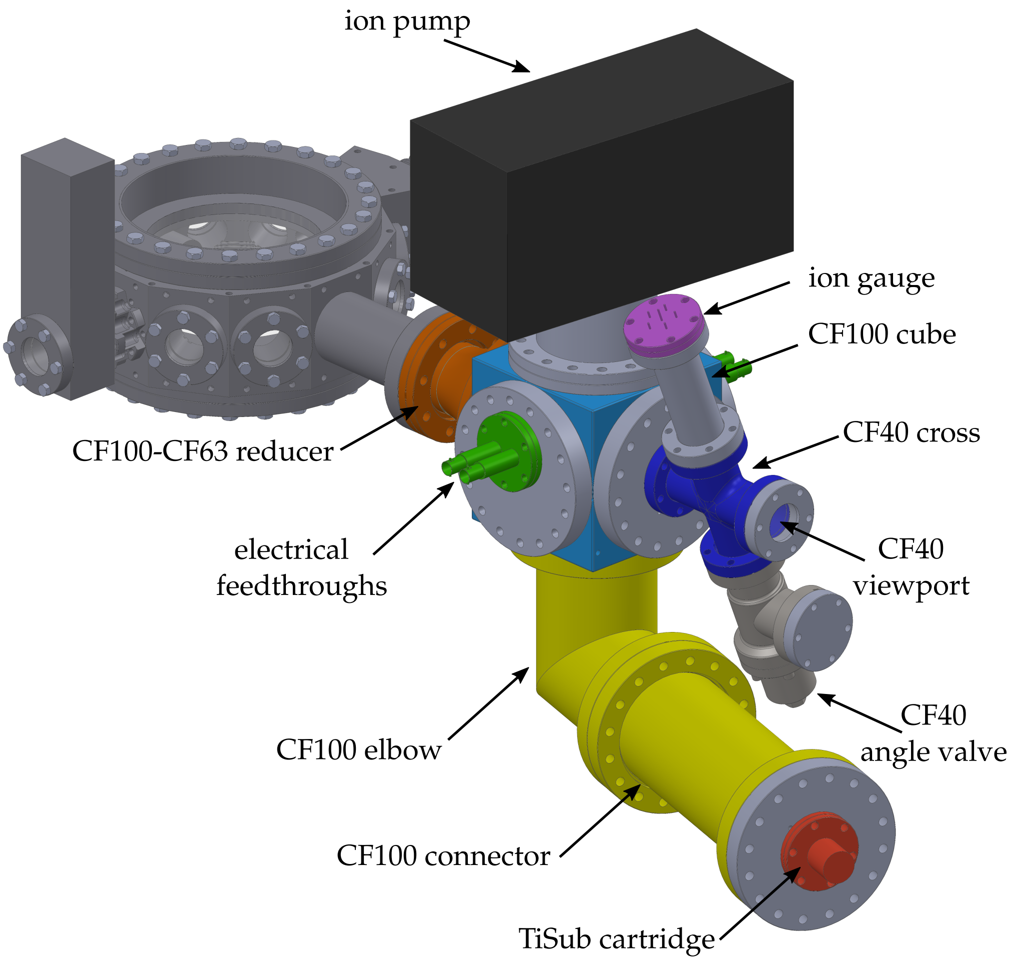

Figure 6.12.: Vacuum pumps section. A CF100 cube (light blue) forms the center of the vacuum pumps section and connects to an ion pump (black), two electrical feedthroughs (green), and a CF100 elbow with a CF100 straight connector (yellow). The straight connector houses a titanium sublimation filaments cartridge (red). Furthermore, a CF40 cross (dark blue) incorporates a pressure ion gauge (purple), a CF40 angle valve, and an anti-reflection coated CF40 viewport. The pumping section is attached to the main chamber via a CF100-to-CF63 conical reducer (orange).

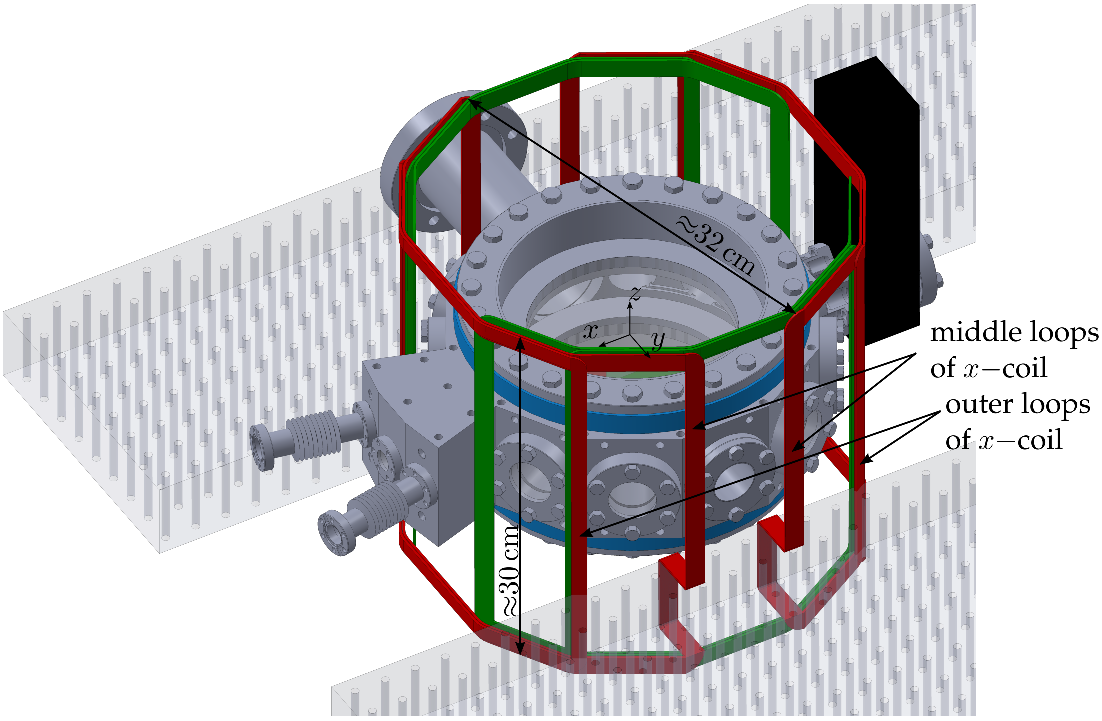

Figure 6.13.: Schematics of the compensation coils around the main chamber. The $z-$compensation coil is shown in blue color, while the $x-$ and $y-$compensation coils are marked in red and green color, respectively. The ribbon cables of the $x-$ and $y-$compensation coils are guided and held by a scaffold of stainless steel rods and aluminum mounts that are not shown here. The layering of the coil loops is altered in the Figure for illustrative reasons. The middle loops of the $x-$coil are partially deformed on the front and back side of the main chamber to go around the optical breadboards.

from nearby laboratory components such as the permanent magnets of the ion pumps. We employ in total three different magnetic coils (*compensation coils*), one for each spatial direction. The three coils can be addressed individually. Since the compensation coils are centered around the main chamber and mechanically screwed to it, we consider them as part of the main vacuum chamber. In this Section we describe the design of the compensation coils, their implementation to the main chamber, and calculate the magnetic field generated by the coils.

6.4.1. Compensation Coil for the $z-$direction (Helmholtz-Like Coil)

We realize the compensation coil for the $z-$axis by winding flat ribbon cables[37] around the flanges of the lower and upper CF200 viewports of the main chamber. Figure 6.13 illustrates the implementation of the $z-$compensation coil to the main chamber. For each viewport, we take a separate flat ribbon cable and wind it twice around. We connect the individual poles of the flat ribbon cable of each viewport into series, i.e. we connect the end of pole i (with $i = 1, 2, \ldots 13$) to the beginning of pole $i+1$ of the same cable. The wire connections are done via D-sub connectors. By means of this serial wiring, we obtain two solenoids, one at each viewport. We use the unconnected beginning of pole 1 of each solenoid as current input and

---

[37] Ribbon cable with 14 poles and wire gauge 26AWG.

the unconnected end of pole 14 as current ouput. Each solenoid now effectively consists of a single wire that is wound around the flange and has 28 windings. The flanges of the CF200 viewports have an outer radius of $127\,\mathrm{mm}$ and are $95\,\mathrm{mm}$ apart from each other (see Fig. 6.4). Taking into account the $17\,\mathrm{mm}$-width of the ribbon cable, the centers of the two solenoids are separated by $112\,\mathrm{mm}$ from each other along the vertical axis. The solenoid separation is nearly as large as the solenoid radii and thus the $z-$compensation coil is close to the Helmholtz configuration.

To determine the strength of the magnetic field $\vec{B}(\vec{r})$ that is generated by the Helmholtz-like coil at the position of the atoms, we perform a finite-element simulation of the magnetic field. Since the position of the atoms within the main chamber coincides with the geometrical center of the main chamber, we define the center of the main chamber to be the origin of a local coordinate system. The $x-$, $y-$, and $z-$ directions of the local coordinate system are defined in Fig. 6.13. We use COMSOL Multiphysics 5.3a as simulation software. In the simulation we assume an input current for the $z-$compensation coil of $1\,\mathrm{A}$. Figure 6.14 shows the calculated magnetic field strength $B(x,y,z) = |\vec{B}(\vec{r})|$ along the $x-$, $y-$, and $z-$ directions. At the center of the main chamber, the magnetic field strength is $B_0^{\text{HHL,sim}} = 2.08(5)$ G, where the number in brackets denotes the estimated uncertainty of the simulated magnetic field strength. The uncertainty results from the finite computational domain and the internal convergence criterion of the simulation. It is estimated to be $2\,\%$ of the magnetic field strength. To quantify the field homogeneity around the origin, we fit harmonic functions of the form $B^{\text{HHL}}(x) = B_0^{\text{HHL}} + B_2^{\text{HHL}}x^2$ to the numerical data. Since the $z-$compensation coil is cylindrically symmetric, it is sufficient to specify B_2^{HHL} for the $x-$ and $z-$ direction. For each of these two directions, the fit range is chosen to be $-3\,\mathrm{mm}< x, z <3\,\mathrm{mm}$, yielding some tens of data points for the fit. We obtain $B_2^{\text{HHL},x} = 3.2(2) \times 10^{-5}$ G/mm^2 and $B_2^{\text{HHL},z} = -2.66(6) \times 10^{-5}$ G/mm^2. Here, the numbers in brackets are the fit errors.

6.4.2. Compensation Coils for the $x-$ and $y-$directions (Birdcage Coils)

We use two magnetic coils to cancel horizontal magnetic field components around the center of the main chamber. To understand the design of the $x-$ and $y-$compensation coils, we first explain the underlying concept of their design.

Birdcage Coil

We consider a circular cylinder with radius R and length L. For the moment we choose the length of the cylinder to be infinite. On the surface of that infinitely long cylinder, an electrical surface current I_S flows along the axial direction $\vec{e}_z$ of the cylinder. We assume that the associated *surface current density* $\vec{j}$ depends on the cylindrical coordinate azimuth angle θ. Figure 6.15 (a) illustrates the situation and defines the angle θ. If the surface current density $\vec{j}(\theta)$ is given by [Jac99b]

$$\vec{j}(\theta) = \frac{I_\text{S}}{2R}\cos(\theta)\vec{e}_z, \tag{6.1}$$

the surface current I_S generates a perfectly uniform, transverse magnetic field $\vec{B}$ inside the cylinder [Jac99b, Nou13]. The magnetic field $\vec{B}$ within the cylinder is antiparallel to the $x-$di-

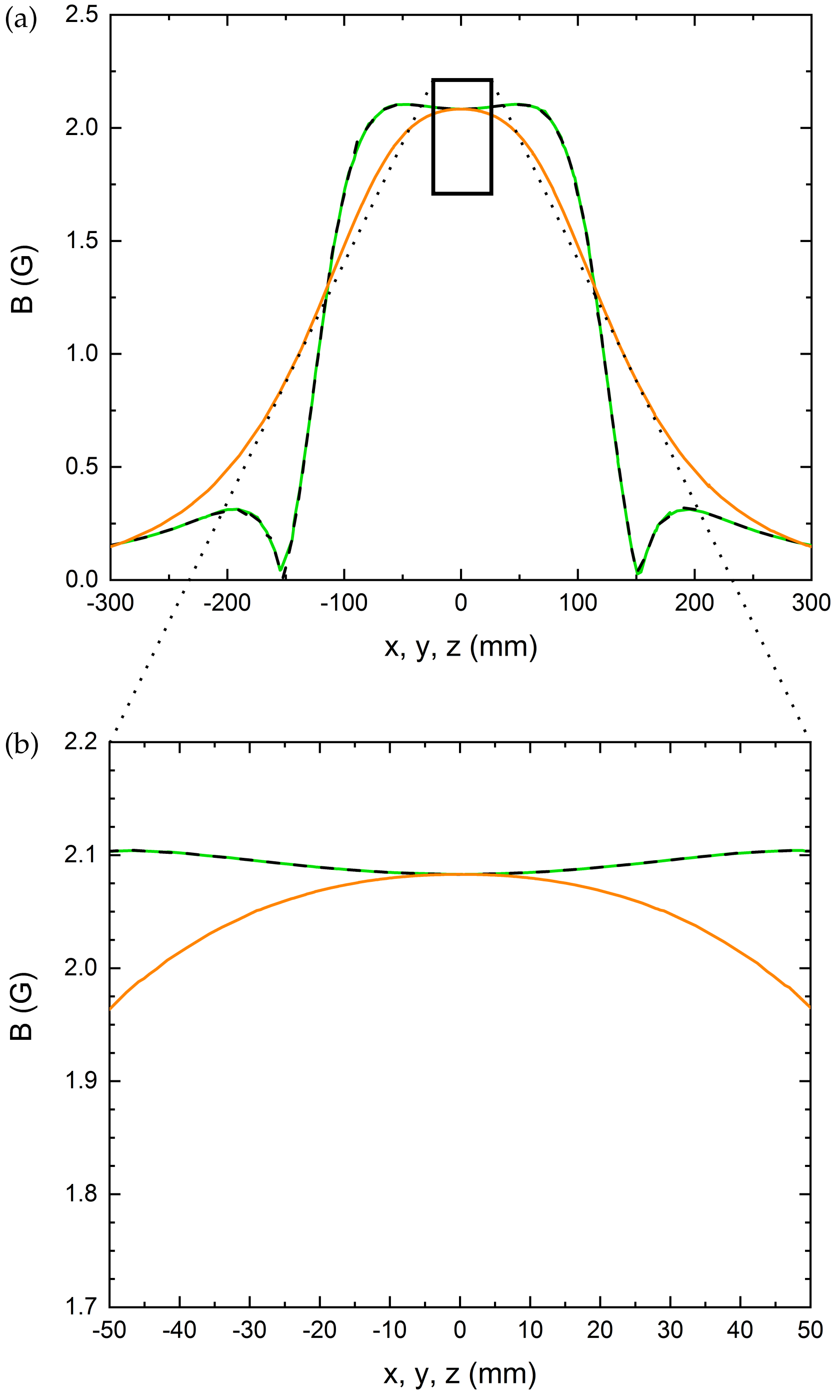

Figure 6.14.: Magnetic field strength of the $z-$compensation coil. (a) Calculated magnetic field strength B along the $x-$ (green), $y-$ (black), and $z-$axis (orange). (b) Zoom into plot (a).

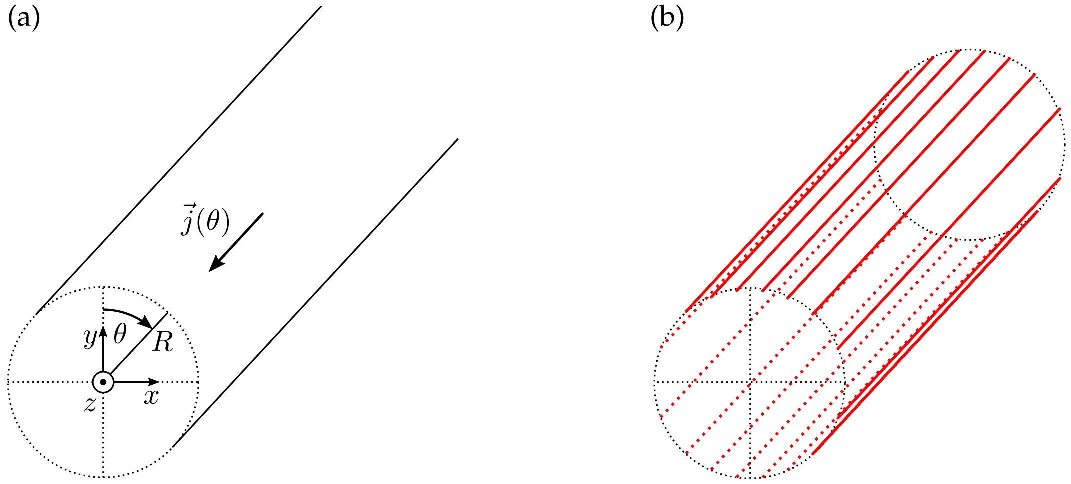

Figure 6.15.: Cosine-theta coil. (a) Ideal cosine-theta coil with radius R, infinite length, and continuous surface current density $\vec{j}(\theta)$. (b) Schematic diagram of a discretized cosine-theta coil with $4N_{\text{wires}} = 16$ wires placed on the cylinder surface.

rection, i.e. $\vec{B} = -B_0\vec{e}_x$, and has a field strength B_0 given by [Jac99b]

$$B_0 = \frac{\mu_0 I_{\text{S}}}{4R}, \tag{6.2}$$

where μ_0 is the *magnetic constant*. A cylinder with a surface current density $\vec{j}(\theta)$ like that given in Eq. (6.1) is known as ideal *cosine-theta coil*. Owing to the (non-realistic) continuous surface current density distribution $\vec{j}(\theta)$ and the infinite length, realization of an ideal cosine-theta coil is not possible. In order to construct a cosine-theta coil, approximations have to be made to the ideal coil design. Common approximations involve discretization of the surface current density $\vec{j}(\theta)$ and replacement of the infinitely long coil by a coil of finite length [Nou13, Bid05, Bol88].

The discretization of the surface current density $\vec{j}(\theta)$ is achieved in practice with conducting wires. The wires are oriented parallel to the cylinder axis and enclose the cylindrical volume. Figure 6.15 (b) illustrates the discretization of $\vec{j}(\theta)$. The discretized cosine-theta coil contains $N_{\text{wires}} \in \mathbb{N}^+$ wires per quadrant. Figure 6.16 shows a cross-section of a discretized cosine-theta coil with $N_{\text{wires}} = 4$. To imitate the original $\cos(\theta)$ surface current density, the wires are positioned such that their projections onto the $x-$axis are equidistant [Nou13, Bid05, Bol88]. The wires $i \in \{1, 2, 3, 4\}$ of the first quadrant must then be placed at angles θ_i defined by the relation [Bid05]

$$\theta_i = -\arcsin\left(1 - \frac{2i-1}{2N_{\text{wires}}}\right). \tag{6.3}$$

The angular positions θ of all $4N_{\text{wires}}$ wires are then given by $\theta = \pm\theta_i$ and $\theta = 180° \pm \theta_i$ and their projections onto the $x-$axis are equidistant.

If the wires of a discretized, finite-sized cosine-theta coil are joined pairwise on both ends of the coil (see Fig. 6.16), the wires form closed, rectangular loops. The discretized cosine-theta coil then takes the form of a birdcage and is thus known as *birdcage coil*. To improve the

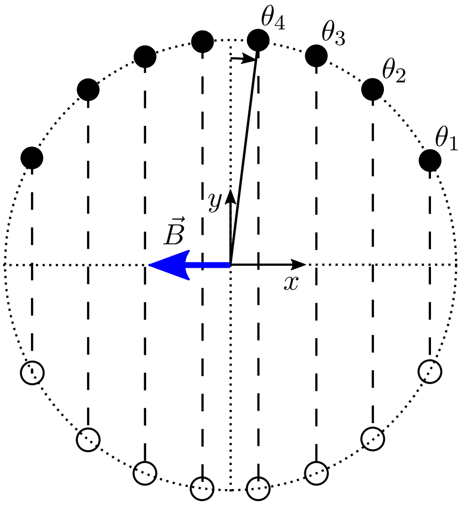

Figure 6.16.: Discretized cosine-theta coil. The wires of a discretized cosine-theta coil are nonuniformly placed on the cylinder surface at angles θ. Their projections onto the $x-$axis yield equidistant spacings along the diameter. The current in the wires of the upper half of the cylinder (solid circles) flows in $+z$-direction and in the opposite direction in the wires of the lower half of the cylinder (empty circles). If the upper wires are joined (dashed lines) pairwise with the lower wires on both ends of the cosine-theta coil, the wires form rectangular, closed loops.

approximation of the cos θ current density, the currents I_i of the different loops are weighted according to $I_i = I_{\text{max}}|\cos(\theta_i)|$, where I_{max} is chosen in view of the desired magnetic field strength B_0 on the coil axis [Hay85]. The homogeneity of the magnetic field within the cylindrical volume of a discretized, finite-sized cosine-theta coil varies with the total number $4N_{\text{wires}}$ of wires and with the ratio L/R. For larger N_{wires} and L/R, the magnetic field becomes more homogeneous.

The Birdcage Coils of the Main Chamber

We use two birdcage coils to cancel horizontal magnetic field components within a region of few millimeters around the center of the main chamber. The coils are mounted concentrically around the main chamber and their common coil axis coincides with the vertical $z-$axis. The current-carrying wires of the birdcage coils therefore run vertically. The two birdcage coils are rotated relative to each other by $90°$ such that one coil produces a transverse magnetic field parallel to the $x-$axis ($x-$compensation coil) and the second coil generates a transverse magnetic field along the $y-$axis ($y-$compensation coil). Figure 6.13 shows the implementation of the two birdcage coils to the K$-$Cs apparatus.

For both birdcage coils, we opted for $N_{\text{wires}} = 2$. With this choice, the angles θ of the vertical wires can be calculated with Eq. (6.3) to be $\pm 49°$, $\pm 131°$ (*outer loops*) and $\pm 15°$, $\pm 165°$ (*middle loops*) with respect to the $y-$axis for the $x-$compensation coil and with respect to the $x-$axis for the $y-$compensation coil. In order to make the outer loops of the $x-$ and $y-$compensation coils coincide and thus to simplify the setup of the birdcage coils, we approximated their calculated angular positions. The true angular positions of the outer loops within the K$-$Cs apparatus are therefore $\approx \pm 45°$ and $\approx \pm 135°$. The vertical wires of the birdcage coils fall between the horizontal CF40 viewports of the main chamber and thus do not block the horizontal optical access to the atoms. Each birdcage coil has a radius $R \approx 16\,\mathrm{cm}$, a length $L \approx 30\,\mathrm{cm}$, and stretches below the optical breadboards that support the main chamber (see Fig. 6.13). Since the coil radii R are larger than the separation of the two optical breadboards, the vertical wires of the $x-$compensation coil must go around the optical breadboards. Thus, the middle loops of the $x-$compensation coil are partially deformed. The vertical wires of each birdcage coil are pairwise connected to form loops. To keep the vertical optical access to the atoms free, the connecting wires at the upper and lower end of the birdcage coils are bent.

We realize both birdcage coils similar to the Helmholtz-like coil described in Sec. 6.4.1. We wind the loops of each birdcage coil separately using a flat ribbon cable[38] with two windings per loop. To weight the current density of each loop with a $\cos(\theta)$-factor, we prepare the flat ribbon cables of the middle loops to have 13 poles and the cables of the outer loops to have 10 poles. We use D-sub connectors to connect the poles of each ribbon cable in series and thereby form solenoids with 26 and 20 windings. The four loops of each birdcage coil are finally connected in series.

In order to obtain information on the magnetic field $\vec{B}(x, y, z)$ that is generated by the $x-$ and $y-$compensation coils around the position of the atoms, we perform a computational simulation. For a coil current of $1\,\mathrm{A}$, the $x-$ and $y-$compensation coils each generate a magnetic field in $x-$ and $y-$direction, respectively, with field strength $B_0^{\mathrm{BC,sim}} = 2.00(4)$ G. The number in brackets is the estimated error of the simulation. The simulated magnetic field of the $x-$compensation coil varies in strength less than 2 mG across a distance of $\pm 5\,\mathrm{mm}$ in $x-$, $y-$, and $z-$direction. We obtain the same value for the magnetic field homogeneity for the $y-$compensation coil.

Due to mechanical restrictions during the winding process, the birdcage coils could not be wound precisely in the originally intended manner. This resulted in the situation that the lower ends of the birdcage coils are not symmetric to the upper coil ends. Because of limited mechanical access, a measurement of the real form of the lower coil ends is not possible. We estimate that the ribbon cables at the lower coil ends are in some places off by $\approx 1\,\mathrm{cm}$. This deviation is small compared to the distance between the lower ends of the birdcage coils and the center of the main chamber, which is about $21\,\mathrm{cm}$. Therefore, geometrical details of the coil ends start to become insignificant for the magnetic field at the position of the atoms. Figure 6.13 shows the intended (symmetric) models of our birdcage coils, which were used for the magnetic field simulations. We expect that the results of the magnetic field simulations are reasonable approximations of the actual magnetic field at the position of the atoms.

---

[38] See footnote 37.

7. Experimental Results

In the course of this Thesis, a new quantum gas apparatus was built and the work described in this Thesis thereby contributed to the following three peer-reviewed publications:

1. M. Gröbner, P. Weinmann, F. Meinert, K. Lauber, E. Kirilov, and H.-C. Nägerl
   A new quantum gas apparatus for ultracold mixtures of K and Cs and KCs ground-state molecules
   J. Mod. Opt. **63** 1829-39 (2016) [Grö16]
2. M. Gröbner, P. Weinmann, E. Kirilov, H.-C. Nägerl, P. S. Julienne, C. Ruth Le Sueur, and J. M. Hutson
   Observation of interspecies Feshbach resonances in an ultracold ^{39}K$-$^{133}Cs mixture and refinement of interaction potentials
   Phys. Rev. A **95**, 022715 (2017) [Grö17c]
3. M. Gröbner, P. Weinmann, E. Kirilov, and H.-C. Nägerl
   Degenerate Raman sideband cooling of ^{39}K
   Phys. Rev. A **95**, 033412 (2017) [Grö17b]

The first publication demonstrates the production of ^{39}K and ^{133}Cs BECs within the new K$-$Cs apparatus. As part of this demonstration, a detailed description of the cooling and evaporation strategies for obtaining degenerate samples of ^{39}K and ^{133}Cs atoms is given. The second publication reports on the observation of interspecies Feshbach resonances in an ultracold mixture of ^{39}K and ^{133}Cs atoms. The experimental data is used to refine K$-$Cs interaction potentials and to make predictions of scattering and bound-state properties for ^{39}K$-$Cs, ^{40}K$-$Cs, and ^{41}K$-$Cs mixtures. The third publication gives a demonstration of 3D degenerate Raman sideband cooling of ^{39}K atoms on the principal D_1 atomic transition. With this cooling technique, it was possible to improve the starting conditions for subsequent evaporative cooling of ^{39}K atoms within the K$-$Cs apparatus. All experiments for the three publications were performed within the main chamber of the K$-$Cs apparatus. A more extensive discussion of the experimental results can be found in Ref. [Grö17a]. The main results of the above-mentioned three publications are summarized in the following Sections.

7.1. Bose-Einstein Condensates of ^{39}K and ^{133}Cs Atoms

In the first publication [Grö16] of the new K$-$Cs apparatus, the production of BECs of ^{39}K and ^{133}Cs atoms was demonstrated. The production of BECs of both atomic species is an important step towards future investigation of ultracold gases of K and Cs atoms as well as KCs ground-state molecules within the K$-$Cs apparatus. For each atomic species, we follow an individual experimental route towards Bose-Einstein condensation. The experimental sequences are summarized in the following and numbers for various experimental parameters e.g. beam waists, temperatures, and so on are given. The experimental values obey statistical errors that are estimated as follows: beam waists (1 µm), laser beam powers (10 %), temperatures (2 %), atom numbers (10 %), phase-space densities (20 %), and magnetic field strengths ($\leq$0.01 %).

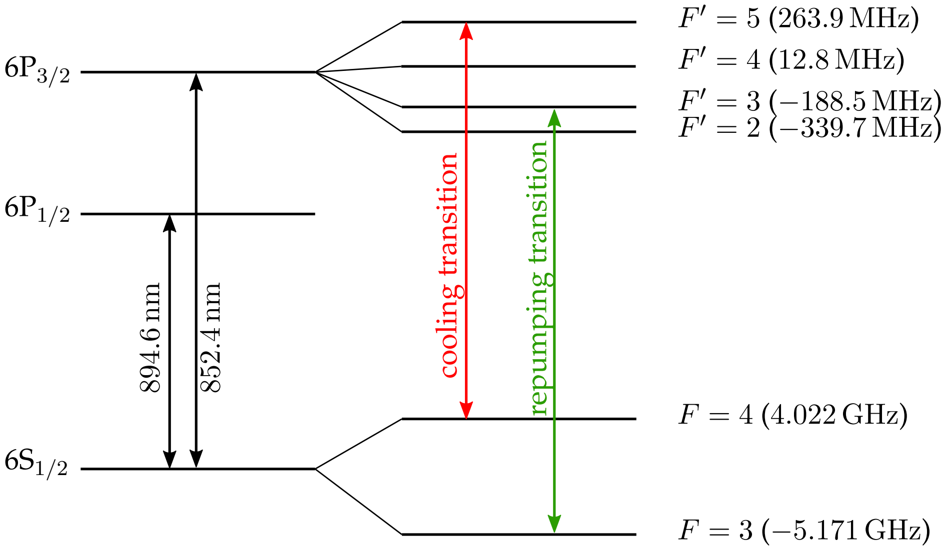

Figure 7.1.: Level scheme of ^{133}Cs. Hyperfine structure of the energetically lowest electronic levels in cesium. The numbers in brackets give the hyperfine energy shift and are calculated with data from Ref. [San09]. Level spacings are not to scale. The $|F = 4\rangle \rightarrow |F' = 5\rangle$ transition (red arrow) is used for laser cooling. The $|F = 3\rangle \rightarrow |F' = 3\rangle$ transition (green arrow) is employed for repumping.

7.1.1. Experimental Sequence for a ^{133}Cs BEC

The experimental procedure for making a ^{133}Cs BEC is essentially the one demonstrated in Ref. [Web03b]. The sequence begins by loading a 3D-MOT with atoms from the atomic beam that is sent from the Cs 2D$^+$-MOT towards the main chamber. The Cs oven at the Cs 2D-MOT chamber is heated and temperature stabilized to a temperature of around $\sim 30\,°\mathrm{C}$. The resulting typical operating pressure inside the Cs 2D-MOT chamber is dominated by the partial pressure of Cs and is between 10^{-6} and 10^{-7} mbar. In contrast, the pressure within the main chamber is below 1×10^{-10} mbar. The latter is measured by lifetimes of atoms trapped within a magnetic quadrupole trap.

Figure 7.1 shows the level scheme of cesium and indicates the atomic transitions that are used for cooling and repumping of Cs atoms within the 2D$^+$- and 3D-MOT. The laser light for cooling and repumping is generated by two diode laser systems, which are described in Ref. [Grö17a]. The laser systems are locked to the hyperfine transitions $|F = 4\rangle \rightarrow |F' = 5\rangle$ and $|F = 3\rangle \rightarrow |F' = 2\rangle$ of the 6S$_{1/2}$ $\rightarrow$ 6P$_{3/2}$ line via modulation transfer spectroscopy. Two subsequent tapered amplifiers increase the available laser power for cooling cesium to in total 300 mW. To change the intensities and frequencies of the laser beams during the cooling procedure, acousto-optical modulators that are placed after the tapered amplifiers allow for experimental control of these parameters. A pair of magnetic coils (*gradient coils*) create the magnetic field gradient (7.5 G/cm) that is required for the 3D-MOT. The gradient coils are installed within the top and bottom inverted viewports of the main chamber (see Sec. 6.3.1) together with five other magnetic coil pairs that are used to generate homogeneous magnetic offset fields. The design of these magnetic coils is described in Ref. [Grö17a].

The 3D-MOT is loaded at a rate of 2×10^8 atoms/s and saturates after about $4\,\mathrm{s}$. Once saturated, the 3D-MOT contains around 3×10^8 atoms at a temperature of $115\,\mu\mathrm{K}$. After the 3D-MOT loading has stopped, the magnetic field gradient is raised to 20 G/cm and the detuning of the 3D-MOT cooling light is increased to $-60\,\mathrm{MHz}$. With these laser parameters the 3D-MOT is compressed (*compressed MOT phase*) and the atomic density increases. The compressed MOT phase lasts for $10\,\mathrm{ms}$. Shortly before the compressed MOT phase ends and the cooling light is switched off, the repumper laser power is ramped down to zero. In this way, the atoms are pumped into the $|F = 3\rangle$ state and are prepared for Raman sideband cooling.

For Raman sideband cooling the compressed Cs cloud, containing around 2×10^8 atoms at a temperature of $42\,\mu\mathrm{K}$, is loaded into a 3D optical lattice (*Raman lattice*). The Raman lattice is generated by four laser beams. The laser light for the Raman lattice stems from the MOT laser setup and is frequency-shifted into resonance with the $|F = 4\rangle \rightarrow |F' = 4\rangle$ transition. To bring the vibrational states $|N\rangle$ of the trapped Cs atoms in the hyperfine Zeeman state $|F = 3, M_F\rangle$ into degeneracy with the vibrational state $|N - 1\rangle$ of the hyperfine Zeeman state $|F = 3, M_F - 1\rangle$, a magnetic offset field is switched on and adjusted in field strength. The Raman lattice laser light then drives degenerate Raman transitions and repumps the atoms that have fallen into the $|F = 4\rangle$ state (*degenerate Raman sideband cooling*) [Web03b, Tre01]. An almost purely σ^+−polarized laser beam that is resonant with the $|F = 3\rangle \rightarrow |F' = 2\rangle$ transition continuously pumps the Cs atoms from the state $|F = 3, M_F = 1\rangle$ back into state $|F = 3, M_F = 3\rangle$. At the end of the $14\,\mathrm{ms}$ long Raman cooling phase, the Cs atom cloud is almost entirely (90 %) spin-polarized into state $|F = 3, M_F = 3\rangle$ with about 5.5×10^7 atoms at a temperature of about $\sim 500\,\mathrm{nK}$. The $1/e$-radius of the atom cloud at this point is around $385\,\mu\mathrm{m}$. Having a phase-space density of $\mathcal{D} = 2 \times 10^{-3}$ and an atom density of $2.4 \times 10^{11}\,\mathrm{cm}^{-3}$, the Raman-cooled atomic sample provides an adequate basis for evaporative cooling.

To evaporatively cool the Cs cloud, the laser cooled Cs atoms are loaded into an optical dipole trap (*reservoir trap*). The dipole trap is formed by two horizontal laser beams that cross each other. The laser beams are formed by one $1064\,\mathrm{nm}$ laser beam in bow-tie configuration, which has a laser power of $20\,\mathrm{W}$. The reservoir trap has a trap depth of about $k_B \times 11\,\mu\mathrm{K}$ and is already switched on during the MOT phase. To capture a large amount of the atoms from the Raman-cooled Cs cloud, the dipole trap laser beams are chosen to be rather wide and have beam waists of $550\,\mu\mathrm{m}$. The confinement of the reservoir trap is too weak to hold the Cs atoms against gravity. For this reason, the Cs atoms are magnetically levitated within the reservoir trap. Magnetic levitation is achieved through a vertical field gradient of 31.4 G/cm, which counterbalances gravity for atoms in the $|F = 3, M_F = 3\rangle$ state. Atoms in other states are not levitated and lost, leaving behind a fully spin-polarized atomic sample.

To load the Raman-cooled Cs atoms into the reservoir trap, the Raman lattice is switched off and the magnetic levitation field is switched on. Within the first $2\,\mathrm{ms}$, the atoms are over-levitated and then held for $800\,\mathrm{ms}$ within the reservoir trap. At the same time, the magnetic offset field is changed to 177 G. At this magnetic field strength, the cesium scattering length is around $a_{\text{scatt}} \approx 1850\,a_0$ and leads to an increased collision rate between Cs atoms. After transfering the Cs atoms into the reservoir trap, the reservoir trap contains about 1.5×10^7 atoms at a slightly increased temperature of $1.7\,\mu\mathrm{K}$ due to phase-space mismatch. To increase the atomic density within the reservoir trap, the optical trapping potential is locally stiffened. For this, two tightly focused $1064\,\mathrm{nm}$ laser beams, one horizontal laser beam (*dimple beam*, beam waist $43\,\mu\mathrm{m}$) and one vertical laser beam (*guide beam*, beam waist $125\,\mu\mathrm{m}$), are overlapped with the reservoir trap. As a result, a dimple is generated within the reservoir trap in which elastically scattered atoms accumulate. To optimize the loading of the dimple trap, the scattering

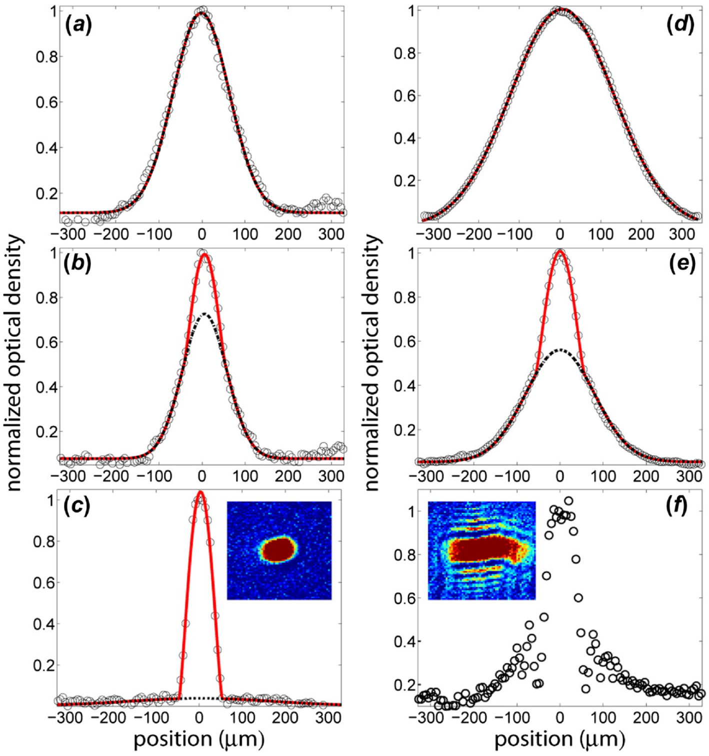

Figure 7.2.: Normalized integrated optical density distributions for ultracold samples of ^{133}Cs (a)-(c) and ^{39}K atoms (d)-(f) during evaporative cooling. The distributions are obtained from integration of the optical density along the horizontal axis of time-of-flight images such as those shown in the insets of (c) and (f). The depicted distributions correspond to different stages of evaporative cooling: (a)+(d) beginning of evaporative cooling, (b)+(e) during evaporative cooling, and (c)+(f) end of evaporation. The red lines correspond to bimodal fits, whereas the dotted lines correspond to Gaussian distributions that describe the thermal fraction of the atom clouds. The distortions within the absorption image of ^{39}K atoms in (f) result from atom-induced lensing effects and lens aberrations. Reprinted Figure with permission from Ref. [Grö16]. Copyright (2016) by Taylor & Francis.

length a_{scatt} of the Cs atoms is tuned first to $900\,a_0$ and then to $380\,a_0$ during the loading. After the Cs atoms have spent about $\sim 1.5\,\text{s}$ within the dimple trap, the number of Cs atoms in state $|F = 3, M_F = 3\rangle$ within the dimple trap is 2.2×10^6 and the local phase-space density is $\mathcal{D} = 8 \times 10^{-2}$.

As a last step towards BEC formation, evaporative cooling of the Cs atoms within the dimple trap is induced. To that end, first the reservoir trap is switched off, such that only Cs atoms within the dimple trap remain. Subsequently, the power of the dimple beam is lowered in two ramps of each $2\,\text{s}$ duration from initially $100\,\text{mW}$ to $1.5\,\text{mW}$. Simultaneously, the power of the guide beam is lowered from $800\,\text{mW}$ to $10\,\text{mW}$. In parallel, to decrease atom losses owing to three-body collisions, the magnetic offset field strength and thus the scattering length a_{scatt} is reduced. Moreover, the magnetic field gradient is increased to 31.9 G/cm and thereby compensates for trapping effects of the magnetic coils. When evaporation is finished, the dimple trap contains a nearly pure BEC of 4×10^4 atoms.

Figure 7.2 (a)-(c) shows the change in the integrated optical density distributions of ultracold Cs samples during evaporative cooling. The integrated optical density distributions are obtained through integration of the optical density along the horizontal direction of time-of-flight absorption images. The time-of-flight images used for the data in Fig. 7.2 were taken after $60\,\mathrm{ms}$ of levitated expansion with nearly zero scattering length. Each integrated optical density distribution curve is the result of averaging over four profiles.

The transition from a thermal Boltzmann gas to a BEC becomes apparent in the integrated optical density distributions. At an early stage of evaporative cooling, the gas is still thermal and the integrated optical density distribution follows a Boltzmann distribution (Fig. 7.2 (a)). At reduced trap depths, the distribution becomes bimodal and shows the onset of an inverted-parabolic distribution, which is also known as *Thomas-Fermi distribution* (Fig. 7.2 (b)). A Thomas-Fermi distribution is characteristic for a BEC within a harmonic trap [San14, Ket99]. Towards the end of evaporative cooling, the integrated optical density distribution is a nearly pure Thomas-Fermi distribution (Fig. 7.2 (c)). From Fig. 7.2 (c) the radius of the in-trap Thomas-Fermi distribution of the atoms is deduced to be $7\,\mu\mathrm{m}$ in horizontal direction and $24\,\mu\mathrm{m}$ in the vertical direction.

7.1.2. Experimental Sequence for a ^{39}K BEC

The experimental sequence for the formation of a ^{39}K BEC within the K$-$Cs apparatus begins by loading of a 3D-MOT. The 3D-MOT captures ^{39}K atoms from the atomic beam that is ejected by the ^{39}K 2D$^+$-MOT. The oven at the K 2D-MOT chamber is heated to a temperature of around $\sim 60\,^{\circ}\mathrm{C}$. The laser light used for the ^{39}K 2D$^+$- and 3D-MOT is generated by a laser system that is locked to the $|F = 2\rangle \to |F' = 3\rangle$ transition of the $4\mathrm{S}_{1/2} \to 4\mathrm{P}_{3/2}$ line of ^{39}K. The level scheme of ^{39}K is depicted in Fig. 5.2. The potassium laser system and its optical setup for frequency shifting the laser light is described in Ref. [Grö17a]. Both, laser system and optical setup, are designed such that cooling laser light for the different potassium isotopes can be generated with the same setup. The experiments in this Chapter, however, are only concerned with the bosonic isotope ^{39}K.

The ^{39}K 3D-MOT (magnetic field gradient 7.5 G/cm) is loaded within $4\,\mathrm{s}$ and then contains around 8.5×10^8 atoms. Once the ^{39}K 3D-MOT is loaded, it is compressed by increasing the detuning of the cooling light to $-40\,\mathrm{MHz}$ and steepening the magnetic field gradient to 30 G/cm, similarly to the experimental Cs sequence. The number of atoms within the compressed 3D-MOT is around 8×10^8 atoms at a temperature of $2.2\,\mathrm{mK}$.

Following the compressed 3D-MOT, the ^{39}K sample is laser cooled via optical molasses cooling on the $4\mathrm{S}_{1/2} \to 4\mathrm{P}_{3/2}$ line. During the molasses phase, the frequency of the molasses light is red-detuned from the $|F = 2\rangle \to |F' = 3\rangle$ transition and the detuning is increased from $-2\,\mathrm{MHz}$ to $-9\,\mathrm{MHz}$. If the detuning of the molasses cooling light were further increased, the ^{39}K sample would heat up. The reason for this heating is the appearance of negative friction forces caused by the $|F = 2\rangle \to |F' = 2\rangle$ transition. Since the hyperfine splitting of the $4\mathrm{P}_{3/2}$ level is comparable to its natural line width, optical molasses cooling on the principal D_2 line is weakened. With optical molasses cooling on the principal D_2 line, a temperature of around $30\,\mu\mathrm{K}$ is achieved for the ^{39}K sample within our setup.

To further reduce the temperature of the ^{39}K sample, gray molasses cooling is performed on the $4\mathrm{S}_{1/2} \to 4\mathrm{P}_{1/2}$ line. Gray-molasses cooling of ^{39}K atoms has first been demonstrated in Ref. [Sal13]. For gray molasses cooling, the cooling and repumper light (derived from a home-built master laser) are both blue-detuned by $26\,\mathrm{MHz}$ relative to the $|F' = 2\rangle$ state of the $4\mathrm{P}_{1/2}$ fine structure level. At the end of gray molasses cooling, the ^{39}K sample has a temperature of $7\,\mu\mathrm{K}$. To polarize the ^{39}K atoms into the $|F=1, M_F=-1\rangle$ state, the magnetic offset field is set to 2 G and a polarizer beam that is resonant with the $|F=1\rangle \rightarrow |F'=1\rangle$ transition and with σ^- polarization is applied. Atoms that have not been transferred into the $|F=1, M_F=-1\rangle$ state are eliminated by loading the laser cooled atoms into a magnetic trap with a field gradient of 30 G/cm. Due to the background scattering length of $a_{\mathrm{bg}} = -33\,a_0$ for ^{39}K a Ramsauer-Townsend minimum in the collisional cross-section shows up at a temperature of $400\,\mu\mathrm{K}$ [Lan12]. The Ramsauer-Townsend minimum compromises the use of forced evaporative cooling in the magnetic trap. For evaporative cooling, the potassium sample is therefore loaded into a dipole trap.

The dipole trap is created by a focused two-color laser beam with wavelengths of $1064\,\mathrm{nm}$ and $880.25\,\mathrm{nm}$. The spatial confinement resulting from the focused $1064\,\mathrm{nm}$ laser beam ($20\,\mu\mathrm{m}$ beam waist) enhances the collisional rate of the ^{39}K atoms. To allow for forced evaporative cooling, the magnetic trap is switched off. Thereafter the power of the $1064\,\mathrm{nm}$ laser beam is reduced from $18\,\mathrm{W}$ to zero in two ramps. In parallel, the power of the $880.25\,\mathrm{nm}$ laser beam is lowered from $28\,\mathrm{mW}$ to $2.8\,\mathrm{mW}$. To reduce three-body losses, the scattering length of the ^{39}K atoms is set to $a_{\mathrm{scatt}} = 57\,a_0$ during the first ramp and to $a_{\mathrm{scatt}} = 225\,a_0$ for the second ramp. At the end of evaporative cooling, the ^{39}K BEC contains around 9×10^4 atoms in state $|F=1, M_F=-1\rangle$.

Analogously to the discussion of the experimental cesium sequence, integrated optical density profiles of the ^{39}K sample are observed during evaporative cooling. Figure 7.2 shows the integrated optical density profiles (d) after the first evaporation ramp, (e) during the second evaporation ramp, and (f) at the end of evaporation. The optical density profiles (d)-(f) visualize the phase transition from a thermal ^{39}K gas to a BEC. The distributions are obtained from time-of-flight absorption images, like that in Fig. 7.2 (f), after $10\,\mathrm{ms}$ of expansion at zero magnetic field. The distortions within the time-of-flight images result most likely from atom-induced lensing effects and aberrations of the imaging system.

7.1.3. Conclusion

The measurements summarized in this Section demonstrate the independent experimental production of ^{39}K and ^{133}Cs BECs in our new quantum gas apparatus. The results show that the design and realization of the K$-$Cs apparatus was successful up to the stage of producing ultracold quantum gases. The different properties of ^{39}K and ^{133}Cs with respect to laser cooling make a parallel BEC production difficult. For that reason, the two species are condensed sequentially within one experimental run. The cooling sequences are designed such that the two atomic samples can be spatially overlapped after independent production. This feature is important for the investigation of interspecies Feshbach resonances in ultracold mixtures of ^{39}K and ^{133}Cs atoms.

7.2. ^{39}K$-^{133}$Cs Interspecies Feshbach Resonances

For future production of KCs molecules within the K$-$Cs apparatus, the knowledge of the positions and widths of interspecies Feshbach resonances in mixtures of ultracold K and Cs atoms is indispensable. Interspecies Feshbach resonance positions and widths in K$-$Cs mixtures have been calculated for all three K isotopes in Ref. [Pat14] on the basis of interaction potentials that were calculated in Ref. [Fer13]. These Feshbach resonances, however, have not been experimentally confirmed so far. Therefore, interspecies Feshbach resonances in an ultracold ^{39}K$-^{133}$Cs mixture are studied experimentally within our second publication [Grö17c] for magnetic field strengths between 0 and 650 G.

7.2.1. Experimental Sequence for Observation of Feshbach Resonances

For the observation of Feshbach resonances, it is sufficient to work with thermal atomic samples in the microkelvin regime. Thus, the production of quantum-degenerate atomic samples is not necessary. In the experiments presented in this Section, atomic ^{39}K$-^{133}$Cs mixtures are created in a sequential way. Each experimental run begins with the preparation of an ultracold ^{39}K sample as described in Ref. [Grö16] and summarized in the previous Section. First, ^{39}K atoms are laser cooled and spin-polarized into the $|F = 1, M_F = -1\rangle$ state with a magnetic quadrupole trap. After spin polarization, the ^{39}K atoms are loaded into a horizontal single-beam optical dipole trap at wavelength $1064\,\mathrm{nm}$. The dipole trap beam has a beam waist of 26 µm and a power of 15 W. To induce evaporative cooling of the optically trapped ^{39}K atoms, the power of the dipole trap beam is decreased over a period of $1.5\,\mathrm{s}$ to $150\,\mathrm{mW}$. During evaporative cooling of the ^{39}K atoms the dipole trap is lifted by $1.2\,\mathrm{mm}$ along the vertical axis using a linear translation stage. By doing so, the center of the magnetic trap is emptied for the following production of an atomic Cs sample. Owing to magnetization effects of the stainless steel main chamber that are induced through the K quadrupole trap, a series of magnetic field pulses with field strengths up to 1000 G and durations of $100\,\mathrm{ms}$ is applied. The magnetic field pulses polarize the main chamber and allow for subsequent laser cooling of Cs atoms without readjustments of the magnetic field.

In a next step, an ultracold ^{133}Cs sample is prepared. To that end, a Cs 3D-MOT is loaded. At the same time a single-beam dipole trap, which is aligned to the center of the Cs 3D-MOT, is switched on. The dipole trap beam has a beam waist of $250\,\mu\mathrm{m}$, power of $15\,\mathrm{W}$, and wavelength of $\sim 1070\,\mathrm{nm}$.

Once the Cs 3D-MOT is loaded, the previously prepared ^{39}K sample is moved downwards by $0.79\,\mathrm{mm}$ to overlap the ^{39}K atoms with the ^{133}Cs atoms. During the vertical transport the beam waist of the dipole trap beam that holds the ^{39}K sample is increased to 63 µm and the power is increased to $1.2\,\mathrm{W}$. To further cool the ^{133}Cs atoms within the 3D-MOT, the Cs 3D-MOT is compressed and 3D degenerate Raman sideband cooling is applied. The ^{133}Cs atoms are cooled into the crossed dipole trap that is formed by the two individual K and Cs dipole traps. Following a hold time of $80\,\mathrm{ms}$, the ^{39}K and ^{133}Cs atoms have thermalized separately at different equilibrium temperatures of $3\,\mu\mathrm{K}$ and $7\,\mu\mathrm{K}$, respectively. The capability to separate thermalization indicates that the background scattering length between ^{39}K and ^{133}Cs, far away from any Feshbach resonance, is relatively small and thus does not enable joint thermalization. At this point, the number of atoms within the crossed dipole trap is for ^{39}K around $\sim 1 \times 10^5$ atoms and about as much for ^{133}Cs. The maximum atom densities are $n_{\mathrm{K}} = 1.2 \times 10^{12}$ cm^{-3} for ^{39}K and $n_{\mathrm{Cs}} = 9 \times 10^{11}$ cm^{-3} for ^{133}Cs. The difference in particle density is a result of different equilibrium temperatures and of the different trap depths that the atoms experience.

The ^{39}K sample within the crossed dipole trap is entirely polarized into the state $|F = 1, M_F = -1\rangle$ whereas $80\,\%$ of the ^{133}Cs atoms occupy the energetically lowest hyperfine sublevel $|F = 3, M_F = 3\rangle$. The remaining ^{133}Cs atoms reside largely in state $|F = 3, M_F = 2\rangle$. To spin-polarize the ^{133}Cs atoms into state $|F = 3, M_F = 3\rangle$, a microwave pulse (resonant with the transition $|F = 3, M_F = 2\rangle \rightarrow |F = 4\rangle$) and a laser pulse (resonant with the transition $6S_{1/2}$ $|F = 4\rangle \rightarrow 6P_{3/2}$ $|F' = 5\rangle$) is used.

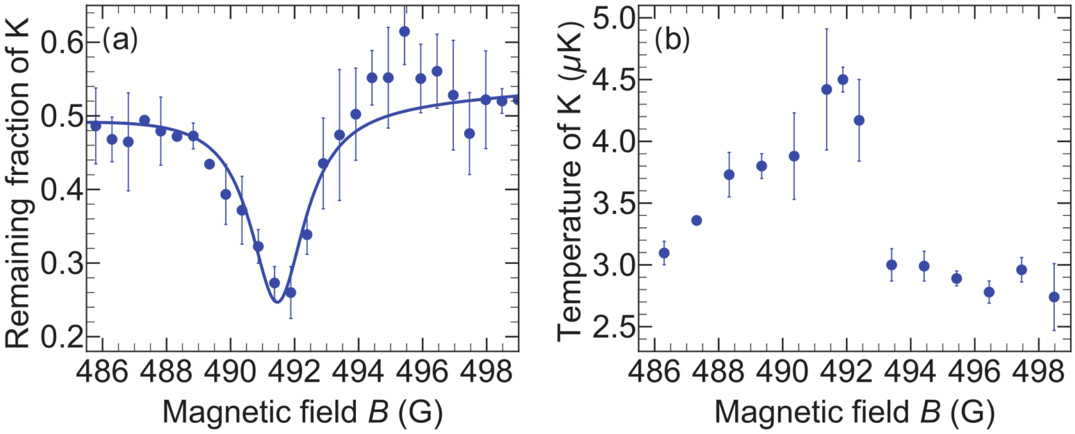

Figure 7.3.: Experimental signatures of an interspecies Feshbach resonance within a |K : c⟩ − |Cs : a⟩ mixture. (a) Remaining fraction of ^{39}K atoms relative to the number of atoms of a ^{39}K sample without ^{133}Cs atoms following a $100\,\mathrm{ms}$−hold time with fixed trap depth. Data points are averages of at least two measurements. The solid curve is a Lorentzian function that is fitted to the experimental data. (b) Temperature of the ^{39}K sample after holding the mixture for $900\,\mathrm{ms}$ within the crossed dipole trap. Data points are averages of five time-of-flight measurements with different expansion times. Magnetization effects of the main chamber inhibited having more repetitions for the temperature measurements. The error bars indicate the statistical errors of the fits used to extract the temperature. Reprinted Figure from Ref. [Grö17c]. Copyright (2017) by the American Physical Society.

At this stage, to observe interspecies Feshbach resonances, the strength of the magnetic offset field is set to any desired value and held there for $900\,\mathrm{ms}$ to $1300\,\mathrm{ms}$. In the present experiments, the chosen magnetic offset field strengths are between 0 G and 650 G. For magnetic field strengths close to an interspecies Feshbach resonance, the interspecies scattering length becomes larger in absolute value and thus atoms are subject to enhanced three-body collisions. As a result, the number of atoms within the crossed dipole trap is reduced. Increased atom loss therefore represents a characteristic signature for the presence of an interspecies Feshbach resonance. In the present case, Feshbach resonances are detected through loss of ^{39}K atoms and heating of the ^{39}K sample owing to intensified interaction with the hotter ^{133}Cs atoms. Atom loss is identified after the hold time through absorption imaging of the remaining ^{39}K atom cloud. To enhance the Feshbach-induced loss of ^{39}K atoms, the trap depth of the crossed dipole trap is lowered during the hold time.

In the remainder of this Section, the Zeeman states of the hyperfine ground state of ^{39}K and ^{133}Cs are designated with letters a, b, c,. . . and so on in order of increasing energy. This designation leads to the notation:

$$\begin{aligned} |\mathrm{K}:\mathrm{a}\rangle &\equiv |F=1, M_F=1\rangle, & \qquad |\mathrm{Cs}:\mathrm{a}\rangle &\equiv |F=3, M_F=3\rangle, \\ |\mathrm{K}:\mathrm{b}\rangle &\equiv |F=1, M_F=0\rangle, & \qquad |\mathrm{Cs}:\mathrm{b}\rangle &\equiv |F=3, M_F=2\rangle, \\ |\mathrm{K}:\mathrm{c}\rangle &\equiv |F=1, M_F=-1\rangle, & & \vdots \end{aligned} \tag{7.1}$$

Table 7.1.: Parameters of interspecies Feshbach resonances. Positions and widths of interspecies Feshbach resonances in mixtures of $|\mathrm{K}:\mathrm{a}\rangle - |\mathrm{Cs}:\mathrm{a}\rangle$, $|\mathrm{K}:\mathrm{b}\rangle - |\mathrm{Cs}:\mathrm{a}\rangle$, and $|\mathrm{K}:\mathrm{c}\rangle - |\mathrm{Cs}:\mathrm{a}\rangle$. The experimentally obtained parameters are fit parameters obtained from fitting Lorentzian functions to the data. The entity δ_{res} corresponds to the FWHM of a Lorentzian function. Reprinted Table from Ref. [Grö17c]. Copyright (2017) by the American Physical Society.

	Experiment		Theory (potentials from Ref. [Fer13])	
Mixture	$\mathbf{B}_{\mathrm{res}}$ (G)	δ_{res} (G)	$\mathbf{B}_{\mathrm{res}}$ (G)	$\mathbf{\Delta}_{\mathrm{res}}$ (G)
$\|\mathrm{K}:\mathrm{a}\rangle + \|\mathrm{Cs}:\mathrm{a}\rangle$	361.1(1)	3.2(4)	341.89	4.7
	442.59(1)	0.28(3)	421.37	0.38
$\|\mathrm{K}:\mathrm{b}\rangle + \|\mathrm{Cs}:\mathrm{a}\rangle$	419.3(1)	3.0(5)	399.93	4.3
	513.12(1)	0.16(6)	491.39	0.55
$\|\mathrm{K}:\mathrm{c}\rangle + \|\mathrm{Cs}:\mathrm{a}\rangle$	491.5(1)	2.1(4)	471.97	3.8
	599.32(3)	0.5(1)	575.67	0.44

7.2.2. Experimental Results

In a first series of measurements, interspecies Feshbach resonances within a $|\mathrm{K}:\mathrm{c}\rangle - |\mathrm{Cs}:\mathrm{a}\rangle$ mixture are investigated. Throughout the magnetic field scan from 0 G to 650 G two loss features are observed at magnetic field strengths of 491.5 G and 599.3 G, respectively. Figure 7.3 (a) shows the detected ^{39}K fraction around the Feshbach resonance at 491.5 G. The fraction of remaining ^{39}K atoms shows a distinct minimum and a clear maximum. The positions B_{res} and the FWHM widths δ_{res} of the minima are found by fitting Lorentzian functions to the data. Table 7.1 summarizes the fit parameters of the experimentally observed Feshbach resonances as well as the statistical errors of the fits. Due to fluctuations of the magnetic polarization of the stainless steel main chamber during the measurements, a systematic error of around ± 0.3 G has to be considered. The maximum of the remaining atom number that appears at a magnetic field strength of 495.5 G in Fig. 7.3 (a) is attributed to the zero-crossing of the scattering length on the high-field side of the Feshbach resonance.

To characterize the heating of the ^{39}K sample in the vicinity of an interspecies Feshbach resonance, the temperature of the ^{39}K sample is deduced from time-of-flight images. The temperature of the ^{39}K sample peaks around a magnetic field strength of 491.5 G, i.e. at the same magnetic field strength as the atom loss feature, and increases from $3.0\,\mu\mathrm{K}$ to $4.5\,\mu\mathrm{K}$. Figure 7.3 (b) shows the experimental results of the temperature measurements for the Feshbach resonance at 491.5 G.

The experimental sequence for determination of interspecies Feshbach resonances in mixtures where the ^{39}K atoms are in state $|\mathrm{K}:\mathrm{b}\rangle$ or $|\mathrm{K}:\mathrm{a}\rangle$ is analogue to the one described above. To transfer the ^{39}K atoms, initially residing in state $|\mathrm{K}:\mathrm{c}\rangle$, to state $|\mathrm{K}:\mathrm{b}\rangle$ and thereafter to state $|\mathrm{K}:\mathrm{a}\rangle$, radio-frequency adiabatic passage is used. The measurements for the two mixtures $|\mathrm{K}:\mathrm{b}\rangle - |\mathrm{Cs}:\mathrm{a}\rangle$ and $|\mathrm{K}:\mathrm{a}\rangle - |\mathrm{Cs}:\mathrm{a}\rangle$ yield two interspecies Feshbach resonances for each mixture. Figure 7.4 (a) shows the experimental results for the remaining ^{39}K atom numbers for all measured Feshbach resonances and Table 7.1 summarizes the fit parameters of all experimentally observed interspecies Feshbach resonances.

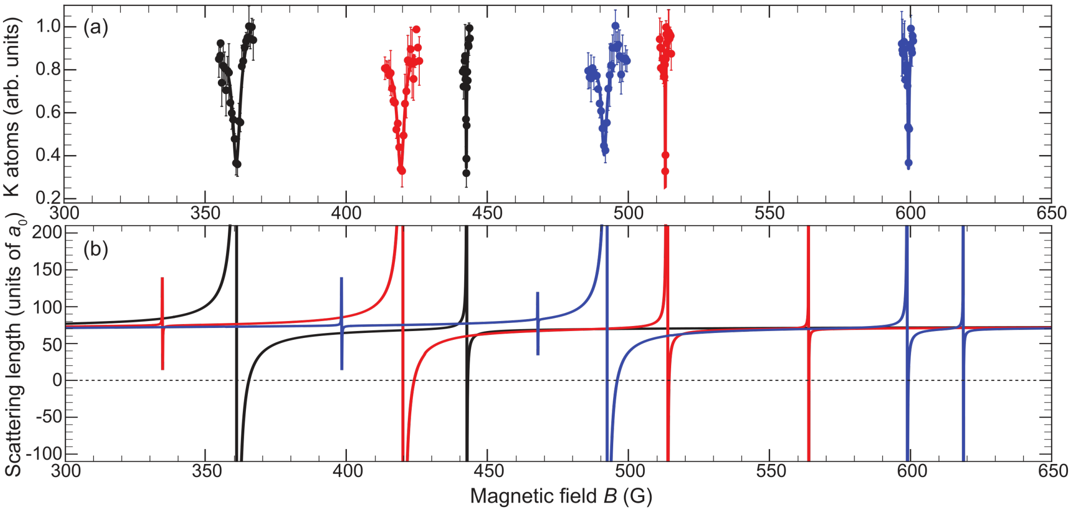

Figure 7.4.: Interspecies Feshbach spectrum of a ^{39}K$-^{133}$Cs mixture. (a) Remaining number of ^{39}K atoms around interspecies Feshbach resonances for mixtures of $|\mathrm{Cs} : \mathrm{a}\rangle$ with $|\mathrm{K} : \mathrm{a}\rangle$ (black), $|\mathrm{K} : \mathrm{b}\rangle$ (red), and $|\mathrm{K} : \mathrm{c}\rangle$ (blue). (b) Interspecies scattering length and Feshbach resonance positions calculated from optimized interaction potentials for ^{39}K$-^{133}$Cs mixtures. Reprinted Figure from Ref. [Grö17c]. Copyright (2017) by the American Physical Society.

7.2.3. Refinement of Interaction Potentials

The experimentally measured Feshbach resonances can be compared to predicted values. The latter are obtained from ^{39}K$-^{133}$Cs interaction potentials that had been previously calculated in Ref. [Fer13]. The right columns of Table 7.1 list the predicted positions and widths of the observed Feshbach resonances. All theoretical resonance positions differ from the experimental ones and are around 20 G lower. The discrepancy in resonance positions indicates that the interaction potentials from Ref. [Fer13] need to be refined in order to reproduce the observed resonance positions. The discussion of the refinement of the interaction potentials is beyond the scope of this Section. A detailed treatment of how the interaction potential were refined can be found in Ref. [Grö17c]. In short, optimized potentials for ^{39}K^{133}Cs molecules are obtained through least-squares fits of potential parameters to the observed resonance positions.

The main results of the potential refinements can be summarized as follows: using the refined interaction potentials, the new calculated resonance positions match with the observed ones within ± 0.8 G. Figure 7.4 (b) depicts the newly calculated ^{39}K$-^{133}$Cs interspecies scattering lengths as a function of the magnetic offset field strength. The new background scattering lengths a_{bg} determined from the calculations are on the order of 70 a_0 [Grö17c]. Specific values for the background scattering lengths are listed in the Supplemental Material of the publication [See]. Besides the six interspecies Feshbach resonances that have been observed in the present measurements, the optimized potentials predict six additional s-wave resonances between 319 G and 619 G. The latter resonances might be useful for formation of KCs molecules.

The measurements of the interspecies Feshbach resonance positions for ^{39}K$-^{133}$Cs mixtures also allow for the refinement of the interaction potentials for ^{40}K$-^{133}$Cs and ^{41}K$-^{133}$Cs mixtures. With this refinement, scattering lengths as well as bound-state energies for ^{40}K$-^{133}$Cs and ^{41}K$-^{133}$Cs mixtures can be calculated and are presented in Ref. [Grö17c].

7.2.4. Conclusion and Outlook

The measurements summarized in this Section led to the observation of interspecies Feshbach resonances in ultracold ^{39}K$-^{133}$Cs mixtures. Since the experimentally observed resonance positions deviated from the calculated positions, the interaction potentials for ^{39}K$-^{133}$Cs, ^{40}K$-^{133}$Cs, and ^{41}K$-^{133}$Cs mixtures were refined. The optimized interaction potentials were then used to improve predictions of the scattering lengths, background scattering lengths, and bound-state properties for ^{39}K$-^{133}$Cs, ^{40}K$-^{133}$Cs, and ^{41}K$-^{133}$Cs mixtures.

In ultracold quantum gas mixtures of different atomic species, the ability to tune collisional interactions can be used to create diatomic, heteronuclear molecules in their rovibrational ground state. In most cases, the production of ultracold diatomic ground-state molecules includes two steps: at first, atoms in the degenerate quantum gas mixtures are associated pairwise into weakly bound Feshbach molecules using the mechanism of interspecies Feshbach resonances (*magneto-association*). The mechanism of magneto-association is discussed in detail in Ref. [Köh06]. Subsequently, the weakly bound Feshbach molecules are transferred into their rovibrational ground state by *stimulated Raman adiabatic passage* (STIRAP) [Ber98].

Magneto-association of ultracold molecules has been demonstrated in 3D bulk quantum gas mixtures as well as with atoms that are prepared in optical lattices [Ni08, Mol14, Tak14, Guo16, Mos15, Rei17]. For formation of ultracold, heteronuclear dimers in optical lattices, ultracold samples of the two atomic species are first loaded into an optical lattice and then merged together to form a quantum mixture. To occupy each lattice site with precisely one atom of each species, the atomic system is brought into a Bose-Bose double-species Mott insulator state [Rei17] or a Bose-Fermi Mott-band insulator state [Mos15]. By using an interspecies Feshbach resonance, the atom pairs at each lattice site are transferred into a molecular state via magneto-association. The experimental procedure just outlined makes use of interspecies Feshbach resonances at two points: initially, an interspecies Feshbach resonance is employed to set the interspecies scattering length to zero and thus to allow for unobstructed mixing of the atomic samples. Later, an interspecies Feshbach resonance is employed for magneto-association. The results of the present measurements therefore form a valuable basis towards the production of ultracold KCs ground-state molecules.

7.3. Degenerate Raman Sideband Cooling of ^{39}K

In order to achieve better starting conditions for evaporative cooling of ^{39}K atoms within our experimental sequence for ^{39}K BECs, degenerate Raman sideband cooling (dRSC) was implemented and the experimental results were presented in our third publication [Grö17b]. The experimental strategy towards formation of atomic BECs is well established nowadays and generally includes two steps: atoms within a trap are first precooled to low temperatures ($\sim 10^{-6}$ μK) and high densities ($\sim 10^{11}$ cm^{-3}) by laser cooling. The phase transition from a thermal gas to a Bose-condensed gas is induced thereafter by subsequent evaporative cooling. To produce condensates with a larger number of atoms, it is beneficial to improve the starting conditions for evaporative cooling, i.e. to achieve a lower temperature and a higher density at the end of the laser cooling stage. For this purpose, 3D dRSC was implemented as final laser cooling step in our ^{39}K cooling sequence, which has been described in Sec. 7.1. Degenerate Raman sideband cooling of atomic samples works efficiently as long as the hyperfine levels of the excited state are well resolved. Since the $4P_{3/2}$ hyperfine splitting of ^{39}K is comparable to the line width of the $4S_{1/2} \rightarrow 4P_{3/2}$ transition, dRSC on the D_2 line is difficult. Therefore, the

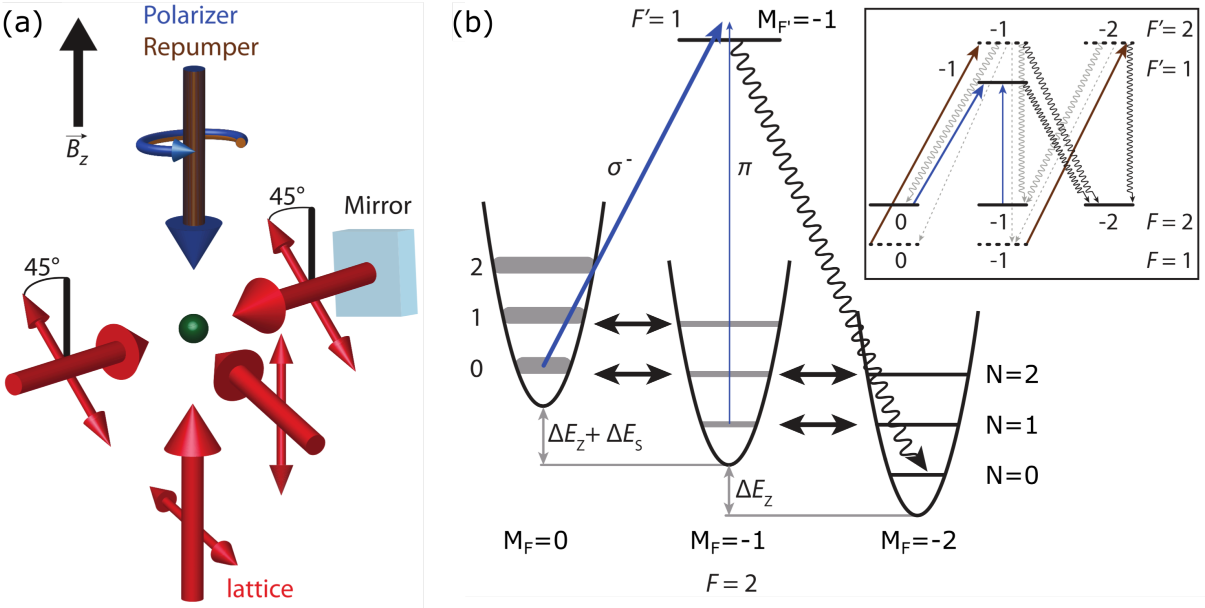

Figure 7.5.: Degenerate D_1 Raman sideband cooling of ^{39}K. The employed scheme for dRSC is similar to that operating on the D_2 transition for production of Cs condensates. (a) Configuration of the Raman lattice beams (red arrows), which have linear polarization, and polarizer beam as well as repumper beam (blue-brown arrow), which both have circular polarization. A magnetic offset field $\vec{B}_Z$ is applied in $z-$direction. (b) The magnetic offset field $\vec{B}_Z$ induces an energy shift ΔE_Z between the Zeeman states of the $F = 2$ hyperfine ground state and brings the vibrational states of different Zeeman states into degeneracy. The Raman lattice light induces two-photon Raman transitions (black, horizontal arrows) and transfers atoms from states $|M_F = -2, N\rangle$ to states $|M_F = 0, N-2\rangle$. A polarizer beam (blue arrows) with a strong σ^- polarization component and a much weaker π polarization component Stark-shifts the state $|F = 2, M_F = 0\rangle$ in energy by ΔE_S and broadens the vibrational levels. The inset shows the repumper beam (brown arrow) as well as spontaneous decay transitions into the $F = 2$ (grey, wiggled arrows) and $F = 1$ (grey, dashed arrows) hyperfine ground states. Spontaneous transitions into the $|F = 2, M_F = -2\rangle$ dark state are shown as black, wiggled arrows. Reprinted Figure from Ref. [Grö17b]. Copyright (2017) by the American Physical Society.

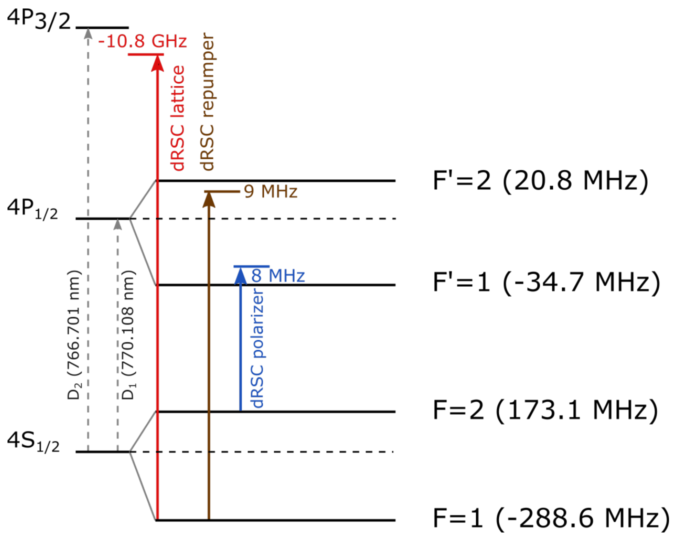

Figure 7.6.: Laser detunings for dRSC of ^{39}K. Detunings of the Raman lattice lasers (red arrow), polarizer laser (blue arrow), and repumper laser (brown arrow). Figure adapted from Ref. [Grö17b].

resolved hyperfine structure of the 4P$_{1/2}$ level was exploited to demonstrate dRSC on the D$_1$ line of ^{39}K within the K$-$Cs apparatus.

7.3.1. Principle of D$_1$ Line Degenerate Raman Sideband Cooling

The experimental scheme for dRSC of ^{39}K atoms that is used in the K$-$Cs apparatus is similar to that generally employed on the D$_2$ transition for production of Cs condensates [Han00, Vul98, Ker00, Ham98]. A far-off resonance 3D optical lattice is used to bind ^{39}K atoms to single lattice sites. The optical lattice is generated by three laser beams of which two are running waves and one is a retro-reflected standing wave. Figure 7.5 (a) depicts the spatial arrangement of the Raman lattice laser beams. The Raman lattice laser light is red-detuned from the 4S$_{1/2}$ $\rightarrow$ 4P$_{3/2}$ transition. Figure 7.6 shows the detunings of all laser beams that are employed for dRSC. The on-site lattice potential of each atom can be approximated by a harmonic potential. The total state of a trapped ^{39}K atom in the $F = 2$ hyperfine ground state is then given through its internal Zeeman state M_F as well as its motional state $|N\rangle$ and can be written as $|M_F, N\rangle$.

At the beginning of dRSC, the energy of the trapped ^{39}K atoms is larger than the spacing of the harmonic oscillator states $|N\rangle$ of the lattice sites. The atoms therefore populate different vibrational states after being loaded into the Raman lattice. By applying a magnetic offset field $\vec{B}_Z$ the Zeeman states of the $F = 2$ hyperfine level are shifted in energy by ΔE_Z relative to each other. To induce dRSC, the strength of the magnetic offset field is chosen such that the state $|M_F = -2, N\rangle$ becomes degenerate with the state $|M_F = -1, N-1\rangle$ and hence also with $|M_F = 0, N-2\rangle$. Figure 7.5 (b) depicts the harmonic on-site potential that is experienced by the atoms in the individual Zeeman states and illustrates the principle of degenerate Raman sideband cooling on the D$_1$ optical transition of ^{39}K. For degeneracy, the Raman lattice laser light drives two-photon Raman transitions between degenerate states $|M_F, N\rangle$ such as the transition $|M_F = -2, N\rangle \leftrightarrow |M_F = -1, N-1\rangle$. To maximize the Raman coupling, the polarizations of the running lattice waves are linear and fixed to lie within one plane. The polarization of the retro-reflected lattice laser beam is linear as well and the polarization vector forms an angle of

$45°$ with the magnetic field axis and lies within the same plane that includes the polarization vectors of the running waves.

During one cooling cycle, an atom that has been originally in state $|M_F = -2, N\rangle$ is transferred into state $|M_F = 0, N-2\rangle$ via two consecutive Raman transitions as shown in Fig. 7.5 (b). A σ^-–polarized laser beam (the so-called *polarizer beam*) excites the atom from state $|M_F = 0, N-2\rangle$ into the excited state $|F' = 1, M_{F'} = -1\rangle$ from which it can decay into state $|M_F = -2, N-2\rangle$, completing one cooling cycle. The polarizer beam propagates along the direction of the magnetic field $\vec{B}_Z$ and is blue-detuned from the $|F = 2\rangle \rightarrow |F' = 1\rangle$ transition by $8\,\mathrm{MHz}$ (see Fig. 7.6). In the Lamb-Dicke regime, the vibrational quantum number N of the atom is conserved during the spontaneous decay from state $|F' = 1, M_{F'} = -1\rangle$. One cooling cycle thus lowers the motional state of a trapped ^{39}K atom by two vibrational quanta. Cooling is repeated until the atom ends in state $|M_F = -2, N = 0\rangle$, which is decoupled from the polarizer beam and hence a dark state. If the atom ends in state $|M_F = -1, 0\rangle$, π–polarized light depopulates that state. The weak π–polarized light is generated by introducing a small angle between the polarizer beam and the magnetic field $\vec{B}_Z$. For the case that atoms decay from state $|F' = 1, M_{F'} = -1\rangle$ into the absolute hyperfine ground state $F = 1$, a repumper laser beam ($9\,\mathrm{MHz}$ red-detuned from the $F = 1 \rightarrow F' = 2$ transition) with σ^- polarization depopulates the lower hyperfine level.

7.3.2. Experimental Cooling Sequence

To implement dRSC of ^{39}K atoms to the experiment, the experimental sequence for laser cooling of ^{39}K atoms that was used in previous experiments (see Sec. 7.1.2) is modified. The adapted experimental sequence starts by loading a ^{39}K 3D-MOT, which works on the D_2 line. The 3D-MOT is loaded from a 2D-MOT within $5\,\mathrm{s}$ with about 3×10^8 atoms. The originally subsequent D_2 optical molasses cooling is omitted and instead the cooling procedure is now adopted from Ref. [Sal13]. In short, a compressed MOT phase is induced by increasing the 3D-MOT magnetic field gradient along the axis of the magnetic coils to 24 G/cm, decreasing the power of the 3D-MOT repumper beam to $10\,\mathrm{mW}$, and increasing the detuning of the 3D-MOT cooling light to $-34\,\mathrm{MHz}$ within $2\,\mathrm{ms}$. Thereafter, the magnetic field gradient is reduced to 6 G/cm, the MOT repumper power is lowered to $2\,\mathrm{mW}$, and the MOT cooling light is detuned to $-40\,\mathrm{MHz}$ and reduced in power to $40\,\mathrm{mW}$. Overall, this cooling step yields atomic samples with temperatures around $150\,\mu\mathrm{K}$. Next, a D_1 gray molasses cools the ^{39}K sample and reduces the requirements on the lattice depth of the Raman lattice. After gray molasses cooling the ^{39}K sample has reached a temperature of $8\,\mu\mathrm{K}$ with insignificant atom loss and has a phase-space density of $\mathcal{D} = 1.2 \times 10^{-5}$. Further details on the gray molasses cooling are discussed in Ref. [Grö17b]. As a last step of the ^{39}K laser cooling sequence, dRSC is initiated. To compensate for the anharmonicity of the on-site Raman lattice potentials and the spatial variation of the Raman lattice depth [Grö16], the magnetic offset field is ramped linearly between 800 mG and 50 mG in the course of the cooling procedure.

For studying the cooling performance of the dRSC scheme, the atoms are released adiabatically from the Raman lattice. A Stern-Gerlach experiment is then used to separate the $|F = 2, M_F = -2\rangle$ spin component. To determine the temperature of the $|F = 2, M_F = -2\rangle$ spin component, the expansion of the atom cloud of that spin component in horizontal direction is measured. As the expansion of the atom cloud is proportional to the temperature, temperatures are given in terms of the cloud radius σ_x after $30\,\mathrm{ms}$ of expansion in the following. In the experiments that are discussed in this Section, a cloud radius of $\sigma_x = 1\,\mathrm{mm}$

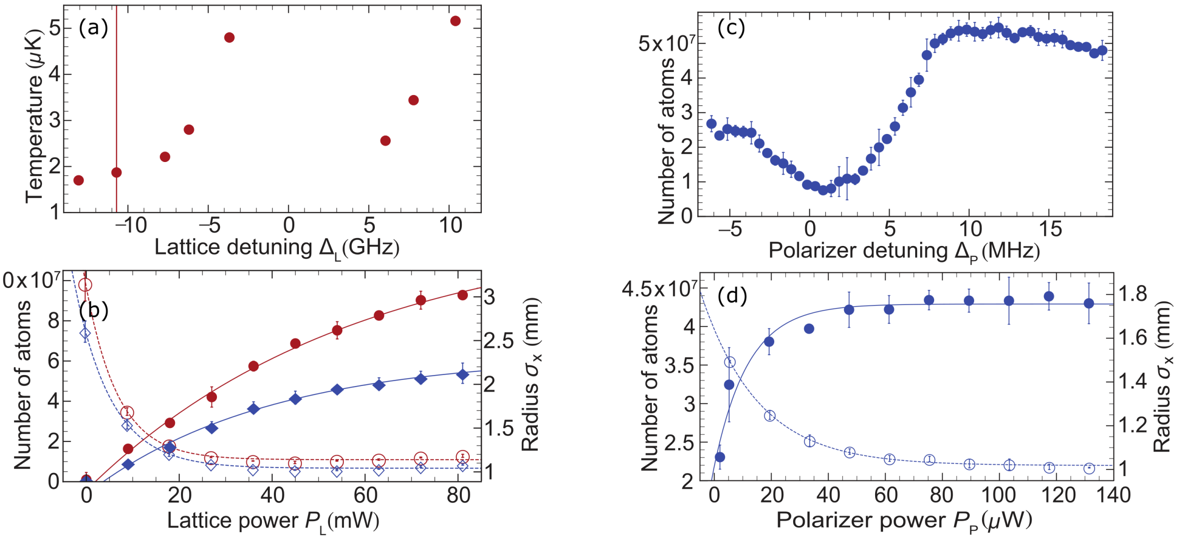

Figure 7.7.: Cooling efficiency of dRSC on ^{39}K. (a) Final temperature after dRSC for various lattice detunings Δ_L at a Raman lattice laser power $P_\mathrm{L} = 80\,\mathrm{mW}$. A detuning of $\Delta_\mathrm{L} = -10.8\,\mathrm{GHz}$ (vertical line) is used for all further measurements in this Section. Error bars are smaller than the size of the symbols. (b) Final atom number (solid symbols) and cloud radius σ_x (open symbols) for different lattice laser powers P_L. Blue symbols correspond to 1.2×10^8 atoms after gray molasses cooling and red symbols relate to 2.8×10^8 atoms. (c) Final atom number as a function of polarizer detuning Δ_P for a fixed polarizer laser power $P_\mathrm{P} = 120\,\mu\mathrm{W}$. (d) Final atom number (solid symbols) and cloud radius σ_x (open symbols) as a function of P_P. In (b) and (d), to guide the eye, the solid lines show a fit with a saturated growth function and the dashed lines a fit with an exponential decay function. Reprinted Figures from Ref. [Grö17b]. Copyright (2017) by the American Physical Society.

corresponds to a temperature of about $1.5\,\mu\mathrm{K}$. The radius σ_x is the standard deviation and is obtained through Gaussian fits to the integrated optical density of the atomic cloud, which in turn is derived from time-of-flight absorption images. The magnetic levitation field that is required for the Stern-Gerlach separation causes a magnetic force that accelerates the atoms along the horizontal directions away from the magnetic coil axis. Thus, the cloud radii σ_x given in this Section are upper bounds.

7.3.3. Experimental Results

In a first series of measurements, the efficiency of D_1 dRSC is studied for different Raman lattice laser detunings Δ_L from the D_2 line. For these measurements, the detunings of the polarizer and repumper beam are kept at $\Delta_\mathrm{P} = 8\,\mathrm{MHz}$ and $\Delta_\mathrm{R} = -9\,\mathrm{MHz}$. Figure 7.7 (a) shows the temperature of the ^{39}K cloud after dRSC at fixed Raman lattice laser power $P_\mathrm{L} = 80\,\mathrm{mW}$ for different detunings Δ_L. With increasing blue detuning ($\Delta_\mathrm{L} > 0$), the final temperature increases. This rise in temperature can be understood by the fact that the ^{39}K atoms within a blue-detuned lattice reside in potential minima where the lattice laser intensity is lowest. The rate of off-resonant excitations is thus reduced as well as the probability for Raman transitions, which, however, are required for dRSC. In contrast, for increasingly red-detuned lattice light ($\Delta_\mathrm{L} < 0$), a reduction of the final temperature is observed. In this detuning range, the ^{39}K

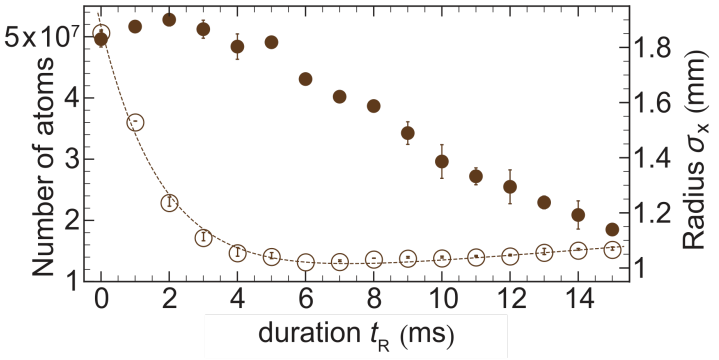

Figure 7.8.: Time dependence of dRSC performance. Final atom number (solid symbols) and cloud radius σ_x (open symbols) for different durations t_R of dRSC. The dashed line shows a combined fit with an exponential decay and a linearly increasing function to the experimental data as a guide to the eye. Reprinted Figure from Ref. [Grö17b]. Copyright (2017) by the American Physical Society.

atoms reside in potential minima where the lattice laser intensity is maximum. For larger $|\Delta_\mathrm{L}|$, off-resonant excitations are now suppressed more strongly than Raman transitions, leading to a lower temperature. On the other hand, a larger $|\Delta_\mathrm{L}|$ is observed to cause intensified atom loss, most likely due to the reduced lattice depth. Since the total power that is available for the Raman lattice light is limited, the lattice detuning for the following measurements is fixed to $\Delta_\mathrm{L} = -10.8\,\mathrm{GHz}$, for which the final phase-space density of the ^{39}K sample is the highest.

To study the influence of the Raman lattice laser power P_L on the cooling efficiency, the atom number and cloud radius σ_x of the atoms in state $|F = 2, M_F = -2\rangle$ after free expansion are measured as a function of P_L. The measurements are repeated for two different starting conditions, i.e. two different initial atom numbers of 1.2×10^8 atoms and 2.8×10^8 atoms. Figure 7.7 (b) shows the experimental data. The minimum cloud radius σ_x, and hence the minimum temperature, is reached for a total lattice power of around $P_\mathrm{L} \approx 30\,\mathrm{mW}$ or higher. At $P_\mathrm{L} \approx 30\,\mathrm{mW}$, the number of laser-cooled atoms has not saturated and continues to grow for higher laser power. In our experiments, a lattice laser power of $P_\mathrm{L} = 80\,\mathrm{mW}$ is therefore used.

Next, the impact of the polarizer beam on the dRSC is examined. To that end, the polarizer detuning Δ_P and laser power P_P are scanned as the number of atoms and the cloud radius σ_x is measured. Figure 7.7 (c) shows the number of atoms after dRSC for different detunings Δ_P at a power $P_\mathrm{P} = 120\,\mu\mathrm{W}$. The final atom number varies strongly with the detuning Δ_P. It is largest for blue detunings between +8 MHz and +15 MHz and has a minimum near resonance ($\Delta_\mathrm{P} \approx 0$). The occurence of the maximum and minimum in the atom number can be explained by the ac Stark shift ΔE_S (see Fig. 7.5) that is induced through the polarizer beam. The polarizer light shifts as well as broadens the vibrational levels of the $|F = 2, M_F = 0\rangle$ state. For detunings larger than +8 MHz, the light shift is sufficiently small to not impair the cooling mechanism. For $\Delta_\mathrm{P} \approx 0$, the light shift eliminates the degeneracy of the vibrational states and thus leads to a degraded cooling efficiency with a reduced number of atoms in state $|F = 2, M_F = -2\rangle$.

For a fixed detuning $\Delta_\mathrm{P} = 8\,\mathrm{MHz}$, now the dependence of the atom number and cloud radius σ_x on the polarizer power P_P is studied. Figure 7.7 (d) shows the measurement results. In order to achieve a noticeable reduction of the cloud radius, i.e. of the temperature, a minimum polarizer power of approximately 20 µW is needed. For obtaining the lowest temperature and simultaneously the largest atom number, a polarizer power of about 120 µW is required.

Table 7.2.: Gray molasses cooling vs. dRSC. Comparison of the performance of gray molasses cooling (GMC) and dRSC for different atom numbers after GMC. The approximate percentage of atoms in state $|F = 2, M_F = -2\rangle$ and the number of atoms in this state is given in the column 'Fraction' and 'Atom number', respectively. The column 'T' gives the final temperature of the atoms and $\mathcal{D}$ is the phase-space density in free space. Reprinted Table from Ref. [Grö17b]. Copyright (2017) by the American Physical Society.

	Fraction (%)	**Atom number**	**T (µK)**	$\mathcal{D}$
GMC		1.3×10^8	8	1.5×10^{-5}
dRSC	83	5.6×10^7	1.6	6×10^{-5}
GMC		3×10^8	8	1.2×10^{-5}
dRSC	78	1.4×10^8	1.8	1×10^{-4}

Finally, the cloud radius σ_x and the atom number are studied as a function of the duration t_R of dRSC. Figure 7.8 shows the measurement results for both quantities for different durations t_R. Within the first $7\,\mathrm{ms}$ of dRSC the temperature decreases by almost a factor of two and increases again for longer cooling times. Opposed to this, the number of atoms in state $|F = 2, M_F = -2\rangle$ stays nearly constant up to $t_\mathrm{R} = 5\,\mathrm{ms}$ and shrinks for larger t_R. One reason for the atom number reduction with longer cooling times could be tunneling of atoms in higher vibrational states. Tunneling can lead to atom diffusion out of the lattice or collisions with atoms of populated lattice sites and thus is a potential reason for atom loss.

A similar study of the dependence of the final temperature on the repumper detuning Δ_R and intensity I_R does not reveal any strong relation, except for a minimum intensity ($I_\mathrm{R} = 0.1\,\mathrm{mW/cm^2}$) that is required for inducing dRSC. A faint temperature minimum is observed for a red-detuned repumper with $\Delta_\mathrm{R} = -9\,\mathrm{MHz}$, which is therefore used for all previously discussed measurements.

Degenerate Raman sideband cooling of ^{39}K samples with the experimentally optimized parameters discussed above leads to samples with temperatures as low as $1.3\,\mathrm{\mu K}$. This temperature is much lower than that achieved with gray molasses cooling within our experimental sequence. Table 7.2 compares the performance of dRSC to gray molasses cooling within the K$-$Cs apparatus. The final temperature as well as the phase-space density $\mathcal{D}$ after dRSC show some dependency on the atomic density that is prevalent after gray molasses cooling and prior to dRSC. For an atom number of 1.3×10^8 atoms (3×10^8 atoms) at the beginning of dRSC, the final temperature was $1.6\,\mathrm{\mu K}$ ($1.8\,\mathrm{\mu K}$) and $\mathcal{D} = 6 \times 10^{-5}$ ($\mathcal{D} = 1 \times 10^{-4}$). To our best knowledge, these values correspond to the lowest temperatures and highest phase-space densities measured for spin-polarized ^{39}K atoms after laser cooling [Grö17b].

7.3.4. Conclusion

The experiments presented in this Section demonstrate the experimental realization of dRSC on the $\mathrm{D_1}$ optical transition for sub-Doppler laser cooling of ^{39}K samples. In comparison with the temperatures and phase-space densities that are obtained after gray molasses cooling within the K$-$Cs apparatus, the modified laser cooling scheme leads to a ten times higher phase-space density and a four times lower temperature. The demonstrated cooling scheme therefore leads to improved initial conditions for evaporative cooling within the K$-$Cs apparatus.

8. Design of the Science Chamber Setup

The science chamber of the K−Cs apparatus facilitates the implementation of the high-resolution imaging system. It is therefore a crucial part for the performance of fluorescence quantum gas microscopy of ultracold atoms and molecules in optical lattices. A significant amount of work of this Thesis thus has been dedicated to the designing and building of the science chamber. This Chapter presents two experimentally realized science chambers and the surrounding vacuum setups that are required to operate them. The two setups are based on different concepts: a stainless steel chamber and a fused silica glass cell. Both setups include an in-vacuo lens for high-resolution imaging and in-vacuo electrodes for polarizing KCs molecules. In the previously built Rb−Cs quantum gas apparatus of the Nägerl group in Innsbruck, the electrodes for generating electric fields have been mounted outside of the fused silica UHV cell. Due to the alkali-coated inner cell walls, the high electric field of the electrodes caused charging of the glass cell [Tak14].[1] These charging effects and the associated electric field drifts can possibly be reduced by having the electrodes internal to the fused silica glass cell. The two science chambers realized for the K−Cs apparatus rely on a number of home-built components, whose design and manufacturing are described in detail. With respect to the glass cell science chamber, the deformation of the glass cell window through which high-resolution imaging will take place due to the atmospheric pressure is analyzed. The glass cell science chamber setup has been successfully attached to the main vacuum system and is ready for operation.

8.1. General Considerations

In this Section, we list the experimental requirements on the science chamber and treat the question of which material is most suited for these purposes.

8.1.1. Experimental Requirements on the Science Chamber

We divide the experimental requirements on the science chamber into three categories: vacuum quality, experimental capabilities, and physical shape.

- Requirements on vacuum quality
  - The science chamber must provide a UHV environment with a pressure of around 10^{-11} mbar
  - To pump on the science chamber independently from the main chamber, the science chamber must have vacuum pumps at its own disposal

---

[1] After switching off the electrodes, the positive and negative charges recombined, leading to time varying electric fields within the glass cell over several days [Tak19].

- Requirements on experimental capabilities
  - The science chamber has to allow for the implementation of the K−Cs high-resolution imaging system (see Sec. 3.5.3)
  - The science chamber must provide in-vacuo electrodes
  - To polarize KCs molecules, the electrodes have to be capable of generating electric fields with field strengths up to $\sim 2.5\,\mathrm{kV/cm}$
  - The electric fields that are generated by the electrodes have to be homogeneous enough to study spin lattice models, e.g. the Heisenberg XXZ spin lattice model (see Sec. 1.2.2), with ^{39}KCs molecules
- Requirements on physical shape and material
  - The science chamber must allow for the optical transport of ultracold atoms from the main chamber into the science chamber as discussed in Sec. 3.5.2
  - For optical lattice generation, internal-state manipulation, and probing optical access to the atoms within the science chamber is needed from different directions
  - The science chamber windows must have anti-reflection coatings on the inner and outer surfaces with minimum reflectivity at the imaging wavelengths for K ($\lambda^{\mathrm{K}}_{\mathrm{image}} = 766\,\mathrm{nm}$) and for Cs ($\lambda^{\mathrm{Cs}}_{\mathrm{image}} = 852\,\mathrm{nm}$) and at $1064\,\mathrm{nm}$ for optical lattices
  - To hold and align the in-vacuo lens of the high-resolution imaging system and the in-vacuo elctrodes, an internal mounting construction is required
  - Because of limited lab space the overall size of the science chamber has to be as compact as possible
  - The design must aim for a non-magnetic environment

8.1.2. Two Science Chambers: Stainless Steel and Fused Silica

Since we do not want to use different metals within the K−Cs apparatus because of their different thermal behavior during baking out of the vacuum chamber, the choice of material for the science chamber restricts to stainless steel and glass. Obviously, the mechanical strength of a stainless steel chamber is ideal for mounting internal components such as electrodes. If in future new lasers with different wavelengths will be installed in the experimental setup, a stainless steel science chamber permits the replacement of viewports with others that have adapted anti-reflection coatings. A stainless steel chamber is thus particularly beneficial with respect to flexibility. A significant drawback of a stainless steel science chamber, however, is the magnetic permeability of stainless steel, which can lead to troubling magnetization effects.

Fused silica glass cells, on the other hand, provide a non-magnetic environment. Fused silica glass cells with cross sections as small as $1\,\mathrm{cm}^2$ have been used in ultracold atom experiments [Gol04]. Thus, the dimensions of a glass cell can be much smaller than for CF stainless steel chambers. The optical access to a glass cell typically exceeds that of a stainless steel chamber but comes at the expense of other limitations. For example, due to the fragility of glass, mounting components within a fused silica cell is more complicated compared to a stainless steel chamber.

Two independent science chamber setups were designed and realized within the course of this Thesis. The first one is centered around a stainless steel chamber and the second one

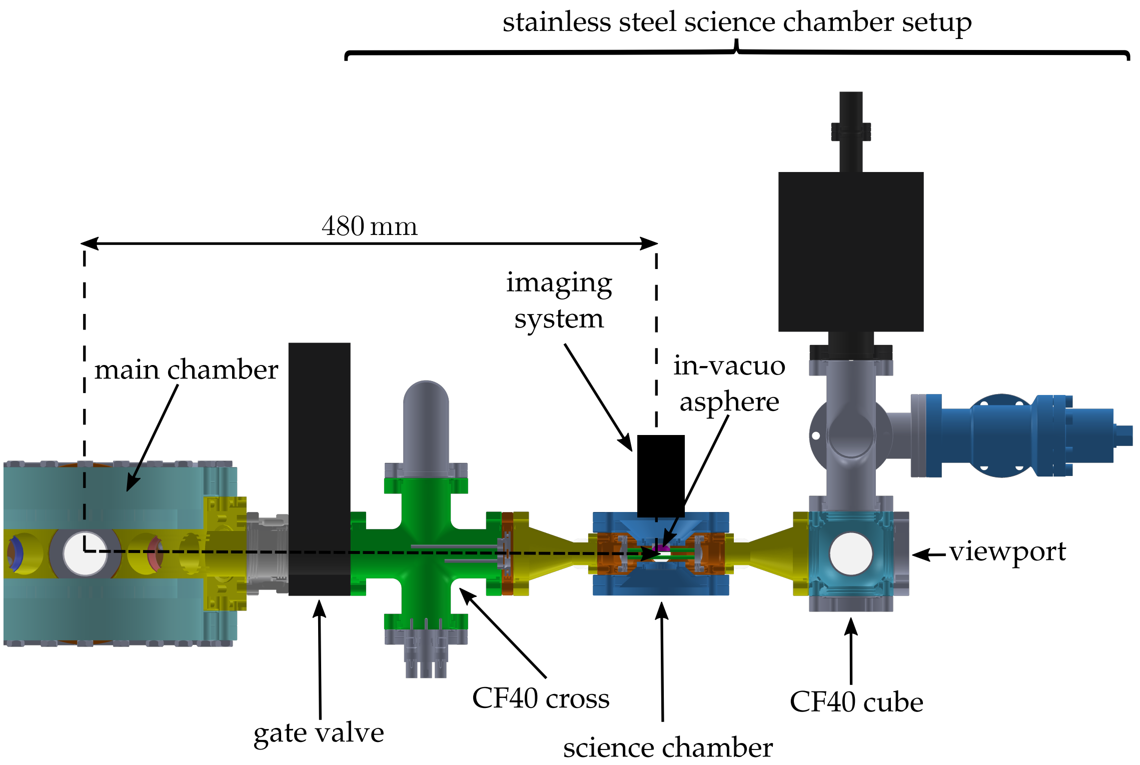

Figure 8.1.: Implementation of the stainless steel science chamber setup to the main chamber. The stainless steel science chamber setup would connect to the gate valve at the main chamber. A CF40 cross and a CF40 cube hold the science chamber on the left and right side. The transportation path of the atoms from the main chamber to the science chamber is indicated through a dashed arrow. At the science chamber, an in-vacuo aspheric lens is held above the center of the science chamber. Together with the externally mounted imaging system, high-resolution imaging of atoms can be performed from the top of the chamber.

involves a glass cell. At first, the goal of having a stainless steel science chamber was pursued. After the magnetization effects at the main chamber became apparent (see Sec. 7.2), the work on the stainless steel science chamber was stopped and the planning of a glass cell science chamber began. Both science chambers including their surrounding vacuum setups that are required to operate the two chambers were assembled and tested. Eventually, the glass cell setup was attached to the main vacuum system.

8.2. Stainless Steel Science Chamber

In this Section, the design and assembly of the stainless steel science chamber and its intended implementation to the K$-$Cs apparatus is discussed. Furthermore, comments on the manufacturing of a series of home-built vacuum parts are given.

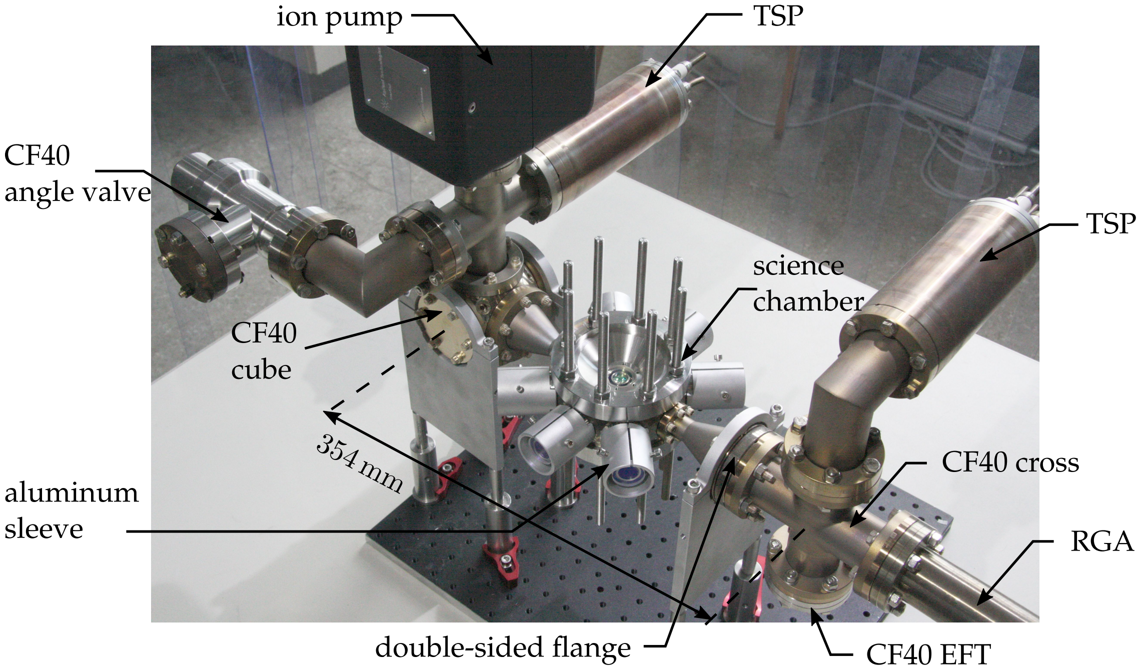

Figure 8.2.: The realized stainless steel science chamber setup. The central part of the stainless steel science chamber setup is a stainless steel science chamber. A CF40 cube and a CF40 cross provide mounting options for an ion pump, two home-built titanium sublimation pumps (TSPs), an angle valve, as well as an electrical feedthrough (EFT). A double-sided flange at the CF40 cross is used to connect the science chamber to it. The viewports that were installed on the CF40 cube are not shown here. Slotted aluminum sleeves protect the horizontal viewports against damage. During the test phase of the setup, a residual gas analyzer (RGA) was connected to the right side of the CF40 cross.

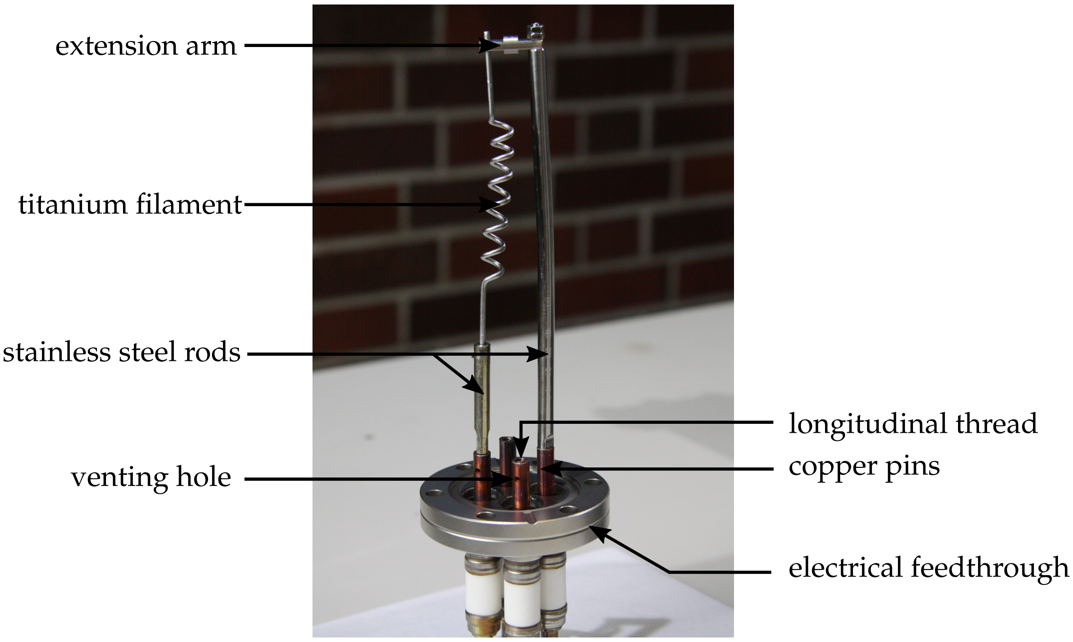

Figure 8.3.: Titanium sublimation pump. Each of the two home-built TiSub pumps consists of a commercial titanium filament that is chucked between a stainless steel rod and a stainless steel extension arm. The stainless steel rods are screwed into the copper pins of a commercial electrical feedthrough, which were first shortened and then processed to have internal threads and venting holes.

8.2.1. Overview

The stainless steel science chamber setup centers around a stainless steel chamber with vacuum equipment being mounted to two opposite sides of the steel chamber. Figure 8.1 shows a vertical cut of the stainless steel science chamber setup and demonstrates its intended implementation to the main vacuum system. The steel chamber was planned to connect to the gate valve at the main chamber through a CF40 cross. To mechanically support the science chamber setup and avoid any torque acting on the gate valve, the science chamber setup would be held by vertical pillars. The optical transport of the atoms from the main chamber to the science chamber would take place along a horizontal axis over a distance of $480\,\mathrm{mm}$. Right above the center of the science chamber, the front lens of the imaging system is installed under vacuum to allow for high-resolution imaging along the vertical axis as shown in Fig. 8.1.

Figure 8.2 shows the completed stainless steel science chamber setup as it was realized. A spherical CF40 cube[2] and a CF40 cross[3] connect to the left and right side of the science chamber in Fig. 8.2 via two opposing, conical CF40-to-CF16 reducers[4]. The cube and cross serve for installation of various vacuum components such as viewports, a CF40 angle valve[5], a 4-pin electrical feedthrough[6], an ion pump[7], and two TiSub pumps. Both TiSub pumps are

---

[2] Kimball Physics, MCF275-SphCube-C6.

[3] Vacom, X40RS-316LNS.

[4] The CF40 and CF16 flanges of the reducers are made out of stainless steel type 1.4429 ESU.

[5] VAT, Easy-close all-metal angle valve, CF40, Series 541.

[6] Lesker, IFTSG041033.

[7] Agilent Technologies, VacIon Plus 20, StarCell.

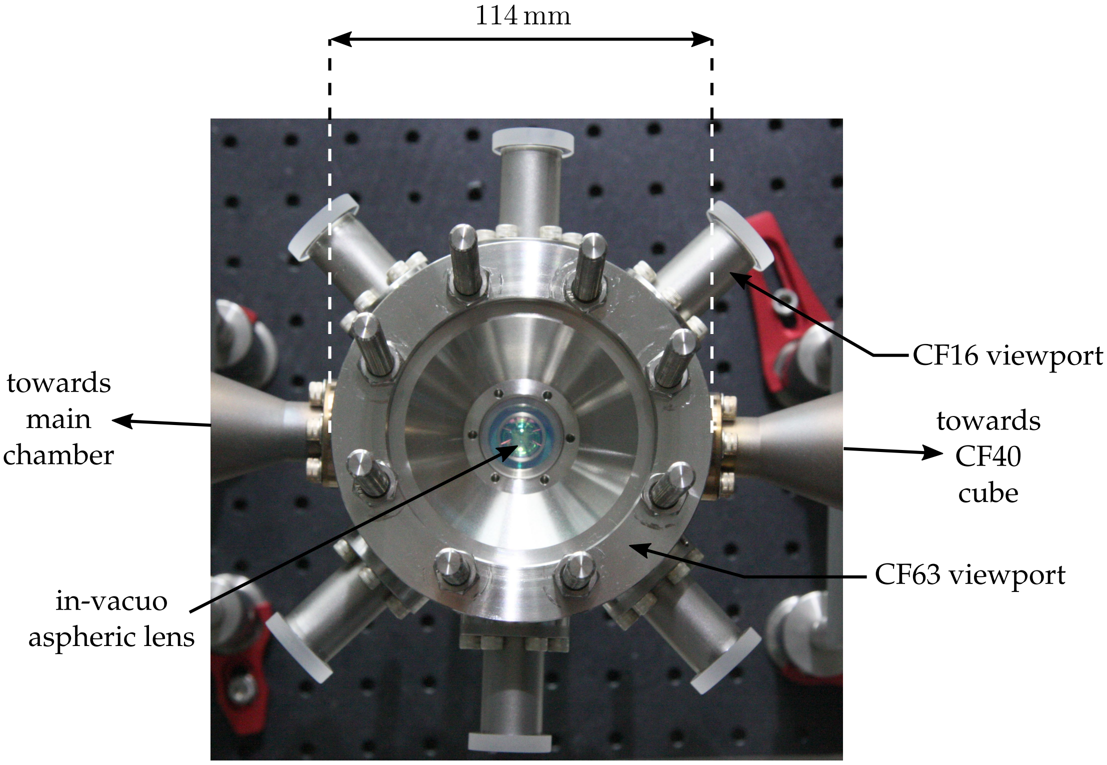

Figure 8.4.: Stainless steel science chamber (top view). The stainless steel science chamber contains six horizontal CF16 viewports and two vertical CF63 viewports. All viewports are home-built and anti-reflection coated. The aspheric lens of the imaging system is inside of the science chamber and is attached to the inner surface of the upper viewport.

home-built. Initially, it was planned to have two science chambers within the K−Cs apparatus. The second science chamber would have been added to the right flange of the CF40 cube in Fig. 8.1. For reasons of a relatively long transportation path, this plan was not realized.

Figure 8.3 shows one of our TiSub pumps after completion. The copper pins on the vacuum side of the electrical feedthrough were first shortened and equipped with longitudinal threads and venting holes. Two stainless steel rods were then screwed into the copper pins. A commercial titanium filament is mechanically clamped in-between the shorter stainless steel rod and a stainless steel extension arm.

8.2.2. Layout of the Stainless Steel Science Chamber

The stainless steel science chamber is a commercial, octagonal chamber[8] that is made out of austenitic stainless steel of type AISI 316L. It has in total two CF63 flanges and eight CF16 flanges. The chamber is oriented within the setup such that the CF63 flanges are horizontal as can be seen from Fig. 8.2. All flanges of the science chamber, except for the two CF16 flanges to which the conical reducers are connected, are equipped with viewports. Figure 8.4 shows a top view of the stainless steel science chamber with the aluminum sleeves from Fig. 8.2 being

---

[8] Kimball Physics, MCF450-SphOct-E2A8.

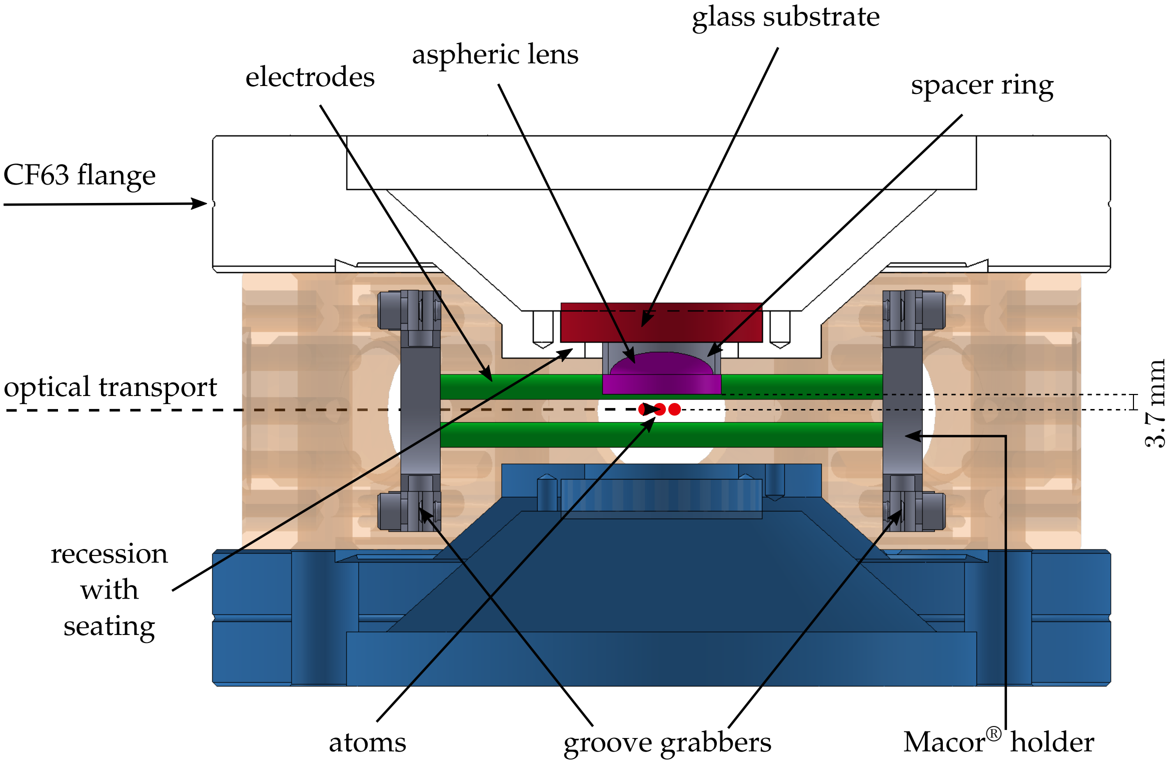

Figure 8.5.: Mounting of the aspheric lens. The figure shows a vertical cut of the stainless steel science chamber. The top (white) and bottom (blue) CF63 viewports are re-entrant viewports with a tapered form. The glass substrate of each viewport is positioned within a recession and glued to the seating. An aluminum ring is glued to the inner surface of the upper glass substrate (red). It serves as spacer ring for the aspheric lens (purple), which is glued to the opposite side of the aluminum ring. Upper and lower viewport are identical except for the aspheric lens and the aluminum ring. Rod electrodes (green), which are held by Macor® holders and groove grabbers within the science chamber, allow the generation of electric fields.

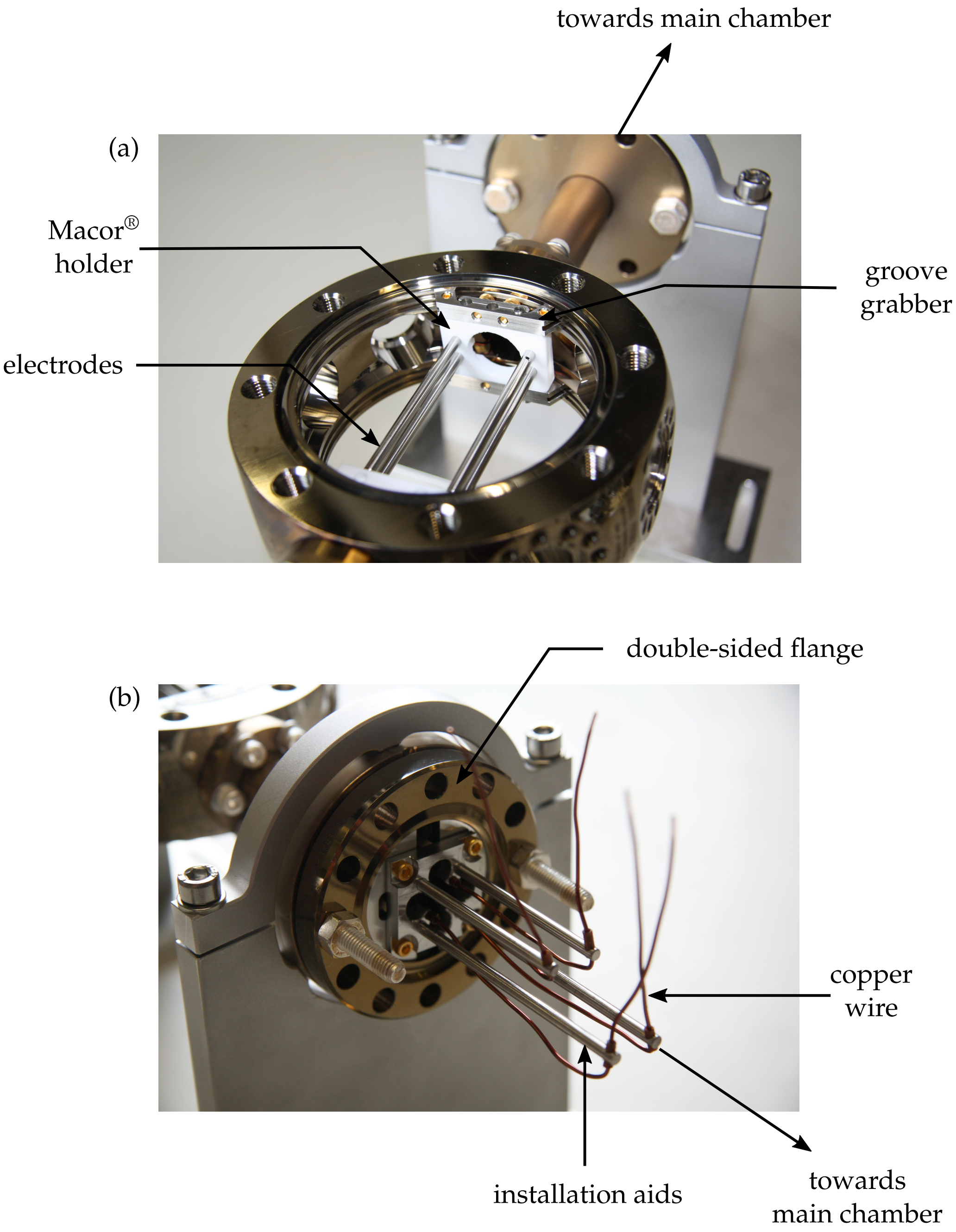

Figure 8.6.: Mounting of the electrodes. (a) Four rod electrodes in parallel, rectangular configuration are mounted inside of the stainless steel science chamber. The electrodes are isolated from the chamber by Macor® holders and are held by groove grabbers. (b) Insulated copper wires make the connections between the electrodes and the electrical feedthrough. The wires are guided from the science chamber to the electrical feedthrough through a CF40-to-CF16 reducer. In order to prevent blocking of the transportation beam, the copper wires meander along four rods. The rods are fixed to a double-sided flange and serve as installation aids for the wires. At an early stage of building the science chamber setup straight CF40-to-CF16 reducers (as shown here) were used. These were replaced by conical reducers because of their enhanced gas flow conductance.

removed from the viewports. The horizontal CF16 viewports are turned to the outside.

The upper CF63 viewport holds the in-vacuo aspheric lens of the high-resolution imaging system. In order to bring the lens close to the center of the science chamber where the atoms would sit, it is a tapered re-entrant viewport. Figure 8.5 shows a vertical cut of the science chamber and illustrates the shape of the CF63 viewport as well as the location of the aspheric lens relative to the atoms. A fine-machined metallic spacer ring embraces the lens. It is glued to the inner surface of the glass substrate of the upper viewport on one side and to the lens on the other side. The thickness of the spacer ring determines the vertical position of the lens. It was chosen such that the distance of the lens to the atoms is $3.7\,\mathrm{mm}$, which corresponds to the working distance of the imaging system. The spacer ring guarantees that the lens is aligned parallel to the viewport and thereby reduces aberrations in the imaging system. The lower viewport is a copy of the upper viewport except that no lens is connected to it.

To generate electric fields within the science chamber, four parallel rod electrodes were installed inside of it. The rod electrodes are each $66\,\mathrm{mm}$ long and $3.15\,\mathrm{mm}$ in diameter. Two home-built holders support the electrodes on both ends and bring them into a rectangular $22 \times 6\,\mathrm{mm}$ configuration parallel to the transportation axis (see Fig. 8.5). The holders are clamped between groove grabbers[9], which fit into internal grooves of the science chamber. To isolate the electrodes against the groove grabbers, the holders are made out of a machinable and low-outgassing glass ceramic called Macor®. Figure 8.6 (a) shows the stainless steel science chamber during the assembly and illustrates the internal mounting of the electrodes. Vacuum-compatible Kapton™-insulated copper wires connect the electrodes to the pins of the electrical feedthrough. To guide the wires through the CF40 cross towards the electrical feedthrough, four rods that are mounted to a double-sided flange[10] between the CF40 cross and the conical reducer serve as installation aids. Figure 8.6 (b) depicts the double-sided flange and the fixing of the copper wires to the installation aids. This construction prevents the wires from blocking the transportation beam, which also would pass through the CF40-to-CF16 reducer. With the described configuration of the electrodes electric field strengths up to $4.2\,\mathrm{kV/cm}$ can be reached as found in a computational simulation. The maximum electric field strength is limited by the maximum voltage that the electrical feedthrough can handle.

8.2.3. Home-Built Viewports

All viewports of the stainless steel science chamber are home-built. This approach opens up the perspective to gain knowledge on manufacturing vacuum-compatible viewports for future applications.

CF16 Viewports

Standard CF16 straight connectors[11], consisting of two CF16 flanges and a stainless steel tube in-between, form the basis for the CF16 viewports. The stainless steel tube of the straight connectors has an inner diameter of $16\,\mathrm{mm}$ and a wall thickness of $1.5\,\mathrm{mm}$. To manufacture viewports, the CF16 straight connectors were cut into two pieces of equal lengths. Figure 8.7 (a) and (b) show one of the home-built CF16 viewports. Once the connectors were cut into halves, the machined surface of each half was first flattened and then polished using sand paper of grain size 600, 800, and finally 1200. Figure 8.7 (c) depicts the polished surface of a cut

---

[9] Kimball Physics, MCF450-GrvGrb-C03.

[10] Kimball Physics, MCF275-ThnFlg-C2-400-ID1500GG.

[11] Vacom, SC16R-316LNS.

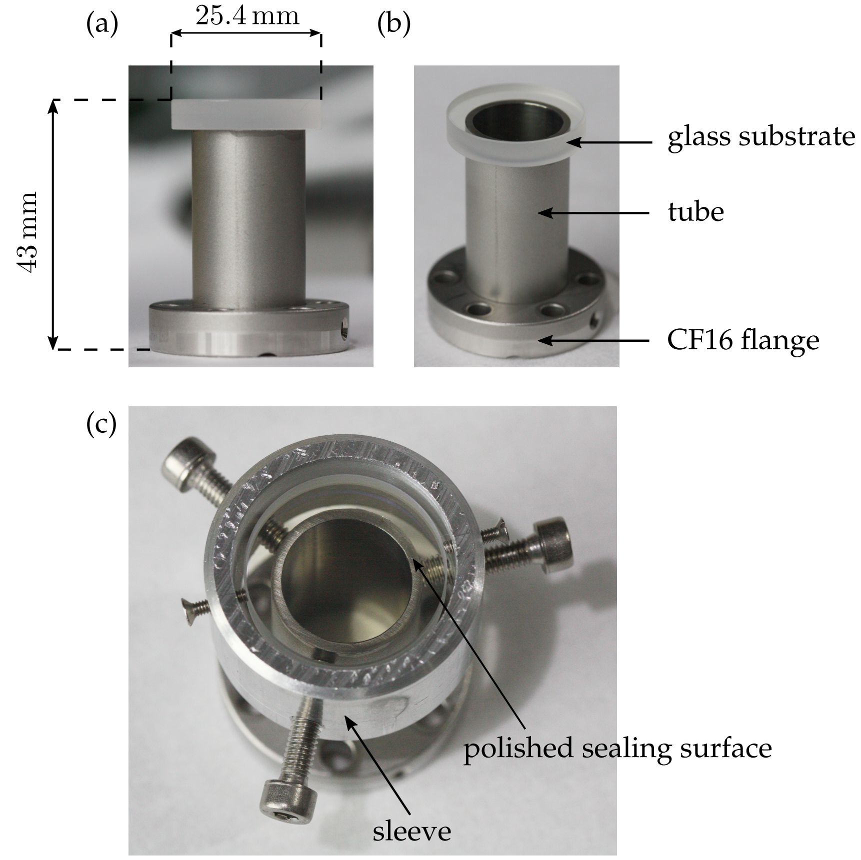

Figure 8.7.: Home-built CF16 viewports. (a)+(b) The CF16 viewports consist of a flat glass substrate that is glued on top of a CF16 half nipple. (c) Before making the contact, the metallic sealing surface is polished with sand paper. During baking, when the glue is still liquid, a sleeve protects the glass substrate against slipping.

straight connector tube. After checking the polished surface for scratches with a microscope, a cylindrical glass substrate was contacted to the polished surface with a continuous, thin layer of the liquid vacuum leak sealant VacSeal. The glass substrates are commercial fused silica windows[12] with a 1-inch diameter, a thickness of $5\,\mathrm{mm}$, and a two-side broadband anti-reflection coating for wavelengths from $650\,\mathrm{nm}$ to $1050\,\mathrm{nm}$. To cure the glue, each viewport was baked in an oven for several hours. Table 8.1 lists the temperature ramps that were used for curing. Cooling down of the oven was reached by switching off the oven and waiting until the heat had dissipated. The oven reached room temperature typically after about $\sim$10 hours. To verify that the sealing line was gapless and undamaged after the baking process, the viewports were once more subjected to a visual check with a microscope. In many cases, the glue migrated during the baking process and left behind sealing lines of reduced width or some that were clearly flawed. Likewise, undesired bubbles, whose origin remained unclear, manifested in the sealing of several viewports. In both cases, to avoid potential breaking of the corrupted sealing and to prevent outgassing of the bubbles, the imperfect viewports were sorted out.

Commercial anti-reflection coated CF viewports (clear view typically around $16\,\mathrm{mm}$ in

---

[12] Thorlabs, WG41050-B.

Table 8.1.: Temperature ramps for curing the home-built viewports.

Ramp from	Ramp to	Within
room temperature	60 °C	60 min
60 °C	60 °C	20 min
60 °C	80 °C	40 min
80 °C	80 °C	20 min
80 °C	100 °C	20 min
100 °C	100 °C	4300 min
100 °C	room temperature	typically 10 h

diameter) suffer from shadowing effects during the coating process. These shadowing effects rule out having the anti-reflection coating over the full clear view of the viewport. In contrast, our home-built CF16 viewports have an anti-reflection coated clear view of 16 mm in diameter, giving us more optical access to the atoms in comparison to commercial CF16 viewports.

CF63 Viewports

The CF63 viewports of the stainless steel science chamber are composed of a CF63 flange onto which a flat glass substrate is glued. The flange is home-built out of austenitic stainless steel of grade 1.4435/BN2. Figure 8.8 (a) and (b) show the upper CF63 viewport with the aspheric lens that is attached to it. The outer diameter of the flange is 113.5 mm and the inwards protrusion is 11 mm. The glass substrate is of the same type as the ones used for the home-built CF16 viewports. It is glued to the seating of the flange with VacSeal. The 19.4 mm-diameter hole in the center of the flange determines the clear view of the viewport. To glue the substrate to the flange, the procedure was similar to the previous description: after polishing and glueing, the CF63 viewports were finally baked with the temperature ramps given in Table 8.1. On the vacuum side of the viewport the aspheric lens of the high-resolution imaging system is glued onto the glass substrate via an aluminum spacer ring. The spacer ring has a venting hole on the side as pointed out in Fig. 8.8 (a). A technical drawing of the CF63 flange is given in Appendix D.1.

8.2.4. Assembly of the Stainless Steel Science Chamber Setup

Prior to the assembly of the stainless steel science chamber setup, all stainless steel vacuum parts were air baked at temperatures between ∼300 °C and 400 °C to form a surface oxide layer that reduces outgassing of the bulk material. Furthermore, each viewport was helium-leak tested separately. During the helium leak tests the partial pressure of helium was constantly in the lower 10^{-12} mbar range, thus indicating a leak-free sealing.

The construction work of the science chamber setup was characterized by different complications. After having built the entire science chamber setup, leaks were detected at the viewports several times. Partially, the leaks could be sealed by external application of VacSeal to the leaks. In other cases, the corrupted viewports were removed and replaced with new ones. The reasons for the occurence of the leaks remained unclear. At another point, an ion gauge[13] that was temporarily mounted to the bottom of the CF40 cube broke during bakeout

---

[13] Agilent Technologies, UHV-24p ion gauge with two tungsten filaments.

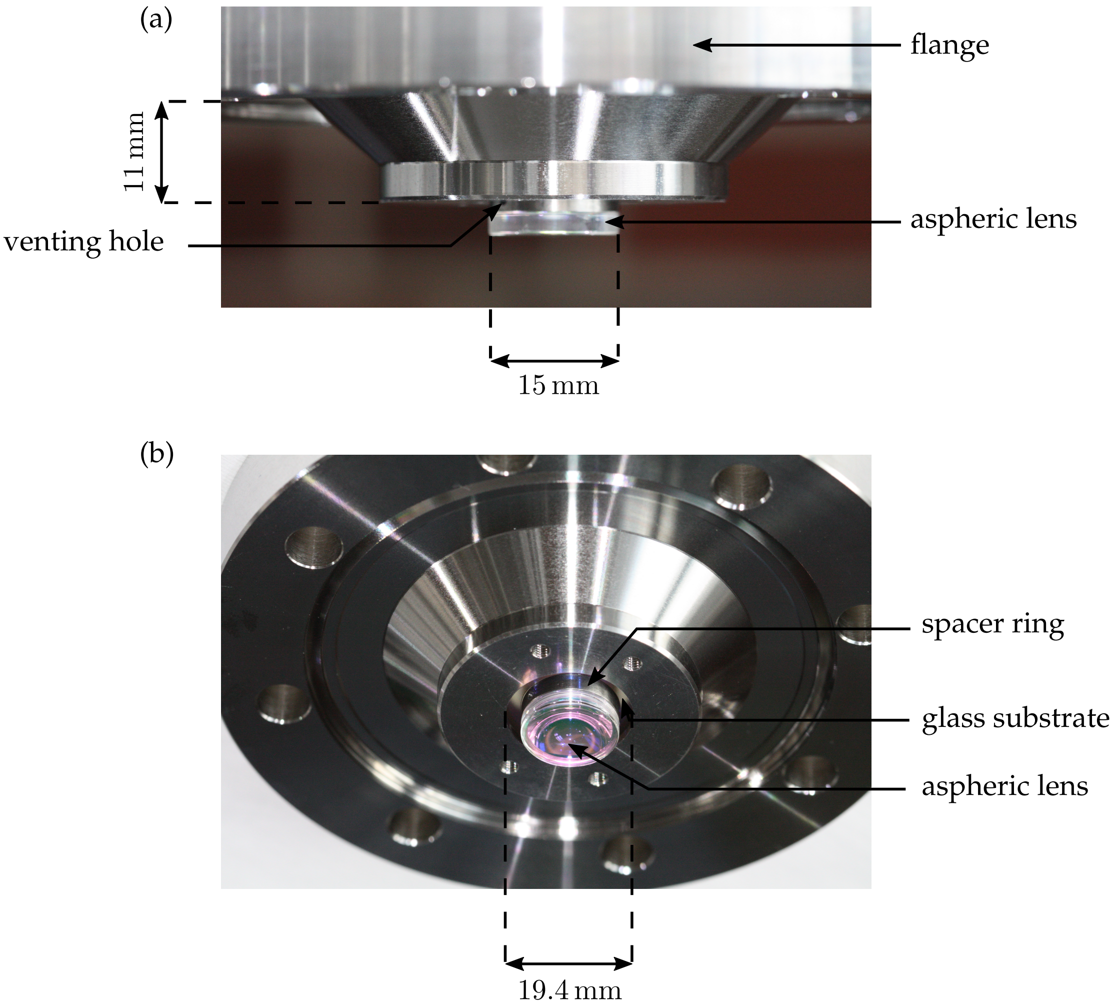

Figure 8.8.: Home-built CF63 viewport. (a) Side view of a CF63 viewport. The viewports are inverted and have a conical protrusion. (b) At the upper viewport we connected the aspheric lens of the imaging system to the inner surface of the glass substrate via an aluminum spacer ring. A hole within the spacer ring allows for venting the cylindrical volume between lens and glass substrate.

and required to exchange the ion gauge and repeat the pumping and baking procedure for another time. Furthermore, presumably inferior copper gaskets demanded to rebuild parts of the setup. In the course of testing the science chamber setup, the setup was also modified a few times. In order to achieve a higher pumping speed at the science chamber, for instance, the formerly mounted CF40-to-CF16 straight connectors were exchanged for conical ones. In addition, a second home-built TiSub pump (besides the one at the CF40 cube) was added to the setup at the CF40 cross.

After having baked the latest version of the science chamber (science chamber baked at $120\,^{\circ}\mathrm{C}$ and all other components at temperatures between $100\,^{\circ}\mathrm{C}$ and $240\,^{\circ}\mathrm{C}$) for six days, a pressure of $4 \times 10^{-10}\,\mathrm{mbar}$ was achieved, which gradually increased to $1.2 \times 10^{-9}\,\mathrm{mbar}$. The pressure was measured with an ion gauge at the CF40 cube and therefore right in the vicinity of the ion pump and TiSub pump. Given the limited gas flow conductance of the conical CF40-to-CF16 reducers, the pressure within the stainless steel science chamber was expected to be higher than the pressure measured by the ion gauge. At about the same time, the experiments within the main chamber pointed out the magnetization effects associated with stainless steel chambers. As a consequence, we stopped working on the stainless steel science chamber setup and focused on a new setup that involves a glass cell.

8.3. Glass Cell Science Chamber

In this Section, the design of the glass cell science chamber setup, its internal mounting construction, and the influence of the atmospheric pressure on the top glass cell window is discussed.

8.3.1. Overview

The glass cell science chamber setup consists of two units: a glass cell that incorporates the aspheric lens of the high-resolution imaging system (see Sec. 3.5.3) and an operational unit that comprises all components for operating the science chamber setup. Figure 8.9 gives an overview of the glass cell science chamber setup and clarifies the distinction between the glass cell and the operational unit. The operational unit centers around a CF40 six-way cube[14]. In Fig. 8.9, the cube holds the glass cell on its right side and makes the connection to the gate valve of the main chamber via a stainless steel joint[15] of minimal length (*close coupler*) on its left side. On top of the cube a CF40 cross[16] joins a CF40 angle valve[17], an ion pump[18], and a commercial TiSub pump[19] for creating and maintaining UHV inside of the glass cell setup. Sidewise, two commercial viewports give optical access to the cube for probing the atoms during their transport to the glass cell. On the bottom side of the cube a four-pin electrical feedthrough[20] facilitates feeding voltages up to $\pm 10\,\mathrm{kV}$ into the setup. The overall transportation distance from the center of the main chamber to the center of the glass cell is $464\,\mathrm{mm}$.

---

[14] Kimball Physics, MCF275-SphCube-C6.

[15] Kimball Physics, MCF275-ClsCplr-C2-1400.

[16] Vacom, X40R-316LNS.

[17] VAT, Easy-close all-metal angle valve, CF40, Series 541.

[18] Agilent Technologies, VacIon Plus 20, StarCell.

[19] Videko, TSP cartridge with three filaments (product number: 360547).

[20] Lesker, SHV-10 CF40 electrical feedthrough, IFTVG041053.

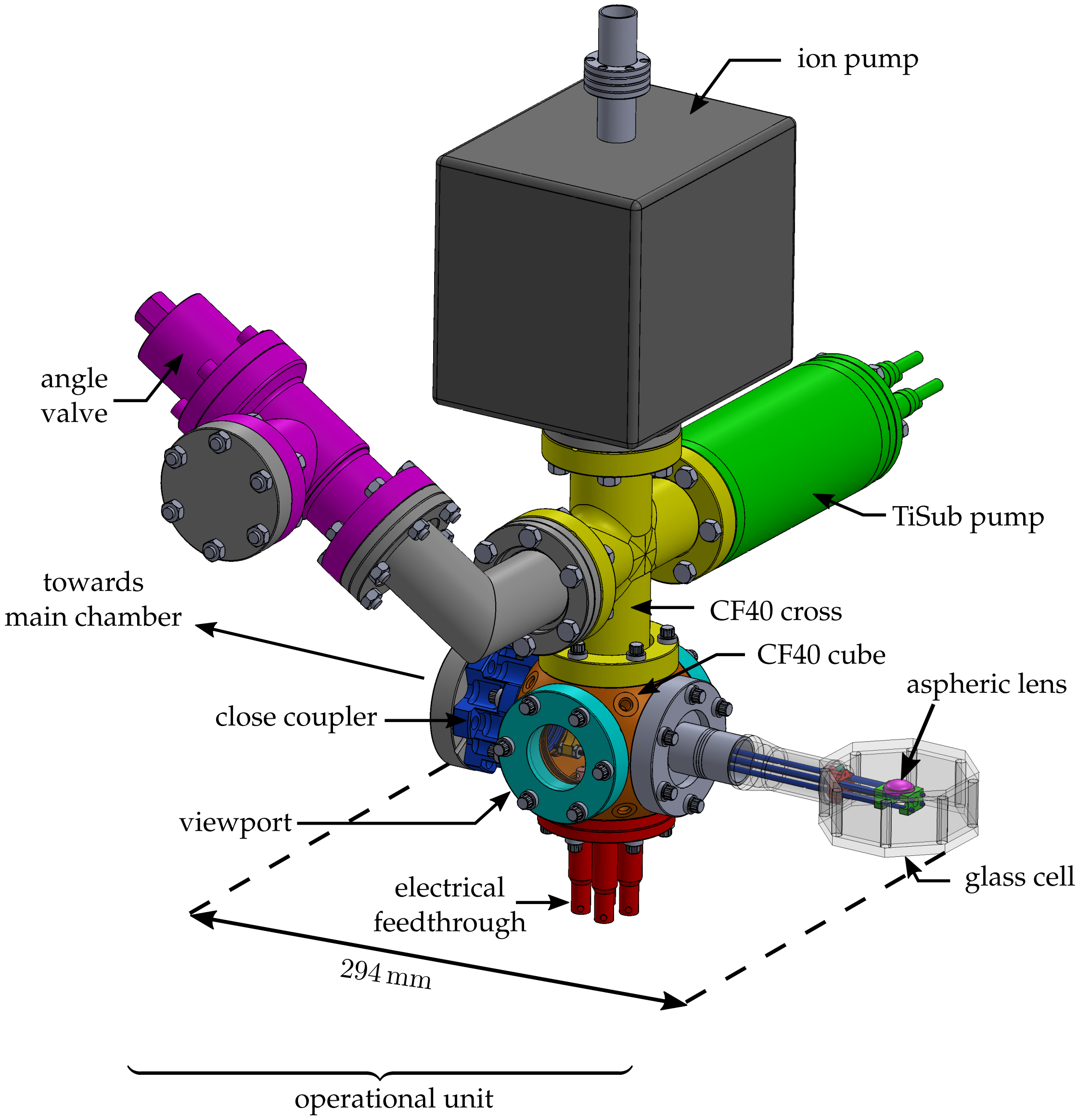

Figure 8.9.: Overview of the glass cell science chamber setup. The glass cell setup centers around a CF40 cube to which a UHV glass cell is connected. To operate the glass cell setup, a number of different components are mounted to the cube. These components include an angle valve, an ion pump, a TiSub pump, viewports, and an electrical feedthrough. A close coupler on the left side of the cube allows the connection of the entire glass cell setup to the gate valve of the main chamber. For the test setup of the glass cell, the close coupler was terminated with a blind flange.

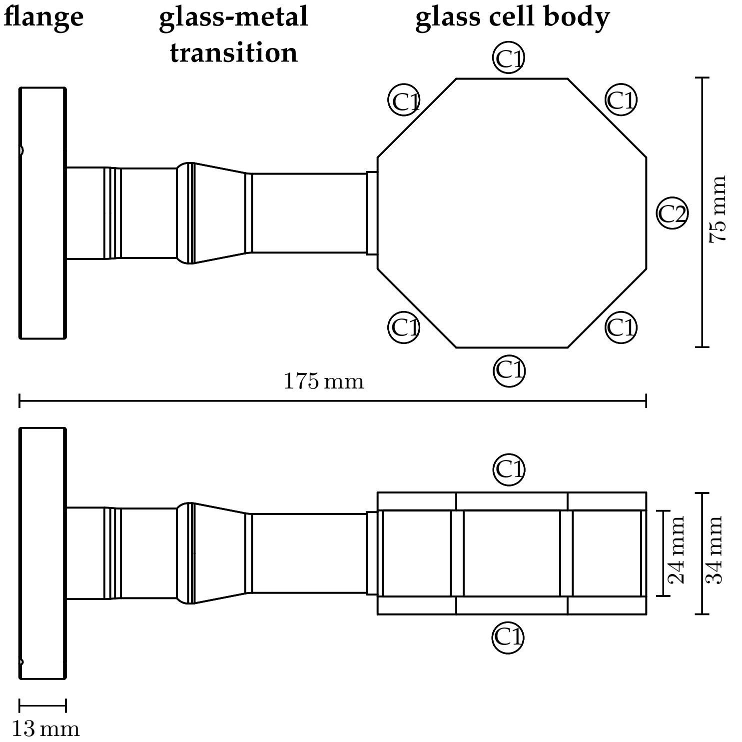

Figure 8.10.: Conceptual drawing of the glass cell. The glass cell can be divided into three parts: a CF40 flange, a glass-metal transition, and a glass cell body. The glass cell body consists of ten individual flat glass substrates that are bonded together. The anti-reflection coating of the individual substrates are indicated through C1 (anti-reflection coating type 1) and C2 (anti-reflection coating type 2). Specifications of the coatings are discussed in the main text.

8.3.2. Layout of the Glass Cell Science Chamber

The glass cell is a custom-made UHV cell and was manufactured by Japan Cell. It consists of an octagonal glass cell body, which connects to a CF40 flange via a glass-metal transition. Figure 8.10 shows a conceptual drawing of the glass cell. The flange is made out of austenitic stainless steel and rotatable. The glass cell body has an outer width of $75\,\mathrm{mm}$ and an outer height of $34\,\mathrm{mm}$. The tubular glass-metal transition matches the thermal expansion coefficients of glass and stainless steel and thus reduces temperature-induced mechanical stress within the glass cell during bake out. It was demanded by us to be non-magnetic. The overall length of the glass cell is $175\,\mathrm{mm}$. A technical drawing of the glass cell is given in Appendix E.1.

The glass cell body is built up of ten individual $5\,\mathrm{mm}$-thick flat fused silica substrates[21] that are bonded together to form an octagonal cylinder. The optical flatness of each substrate was specified to be $\lambda/6$ at $632\,\mathrm{nm}$ and the parallelism to be smaller than $20''$. Each of the glass substrates is anti-reflection coated on both sides with one of the following two coating types:

---

[21] Japan Cell did not disclose the name of the fused silica type that was used for the glass cell substrates. Instead, Japan Cell referred to the similarity between the optical properties of the fused silica of the glass substrates and the originally requested material Corning® HPFS® 7980.

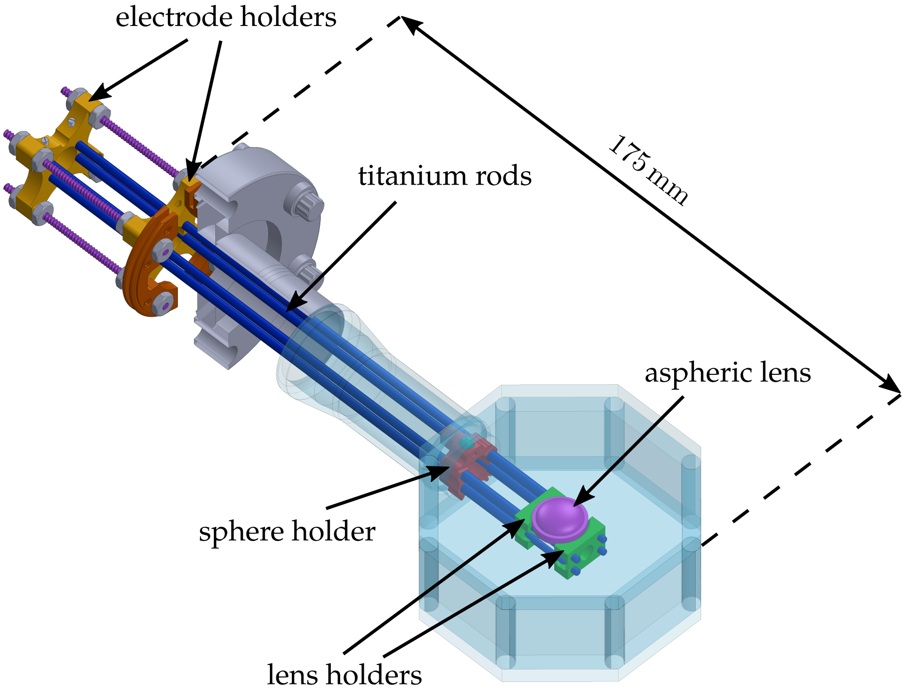

Figure 8.11.: Internal mounting construction. Several components are mounted within the glass cell setup. Two electrode holders (dark yellow) support a set of 4 rods (dark blue) and are mounted within the CF40 cube (not shown here). To minimize mechanical vibrations of the rods, a sphere holder (red) is positioned at the glass cell body. Furthermore, two lens holders (green) carry the aspheric lens (purple) within the glass cell.

- Coating 1 (C1)
  This coating has minimum reflectivity at the imaging wavelengths of K ($\lambda^{\mathrm{K}}_{\mathrm{image}} = 766\,\mathrm{nm}$) and Cs ($\lambda^{\mathrm{Cs}}_{\mathrm{image}} = 852\,\mathrm{nm}$) and at $1064\,\mathrm{nm}$ for optical dipole traps and optical lattice beams each for perpendicular incidence.
- Coating 2 (C2)
  This coating has minimum reflectivity within the wavelength band from $1064\,\mathrm{nm}$ to $1500\,\mathrm{nm}$. It is mainly designed for transmitting the transportation beam and for laser beams that drive molecular transitions.

Figure 8.10 clarifies which coating type is applied to which glass substrate. The calculated reflectivity charts of the anti-reflection coatings, which were provided by Japan Cell, are shown in Appendix F.1 and Appendix F.2. The fused silica substrates of the glass cell are bonded together using epoxy glue EPO-TEK 353ND-T. Our preferred choice of bonding for the glass cell was optical contact bonding, which forms a vacuum-tight bond. Glass cells for ultra-high vacuum applications with two-sided anti-reflection coatings that are bonded by optical contact have become available only lately [Bra15].

The wall thickness of the glass tube at the glass-metal transition is about $1.5\,\mathrm{mm}$. To guarantee that the aspheric lens fits through the glass-metal transition, the clear view of the glass-metal transition was specified to be $19\,\mathrm{mm}^{+0.500\mathrm{mm}}_{-0\mathrm{mm}}$. The aspheric lens was coated by

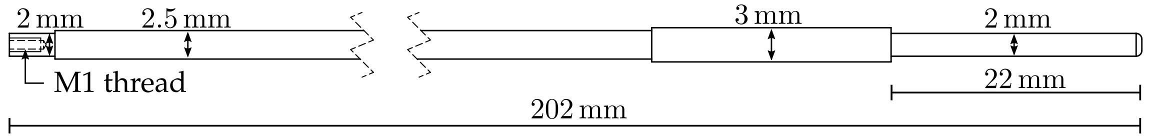

Figure 8.12.: Titanium rod. The titanium rods have a profile with regions of different diameters. On the left end, the rods have an internal M1 thread.

Lens-Optics. The anti-reflection coating of the aspheric lens has the following theoretical specifications:

- Coating on the plane lens surface
  - reflectivity at 1064 nm larger than 99.9 % for perpendicular incidence
  - transmission at 766 nm and 852 nm larger than 95 % for angles of incidence between $0 - 45°$
- Coating on the convex lens surface
  - transmission at 766 nm and 852 nm larger than 99.5 % within a radius of 4 mm around the optical axis of the lens
  - transmission at 766 nm and 852 nm larger than 98.5 % outside of that radius

8.3.3. Internal Mounting Construction

While the outer design of the glass cell setup is rather straightforward, the internal design is more involved. The lens within the glass cell is centered 3.7 mm above the midpoint of the glass cell to which the atoms from the main chamber will be transported. This distance corresponds to the working distance of the imaging system (see Sec. 3.5.3). The lens rests on two holders, which are called *lens holders*. Figure 8.11 shows the internal mounting of the glass cell including the lens and lens holders. The lens holders are held in place by four identical rods (marked dark blue in Fig. 8.11), which extend into the glass cell body. For mounting the rods and carrying the weight of the lens, two additional holders (marked dark yellow in Fig. 8.11) are installed inside of the CF40 cube. These two holders are simultaneously used to align the lens relative to the glass cell and are called *electrode holders*. Another holder (marked red in Fig. 8.11) is positioned right at the transition from the glass cell body to the glass-metal transition. It mechanically fixes the rods and thereby minimizes potential vibrations of the lens. The latter holder is denoted as *sphere holder*.

Rods

The rods are custom-made and machined out of titanium grade 2 (material number 3.7035). Titanium is used in order to avoid stainless steel nearby the atoms and thus magnetization effects as they occured at the main chamber. Even though titanium is considered to be non-magnetic, it has a finite relative magnetic permeability. Pure titanium has a relative magnetic permeability of $\mu_r = 1.00005$ [Boy94], which is a factor of 100 smaller than the relative magnetic permeability of the stainless steel material of our main chamber (see Sec. 6.3.1).

The rods have an overall length of 202 mm and a diameter that varies stepwise between 2 mm and 3 mm. Figure 8.12 shows a schematic drawing of one of the titanium rods. The radial

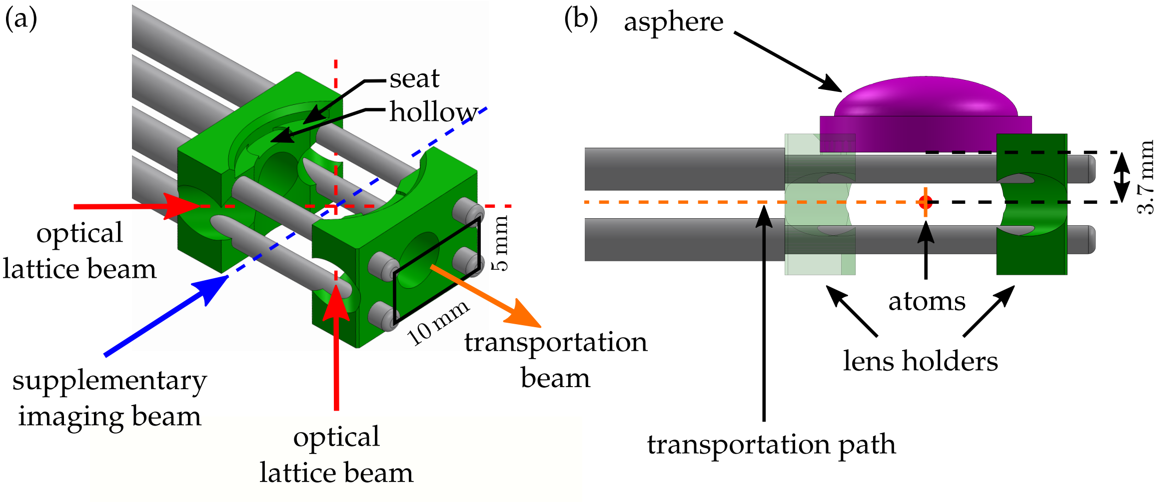

Figure 8.13.: Lens holders. (a) The aspheric lens rests on two identical lens holders that are carried by four titanium rods. To position the lens, the holders have a circular seat with a hollow. Horizontal laser beams (red, blue, and orange arrows) can be directed towards the atoms through each window of the glass cell. (b) The holders define the distance between the atoms and the lens.

steps serve as position markers for accurate placement of the lens holders, sphere holder, and electrode holders and thereby ensure that the lens is correctly positioned within the glass cell. To prevent transfer of stress to the sensitive glass-metal transition during mounting of the glass cell, the rods are straightened to within $0.1\,\mathrm{mm}$ over their entire length. The surface of the titanium rods is of $R_z = 4$ quality, corresponding to an averaged peak-to-peak surface roughness of $4\,\mu\mathrm{m}$. It is the best surface finishing that could be obtained for these rods. The rods have an internal M1 x 0.25 thread on one end. A technical drawing of the titanium rods is shown in Appendix E.2.

The small ratio of rod radius to rod length was a knock-out criterion for many manufacturers. In addition, the requirements on concentricity, run-out, and surface finishing made the search for a possible manufacturer quite difficult. After a time consuming search, luckily a company[22] was found that has the technical equipment and knowledge to manufacture titanium rods with the required specifications.

Lens Holders

Two identical, home-built lens holders are slipped over the titanium rods and accept the aspheric lens. The lens holders have four parallel holes to fix the relative positions of the rods and thereby bring them into a rectangular configuration of $10 \times 5\,\mathrm{mm}$. A circular recession on top of the holders creates a seating for the lens. Figure 8.13 (a) and (b) illustrate the affixing of the lens holders and the seating of the aspheric lens. To minimize the risk of virtual leaks, the recession has a hollow and its edge is chamfered. Three horizontal holes in each lens holder make it possible to send laser beams through each glass cell window to the atoms. The central hole has a diameter of $5\,\mathrm{mm}$ and creates a pathway for the transportation beam (orange arrow in Fig. 8.13 (a)). Another two holes with $4.5\,\mathrm{mm}$ diameter allow for generation of opti-

---

[22] August Müller CNC-Zerspanungstechnik, Uelzen (Germany).

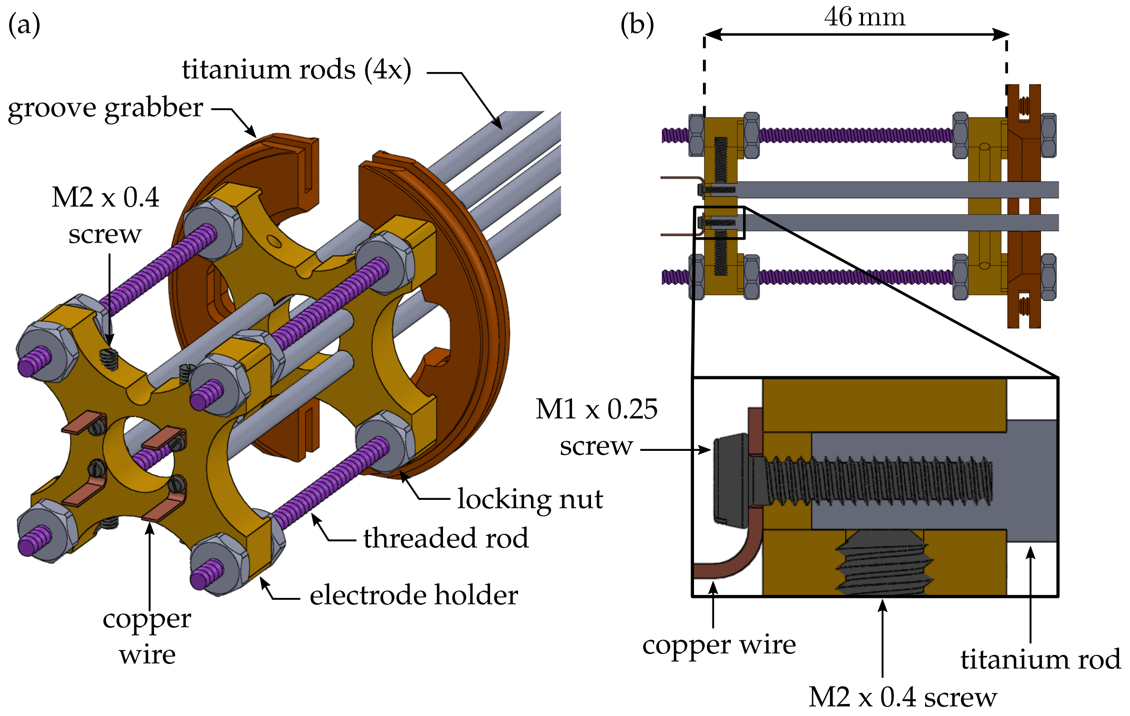

Figure 8.14.: Electrode holders. (a) A pair of groove grabbers (orange) is installed to the glass cell port of the CF40 cube and carries a construction of two electrode holders (dark yellow) and four threaded rods (purple). The electrode holders are fixed by locking nuts and hold the four titanium rods (gray). To secure the rods against slipping, four M2 screws are used. (b) Copper wires establish electrical contact between the electrodes and the electrical feedthrough.

cal lattices with laser beams (red arrows) at angles of ±45° relative to the transportation axis. Supplementary imaging of the atoms, if needed, can be performed perpendicular to the transportation axis (blue arrow). As the lens holders are located within a UHV environment, their material has to be vacuum compatible. Thus, the holders were manufactured out of Macor®. Macor® is bakeable, remains mechanically stable at temperatures of up to 800 °C, and is an electric insulator [Corb]. To fix the lens to the lens holders, a tiny amount of VacSeal was used for the sake of safety. A technical drawing of the lens holders is given in Appendix E.3.

Electrode Holders

Two home-built electrode holders made out of Macor® support the titanium rods within the CF40 cube. Figure 8.14 (a) and (b) show the electrode holders and the surrounding construction that holds them. The electrode holders are oriented parallel to each other and are lined up on four threaded stainless steel rods[23]. The threaded rods themselves are bolted to a pair of groove grabbers[24] that are mounted to internal grooves of the CF40 cube. The electrode holders absorb the torque that originates from the weight of the titanium rods and the lens. The electrode holders are fixed in longitudinal position by a set of locking nuts. To mount the titanium rods to the electrode holders, the titanium rods were pushed through four, parallel

---

[23] Kimball Physics, SS-TR-4-40-12000.

[24] Kimball Physics, MCF275-GrvGrb-C01.

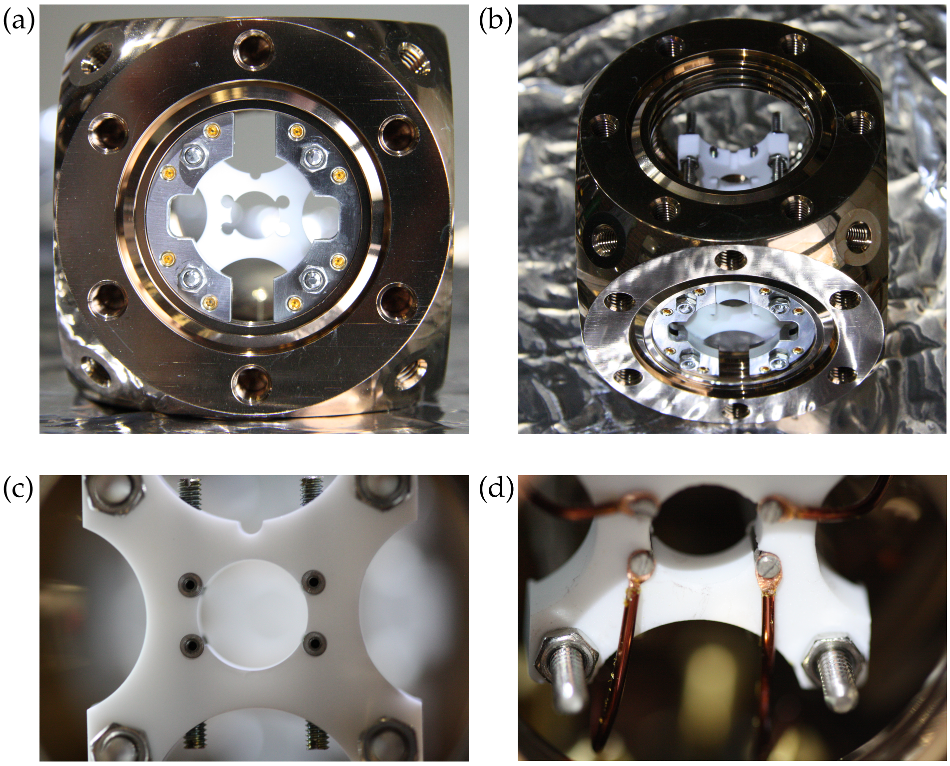

Figure 8.15.: Internal fitting. (a) Glass cell port of the CF40 cube with mounted groove grabbers and electrode holders. (b) Top view of the CF40 cube. The rear electrode holder and the threaded rods become visible. (c) Rear electrode holder with inserted titanium rods. (d) Flattened copper wires are screwed to the titanium rods. All images were taken during the assembly of the internal mounting construction.

holes in the electrode holders. Unwanted sliding of the titanium rods is inhibited by four M2 titanium grade 2 set screws[25] that are screwed laterally into the left electrode holder in Fig. 8.14 and jam the titanium rods.

By applying voltages to the titanium rods, the rods can be used as rod electrodes to generate electric fields within the glass cell. To that end, the titanium rods were connected individually to the pins of the electrical feedthrough with 1 mm thick vacuum-compatible Kapton™-insulated copper wires[26]. On one end of each wire, the insulation was first stripped off and then the end of the blank wire was pressed flat. After this, a hole was drilled in the flattened copper disk. Finally, copper was filed off from the disk until a round eyelet was left. To mount these ends of the copper wires to the internal threads of the titanium rods, titanium grade 2 screws[27] were utilized. The screws jam the copper eyes between the electrode holder and the screw heads. The inset of Fig. 8.14 (b) shows a section view of a titanium rod and illustrates the mounting of the titanium rods and the copper wires to the electrode holder. The untreated ends of the copper wires were screwed to set screw connectors[28] at the electrical feedthrough. Figure 8.15 (a)-(d) show the CF40 cube of the glass cell science chamber setup during the as-

---

[25] DIN 551 set screws.

[26] Lesker, FTAK10010.

[27] DIN 84 screw.

[28] Lesker, FTASSC050.

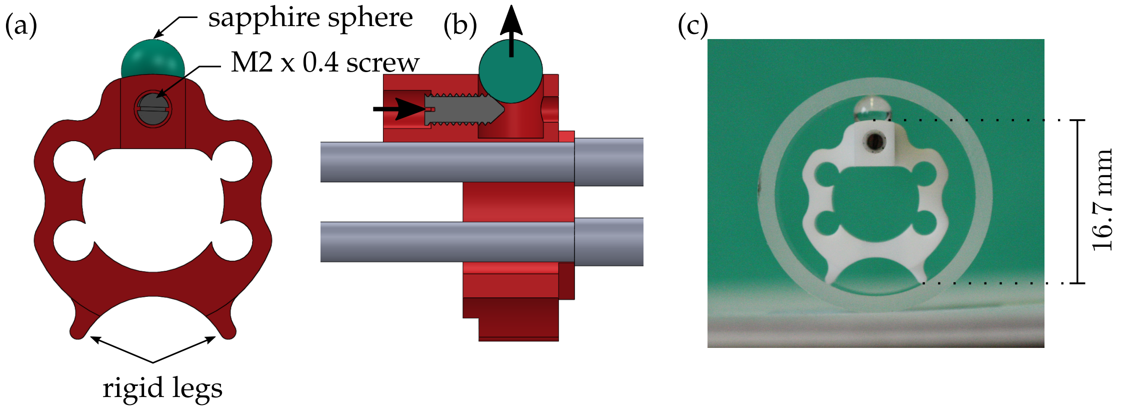

Figure 8.16.: Sphere holder. (a) The sphere holder seen from the main chamber. (b) Sectional side view. As one turns an M2 set screw into the sphere holder, the sapphire sphere moves upwards. (c) The sphere holder mounted to a dummy quartz glass ring for testing.

sembly of the internal mounting construction and demonstrate the mounting of the electrode holders and the realization of the wire connections. A technical drawing of the electrode holders is shown in Appendix E.4.

Sphere Holder

The sphere holder is a home-built part that stabilizes the titanium rods against vibrations and additionally sets the correct position of the aspheric lens. It is made out of Macor®. Figure 8.16 (a) shows a rear view of the sphere holder and illustrates its annular shape. Two rigid legs stick out from the lower half of the sphere holder. The upper half of the sphere holder contains a $4\,\mathrm{mm}$-diameter sapphire sphere, which resides entirely within the sphere holder in unmounted position. When the sphere holder is mounted within the glass cell, the two legs rest on the inner wall of the clearance hole of the glass cell body. Their length is chosen such that in this position the aspheric lens is placed $3.7\,\mathrm{mm}$ above the glass cell center. By screwing an M2 titanium grade 2 set screw[29] with a tapered nose into the sphere holder one pushes the sapphire sphere outwards and clamps the sphere holder to the glass cell. Figure 8.16 (b) explains how the set screw pushes the sphere outwards. The two legs together with the sapphire sphere thus form a manual 3-point clamping mechanism. Figure 8.16 (c) shows the sphere holder when clamped to a dummy quartz glass ring. A technical drawing of the sphere holder is shown in Appendix E.5.

8.3.4. Influence of Atmospheric Pressure

Under the influence of the atmospheric pressure the glass windows of the glass cell will bend inwards. To check whether this bending is troublesome to the performance of the high-resolution imaging system, a finite element simulation of the expected deformation is performed. The simulation is carried out with the software SOLIDWORKS by using a static deformation analysis of a 3D computer-aided design (CAD) model of the glass cell. All glass

---

[29] DIN 553 set screw.

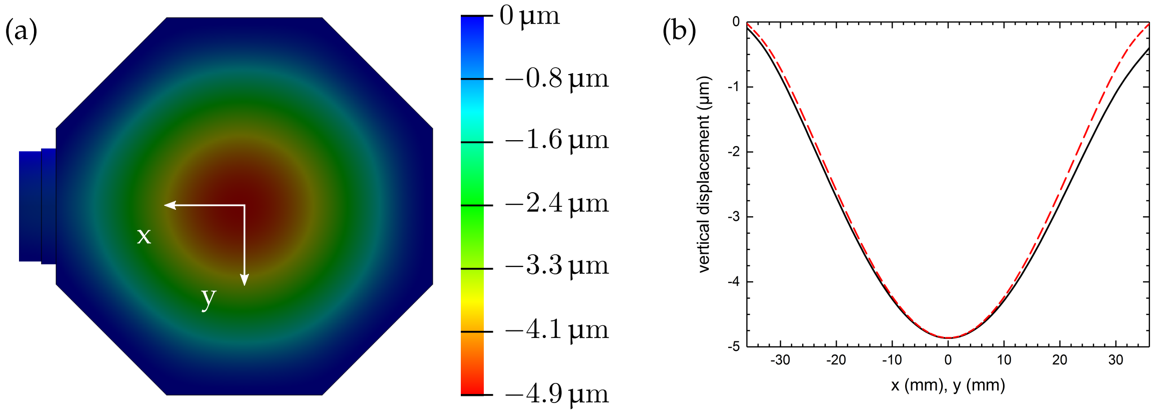

Figure 8.17.: Bending of the top glass cell window. (a) Surface plot of the vertical deformation of the top glass cell window. (b) Numerical results of the vertical deformation of the top glass cell window along the $x-$direction (black, solid line) and $y-$direction (red, dashed line).

parts are assigned to have material properties of the fused silica grade[30] Corning® HPFS® 7980. Furthermore, a pressure of $1 \times 10^5\,\mathrm{N/m^2}$ acting on all surfaces of the glass cell model is assumed. To resolve the bending of the glass window, the mesh applied to the model has a maximum element size of $0.92\,\mathrm{mm}$, which is much smaller than the width of the glass cell. The minimum mesh element size is $0.05\,\mathrm{mm}$.

Figure 8.17 (a) shows a surface plot of the numerical results for the deformation of the top glass window along the vertical $z-$direction. The deformation is nearly radially symmetric around the center of the glass window. The simulated vertical deformation is assessed along the $x-$ and $y-$ directions, which are defined in Fig. 8.17 (a). Figure 8.17 (b) shows the obtained vertical displacement curves along the $x-$ and $y-$ directions. The vertical displacement is maximum ($-4.9\,\mu\mathrm{m}$) at $x = y = 0$ and decreases towards the walls of the glass cell as expected. While the vertical deformation is symmetric along the $y-$direction, it is asymmetric for the $x-$axis. This asymmetry is presumably due to the fact that the glass cell design is asymmetric with a glass-metal transition on the left side and a simple glass substrate on the right side in Fig. 8.17 (a).

For the performance of the imaging system, only the variation in vertical deformation over an aperture of about $5\,\mathrm{mm}$ radius around the center of the glass window is relevant. The change in vertical deformation over that region is determined to be approximately $\sim 160\,\mathrm{nm}$. A simulation of the optical performance of the imaging system with a bent glass cell window as that discussed here was performed by E. Kirilov, who designed the imaging system, using the software Zemax. The simulation yielded no impairment of the optical performance by the cell window.

8.3.5. Assembly of the Glass Cell Science Chamber Setup

Before the glass cell setup was assembled, the clamping mechanism of the sphere holder was tested. The two materials Macor® and fused silica have unequal coefficients of thermal ex-

---

[30] See footnote 21.

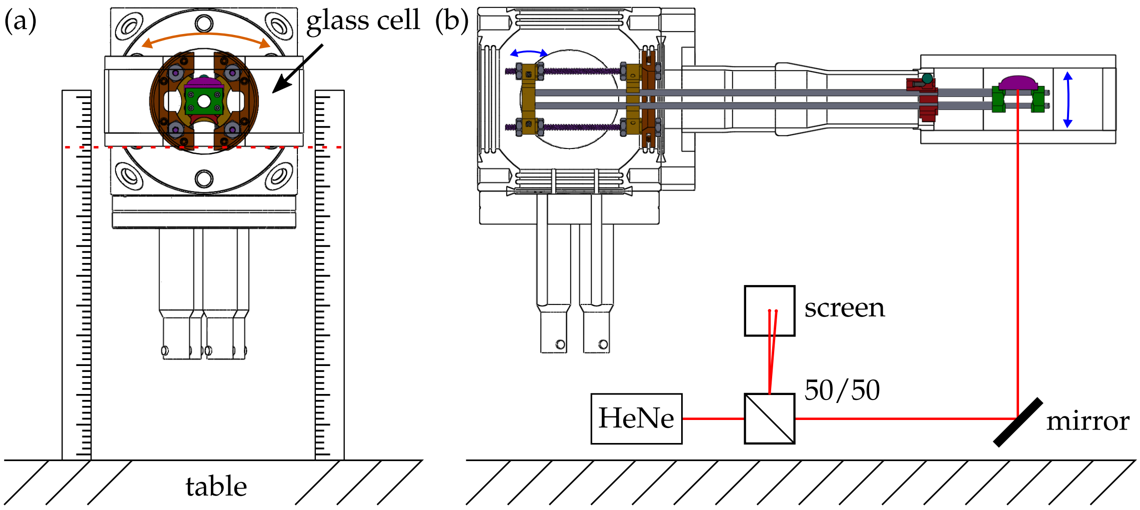

Figure 8.18.: Alignment of glass cell and lens. (a) By measuring the distance between the table and the glass cell it was verified that the glass cell is aligned horizontally. (b) A laser beam from a helium-neon laser was guided to the plane surface of the lens. Using a 50/50-beam splitter, two back reflections of the lens and the bottom glass cell window were observed on a distant screen. If the rear electrode holder were tilted, the lens would move up or down. The alignment procedure is described in the main text.

pansion, which differ in magnitude by a factor of 16.[31] For this reason, it was verified that the clamped sphere holder inside the glass cell will withstand the bake out and will not induce tensions that potentially could crack the glass cell. To that end, the bake-out process was imitated by baking a duplicate of the sphere holder that had been mounted inside a dummy quartz glass ring at a temperature of 100 °C for ten hours as shown in Fig. 8.16 (c). No damages were observed of both parts after cooling down. It was therefore concluded that the bake out will not damage the glass cell owing to the clamped sphere holder.

Once the entire internal mounting structure had been installed to the CF40 cube, the following iterative aligning procedure was pursued to align the aspheric lens and the glass cell relative to each other.

1. **Rotational alignment of the glass cell.** The glass cell was loosely connected to the CF40 cube and rotated until it was aligned horizontally. To validate the horizontal alignment of the cell, the height of the bottom glass substrate relative to the table surface on which the setup had been mounted was measured on two opposing sides. Figure 8.18 (a) illustrates the approach for rotational alignment.

2. **Rotational alignment of the aspheric lens.** After the glass cell had been aligned rotationally, the horizontal glass cell was taken as reference for the alignment of the lens. To align the lens, a laser beam from a helium-neon laser was reflected from the plane surface of the lens. Two back reflections were observed on a distant screen. Figure 8.18 (b)

---

[31] For Macor® the coefficient of thermal expansion is 9×10^{-6} /K within a temperature range between 25 °C and 300 °C [Corb]. The coefficient of thermal expansion for the fused silica of the glass cell was assumed to be similar to that of Corning® HPFS® 7980 (see also footnote 21), which is 0.57×10^{-6} /K for temperatures between 0 °C and 200 °C [Cora].

shows the laser setup that was used for alignment of the lens. One back reflection came from the flat side of the lens and the other one from the bottom window of the glass cell. By means of the two reflections, it could be checked whether lens and glass cell were rotationally parallel to each other. When the lens was parallel to the glass cell, the two back reflections overlapped. If lens and cell were rotationally tilted relative to each other, the glass cell needed to be removed and the groove grabbers must be rotated. Thereafter step 1 and 2 of this procedure must be repeated.

3. **Longitudinal alignment of the aspheric lens.** Once the lens was aligned rotationally to be horizontal, the sphere holder was pushed to its intended position and clamped to the glass cell. It was then necessary to test whether the asphere was parallel to the glass cell along the transportation axis. At the beginning of the alignment, tightening the sphere holder often bent the titanium rods due to longitudinal misalignment. Thus, the laser back reflections started moving relative to each other. Longitudinal misalignment had different origins. First, because of the clearance of the glass cell flange, the glass cell was sometimes mounted too high (too low) or too much to the left (or right) side. Second, the electrodes were initially not horizontal. To align the lens longitudinally, the glass cell was repositioned. Alternatively, the electrodes were tilted by tilting the rear electrode holder. The latter option is indicated through blue arrows in Fig. 8.18 (b).
4. **Tightening the glass cell flange.** Next, the sphere holder was loosened and the glass cell flange was tightened to the CF40 cube in incremental steps. The tightening inclined the glass cell a bit probably due to asymmetric tightening of the screws. Therefore, the lens needed to be realigned relative to the glass cell. The realignment was achieved by tilting the electrode holders and checking the overlap of the back reflections.
5. **Completing the setup.** Once the glass cell flange was fully tightened, all Macor® holders were fixed, the copper wires were connected to the titanium rods, and all remaining vacuum parts[32] were mounted to the CF40 cube.

In the final glass cell setup the glass cell is found to be aligned horizontally to around $\sim 0.08°$. A residual tilt between the aspheric lens and the glass cell was found and measured to be 0.16(4)° via the laser back reflections. This tilt is smaller than the maximum tilt of $\sim 1°$ that the high-resolution imaging system can compensate [Kir].

After having assembled the glass cell setup, the entire setup was baked out. In order to achieve a homogeneous temperature distribution across the glass cell, a closed box out of copper sheets was built around the glass cell. The entire glass cell setup was then wrapped with heating wires and coated with several layers of aluminum foil. The maximum bake-out temperature of the glass cell is specified by the manufacturer to be $120\,°\mathrm{C}$. During the bake out the temperature of the copper box was therefore kept at about $105\,°\mathrm{C}$ while the temperature of the stainless steel vacuum parts was between $100\,°\mathrm{C}$ and $200\,°\mathrm{C}$. The setup was baked out for 19 days.

To be able to determine the pressure within the glass cell setup, an ion gauge[33] was initially installed to the setup. The ion gauge was mounted within a horizontal CF40 nipple to the CF40 cube right opposite of the glass cell. The ion gauge at that position read a pressure within the low $10^{-10}\,\mathrm{mbar}$ after bake out. This pressure is higher than the originally intended

---

[32] All stainless steel parts used in the glass cell science chamber setup were air baked at $400\,°\mathrm{C}$ for 24 hours prior to the assembly.

[33] Agilent Technologies, UHV-24p ion gauge.

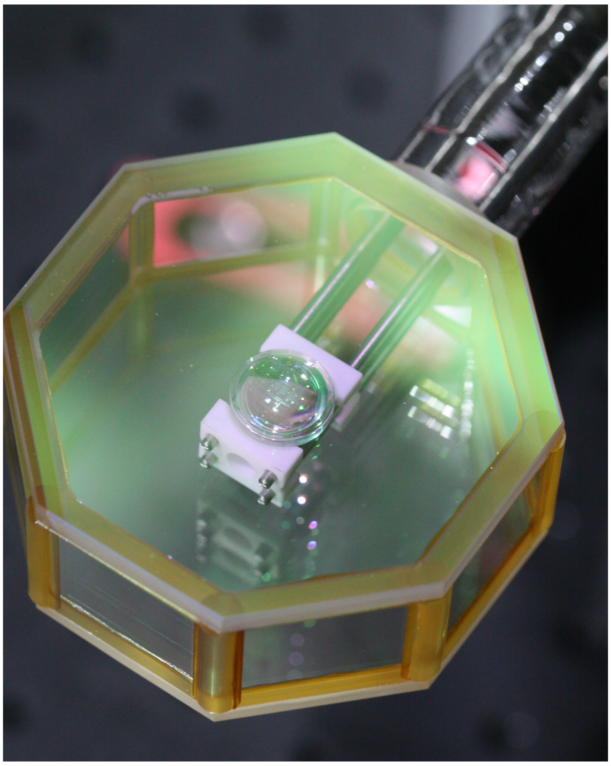

Figure 8.19.: Top view of the glass cell science chamber. The picture shows the fully assembled and evacuated glass cell. The aspheric lens as well as the lens holders and the rod electrodes are clearly visible. After the bake out of the glass cell the glue of the glass substrates had changed its color into reddish.

pressure (see Sec. 8.1.1). The ion gauge heats up during operation and therefore causes enhanced outgassing from its filament as well as surrounding vacuum parts (e.g. the CF40 full nipple). Since the aperture of the CF40 nipple was largely blocked by the nearby electrode holder, the high pressure displayed by the ion gauge was explained with a reduced pumping speed within the full nipple. It is expected that lifetime measurements of trapped atoms in future experiments will confirm a lower pressure within the glass cell than that originally measured by the ion gauge.

The glass cell setup (without the ion gauge) was successfully attached to the main vacuum system during this Thesis and is ready for operation. Figure 8.19 shows a close-up of the evacuated, final glass cell setup with the mounted aspheric lens.

9. Calculation of Electric Dipole Moments, Electric Fields, and Dipolar Spin Exchange

In future experiments the titanium rod electrodes within the glass cell science chamber will be used to generate electric fields and thereby polarize KCs molecules. Polarized molecules possess an induced electric dipole moment that depends on the strength of the external electric field. In this Chapter, the induced electric dipole moment of bosonic ^{39}KCs ground-state molecules is computed for different molecular states and as a function of the external electric field strength. Furthermore, different electric field configurations that can be generated by the titanium electrodes are simulated. The resulting electric field distributions are numerically analyzed and their field homogeneity is quantified. Finally, the results of the electric dipole moment calculations and the electric field simulations are combined to study the influence of residual electric field inhomogeneities on future experiments within the K−Cs apparatus. This analysis is done with respect to the experimental realization of the spin−1/2 Heisenberg XXZ lattice model with ^{39}KCs molecules on a 2D square lattice. The numerical results show that the electric field within the glass cell science chamber is homogeneous enough to study this particular spin lattice model with ^{39}KCs molecules.

9.1. Calculation of Electric Dipole Moments of ^{39}KCs Molecules

In heteronuclear molecules, the difference in electronegativity of the individual atoms causes the atoms to share electrons unequally. For diatomic, heteronuclear molecules, the charge separation that occurs due to this imbalance leads to a permanent electric dipole moment (*pEDM*) [Atk17]. The pEDM $\vec{p}_{\text{perm}}$ within the body-fixed frame of these molecules points along the internuclear axis [Boh09]. It vanishes within the lab frame, however, in the absence of an external electric field [Car09]. To induce an electric dipole moment $\vec{p}$ within the lab frame, the molecules can be polarized by an external electric field $\vec{F}$.

In this Section, the induced electric dipole moment $p = |\vec{p}|$ of ^{39}KCs molecules is calculated as a function of the strength F of an external electric field $\vec{F}$. The induced electric dipole moment p is calculated for those molecular states that will be relevant for future experiments. This Section therefore focuses on the induced electric dipole moment p of the energetically lowest lying rotational states of the electronic and vibrational ground state of ^{39}KCs molecules.

Due to the nuclear spin of ^{39}K ($I = 3/2$ [Ari77]) and ^{133}Cs ($I = 7/2$ [Ari77]), the individual nuclear spin magnetic moments within a ^{39}KCs molecule interact with each other [Bro03]. Furthermore, the electric quadrupole moments of the ^{39}K and ^{133}Cs nuclei interact with the gradient of the local electric field that is generated by the electrons and the respective other

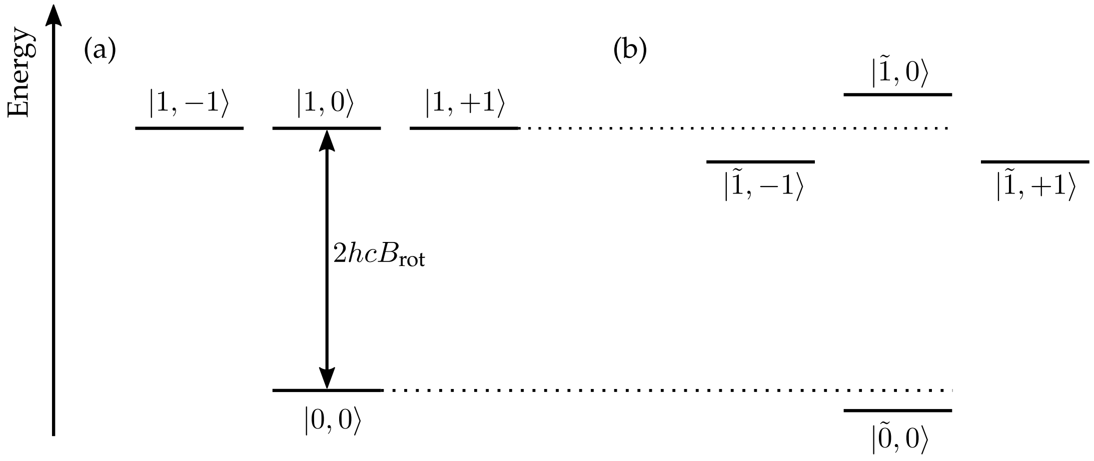

Figure 9.1.: Rotational states of a diatomic molecule. (a) The rotational states $|J_{\mathrm{rot}}, M_{\mathrm{rot}}\rangle$ for the lowest ($J_{\mathrm{rot}} = 0$) and first excited ($J_{\mathrm{rot}} = 1$) rotational level of a diatomic molecule are shown. The $(2J_{\mathrm{rot}}+1)$ states of each rotational level are degenerate in the absence of an external electric field. (b) In the presence of an external electric field, the degeneracy is partially lifted. Only states with the same absolute value of M_{rot} for each $\tilde{J}_{\mathrm{rot}}$ remain degenerate.

nucleus within the molecule.[1] Both interactions lead to a hyperfine splitting within the rotational levels of ^{39}KCs molecules [Bro03]. For reasons of simplification, the hyperfine structure is neglected in the following.

9.1.1. Rotating Diatomic Molecules

A diatomic molecule in its electronic and vibrational ground state can be described as a (linear) rigid rotor with Hamilton operator [Bro03]

$$\hat{H}_{\mathrm{rot}} = hcB_{\mathrm{rot}}\hat{J}^2, \tag{9.1}$$

where $\hat{J}$ is the *angular momentum operator* in units of $\hbar$ and B_{rot} is the *rotational constant* of the molecule given by [Hak06]

$$B_{\mathrm{rot}} = \frac{h}{8\pi^2 \cdot c \cdot \Xi}. \tag{9.2}$$

The rotational constant B_{rot} is inversely proportional to the molecule's *moment of inertia* $\Xi = m_{\mathrm{r}}R_{\mathrm{eq}}^2$, where m_{r} is the *reduced mass* and R_{eq} is the *equilibrium internuclear distance* [Hak06]. It thus depends on the molecule itself as well as on the electronic and vibrational state. The eigenstates of the Hamiltonian $\hat{H}_{\mathrm{rot}}$ are the angular momentum eigenstates $|J_{\mathrm{rot}}, M_{\mathrm{rot}}\rangle$ with *rotational angular momentum quantum number* J_{rot} and the projection M_{rot} of the angular momentum on an externally defined direction, which can be for instance the direction of an applied electric field. As usual, the relation $-J_{\mathrm{rot}} \leq M_{\mathrm{rot}} \leq +J_{\mathrm{rot}}$ restricts the values of M_{rot}. The states

---

[1] Numerical values for the nuclear electric quadrupole moments of ^{39}K and ^{133}Cs can be found in the compilation of Ref. [Pyy18].

$|J_{\text{rot}}, M_{\text{rot}}\rangle$ have eigenenergies $E_{J_{\text{rot}},M_{\text{rot}}}$ with [Bro03]

$$E_{J_{\text{rot}},M_{\text{rot}}} = hcB_{\text{rot}}J_{\text{rot}}\left(J_{\text{rot}}+1\right). \tag{9.3}$$

Each rotational level is thus $(2J_{\text{rot}}+1)-$fold degenerate and successive rotational levels with quantum numbers J_{rot} and $J'_{\text{rot}} = J_{\text{rot}}+1$ have an increasing energy spacing of $E_{J'_{\text{rot}},M'_{\text{rot}}} - E_{J_{\text{rot}},M_{\text{rot}}} = 2hcB_{\text{rot}}(J_{\text{rot}}+1)$. Figure 9.1 (a) illustrates the eigenenergies of the ground ($J_{\text{rot}}=0$) and first excited ($J_{\text{rot}}=1$) rotational level of a rotating diatomic molecule.

9.1.2. Rotating Diatomic Molecules in Electric Fields

A diatomic, heteronuclear molecule in a rotational state $|J_{\text{rot}}, M_{\text{rot}}\rangle$ has a well-defined parity, i.e. a transformation between two coordinate systems (x, y, z) and $(-x, -y, -z)$ leaves the molecular wavefunction either unchanged or alters its sign. Rotational states with odd or even quantum number J_{rot} have opposite parity [Hak06]. In the absence of electric fields, a molecule in state $|J_{\text{rot}}, M_{\text{rot}}\rangle$ thus does not possess a pEDM $\vec{p}_{\text{perm}}$ in the lab frame.

The Hamiltonian for a rotating, diatomic polar molecule in its electronic and vibrational ground state within an external electric field $\vec{F} = F\vec{\mathcal{E}}$ reads [Boh09]

$$\hat{H}_{\text{rot,Stark}} = \hat{H}_{\text{rot}} - \hat{p}\cdot F\vec{\mathcal{E}}. \tag{9.4}$$

The matrix elements of the Hamiltonian $\hat{H}_{\text{rot,Stark}}$ are given through

$$\langle J'_{\text{rot}}, M'_{\text{rot}}|\hat{H}_{\text{rot,Stark}}|J_{\text{rot}}, M_{\text{rot}}\rangle = hcB_{\text{rot}}J_{\text{rot}}(J_{\text{rot}}+1)\delta_{J_{\text{rot}},J'_{\text{rot}}}\delta_{M_{\text{rot}},M'_{\text{rot}}} - F\langle J'_{\text{rot}}, M'_{\text{rot}}|\hat{p}\vec{\mathcal{E}}|J_{\text{rot}}, M_{\text{rot}}\rangle. \tag{9.5}$$

By expressing the polarization vector $\vec{\mathcal{E}}$ and the electric dipole moment operator $\hat{p}$ in terms of spherical polarization vectors $\vec{u}_\xi$ (as defined in Sec. 5.3.3) and spherical components $\hat{p}_\xi$, respectively, with [Wal15]

$$\hat{p}_{\pm1} = \mp\frac{\hat{p}_x \pm i\hat{p}_y}{\sqrt{2}}, \tag{9.6}$$

$$\hat{p}_0 = \hat{p}_z, \tag{9.7}$$

the last term in Eq. (9.5) can be rewritten as

$$-F\langle J'_{\text{rot}}, M'_{\text{rot}}|\hat{p}\vec{\mathcal{E}}|J_{\text{rot}}, M_{\text{rot}}\rangle = -F\sum_\xi\langle J'_{\text{rot}}, M'_{\text{rot}}|\hat{p}_\xi|J_{\text{rot}}, M_{\text{rot}}\rangle. \tag{9.8}$$

In the special case of a molecular state with zero electronic orbital angular momentum, denoted as Σ state, the matrix element $\langle J'_{\text{rot}}, M'_{\text{rot}}|\hat{p}_\xi|J_{\text{rot}}, M_{\text{rot}}\rangle$ can be expressed as [Boh09, Wal15]

$$\begin{aligned}\langle J'_{\text{rot}}, M'_{\text{rot}}|\hat{p}_\xi|J_{\text{rot}}, M_{\text{rot}}\rangle =& p_{\text{perm}}(-1)^{M'_{\text{rot}}}\sqrt{(2J'_{\text{rot}}+1)(2J_{\text{rot}}+1)}\\ &\times\begin{pmatrix} J'_{\text{rot}} & 1 & J_{\text{rot}} \\ -M'_{\text{rot}} & \xi & M_{\text{rot}}\end{pmatrix}\begin{pmatrix} J'_{\text{rot}} & 1 & J_{\text{rot}} \\ 0 & 0 & 0\end{pmatrix}.\end{aligned} \tag{9.9}$$

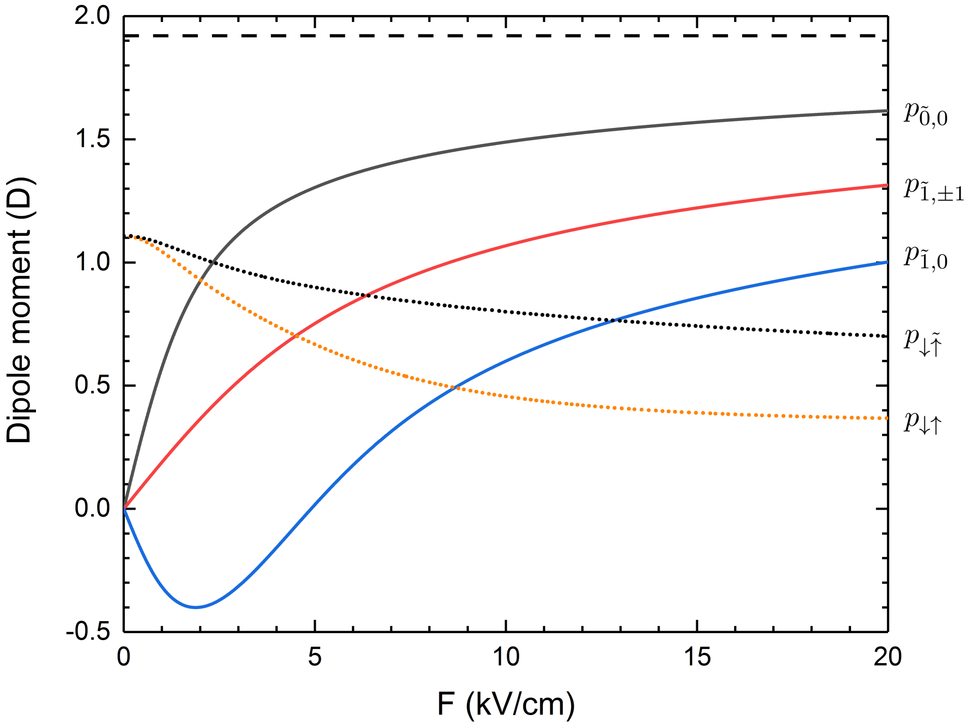

Figure 9.2.: Dipole moments of the ^{39}KCs molecule. Induced electric dipole moments $p_{\tilde{0},0}$, $p_{\tilde{1},0}$, and $p_{\tilde{1},\pm 1}$ as a function of electric field strength F. For zero electric field, the induced dipole moments vanish. The horizontal, dashed line indicates the permanent electric dipole moment $p_{\text{perm}} = 1.92$ D for the electronic-vibrational ground state of ^{39}KCs. The transition dipole moments $p_{\downarrow\uparrow}$ and $p_{\downarrow\tilde{\uparrow}}$ are maximum for zero electric field and decrease monotonously with increasing electric field (see discussion in Sec. 9.3.1). Values for the (transition) dipole moments were calculated by considering the 26 lowest rotational levels.

The factor p_{perm} in Eq. (9.9) is the absolute value of the pEDM of the molecule, i.e. $p_{\text{perm}} = |\vec{p}_{\text{perm}}|$. The first Wigner 3J-symbol in Eq. (9.9) can take non-zero values only if the entries of its lower row add up to zero [Mes65b]. A linearly polarized electric field ($\xi = 0$) thus only couples rotational states with $M_{\text{rot}} = M'_{\text{rot}}$. Selection rules for the top row entries of the second Wigner 3J-symbol restrict coupling of rotational states to those with opposite parity, i.e. $J'_{\text{rot}} = J_{\text{rot}} \pm 1$ [Mes65b].

Diagonalization of the Hamiltonian $\hat{H}_{\text{rot,Stark}}$ in Eq. (9.4) leads to the eigenstates, denoted as $|\tilde{J}_{\text{rot}}, M_{\text{rot}}\rangle$, and eigenenergies $E_{\tilde{J}_{\text{rot}},M_{\text{rot}}}$ of the molecule within an electric field. For a static electric field in $z-$direction, the states $|\tilde{J}_{\text{rot}}, M_{\text{rot}}\rangle$ are coherent linear superpositions of the field-free states $|J_{\text{rot}}, M_{\text{rot}}\rangle$ with [Lem13]

$$|\tilde{J}_{\text{rot}}, M_{\text{rot}}\rangle = \sum_{J_{\text{rot}}} a_{J_{\text{rot}}}^{\tilde{J}_{\text{rot}},M_{\text{rot}}} |J_{\text{rot}}, M_{\text{rot}}\rangle. \tag{9.10}$$

The coefficients $a_{J_{\text{rot}}}^{\tilde{J}_{\text{rot}},M_{\text{rot}}}$, and therefore mixing of the rotational states, depend on the electric field strength F, i.e. $a_{J_{\text{rot}}}^{\tilde{J}_{\text{rot}},M_{\text{rot}}} = a_{J_{\text{rot}}}^{\tilde{J}_{\text{rot}},M_{\text{rot}}}(F)$. For $F \to 0$, the state $|\tilde{J}_{\text{rot}}, M_{\text{rot}}\rangle$ converts adiabatically into the field-free rotational state $|J_{\text{rot}}, M_{\text{rot}}\rangle$ [Lem13]. Since the coupling of the molecule to the electric field $\vec{F}$ in Eq. (9.9) depends on M_rot, the states $|\tilde{J}_\text{rot}, -J_\text{rot}\rangle, |\tilde{J}_\text{rot}, -J_\text{rot}+1\rangle, \ldots, |\tilde{J}_\text{rot}, +J_\text{rot}\rangle$ that originate from the same rotational level are not degenerate. Only states with the same absolute value $|M_\text{rot}|$ remain degenerate.[2] Figure 9.1 (b) depicts the eigenenergies $E_{\tilde{J}_\text{rot},M_\text{rot}}$ of the states $|\tilde{0}, 0\rangle$ and $|\tilde{1}, M_\text{rot}\rangle$. The eigenenergies $E_{\tilde{J}_\text{rot},M_\text{rot}}$ vary with field strength F. The induced electric dipole moment $p_{\tilde{J}_\text{rot},M_\text{rot}}$ of a molecule in state $|\tilde{J}_\text{rot}, M_\text{rot}\rangle$ at field strength F can be deduced from the derivative of the eigenenergy $E_{\tilde{J}_\text{rot},M_\text{rot}}$ through [Cov18]

$$p_{\tilde{J}_\text{rot},M_\text{rot}}(F) = -\frac{\partial E_{\tilde{J}_\text{rot},M_\text{rot}}(F)}{\partial F}. \tag{9.11}$$

The induced electric dipole moment $\vec{p}_{\tilde{J}_\text{rot},M_\text{rot}}$ of a diatomic molecule is aligned along its molecular axis [Boh09].

9.1.3. Calculation of Induced Electric Dipole Moments for ^{39}KCs Molecules

The electronic ground state of a ^{39}KCs molecule is a singlet state, denoted as $X^1\Sigma^+$ [Fer08].[3] For a ^{39}KCs molecule in its vibrational ground state of the electronic ground state $X^1\Sigma^+$, the pEDM is $p_\text{perm} = 1.92$ D [Aym05] and the rotational constant B_rot takes the value $B_\text{rot} = 3.048(5)\,\text{m}^{-1} \equiv 0.030\,48(5)\,\text{cm}^{-1}$ [Fer08].[4] If hyperfine interaction is neglected, the energy splitting of the ground and first excited rotational level for a ^{39}KCs molecule in its electronic-vibrational ground state can be computed with Eq. (9.3). The splitting amounts to an energy of $h \times 1.828\,\text{GHz}$.

To calculate the induced electric dipole moment $p_{\tilde{J}_\text{rot},M_\text{rot}}$ of states $|\tilde{J}_\text{rot}, M_\text{rot}\rangle$ for ^{39}KCs molecules in their electronic and vibrational ground state, first the corresponding eigenvalue problem of the Hamiltonian $\hat{H}_\text{rot,Stark}$ in Eq. (9.4) was numerically solved. Thereafter the derivative in Eq. (9.11) was calculated for the obtained sets of eigenenergies. The induced electric dipole moment $p_{\tilde{J}_\text{rot},M_\text{rot}}$ was calculated for the states $|\tilde{J}_\text{rot} = 0, M_\text{rot} = 0\rangle$, $|\tilde{1}, 0\rangle$, and $|\tilde{1}, \pm 1\rangle$ for electric field strengths F up to $20\,\text{kV/cm}$.

Figure 9.2 presents the numerical values for the induced dipole moments $p_{\tilde{0},0}$, $p_{\tilde{1},0}$, and $p_{\tilde{1},\pm 1}$. For increasing field strength F, $p_{\tilde{0},0}$ and $p_{\tilde{1},0}$ approach the maximum value p_perm, which is indicated through a horizontal, dashed line in Fig. 9.2. The induced electric dipole moment of state $|\tilde{0}, 0\rangle$ equals $p_{\tilde{0},0} = 1$ D at a field strength of $F \approx 2.2\,\text{kV/cm}$. For the same field strength, the induced dipole moment of state $|\tilde{1}, 0\rangle$ is $p_{\tilde{1},0} = -0.38$ D. State $|\tilde{1}, 0\rangle$ reaches an induced electric dipole moment of 1 D at a field strength of $F \approx 18.8\,\text{kV/cm}$. The induced dipole moments $p_{\tilde{1},\pm 1}$ equal 1 D at a field strength of $F \approx 8.1\,\text{kV/cm}$.

9.2. Simulation of Electric Fields

In order to perform electric field simulations for the rod electrodes within the glass cell science chamber, the software COMSOL Multiphysics was used. This software solves Gauss' Law and

---

[2] Hyperfine interaction breaks the degeneracy of states with the same value of $|M_\text{rot}|$ within a rotational level [Wal15].

[3] In this notation, X marks the electronic ground state of the molecule and the superscript *1* indicates that the molecular state is a singlet state. The label + states that the total molecular wavefunction is symmetric under reflection on an arbitrary plane that includes the molecular axis [Hak06].

[4] The electric dipole moment of polar molecules is commonly given in units of Debye (D). In SI units, an electric dipole moment of 1 D is equivalent to $\approx 3.336 \times 10^{-30}\,\text{C m}$ [Yan13].

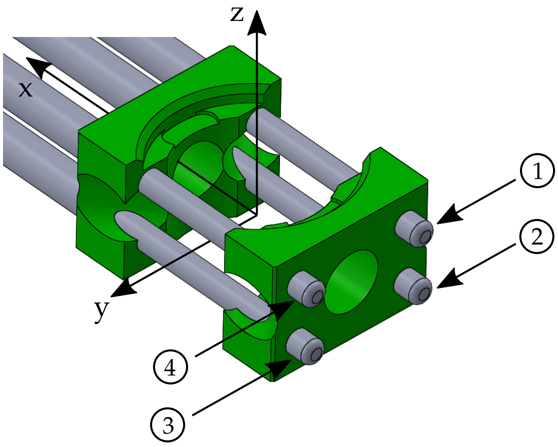

Figure 9.3.: Arrangement of the electrodes. The electrodes are labeled with index $i \in \{1, 2, 3, 4\}$. The origin of the local coordinate system (x, y, z) coincides with the position of the molecules. The $x-$axis lies on the transportation axis.

uses the scalar electric potential as dependent variable [COM]. It utilizes an iterative algorithm, which stops as soon as the numerical solution has converged. The numerical convergence criterion is fulfilled if the relative difference in the solutions of two consecutive iteration steps is smaller than a predefined value. Due to limited computational power, the numerical convergence criterion for the present simulations was set to $0.1\,\%$. The electric field simulations were performed for two specific combinations of voltages applied to the electrodes, which resulted in different electric fields.

9.2.1. Setting up the Simulation

For an unambiguous voltage assignment to the electrodes, the electrodes are labeled with an index $i \in \{1, 2, 3, 4\}$. Figure 9.3 shows the arrangement of the electrodes within the glass cell science chamber and the allocation of the index i. Since the resulting electric field is linear in the applied voltages, the simulations are performed for voltages V_i of $\pm\,1\,\mathrm{V}$ for reasons of better scaling. Figure 9.3 also introduces a local coordinate system (x, y, z) for the following discussion of the simulation results. To obtain reliable simulation results for the electric field distributions, the following procedure is applied:

1. **Simplifying the geometry.** The arrangement of the electrodes in Fig. 9.3 has two symmetry planes, namely the $xy-$plane and the $xz-$plane. The two symmetry planes split the geometry into four quadrants. Each quadrant contains a single rod electrode. The electric fields that are considered in this Thesis derive from electric potentials that are antisymmetric to the $xz-$ or $xy-$plane. In other words, the voltage assignments are of the kind $V_{1,2} = -V_{3,4}$ and $V_{1,4} = -V_{2,3}$. The (anti-)symmetry planes can be exploited to reduce the computational effort of the simulation. To be more precise, the total electric field of the four rod electrodes can be determined by first solving for the electric field of a single electrode within a single quadrant. The results of that quadrant are thereafter projected onto the other quadrants in consideration of the symmetric and antisymmetric

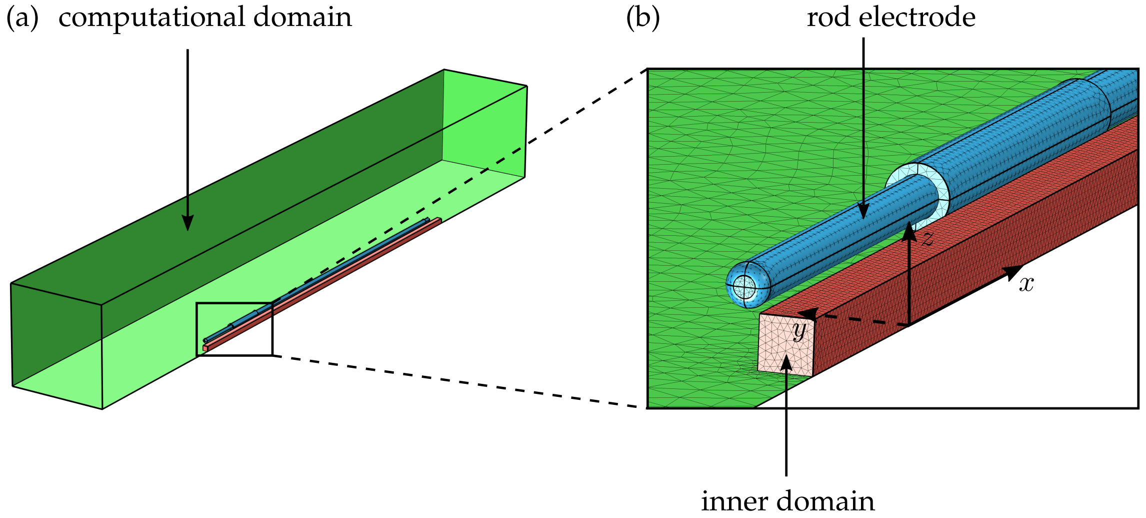

Figure 9.4.: Domains of the electric field simulation. (a) The computational domain (green box) of the electric field simulations includes a single electrode (blue). (b) To allow for a higher spatial resolution of the simulated electric field around the position of the molecules, a square box (red; inner domain) along the transportation axis ($x-$axis) is defined.

transformation. To that end, the simulation makes use of a 3D CAD geometry of a single rod electrode i. In this way, the model size of the simulation is reduced to a quarter of the full geometry, allowing for a finer mesh.

2. **Defining the computational domain.** The domain within which the electric potential and thus the electric field is calculated (*computational domain*) is defined by a box that encloses the entire electrode. Figure 9.4 (a) portrays the computational domain together with the electrode in it. To implement the field boundary conditions at infinite distance to the simulation, the left, upper, front, and rear boundaries of the computational domain in Fig. 9.4 (a) are set to ground. The boundary conditions of the right and lower boundaries (corresponding to the $xy-$ and $xz-$plane) take into account the respective symmetry or antisymmetry of the simulated electric potential. The material of the computational domain is set to *air*, which has the same properties that are relevant for the electric field simulation than vacuum. The boundary surface of the electrode is set to be at a potential V_i relative to ground.

3. **Meshing.** For capturing the physics in the simulation, the computational domain is divided into three sub-domains. Each sub-domain has a mesh of different element size. A square channel (cross-section 2.5×2.5 mm) along the $x-$axis is defined to have a rather small element size. The volume of this channel is denoted as *inner domain*. The inner domain allows a higher spatial resolution for the simulation around the center of the glass cell where the molecules will be investigated and along the $x-$axis. Figure 9.4 (b) clarifies the dimensions and the relative position of the inner domain within the computational domain. To resolve the surface curvature of the rod electrode, the mesh of the rod is set to have an element size that is smaller than the radius of the electrode. The remaining volume of the computational domain is meshed rather coarsely.

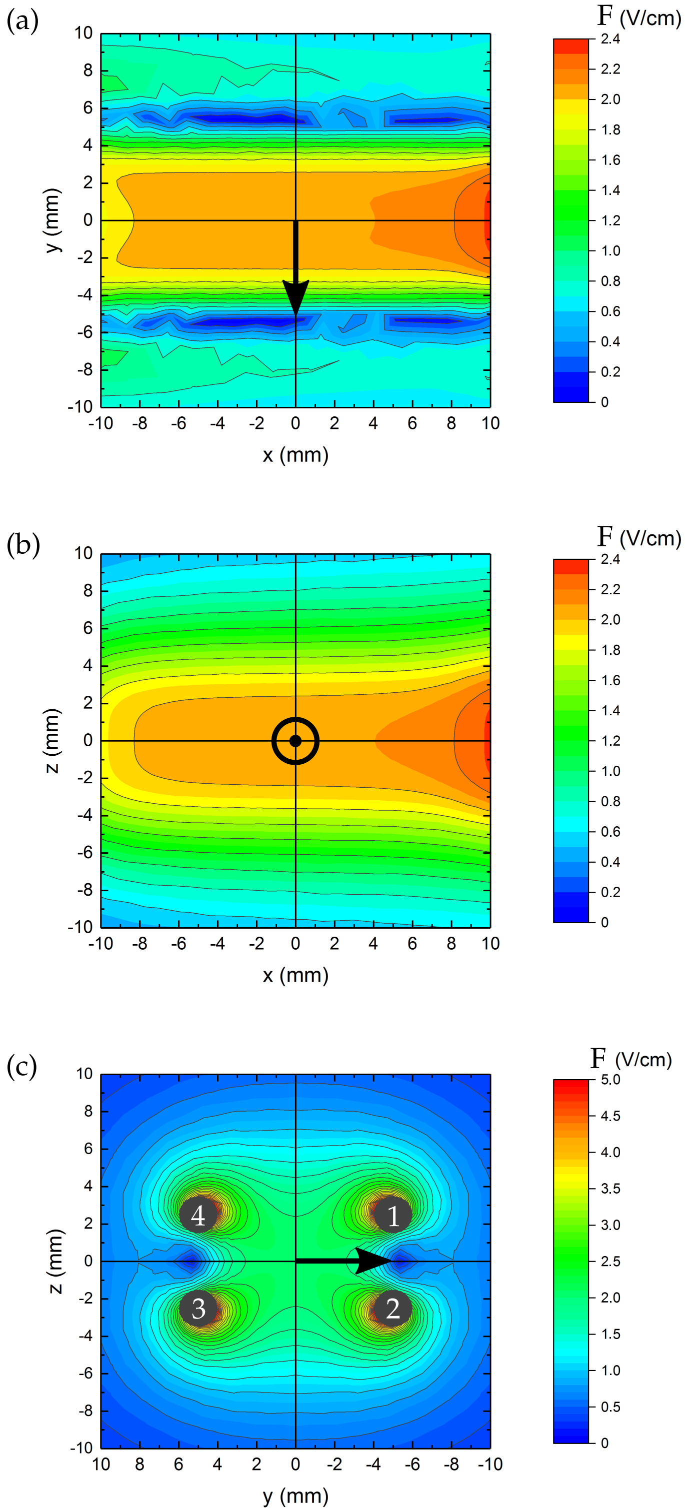

Figure 9.5.: Electric field distribution of simulation 1 (horizontal electric field). Electric field strength plots for the (a) $xy-$plane, (b) $xz-$plane, and (c) $yz-$plane. The black arrows and the black circle at the origins of the plots indicate the direction of the local electric field.

4. **Limiting the influence of the computational domain boundaries.** The dimensions of the computational domain (length, width, height) are swept individually from small to large and each time the electric field simulation is repeated. When the relative difference in electric field strength at the position of the molecules of two consecutive simulations becomes less than $1\,\%$, the respective dimension of the computational domain is noted and used for all of the following simulations. The value of $1\,\%$ is chosen because of limited computational power.

5. **Analyzing the model convergence.** The element sizes of all three mesh domains are scanned independently from each other towards smaller values and each time the simulation is repeated. After every simulation run it is checked by how much the electric field strength has changed. If the relative difference in electric field strength at the position of the molecules of two consecutive simulations comes below $1\,\%$, the respective mesh size is used for all following simulations. If the relative difference is larger than $1\,\%$, the electric field simulation would be regarded as mesh dependent. The value of $1\,\%$ is chosen with respect to limited computational power.
   The final element size of the inner domain determined in this way is smaller than $400\,\mu\mathrm{m}$, for the electrode it is comparable to that of the inner domain, and the element size of the remaining volume of the computational domain is smaller than $2\,\mathrm{mm}$. Given the residual influence of the boundaries and the meshing on the simulation results, a total systematic error of $\pm 2\,\%$ is assumed for the numerical results of the electric field simulations.

9.2.2. Horizontal Electric Field (Simulation 1)

The first electric field simulation treats the case of a voltage assignment to the electrodes according to $V_{1,2} = -1\,\mathrm{V}$ and $V_{3,4} = +1\,\mathrm{V}$. For this voltage configuration, the electric field vector $\vec{F}$ at the origin of the local coordinate system is antiparallel to the $y-$direction and thus lies within the horizontal $xy-$plane. According to the numerical results of the simulation, the $x-$ and $z-$components of the electric field vector $\vec{F}$ along the $x-$, $y-$, and $z-$axis are about a factor of 10^{-3} smaller in strength than the absolute electric field strength F and thus negligible. Figure 9.5 (a)-(c) shows the resulting electric field distribution $F(x, y, z)$ for the $xy-$plane, $xz-$plane, and $yz-$plane. In the following, the spatial dependence of the electric field strength $F(x, y, z)$ along the $x-$, $y-$, and $z-$ direction is analyzed separately.

Figure 9.6 (a) shows the absolute electric field strength F along the $y-$axis, i.e. $F(x = 0, y, z = 0) = F(y)$. The electric field distribution $F(y)$ has three peaks, which are separated from each other by two local minima. The minima are located at $y \approx \pm 5.3\,\mathrm{mm}$. At these positions the contributions of all electrodes to the electric field add up to $0.13(1)\,\mathrm{V/cm}$ and thus almost entirely cancel each other. Around $y \approx 0$, $F(y)$ takes the form of a maximum with a broad plateau. Figure 9.6 (b) gives a closer look on that plateau and reveals that the field distribution $F(y)$ has a local minimum at $y = 0$. The field strength at the center of that local minimum is $F_0^{\mathrm{sim1}} = 2.09(5)\,\mathrm{V/cm}$. To get knowledge of the variation of $F(y)$ in the vicinity of $y = 0$, a harmonic function of the form $F(y) = F_0 + F_2 \cdot y^2$ is fitted to the numerical data (dashed curve in Fig. 9.6 (b)). Since the mesh size in this region of the inner domain is on the order of $150\,\mu\mathrm{m}$, the fit region is chosen to be $|y| \lesssim 1\,\mathrm{mm}$. In this way, the fit region provides a sufficient number (here, 13 data points) for fitting. The fit yields $F_{0,\mathrm{y}}^{\mathrm{sim1}} = 2.089\,13(6)\,\mathrm{V/cm}$ and $F_{2,\mathrm{y}}^{\mathrm{sim1}} = 0.0033(1)\ \mathrm{V/(cm \cdot cm^2)}$. The error given in brackets is the fit error.

In a next step, the electric field along the $z-$direction is studied. Figure 9.6 (c) shows

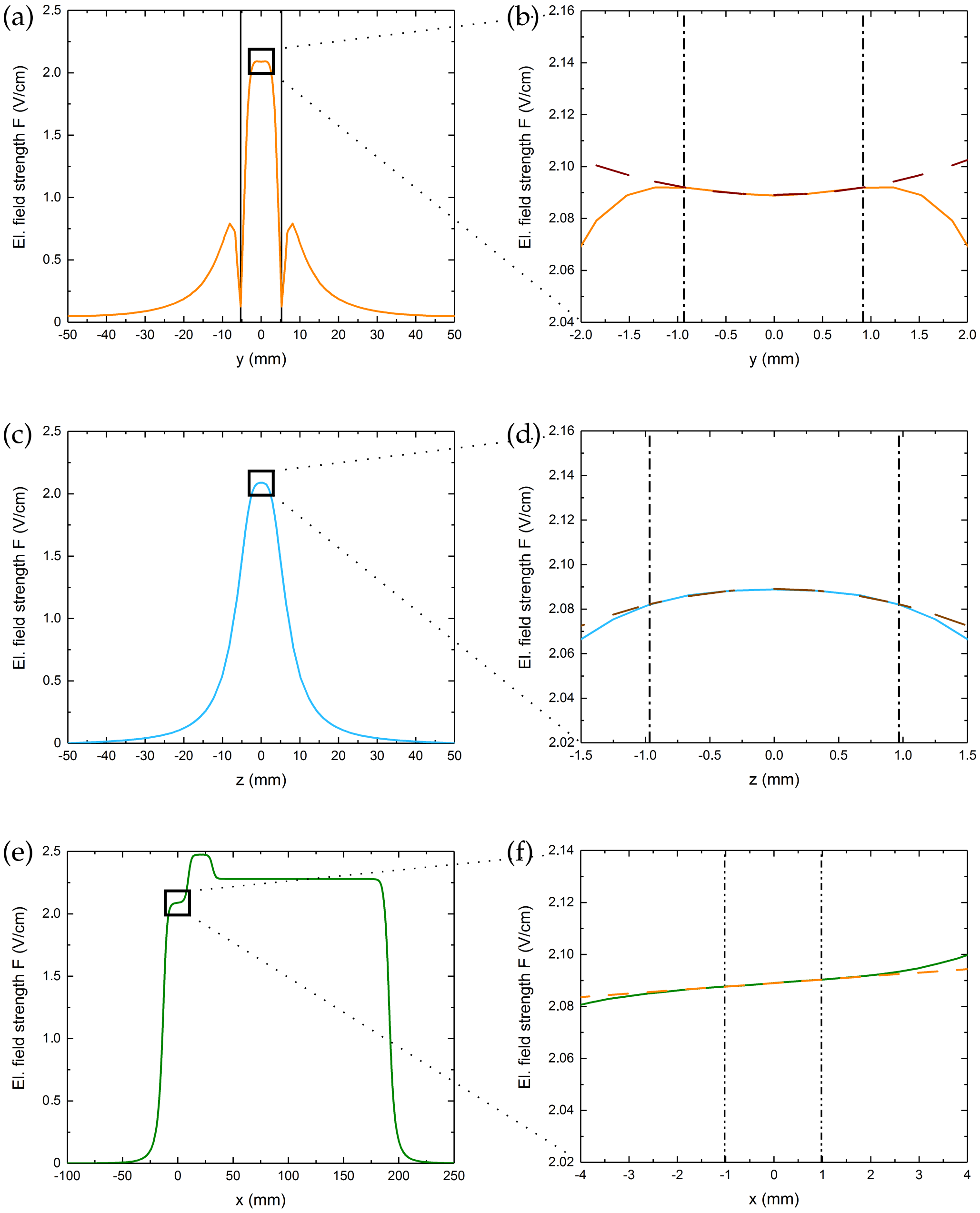

Figure 9.6.: Electric field strengths of simulation 1 (horizontal electric field). Computed results for the absolute electric field strength F along the (a) $y-$axis, (c) $z-$axis, and (e) $x-$axis. In (a), the vertical solid lines indicate the $y-$positions of the local field strength minima. The plots (b), (d), and (f) are zooms into the corresponding plots (a), (c), and (e). The dashed curves in (b) and (d) are fitted harmonic functions and the dashed line in (f) shows the fitted field gradient. Vertical, dash-dotted lines mark the fit region for each fit.

the electric field distribution $F(0,0,z) = F(z)$ as a function of the $z-$coordinate. The field distribution $F(z)$ has one maximum that is located at $z = 0$ and decreases monotonously for $|z| > 0$. Figure 9.6 (d) shows a zoom into the field strength maximum. In order to characterize the electric field variation around $z = 0$, a harmonic function (dashed curve in Fig. 9.6 (d)) is fitted to the numerical data. For the same reason as before, the fit region is chosen to be $|z| < 1\,\mathrm{mm}$. The obtained fit results are $F_{0,\mathrm{z}}^{\mathrm{sim1}} = 2.0891(8)\,\mathrm{V/cm}$ and $F_{2,\mathrm{z}}^{\mathrm{sim1}} = -0.0074(2)$ V/(cm · cm^2).

In Fig. 9.6 (e) the numerical results for the electric field distribution $F(x,0,0) = F(x)$ along the $x-$axis are plotted. The numerical results show that the field strength F changes rapidly in certain regions and stays constant inbetween those regions. The jumps in field strength at $x \approx -12\,\mathrm{mm}$ and $x \approx 192\,\mathrm{mm}$ are due to the finite length of the electrodes. In contrast, the field strength jumps at $x \approx 10\,\mathrm{mm}$ and $x \approx 32\,\mathrm{mm}$ result from changes in the diameter of the electrodes. Figure 9.6 (f) shows that at $x = 0$ the curve has a saddle-point-like shape. The interpolated electric field strength at $x = 0$ is $F_{0,\mathrm{x}}^{\mathrm{sim1}} = 2.088\,99(2)\,\mathrm{V/cm}$. The gradient F_1 along the $x-$direction within the fit region $|x| \lesssim 1$ mm is determined to be $F_{1,\mathrm{x}}^{\mathrm{sim1}} =$ 0.00134(3) V/(cm · cm).

9.2.3. Vertical Electric Field (Simulation 2)

The second electric field simulation assumes a voltage assignment to the electrodes according to $V_{1,4} = -1\,\mathrm{V}$ and $V_{2,3} = +1\,\mathrm{V}$. The electric field vector $\vec{F}$ at the origin of the local coordinate system is now parallel to the $z-$direction and thus points along the vertical direction. The $x-$ and $y-$components of the electric field vector are a factor of 10^{-2} smaller than the absolute electric field strength F along all three spatial directions and thus again negligible. Figure 9.7 (a)-(c) shows the resulting electric field distribution $F(x,y,z)$ for the $xy-$plane, $xz-$plane, and $yz-$plane.

Figure 9.8 (a) shows the electric field distribution $F(y)$ along the $y-$axis. The electric field distribution $F(y)$ exhibits two maxima at $y \approx \pm\, 5.3\,\mathrm{mm}$ and a local minimum at $y = 0$. At $y = 0$, the field strength is $F_0^{\mathrm{sim2}} = 1.77(4)\,\mathrm{V/cm}$, which is a factor of 0.85 smaller than the field strength F_0^{sim1} of the first electric field simulation. Figure 9.8 (b) shows a zoom into the electric field distribution around $y = 0$. The dashed curve in Fig. 9.8 (b) corresponds to a harmonic function that is fitted to the numerical data within the range $|y| < 1.6\,\mathrm{mm}$. Since the average element size of the mesh in this region of the inner domain is about $140\,\mu\mathrm{m}$, the fit is based on about 20 data points. The fit yields $F_{0,\mathrm{y}}^{\mathrm{sim2}} = 1.766(1)\,\mathrm{V/cm}$ and $F_{2,\mathrm{y}}^{\mathrm{sim2}} = 0.1516(9)$ V/(cm · cm^2).

Next, the electric field distribution along the $z-$direction is analyzed. Figure 9.8 (c) shows the electric field distribution $F(z)$. The electric field distribution $F(z)$ has three maxima. The central peak is located at $z = 0$ while the smaller side peaks are at positions $z \approx \pm\, 9\,\mathrm{mm}$. At $z \approx \pm\, 5\,\mathrm{mm}$, the electric field has two local minima with local field strengths of $0.11(1)\,\mathrm{V/cm}$. Figure 9.8 (d) shows a zoom into the central maximum. A harmonic function is fitted to the numerical data within the range $|z| \lesssim 1\,\mathrm{mm}$ (dashed curve in Fig. 9.8 (d)). The fit yields $F_{0,\mathrm{z}}^{\mathrm{sim2}} =$ $1.7703(7)\,\mathrm{V/cm}$ and $F_{2,\mathrm{z}}^{\mathrm{sim2}} = -0.139(1)$ V/(cm · cm^2).

Finally, the electric field strength dependence along the $x-$direction is studied. Figure 9.8 (e) shows the numerical results for the electric field distribution $F(x)$. The field curve exhibits the same qualitative features as the results of simulation 1 in Fig. 9.6 (e). Figure 9.8 (f) shows a zoom into the region around $x \approx 0$. A linear fit to the numerical data within the region $|x| \lesssim 1\,\mathrm{mm}$ yields a field strength $F_{0,\mathrm{x}}^{\mathrm{sim2}} = 1.7698(7)\,\mathrm{V/cm}$ and a gradient of $F_{1,\mathrm{x}}^{\mathrm{sim2}} = 0.008(1)$ V/(cm · cm).

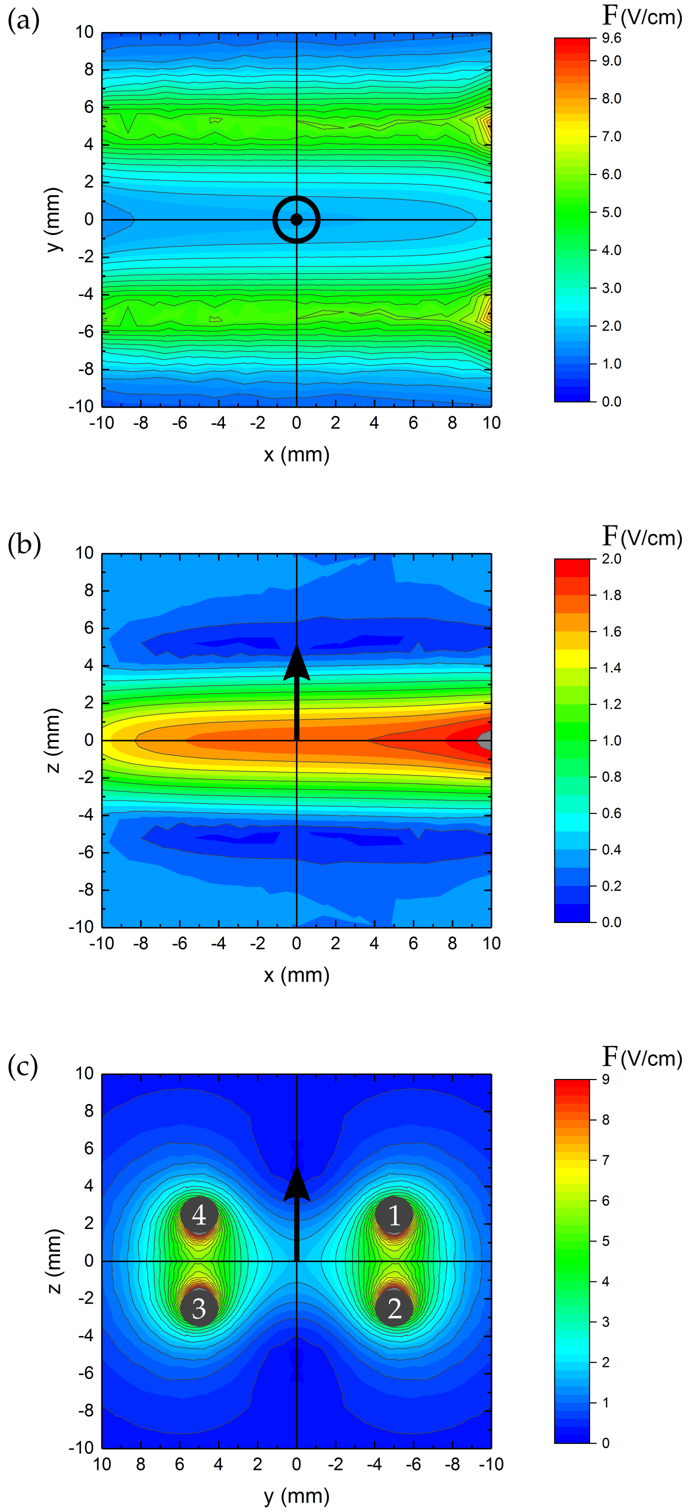

Figure 9.7.: Electric field distribution of simulation 2 (vertical electric field). Electric field strength plots for the (a) $xy-$plane, (b) $xz-$plane, and (c) $yz-$plane. The black arrows and the black circle at the origins of the plots indicate the direction of the local electric field.

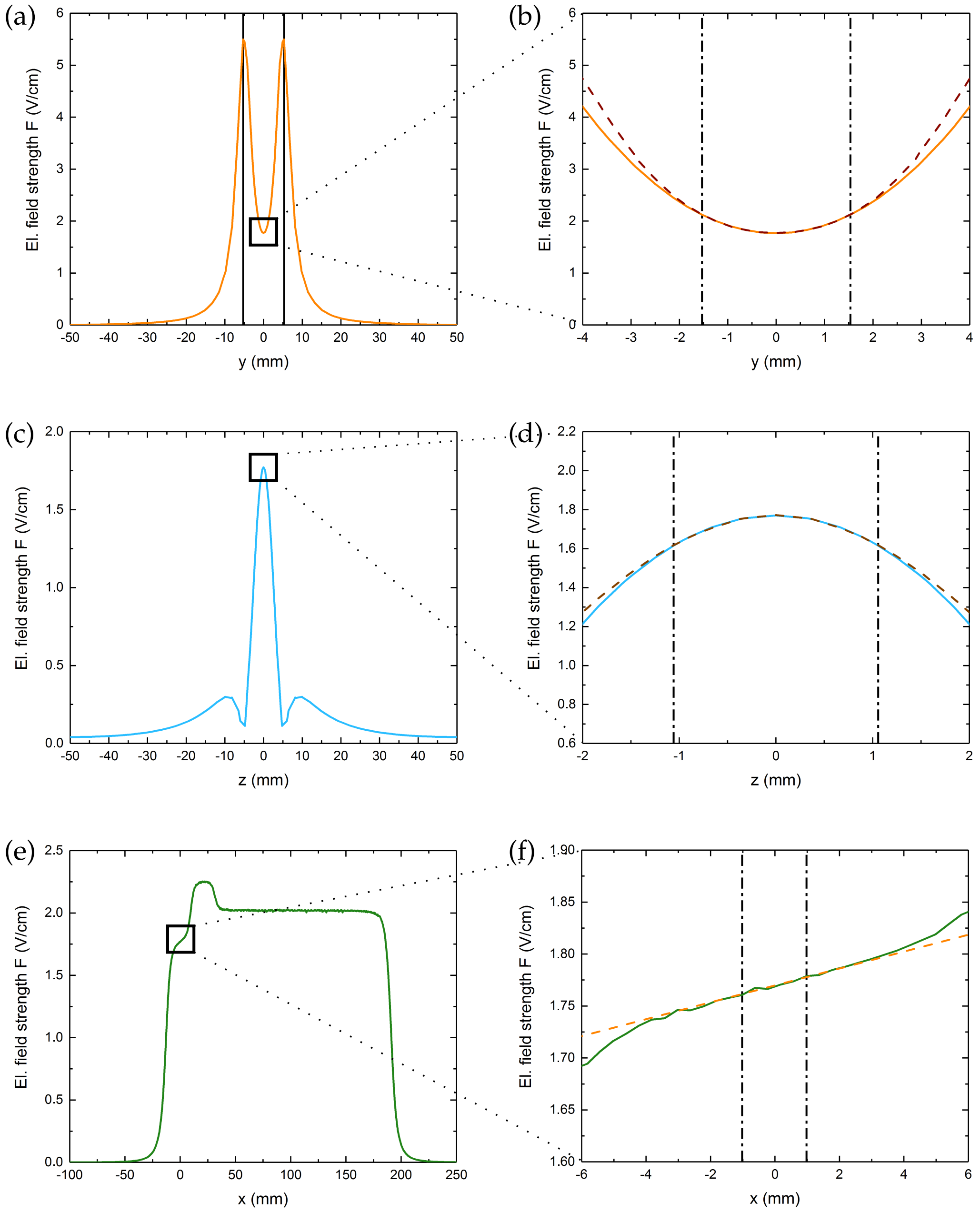

Figure 9.8.: Electric field strengths of simulation 2 (vertical electric field). Computed results for the absolute electric field strength F along the (a) $y-$axis, (c) $z-$axis, (e) and $x-$axis. In (a), the vertical solid lines indicate the $y-$position of the field strength maxima. The plots (b), (d), and (f) are zooms into the corresponding plots (a), (c), and (e). The dashed curves in (b) and (d) are fitted harmonic functions and the dashed line in (f) shows the fitted field gradient. Vertical, dash-dotted lines mark the fit region for each fit.

Table 9.1.: Fit results of the electric field simulations for an horizontal and vertical electric field. For the absolute electric field strength F_0 the fit result with the largest fit error is stated. The field gradient $F_{1,\mathrm{x}}$ and the field curvatures $F_{2,\mathrm{y}}$ and $F_{2,\mathrm{z}}$ are given individually for each simulation. Numbers in brackets indicate the fit error.

	Fit results			
	F_0 (V/cm)	$F_{1,\mathrm{x}}$ (V/(cm · cm))	$F_{2,\mathrm{y}}$ (V/(cm · cm^2))	$F_{2,\mathrm{z}}$ (V/(cm · cm^2))
Horizontal el. field	2.0891(8)	0.00134(3)	0.0033(1)	−0.0074(2)
Vertical el. field	1.766(1)	0.008(1)	0.1516(9)	−0.139(1)

9.2.4. Summary of the Electric Field Simulations

The electric field simulations revealed residual field inhomogeneities at the position of the molecules for the horizontal as well as for the vertical electric field configuration. The field strength inhomogeneities were specified in terms of a field gradient $F_{1,\mathrm{x}}$ in $x-$direction and field curvatures $F_{2,\mathrm{y}}$ and $F_{2,\mathrm{z}}$ in $y-$ and $z-$directions, respectively. Table 9.1 summarizes the fit results of the two field simulations. A comparison of the fit results shows that the field strength inhomogeneities are stronger for the vertical field orientation.

The maximum voltages for which the electrical feedthrough of the glass cell science chamber setup is rated are $\pm 10\,\mathrm{kV}$. At these high voltages, the resulting field strength F_0 at the position of the molecules is about $21\,\mathrm{kV/cm}$ (horizontal electric field) and $18\,\mathrm{kV/cm}$ (vertical electric field). These field strengths are much larger than those originally required for the K−Cs apparatus (see Sec. 8.1.1).

9.2.5. Comments on Electrical Breakdown

The generation of high electric field strengths within the glass cell science chamber of the K−Cs apparatus is only possible if electrical breakdown between the rod electrodes is prohibited. In principle, an electrical breakdown between the titanium electrodes can occur through a dielectric breakdown of the Macor® holders, surface currents that could flow across the Macor® holders, and field emission of the rod electrodes.

The dielectric strength of Macor® is $1.290\,\mathrm{MV/cm}$ [Corb]. Due to machining marks, the dielectric strength of insulating solids, however, can be lower than the specified one [Küc09]. Nevertheless, the electric field strengths that can be generated with the titanium electrodes are much weaker than those required for Macor® loosing its insulating properties. The effect of surface currents across the Macor® holders on the maximum electric field strength that can be realized with the rod electrodes is hard to predict from theoretical considerations. Obviously, a longer leakage path between the electrodes is beneficial for preventing electrical flashover. Because of limited space within the glass cell and due to the spatial configuration of the electrodes, a lengthening of the leakage path would have caused significant difficulties, e.g. a largely restricted optical access to the molecules. Finally, to minimize the risk of field emission of electrons from the electrodes due to microscopic scratches in the surfaces of the electrodes, the surfaces must be smooth. The titanium rods therefore have the best surface finish that we could get for their specific geometry (see p. 143).

In conclusion, different provisions are made against electrical breakdown between the

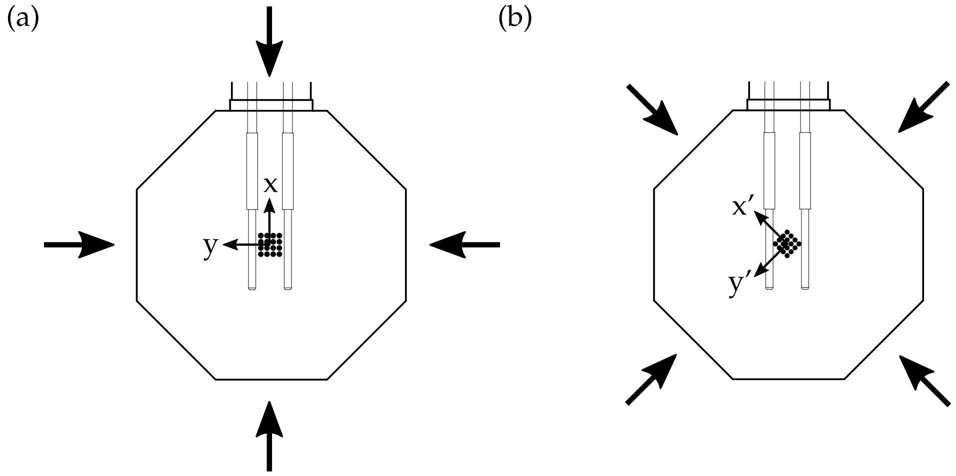

Figure 9.9.: Two lattice configurations are conceivable within the glass cell. (a) If the lattice axes of the 2D square lattice coincide with the $x-$ and $y-$axis defined in Fig. 9.3, the lattice laser beams (black arrows) along the $x-$axis need to pass through the CF16 viewport at the main chamber. (b) The lattice axes (x', y') are rotated by $45°$ relative to the rod electrodes within the horizontal plane. All lattice laser beams enter the glass cell through one of its horizontal glass windows.

titanium electrodes. The maximum realizable electric field strength, however, has to be tested experimentally.

9.2.6. Effects of Electric Field Inhomogeneities on Optical Trapping of ^{39}KCs Molecules

Lattice-confined polar molecules experience an optical lattice potential $V_{\text{latt}}(\vec{r})$ and, in the presence of an external electric field $\vec{F}$, a field-induced Stark shift U_{Stark}. The Stark shift depends on the local electric field strength $F(\vec{r})$ and can be casted in the form [Bon97]

$$U_{\text{Stark}}(\vec{r}) = -\int_0^{F(\vec{r})} \vec{p}(\vec{F}') \cdot \mathrm{d}\vec{F}' \,. \tag{9.12}$$

The two energy contributions $V_{\text{latt}}(\vec{r})$ and $U_{\text{Stark}}(\vec{r})$ lead to a combined potential $U_{\text{molecule}}(\vec{r})$ for the molecules. In the K$-$Cs apparatus the ^{39}KCs molecules within the glass cell will be trapped within a 2D optical lattice plane in the $xy-$plane (see Fig. 9.3). The potential $U_{\text{molecule}}(\vec{r})$ for the trapped ^{39}KCs molecules can thus be written as

$$U_{\text{molecule}}(x, y) = V_{\text{latt}}(x, y) + U_{\text{Stark}}(x, y), \tag{9.13}$$

where $U_{\text{Stark}}(x, y)$ is position dependent due to the residual field gradient and field curvature along the $x-$ and $y-$direction, respectively (see Table 9.1). The spatial variation of $U_{\text{Stark}}(x, y)$ leads to a perturbation of the lattice confinement of the ^{39}KCs molecules. If the spatial variation of $U_{\text{Stark}}(x, y)$ is too strong, trapped ^{39}KCs molecules will be able to move between lattice sites or even escape from the optical lattice.

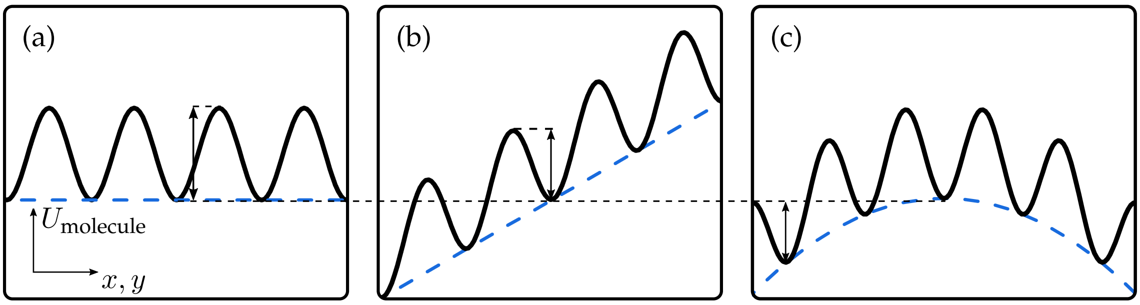

Figure 9.10.: Effect of electric field inhomogeneities on an optical lattice potential. (a) If the Stark shift $U_{\text{Stark}}(x, y)$ (blue dashed line) was homogeneous across the 2D optical lattice plane, the optical lattice potential $V_{\text{latt}}(x, y)$ (black curve) experienced by the molecules would be not distorted. (b) An electric field gradient results in a tilted lattice with a constant energy shift between adjacent lattice sites. (c) For an electric field curvature, the energy shift between neighboring lattice sites varies with position and increases for lattice sites that are further away from the center of the curvature. In (b) and (c), the potential barrier of the lattice sites (vertical black arrows) is reduced compared to the undistorted lattice in (a). Figure based on figure in Ref. [Gem16].

There are two laser beam configurations that are conceivable for the generation of a 2D square lattice within the glass cell. Figure 9.9 (a) and (b) illustrates the two possible beam configurations. In the configuration that is depicted in Fig. 9.9 (a) the direction of the electric field gradient in $x-$direction coincides with a lattice axis. The field gradient causes an energy shift between adjacent lattice sites that is constant along the lattice axis. In contrast, the field curvature along the $y-$axis gives rise to an energy shift between neighboring sites that increases with larger distance from the center of the glass cell. Figure 9.10 illustrates the effect of a field gradient and a field curvature on the lattice confinement. Both, field gradient and field curvature, reduce the potential barrier height of the lattice sites.

In the following, an upper limit for the expected reduction of the lattice site potential barrier height for ^{39}KCs molecules within an optical lattice in the glass cell is calculated. To that end, a 2D square lattice ($\lambda_{\text{L}} = 1064\,\text{nm}$) with lattice constant $a = 532\,\text{nm}$ is considered. The calculation is restricted to ^{39}KCs molecules within the ground and first excited rotational level of the electronic and vibrational ground state. To give an upper limit, the experimental setting that leads to the maximum perturbation of the lattice potential is examined. For field strengths up to $20\,\text{kV/cm}$, the largest induced dipole moment of the considered rotational states is obtained in state $|\tilde{0}, 0\rangle$ at the maximum field strength (see Fig. 9.2). The energy shift between adjacent lattice sites for a ^{39}KCs molecule in state $|\tilde{0}, 0\rangle$ due to the electric field inhomogeneities is maximum for the field gradient of the vertical electric field simulation pointing along a lattice axis. Assuming undisturbed lattice depths V_0 between 20 and 50 $E_{\text{rec}}^{\text{KCs}}$, where $E_{\text{rec}}^{\text{KCs}}$ is the lattice recoil energy of a ^{39}KCs molecule, it is found that for these experimental settings the lattice depth V_0 is then reduced between about $2-5\%$. The lattice distortion is expected to be smaller along the $y-$direction, at smaller electric field strengths F, and for the rotated lattice configuration in Fig. 9.9 (b). It is therefore concluded that ultracold ^{39}KCs molecules at lattice depths V_0 larger than 20 $E_{\text{rec}}^{\text{KCs}}$ will not be spilled out of the optical lattice due to the residual electric field inhomogeneities.

For lattice depths V_0 of few recoil energies $E_{\text{rec}}^{\text{KCs}}$, ^{39}KCs molecules can tunnel between lattice sites of the 2D optical lattice monolayer. Tunneling takes place as long as the on-site harmonic oscillator states of the individual lattice sites are resonant with each other. Electric field inhomogeneities cause a site-to-site energy offset of the molecules, which can shift the oscillator states of different lattice sites out of resonance. If the electric field inhomogeneities are strong enough, tunneling is suppressed in this way. Early experiments with ultracold ^{39}KCs molecules within the glass cell of the K−Cs apparatus will concentrate on molecules that are deeply bound ($V_0 \gtrapprox 40E_{\mathrm{rec}}^{\mathrm{KCs}}$). This is for instance the case for the spin$-1/2$ Heisenberg XXZ lattice model with ^{39}KCs molecules. At such deep lattices tunneling does not play a role and thus the effect of electric field inhomogeneities on tunneling is not of any matter.

9.3. Calculation of Dipolar Spin Exchange Probability Amplitudes for ^{39}KCs Molecules

This Section studies the effect of electric field inhomogeneities on future experiments on the spin$-1/2$ Heisenberg XXZ lattice model with ultracold ^{39}KCs molecules in an optical lattice. For this reason, first the question is addressed how this particular spin lattice model can be realized with ultracold polar molecules and how its parameters relate to molecular quantities. The parameters of the spin$-1/2$ Heisenberg XXZ lattice model are evaluated thereafter specifically for ^{39}KCs molecules at different electric field strengths. The calculation gives valuable insight for future experiments of the K−Cs apparatus. Finally, the influence of the electric field inhomogeneities of the glass cell electrodes found in Sec. 9.2.3 on dipolar spin exchange between ultracold, polarized ^{39}KCs molecules on a 2D square lattice is numerically studied.

9.3.1. Spin−1/2 Heisenberg XXZ Lattice Model with Polar Molecules

For a stationary observer, a rotating polar molecule, because of its pEDM, appears to possess an oscillating electric dipole moment [Atk17]. An electromagnetic wave can act on this fluctuating dipole moment and drive dipole transitions between rotational states that belong to the same vibrational and electronic state. That is, polar molecules exhibit a purely rotational spectrum in contrast to nonpolar molecules for which this is not the case [Atk17]. Transition wavelengths of rotational transitions within the electronic and vibrational ground state of a molecule typically lie within the microwave regime and radiative lifetimes of excited rotational states are usually larger than $\sim 10\,\mathrm{s}$ [Hak06, Wal15].

The remainder of this Section is concerned with diatomic polar molecules in their electronic and vibrational ground state. The rotational levels of diatomic polar molecules in their electronic and vibrational ground state are spaced unequally in energy (see Eq. (9.3)). Driving an arbitrary rotational transition within this manifold of rotational states therefore does not couple to other rotational states. In the presence of an external electric field the states $|\tilde{J}_{\mathrm{rot}}, M_{\mathrm{rot}}\rangle$ can thus be addressed individually. It is therefore possible to isolate two states $|\tilde{J}_{\mathrm{rot}}, M_{\mathrm{rot}}\rangle$ and $|\tilde{J}'_{\mathrm{rot}}, M'_{\mathrm{rot}}\rangle$ from all other states. A polar molecule can then be treated as an effective two-level system. For ultracold polar molecules that are pinned to the sites of an optical lattice, these two states represent an internal degree of freedom of the molecules, which can be identified as an effective spin degree of freedom. The two states may be then interpreted as 'spin-up' and 'spin-down' of a spin$-1/2$. It is thus possible to describe ultracold polar molecules within optical lattices as effective spins$-1/2$ [Wal15].

The ground and first rotational level provide different combinations of states that can be used to realize an effective spin$-1/2$. These combinations correspond to $\{|\tilde{0}, 0\rangle, |\tilde{1}, 0\rangle\}$,

$\{|\tilde{0},0\rangle,|\tilde{1},-1\rangle\}$, and $\{|\tilde{0},0\rangle,|\tilde{1},1\rangle\}$. To abbreviate the notation of field-dressed states and induced electric dipole moments, this Thesis follows the notation used in Ref. [Wal15]:

$$\begin{aligned} |{\downarrow}\rangle &= |\tilde{0},0\rangle, & p_{\downarrow} &= \langle{\downarrow}|\hat{p}_0|{\downarrow}\rangle, \\ |{\uparrow}\rangle &= |\tilde{1},0\rangle, & p_{\uparrow} &= \langle{\uparrow}|\hat{p}_0|{\uparrow}\rangle, \\ |\tilde{\uparrow}\rangle &= |\tilde{1},\pm 1\rangle, & p_{\tilde{\uparrow}} &= \langle\tilde{\uparrow}|\hat{p}_0|\tilde{\uparrow}\rangle. \end{aligned} \tag{9.14}$$

Polar molecules within an applied electric field $\vec{F}$, due to their induced electric dipole moment $\vec{p}$, interact with each other via dipole-dipole interaction. For two polarized molecules i and j at positions $\vec{r}_i$ and $\vec{r}_j$, the dipole-dipole interaction Hamiltonian reads [Lah09, Wal15]

$$\hat{H}_{\mathrm{DDI}} = \frac{1}{4\pi\epsilon_0}\frac{\hat{p}_i\cdot\hat{p}_j - 3\left(\hat{p}_i\cdot\vec{e}_r\right)\left(\hat{p}_j\cdot\vec{e}_r\right)}{|\vec{r}_i-\vec{r}_j|^3}, \tag{9.15}$$

where the operator $\hat{p}_i$ is the dipole operator of molecule i and $\vec{e}_r$ is the unit vector along the intermolecular axis. The dipole-dipole interaction of two polarized molecules depends on their relative orientation and is thus anisotropic. Since the dipole-dipole interaction decays proportional to $1/|\vec{r}_i-\vec{r}_j|^3$, it is furthermore long-range in three dimensions [Lah09].

Describing each of the two polarized molecules within the subspace $\{|{\downarrow}\rangle,|{\uparrow}\rangle\}$, the interaction Hamiltonian $\hat{H}_{\mathrm{DDI}}$ in Eq. (9.15) can be written in the basis $\{|{\uparrow_i}\rangle|{\uparrow_j}\rangle,|{\uparrow_i}\rangle|{\downarrow_j}\rangle,|{\downarrow_i}\rangle|{\uparrow_j}\rangle,|{\downarrow_i}\rangle|{\downarrow_j}\rangle\}$ as [Wal15]

$$\hat{H}_{\mathrm{DDI}} = \frac{1-3\cos^2(\Theta_{ij})}{4\pi\epsilon_0|\vec{r}_i-\vec{r}_j|^3}\begin{pmatrix} p_{\uparrow}^2 & 0 & 0 & 0 \\ 0 & p_{\downarrow}p_{\uparrow} & p_{\downarrow\uparrow}^2 & 0 \\ 0 & p_{\downarrow\uparrow}^2 & p_{\downarrow}p_{\uparrow} & 0 \\ 0 & 0 & 0 & p_{\downarrow}^2 \end{pmatrix}, \tag{9.16}$$

where Θ_{ij} is the angle enclosed by $\vec{e}_r$ and the electric field direction. The parameter $p_{\downarrow\uparrow}$ in Eq. (9.16) is defined as [Wal15]

$$p_{\downarrow\uparrow} = \langle{\downarrow}|\hat{p}_0|{\uparrow}\rangle. \tag{9.17}$$

It is denoted as *transition dipole moment*.

The dipole-dipole interaction Hamiltonian $\hat{H}_{\mathrm{DDI}}$ for two polarized molecules in Eq. (9.16) serves as a basis for the derivation of the many-body Hamiltonian for polarized molecules in an optical lattice. The further discussion deals with polarized diatomic, heteronuclear molecules within an optical lattice (2D square or 3D simple cubic) with unit filling, i.e. one molecule per lattice site. The molecules can be either in state $|{\downarrow}\rangle$ or state $|{\uparrow}\rangle$ and shall occupy the motional ground state of their respective lattice site. If tunneling of the molecules is suppressed, intermolecular interaction is limited to dipole-dipole interaction. When the dipole-dipole interaction energy of the trapped molecules is small compared to the energy splitting of the ground and first excited rotational level of the molecules, a molecule at lattice site i cannot change its internal state $|{\downarrow_i}\rangle$ (or $|{\uparrow_i}\rangle$) independently from the other molecules. Processes of the type $|{\downarrow_i}\rangle|{\uparrow_j}\rangle \rightarrow |{\uparrow_i}\rangle|{\uparrow_j}\rangle$ that change the magnetization of the system are therefore energetically off-resonant [Wal15]. Since each molecule can be described as a spin$-1/2$, one can introduce spin$-1/2$ operators for the molecules. Within the subspace of states $\{|{\downarrow}\rangle, |{\uparrow}\rangle\}$, the spin operators for a molecule at lattice site i read [Wal15]

$$\hat{S}_i^z = \frac{1}{2}\left(|{\uparrow_i}\rangle\langle{\uparrow_i}| - |{\downarrow_i}\rangle\langle{\downarrow_i}|\right), \tag{9.18}$$

$$\hat{S}_i^+ = |{\uparrow_i}\rangle\langle{\downarrow_i}|, \tag{9.19}$$

$$\hat{S}_i^- = |{\downarrow_i}\rangle\langle{\uparrow_i}|, \tag{9.20}$$

with $\hat{S}_i^z$ being the Cartesian $z-$component of the *spin vector operator* $\hat{S}_i$ and $\hat{S}_i^+ (\hat{S}_i^-)$ being the *spin raising* (*spin lowering*) operator.

The effective many-body Hamiltonian that describes the trapped molecules is obtained through summation of Eq. (9.16) over all pairs of molecules within the lattice. Using the definitions in Eqs. (9.18)$-$(9.20) and choosing the electric field direction to be the quantization axis, the effective many-body Hamiltonian can be expressed as [Wal15]

$$\hat{H}_{\text{DXXZ}} = \frac{1}{2}\sum_{i\neq j} \frac{1-3\cos^2(\Theta_{ij})}{|\vec{r}_i - \vec{r}_j|^3}\left[\frac{J_\perp}{2}\left(\hat{S}_i^+\hat{S}_j^- + \hat{S}_i^-\hat{S}_j^+\right) + J_z \hat{S}_i^z \hat{S}_j^z\right]. \tag{9.21}$$

Here, $\vec{r}_i$ and $\vec{r}_j$ are given in units of the lattice constant a whereas in Eq. (9.15) and (9.16) the common definition for these vectors applies. If the dipole-dipole interaction between the polarized molecules is truncated to nearest neighbors, Eq. (9.21) simplifies to

$$\hat{H}_{\text{DXXZ}} = \sum_{\langle i,j\rangle} J_{\text{ex}}(\vec{r}_i - \vec{r}_j)\left[\frac{J_\perp}{2}\left(\hat{S}_i^+\hat{S}_j^- + \hat{S}_i^-\hat{S}_j^+\right) + J_z \hat{S}_i^z \hat{S}_j^z\right] \tag{9.22}$$

with

$$J_{\text{ex}}(\vec{r}_i - \vec{r}_j) = \frac{1-3\cos^2(\Theta_{ij})}{|\vec{r}_i - \vec{r}_j|^3}. \tag{9.23}$$

The Hamiltonian $\hat{H}_{\text{DXXZ}}$ in Eq. (9.22) is identical to the Hamiltonian $\hat{H}_{\text{XXZ}}$ in Eq. (1.37) except for the factor $J_{\text{ex}}(\vec{r}_i - \vec{r}_j)$. The latter arises due to the anisotropy of the dipole-dipole interaction. The parameters $J_\perp$ and J_z in Eq. (9.22) can be expressed through molecular quantities and are given through [Wal15, Yan13]

$$J_\perp = \frac{2p_{\downarrow\uparrow}^2}{4\pi\epsilon_0 a^3}, \tag{9.24}$$

$$J_z = \frac{(p_\uparrow - p_\downarrow)^2}{4\pi\epsilon_0 a^3}. \tag{9.25}$$

Since $p_{\downarrow\uparrow}, p_\uparrow$, and $p_\downarrow$ depend on the electric field strength F, the parameters $J_\perp$ and J_z can be tuned in experiments.

Choosing the alternative subspace $\{|{\downarrow}\rangle, |\tilde{\uparrow}\rangle\}$, instead of $\{|{\downarrow}\rangle, |{\uparrow}\rangle\}$, to describe the molecules within the lattice, leads to a Hamiltonian $\hat{H}_{\text{DXXZ}}$ that has precisely the same form of that in Eq. (9.22) [Wal15]. The only difference is the definition of the parameters $J_\perp$ and J_z, which now becomes [Wal15, Yan13]

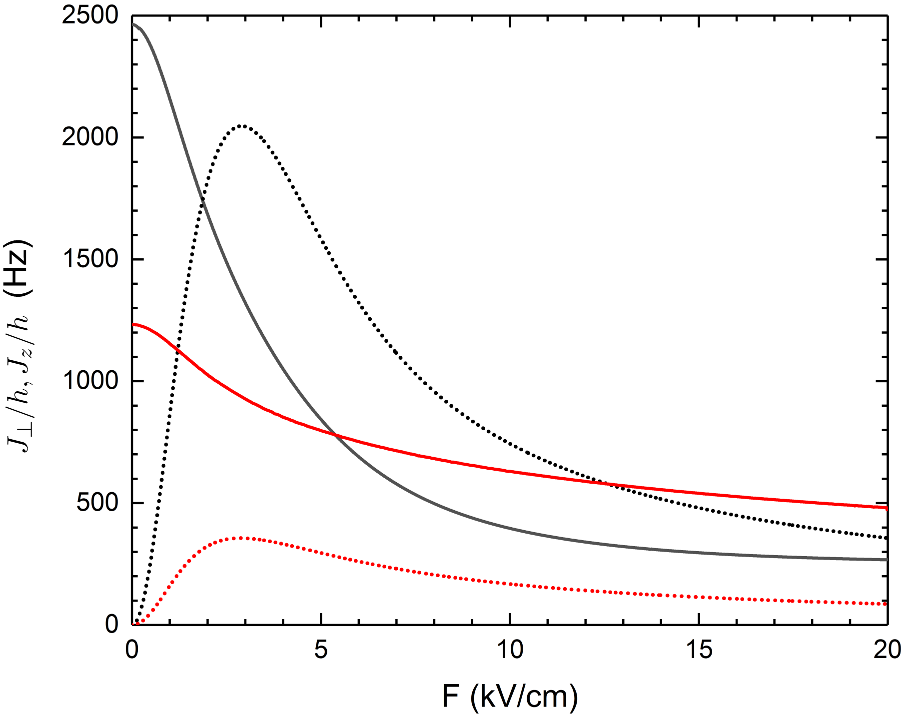

Figure 9.11.: Field dependence of spin-coupling constants. The coupling constants $J_\perp$ (solid lines) and J_z (dotted lines) for the $\{|\downarrow\rangle, |\uparrow\rangle\}$ (black) and $\{|\downarrow\rangle, |\tilde{\uparrow}\rangle\}$ (red) manifold as a function of the electric field strength F. Here, the absolute value of $J_\perp$ for the $\{|\downarrow\rangle, |\tilde{\uparrow}\rangle\}$ manifold is shown.

$$J_\perp = \frac{-p^2_{\downarrow\tilde{\uparrow}}}{4\pi\epsilon_0 a^3}, \tag{9.26}$$

$$J_z = \frac{\left(p_{\tilde{\uparrow}} - p_{\downarrow}\right)^2}{4\pi\epsilon_0 a^3}, \tag{9.27}$$

where $p_{\downarrow\tilde{\uparrow}} = -\langle\downarrow|\hat{p}_{-1}|\tilde{\uparrow}\rangle$. Switching between the two subspaces of rotational states thus changes $J_\perp$ by a factor of -2 and therefore allows one to change the sign of $J_\perp$ next to its magnitude.

9.3.2. Spin$-1/2$ Heisenberg XXZ Lattice Model with ^{39}KCs Molecules

The spin-coupling constants $J_\perp$ and J_z of the dipolar spin$-1/2$ Heisenberg XXZ lattice model in Eq. (9.22) are now evaluated for ^{39}KCs molecules within a 2D square lattice with lattice spacing $a = 532\,\mathrm{nm}$. If the applied electric field $\vec{F}$ is perpendicular to the lattice plane ($\Theta_{ij} = \pi/2$), the factor $J_{\mathrm{ex}}(\vec{r}_i - \vec{r}_j)$ equals unity and hence dipole-dipole interaction between the trapped molecules is isotropic. The dipole-dipole interaction energy between two fully polarized ^{39}KCs molecules on neighboring lattice sites can then be calculated with Eq. (9.15) to be on the order of $h\times$ 3.7 kHz. It is thus much smaller than the energy splitting of the ground and first excited rotational level of the electronic and vibrational ground state of ^{39}KCs (see Sec. 9.1.3).

To calculate the spin-coupling constants $J_\perp$ and J_z as a function of the external electric field strength F for the subspace $\{|\downarrow\rangle, |\uparrow\rangle\}$ ($\{|\downarrow\rangle, |\tilde{\uparrow}\rangle\}$), Eqs. (9.24) and (9.25) (Eqs. (9.26) and (9.27)) are used. For the dipole moments $p_{\tilde{0},0}$, $p_{\tilde{1},0}$, and $p_{\tilde{1},\pm 1}$ that appear in these equations the numerical results obtained in Sec. 9.1.3 are used. The transition dipole moments $p_{\downarrow\uparrow}$ and $p_{\downarrow\tilde{\uparrow}}$ are determined by inserting Eq. (9.10) into the definitions of $p_{\downarrow\uparrow}$ and $p_{\downarrow\tilde{\uparrow}}$. Figure 9.2 shows the numerical results for $p_{\downarrow\uparrow}$ and $p_{\downarrow\tilde{\uparrow}}$ as a function of the electric field strength F. The transition dipole moments $p_{\downarrow\uparrow}$ and $p_{\downarrow\tilde{\uparrow}}$ are maximum ($\approx$ 1.1 D) for zero electric field and become smaller for stronger electric fields.

Figure 9.11 shows the numerical results for $J_\perp$ and J_z for electric field strengths up to $20\,\mathrm{kV/cm}$. As the electric field strength F is varied, the magnitude of $J_\perp$ and J_z changes. The coupling constant J_z vanishes in the absence of an external electric field ($F = 0$), since for this case $p_\downarrow, p_\uparrow$, and $p_{\tilde{\uparrow}}$ are zero. It is maximum at field strengths $2.9\,\mathrm{kV/cm}$ ($2.9\,\mathrm{kV/cm}$) with $J_z/h = 2047\,\mathrm{Hz}$ ($J_z/h = 356\,\mathrm{Hz}$). In contrast, at zero electric field the factor $J_\perp/h$ takes the value $2462\,\mathrm{Hz}$ ($-1232\,\mathrm{Hz}$) and decreases (increases) monotonously for higher electric field strengths.

9.3.3. Dipolar Spin Exchange

The dipolar spin$-1/2$ Heisenberg XXZ Hamiltonian is of experimental interest to the K$-$Cs apparatus, especially for the case of a 2D square lattice. Following discussion is hence restricted to polar molecules on a 2D square lattice that can be described by Eq. (9.22). To quantify dipolar spin exchange between polarized molecules that sit on the sites of such an optical lattice, two isolated molecules at nearest-neighbor sites i and j are considered. Both molecules are exposed to an external electric field $\vec{F}(\vec{r})$ perpendicular to the lattice plane, i.e. $\Theta_{ij} = \pi/2$. The molecule at site i is in state $|\uparrow\rangle$ and the molecule at site j is in state $|\downarrow\rangle$. The total state $|\Psi\rangle$ of both molecules is thus $|\Psi\rangle = |\uparrow_i\downarrow_j\rangle$. The Stark shifts of the molecules, $U^{\uparrow}_{\text{Stark}}(\vec{r}_i)$ and $U^{\downarrow}_{\text{Stark}}(\vec{r}_j)$, contribute to the energy of state $|\Psi\rangle$ and yield a Stark energy that is given by the sum of the individual Stark shifts:

$$U^{\uparrow\downarrow}_{\text{Stark}} = U^{\uparrow}_{\text{Stark}}(\vec{r}_i) + U^{\downarrow}_{\text{Stark}}(\vec{r}_j). \tag{9.28}$$

If the electric field $\vec{F}(\vec{r})$ is homogeneous, i.e. $\vec{F}(\vec{r}) = \vec{F}$, the states $|\uparrow_i\downarrow_j\rangle$ and $|\downarrow_i\uparrow_j\rangle$ (Stark energy $U^{\downarrow\uparrow}_{\text{Stark}} = U^{\downarrow}_{\text{Stark}}(\vec{r}_i) + U^{\uparrow}_{\text{Stark}}(\vec{r}_j)$) with exchanged spins are degenerate.

Both states, $|\uparrow_i\downarrow_j\rangle$ and $|\downarrow_i\uparrow_j\rangle$, are no eigenstates of the Hamiltonian $\hat{H}_{\text{DXXZ}}$ in Eq. (9.22).[5] The considered initial state $|\Psi(t{=}0)\rangle = |\uparrow_i\downarrow_j\rangle$ therefore undergoes an evolution in time according to

$$|\Psi(t)\rangle = \cos\left(\frac{J_\perp}{2\hbar}t\right)|\uparrow_i\downarrow_j\rangle - i\sin\left(\frac{J_\perp}{2\hbar}t\right)|\downarrow_i\uparrow_j\rangle. \tag{9.29}$$

The total state $|\Psi(t)\rangle$ oscillates between $|\uparrow_i\downarrow_j\rangle$ and $|\downarrow_i\uparrow_j\rangle$, leading to spin swapping between the molecules at a frequency $J_\perp/h$. The spin oscillation is mediated by the dipole-dipole interaction between the two molecules and corresponds to an exchange of rotational angular momentum [Yan13].

Spin swapping as described by Eq. (9.29) is called *resonant spin exchange*. Resonant spin exchange requires that for a molecule at site i the field-induced energy shift of the states $|\uparrow\rangle$

---

[5] This can be seen from the matrix in Eq. (9.16), which contains off-diagonal matrix elements.

and $|{\downarrow}\rangle$ relative to each other, denoted as $E^i_{\uparrow\downarrow}$ with

$$E^i_{\uparrow\downarrow} = U^{\uparrow}_{\text{Stark}}(\vec{r}_i) - U^{\downarrow}_{\text{Stark}}(\vec{r}_i), \tag{9.30}$$

must be equal to the relative shift in energy $E^j_{\uparrow\downarrow}$ at site j, i.e. $E^i_{\uparrow\downarrow} = E^j_{\uparrow\downarrow}$. For inhomogeneous electric fields, the relative energy shift $E^i_{\uparrow\downarrow}$ is site-dependent. Equation (9.22) must then be replaced by [Wal15]

$$\hat{H}^{\text{inh}}_{\text{DXXZ}} = \sum_{\langle i,j\rangle} J_{\text{ex}}(\vec{r}_i - \vec{r}_j) \left[\frac{J_\perp}{2}\left(\hat{S}^+_i \hat{S}^-_j + \hat{S}^-_i \hat{S}^+_j\right) + J_z \hat{S}^z_i \hat{S}^z_j\right] + \sum_i h_i \hat{S}^z_i. \tag{9.31}$$

The last term in Eq. (9.31), $\sum_i h_i \hat{S}^z_i$, arises due to the inhomogeneous electric field. It describes the potential energy of the effective spins within an effective, site-dependent magnetic field [Zha05].

The variation of the relative energy shift $E^i_{\uparrow\downarrow}$ between neighboring lattice sites i and j is defined in the following as

$$\Delta E^{ij}_{\uparrow\downarrow} = E^i_{\uparrow\downarrow} - E^j_{\uparrow\downarrow}. \tag{9.32}$$

If the electric field strength F varies from site i to site j by $(\Delta F)_{ij}$ with $(\Delta F)_{ij} \ll F$, $\Delta E^{ij}_{\uparrow\downarrow}$ can be approximately written as

$$\Delta E^{ij}_{\uparrow\downarrow} = -\left(p_\uparrow - p_\downarrow\right)(\Delta F)_{ij}. \tag{9.33}$$

The temporal evolution of the two molecules initially in state $|\Psi(t{=}0)\rangle = |{\uparrow_i}{\downarrow_j}\rangle$ is then determined by the Hamiltonian

$$\hat{H} = \begin{pmatrix} -\Delta E^{ij}_{\uparrow\downarrow}/2 & J_\perp/2 \\ J_\perp/2 & \Delta E^{ij}_{\uparrow\downarrow}/2 \end{pmatrix}. \tag{9.34}$$

The probability to find the two molecules after some time t in state $|{\downarrow_i}{\uparrow_j}\rangle$ with interchanged spins is then

$$|\langle {\downarrow_i}{\uparrow_j}|\Psi(t)\rangle|^2 = \mathcal{S}\cdot \sin^2\left(\frac{\Omega_{\text{ex}}}{2}t\right), \tag{9.35}$$

where the *spin exchange probability amplitude* $\mathcal{S}$ is given by

$$\mathcal{S} = \frac{J_\perp^2}{J_\perp^2 + (\Delta E^{ij}_{\uparrow\downarrow})^2} \tag{9.36}$$

and the Rabi frequency Ω_{ex} can be calculated through

$$\Omega_{\text{ex}} = \frac{1}{\hbar}\sqrt{\left(\Delta E^{ij}_{\uparrow\downarrow}\right)^2 + (J_\perp)^2}. \tag{9.37}$$

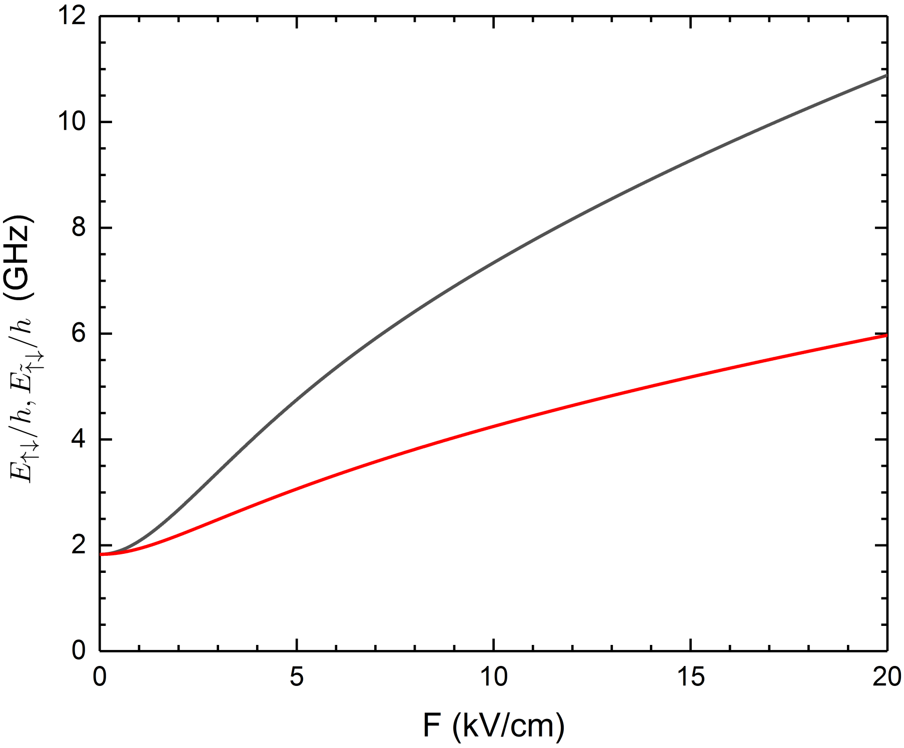

Figure 9.12.: Energy splittings $E_{\uparrow\downarrow}$ and $E_{\tilde{\uparrow}\downarrow}$ as a function of electric field strength F. Energy splitting $E_{\uparrow\downarrow}$ (black curve) and $E_{\tilde{\uparrow}\downarrow}$ (red curve) of the states $|\uparrow\rangle$ and $|\downarrow\rangle$, respectively, $|\tilde{\uparrow}\rangle$ and $|\downarrow\rangle$ for ^{39}KCs. For zero electric field ($F = 0$), the splitting is $2hcB_{\text{rot}}$ in both cases.

Electric field inhomogeneities ($|\Delta E^{ij}_{\uparrow\downarrow}| > 0$) lead to a reduction of the spin exchange probability amplitude $\mathcal{S}$, i.e. $\mathcal{S} < 1$, as can be seen from Eq. (9.36). To observe spin exchange at nearly full amplitude, $\Delta E^{ij}_{\uparrow\downarrow}$ must be much smaller than $J_\perp$.

In practice, dipolar spin exchange is not restricted to nearest-neighbor molecules and can in principle take place between any two molecules with opposite effective spins as long as the electric field is sufficiently homogeneous across the 2D square lattice. For two molecules at different lattice sites, the effective spin coupling strength depends on their mutual separation, which enters Eq. (9.22) through the factor $J_{\text{ex}}(\vec{r}_i - \vec{r}_j)$. Due to the dependence of the factor $J_{\text{ex}}(\vec{r}_i - \vec{r}_j)$ on the spatial separation of the spins, the spin exchange probability amplitude $\mathcal{S}$ and Rabi frequency Ω_{ex} differ for different pairs of molecules.

9.3.4. Dipolar Spin Exchange with ^{39}KCs Molecules

Since the rod electrodes within the glass cell science chamber will generate electric fields that are not perfectly homogeneous, the energy splitting $E_{\uparrow\downarrow}$ of ^{39}KCs molecules within an optical lattice will be site dependent. For this reason, the reduction of the spin exchange probability amplitude $\mathcal{S}$ due to the electric field inhomogeneities is numerically studied. The following calculations consider ^{39}KCs molecules that are trapped within a 2D square lattice (lattice spacing $a = 532\,\text{nm}$) that lies within the $xy-$plane in Fig. 9.3 and that is oriented such that its lattice axes coincide with the $x-$ and $y-$direction. Within this setting, the spin exchange probability amplitude $\mathcal{S}$ is evaluated for the electric field distribution of the electric field simulation

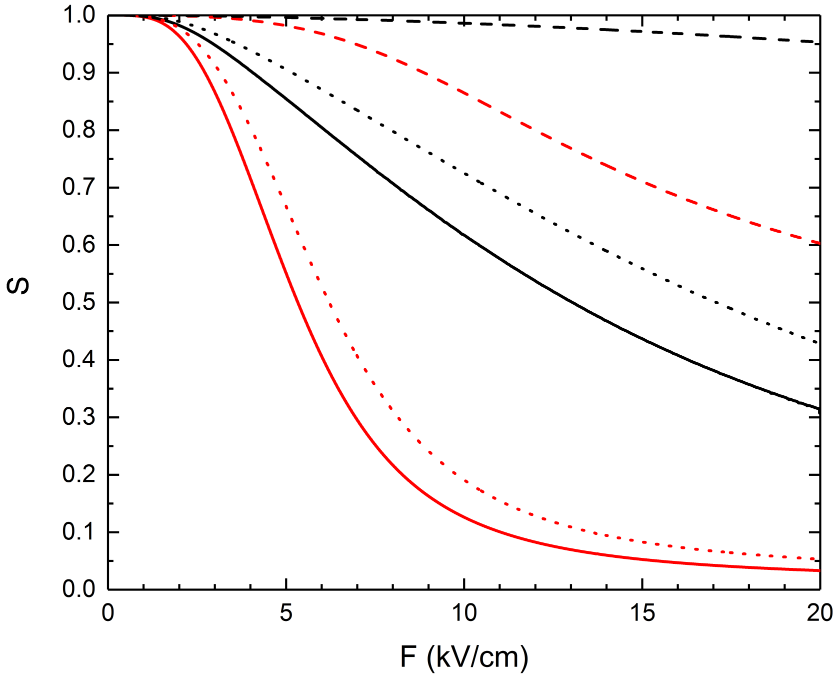

Figure 9.13.: Spin exchange probability amplitude. Calculated spin exchange probability amplitude $\mathcal{S}$ for dipolar spin exchange between ^{39}KCs molecules at nearest-neighbor sites within a 2D square lattice (lattice spacing $a = 532\,\mathrm{nm}$). The amplitudes $\mathcal{S}$ are given for the $\{|{\downarrow}\rangle, |{\uparrow}\rangle\}$ (red) and $\{|{\downarrow}\rangle, |\tilde{\uparrow}\rangle\}$ (black) subspace. Solid curves indicate the amplitude $\mathcal{S}_x$ for dipolar spin exchange along the $x-$axis and dashed curves show the amplitude $\mathcal{S}_y$ for dipolar spin exchange along the $y-$direction. The dotted curves give the spin exchange probability amplitude $\mathcal{S}_{x'}$ for dipolar spin exchange along the $x'-$axis of the rotated lattice configuration.

2 (vertical electric field) in Sec. 9.2.3 and for field strengths up to $20\,\mathrm{kV/cm}$. The spin exchange probability amplitude is studied for the two subspaces $\{|{\downarrow}\rangle, |{\uparrow}\rangle\}$ and $\{|{\downarrow}\rangle, |\tilde{\uparrow}\rangle\}$ for spin exchange between nearest-neighbor lattice sites. Figure 9.12 presents the energy splittings $E_{\uparrow\downarrow}$ and $E_{\tilde{\uparrow}\downarrow}$ as a function of the electric field strength F. The energy splittings $E_{\uparrow\downarrow}$ and $E_{\tilde{\uparrow}\downarrow}$ grow for increasing electric field strength F and reach values of $h \times 10.9\,\mathrm{GHz}$ and $h \times 6\,\mathrm{GHz}$, respectively, at an electric field strength of $20\,\mathrm{kV/cm}$. For zero electric field ($F = 0$), the splitting is $2hcB_{\mathrm{rot}}$ in both cases, as expected.

The inhomogeneity of the electric field of simulation 2 was specified in terms of an electric field gradient $F_{1,\mathrm{x}}^{\mathrm{sim2}}$ in $x-$direction and an electric field curvature $F_{2,\mathrm{y}}^{\mathrm{sim2}}$ along the $y-$axis. The variation of the (transition) dipole moments within the field of view of the K$-$Cs imaging system around the center of the glass cell science chamber is small compared to their absolute values. Hence, $J_\perp$ can be approximately regarded as constant across the field of view. Along the $x-$direction the nearest-neighbor variation $\Delta E_{\uparrow\downarrow}^{i,i+1}$ ($\Delta E_{\tilde{\uparrow}\downarrow}^{i,i+1}$) and associated spin exchange probability amplitude $\mathcal{S}_x$ are thus constant (compare with Eq. (9.33)). Along the $y-$direction, however, the energy splitting $\Delta E_{\uparrow\downarrow}^{i,i+1}$ ($\Delta E_{\tilde{\uparrow}\downarrow}^{i,i+1}$) changes from site to site and is largest for lattice sites far away from the center of the glass cell. To obtain a lower limit for $\mathcal{S}_y$ along the $y-$axis, $\mathcal{S}_y$ is computed for spin exchange between the two lattice sites on the $y-$axis that are most outer of the field of view of the K$-$Cs imaging system. These lattice sites have local coordinates ($0/+39.368\,\mu\mathrm{m}$) and ($0/+39.9\,\mu\mathrm{m}$). Figure 9.13 shows the calculated spin exchange

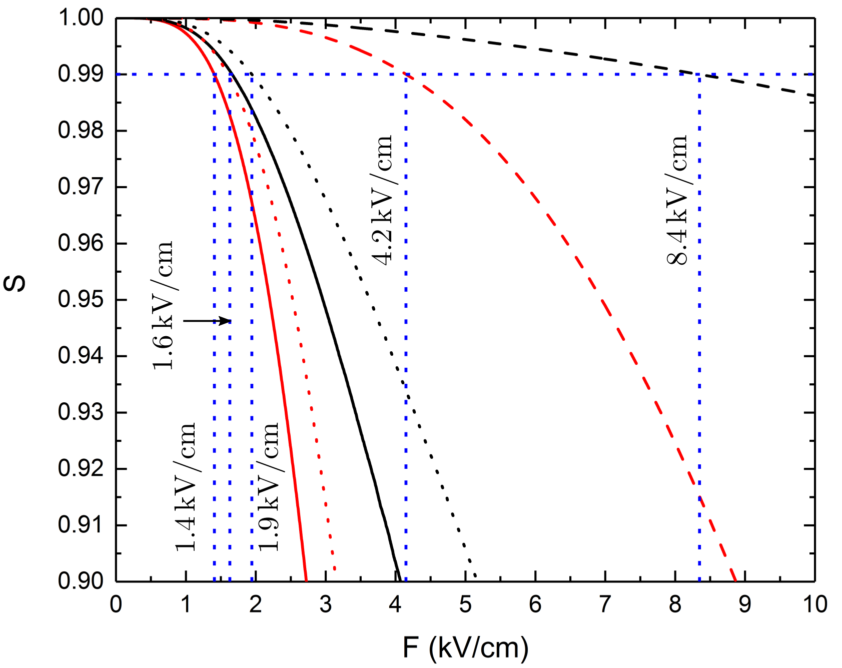

Figure 9.14.: Critical electric field strengths. Zoom into Fig. 9.13 for electric field strengths up to $10\,\mathrm{kV/cm}$. The spin exchange probability amplitudes are given for the $\{|\downarrow\rangle, |\uparrow\rangle\}$ (red) and $\{|\downarrow\rangle, |\tilde{\uparrow}\rangle\}$ (black) subspace. Solid curves indicate the amplitude $\mathcal{S}_x$ for dipolar spin exchange along the $x-$axis and dashed curves the amplitude $\mathcal{S}_y$ for dipolar spin exchange along the $y-$direction. The dotted curves give the spin exchange probability amplitude $\mathcal{S}_{x'}$ for dipolar spin exchange along the $x'-$axis of the rotated lattice configuration. The blue, dotted horizontal line illustrates the amplitude benchmark value of 0.99. The vertical, blue dotted lines indicate the critical electric field strengths F_{crit}.

probability amplitudes $\mathcal{S}_x$ and $\mathcal{S}_y$ as a function of the external electric field strength F for the subspaces $\{|\downarrow\rangle, |\uparrow\rangle\}$ and $\{|\downarrow\rangle, |\tilde{\uparrow}\rangle\}$. The amplitude $\mathcal{S}_x$ decreases faster for stronger fields than $\mathcal{S}_y$.

Next, the probability amplitude $\mathcal{S}$ for nearest-neighbor spin exchange along the lattice axes of the rotated lattice configuration is analyzed. The results for the rotated lattice configuration are obtained by Taylor expansion of the electric field strength $F(x, y)$ around the origin of the local coordinate system. The mixed derivative $\partial^2 F(x, y)/\partial x \partial y$ that appears in the expansion is neglected in our calculations. Thus, the results for the rotated lattice configuration are approximations. Since dipolar spin exchange along the rotated $x'-$ and $y'-$axes is affected in the same way by the field inhomogeneities, the results for the nearest-neighbor spin exchange probability amplitudes $\mathcal{S}_{x'}$ and $\mathcal{S}_{y'}$ overlap with each other. Figure 9.13 therefore shows only the results for $\mathcal{S}_{x'}$.

Dipolar spin exchange between ultracold polar molecules within an optical lattice was observed in the past in Ref. [Yan13]. In these experiments, ^{40}K^{87}Rb molecules were confined within a cubic lattice (lattice constant $a = 532\,\mathrm{nm}$) to realize the spin$-1/2$ quantum XY model. To encode the spin$-1/2$ to the molecules, the rotational subspace $\{|\downarrow\rangle, |\tilde{\uparrow}\rangle\}$ was used. Within the given experimental setting, the constant $|J_\perp/2h|$ for nearest-neighbor dipolar spin exchange was measured to be 48(2) Hz and $|\Delta E^{i,i+1}_{\tilde{\uparrow}\downarrow}/h|$ was determined to be $6\,\mathrm{Hz}$ [Yan13], yielding a spin exchange probability amplitude $\mathcal{S} \approx 0.99$ [Mos16]. The value of 0.99 is used as a benchmark for the spin exchange probability amplitude $\mathcal{S}$ within the K$-$Cs apparatus.

Next, the critical electric field strengths F_{crit} for which the previously calculated spin exchange probability amplitudes $\mathcal{S}$ have decreased to 0.99 are determined. Figure 9.14 shows a zoom into Fig. 9.13 for electric field strengths up to $10\,\mathrm{kV/cm}$ and gives the critical electric field strengths F_{crit}. For the subspace $\{|\downarrow\rangle, |\uparrow\rangle\}$ ($\{|\downarrow\rangle, |\tilde{\uparrow}\rangle\}$), the critical electric field strength F_{crit} with respect to the $x-$axis is $1.4\,\mathrm{kV/cm}$ ($1.7\,\mathrm{kV/cm}$) and with regards to the $y-$axis $4.2\,\mathrm{kV/cm}$ ($8.4\,\mathrm{kV/cm}$). For the $x'-$axis, the spin exchange probability amplitude reaches the benchmark value for an electric field strength of $1.6\,\mathrm{kV/cm}$ ($1.9\,\mathrm{kV/cm}$).

The results in Fig. 9.14 suggest that the electric field that is generated by the titanium electrodes within the glass cell science chamber will be homogeneous enough to observe nearest-neighbor dipolar spin exchange between ^{39}KCs molecules across the entire field of view of the imaging system for field strengths up to $1.4\,\mathrm{kV/cm}$.

10. Setting up a Diode Laser System for Violet Fluorescence Imaging of ^{39}K Atoms

To image ultracold ^{39}K atoms within optical lattices in future, the K−Cs apparatus aims to use violet fluorescence quantum gas microscopy on the $4S_{1/2} \rightarrow 5P_{3/2}$ transition ($\lambda_{\text{image}} = 404.4\,\text{nm}$). Therefore, as part of this Thesis, a home-built diode laser system was set up that generates laser light at $404.4\,\text{nm}$. Additionally, in order to control the frequency of the violet laser light that is sent to the ^{39}K atoms within the vacuum chamber, a frequency stabilization and shifting setup was built. This Chapter summarizes the status quo of (ultra-) violet fluorescence imaging of ultracold alkali atoms. It further describes the laser design and the optical setup for frequency stabilization and shifting of the laser light that were set up. Finally, it presents the first results on imaging ^{39}K atoms with violet laser light within the K−Cs apparatus.

10.1. (Ultra-) Violet Fluorescence Imaging

Over the last years fluorescence quantum gas microscopes have been designed for various atomic species including elements of the alkalis and lanthanides. Table 3.2 indicates that 7 out of at least 9 presently existing FQGMs are operated with alkali atomic species on the respective principal D_1 or D_2 atomic transition, resulting in spatial resolutions of around $600\,\text{nm}$. To build a FQGM with a higher spatial resolution, one faces two options: one can either design the imaging system to have a larger lens diameter or a shorter working distance. Both increases the numerical aperture and thus the resolution of the imaging system. Objectives with increased diameter or reduced working distance, however, might be unfavorable in some quantum gas apparatuses due to geometrical restrictions coming from the vacuum apparatus or laser beams that will be blocked otherwise. Alternatively, one can employ atomic transitions with transition wavelengths in the violet or ultraviolet for fluorescence imaging.

Currently, FQGMs that work in the (ultra-) violet part of the spectrum have been realized only for lanthanide atoms (see Table 3.2). In the related experiments single lattice-confined ^{174}Yb atoms were detected via fluorescence imaging on the dipole-forbidden $^1S_0 \rightarrow {}^1P_1$ atomic transition with $\lambda_{\text{image}} = 399\,\text{nm}$. The resultant FWHM resolution of the employed imaging systems was determined to be around $340\,\text{nm}$. For alkali atoms, atomic ground-state transitions with transition wavelengths in the (ultra-) violet region require intershell transitions $nS_{1/2} \rightarrow n'P_{J'}$ with $n' > n$ and $J' \in \{1/2, 3/2\}$. Table 10.1 summarizes the transition wavelengths of the two lowest lying ground-state intershell transitions ($n' = n+1$) for alkali atoms. The energy gap between the energetically lower $(n{+}1)P_{1/2}$ level and the upper $(n{+}1)P_{3/2}$ level increases for heavier atoms and becomes smaller with increasing principal quantum number n. With regard to potassium, the two ground-state intershell transitions $4S_{1/2} \rightarrow 5P_{1/2}$ and

Table 10.1.: Ground-state intershell D line transitions in alkali atoms. Transition wavelengths of ground-state transitions $n\mathrm{S}_{1/2} \rightarrow (n+1)\mathrm{P}_{1/2,3/2}$ in alkali atoms [Kra49].

	Element				
Transition	**Li**	**Na**	**K**	**Rb**	**Cs**
$n\mathrm{S}_{1/2} \rightarrow (n+1)\mathrm{P}_{1/2}$	323.4 nm	330.3 nm	404.7 nm	421.6 nm	459.3 nm
$n\mathrm{S}_{1/2} \rightarrow (n+1)\mathrm{P}_{3/2}$	323.4 nm	330.2 nm	404.4 nm	420.2 nm	455.5 nm
Reference	[Rad95]	[Kraa]	[Kra49]	[Kra49]	[Kra49]

$4\mathrm{S}_{1/2} \rightarrow 5\mathrm{P}_{3/2}$ have a transition wavelength of 404.7 nm and 404.4 nm [Kraa], respectively.

Intershell transitions in alkali atoms have attracted experimental interest within the ultracold quantum gas community in the past. In Ref. [Dua11], P. M. Duarte *et al.* made use of the narrow but dipole-allowed $2\mathrm{S}_{1/2} \rightarrow 3\mathrm{P}_{3/2}$ transition ($\lambda = 323\,\mathrm{nm}$) of ^{6}Li to laser cool and magneto-optically trap ensembles of ^{6}Li atoms. The authors of the publication demonstrated that ultraviolet laser cooling can increase the atom number and production rate of a quantum degenerate gas of ^{6}Li atoms. Related work was done by D. C. McKay *et al.* with ^{40}K atoms [McK11]. Here, laser cooling was performed on the $4\mathrm{S}_{1/2} \rightarrow 5\mathrm{P}_{3/2}$ transition. For similar reasons the violet transition of potassium was also studied by A. Ridinger in the group of C. Salomon [Rid11b]. Even though the intention of these experiments, namely narrow-line laser cooling, is different from the plan for the K−Cs apparatus, their experimental results point out that experiments with ultracold atoms can benefit from addressing excited, higher-lying atomic levels.

Violet fluorescence quantum gas microscopy of trapped alkali atoms has not been demonstrated so far. However, efforts in that direction have been undertaken in the group of J. H. Thywissen. There, optical molasses cooling and EIT cooling were tried out to cool ^{40}K atoms trapped in an optical lattice during fluorescence imaging on the $4\mathrm{S}_{1/2} \rightarrow 5\mathrm{P}_{3/2}$ transition. Both attempts were reported to not be successful most likely due to inefficient cooling of the atoms [Edg17].

10.2. Laser Design and Laser Diodes

Violet diode lasers for laboratory use are available as commercial laser systems or can be realized by home-built laser setups. Commercial lasers, due to their ready-to-use state upon delivery, represent a fast and efficient solution, however, typically cost tens of thousands of euro and are thus rather costly in purchasing. If not much violet laser power is needed, a home-built laser system can be more economic but at the same time is more elaborate, risky, and time consuming in setting up. For the generation of violet laser light experimental groups within the ultracold quantum gas community often fall back upon commercial laser systems. In Innsbruck, for example, the Ferlaino group and the Grimm group use commercial laser systems to generate 401 nm and 421 nm light in ultracold quantum gas experiments with erbium [Ilz18] and dysprosium [Rav18] atoms. Within the Nägerl group, many home-built diode laser systems for infrared and visible laser light were developed and built over the past years. For the generation of violet laser light at 404.4 nm, it was therefore decided to set up another home-built diode laser system. This gives the chance to expand the knowledge of home-built laser systems within the Nägerl group from the infrared and visible spectrum towards the violet

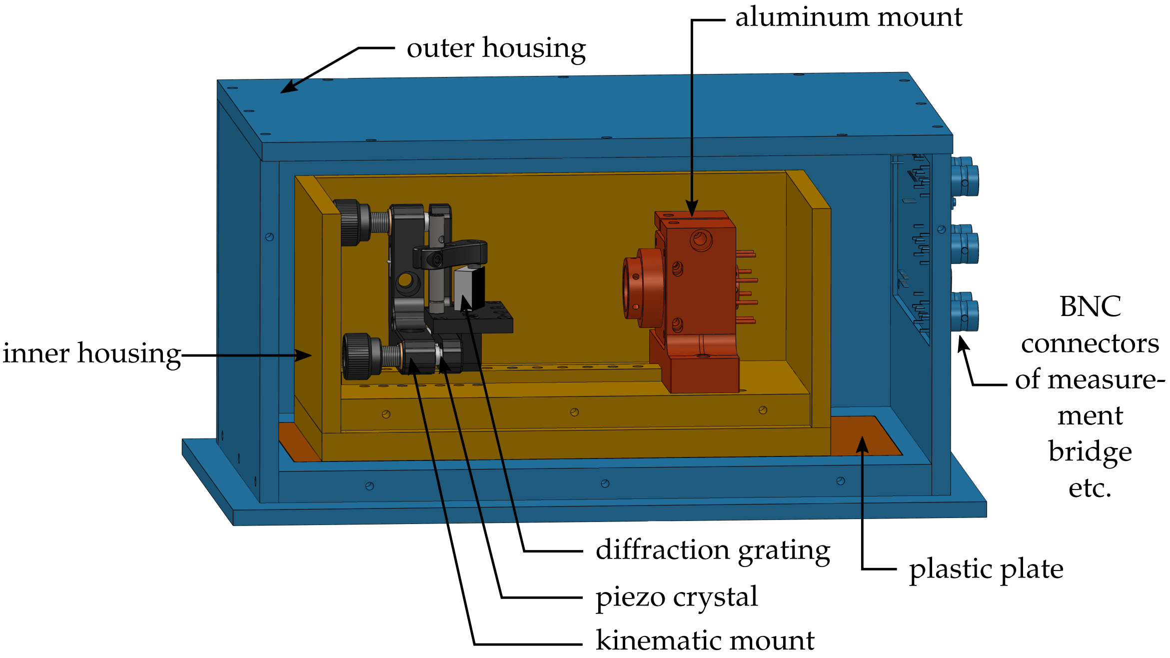

Figure 10.1.: Laser design of the violet laser. The laser diode and a collimation lens are held inside an aluminum mount. At the right side of the aluminum mount the connectors of the laser diode and of Peltier elements can be seen. A diffraction grating in Littrow configuration optically stabilizes the laser diode. The grating is mounted to a commercial kinematic mount. A piezo element allows the variation of the length of the external cavity of the laser. The laser diode and the grating reside within an inner and outer housing. The front covers of the housings as well as the cap of the inner housing are removed here for illustrative reasons. The outer housing incorporates a measurement bridge for electronic control. A plastic plate helps to thermally isolate the inner housing from the outer housing.

regime.

The home-built violet diode laser is an external-cavity diode laser. It uses a commercial laser diode that is optically stabilized by feedback from a diffraction grating. The laser diode and the grating are part of a mechanical laser design that was developed before this Thesis. Figure 10.1 shows the mechanical design of the violet diode laser. It consists of two aluminum housings of which the smaller housing is placed inside the larger one. The inner housing encapsulates the laser diode and the grating, which are mounted to a common base plate. In order to thermally insulate the inner housing from the outer one, the common base plate rests upon a plastic plate. The plastic plate separates both housings from each other. A heating pad between the plastic plate and the inner base plate enables one to electronically control the temperature of the inner housing. The inner housing temperature is set to be higher than the temperature of the outer housing, which is at room temperature. Since any air flow within the laser housing leads to heat convection between the inner and outer housings and additionally can transfer acoustics to the laser, the aluminum case structure is entirely closed except for two small, horizontal holes in the housing. These holes are needed to transmit the laser beam to the optical table.

The laser diode is mechanically clamped inside an aluminum mount. To temperature stabilize the laser diode, several Peltier elements surround the laser diode socket. The temperature of the laser diode and the inner housing is measured by two separate 10k-NTC thermistors. The thermistors are evaluated by a measurement bridge, which is mounted to the inner side of the outer housing. The measurement bridge generates temperature error signals and feeds those to an external temperature proportional-integral-derivative (PID) controller. On the basis of these error signals, the PID controller adjusts the electric currents of the Peltier elements and the heating pad and thereby regulates the temperature error signals to zero.

Opposed to the output facet of the laser diode a diffraction grating is placed. The grating is aligned in Littrow configuration [Wie91, Ric95] and thus diffracts the incident laser light such that the first diffraction order is sent back to the laser diode and the zeroth diffraction order is reflected out of the housing as output beam. The grating is braced onto a standard optomechanical kinematic platform mount, which allows for the optimization of the optical feedback to the laser diode. A small piezo crystal that is connected to the horizontal micrometer screw of the kinematic mount facilitates changing the length of the external cavity and thereby allows for scanning the laser wavelength. Laser diodes are a source of strongly diverging laser beams with elliptical beam profiles. To collimate the output beam of the violet laser diode, a moveable aspheric lens is positioned in front of the laser diode. The collimation lens is mounted within the aluminum mount.

To realize a budget-friendly diode laser, various laser diodes were tried out. In total ten laser diodes were purchased and all of them were tested. Among those laser diodes were nine cheap ($\sim$60€/piece) laser diodes of two different types[1,2] from Thorlabs and a single upmarket ($\sim$1700€) laser diode[3] from Nichia. Thorlabs could not give any information on whether the laser diodes had an anti-reflection coating on their output facets and on their glass windows. Nichia in contrast confirmed that the laser diode has an anti-reflection coating on the glass window but not on the diode chip front facet.

The first nine laser diodes that were tried out, were Thorlabs laser diodes. Since these laser diodes came untested in wavelength, the center wavelength of each laser diode was first measured with an optical spectrum analyzer. The measured center wavelengths covered a range from $401.9\,\mathrm{nm}$ to $407.4\,\mathrm{nm}$. Some of the tested diodes thus had center wavelengths that were far off from the desired wavelength of $404.4\,\mathrm{nm}$. Attempts to bring the center wavelengths of these laser diodes closer to $404.4\,\mathrm{nm}$ by adjusting the laser diode temperature lead to new problems such as unstable laser operation. Some Thorlabs laser diodes failed to run single-mode within the laser setup and yet others delivered only a few milli watts single-mode output power, which was too little for the intended optical setup. In the course of trying to get the Thorlabs laser diodes to run single mode in a stable fashion, several strategies were tried out. These strategies included using different gratings, changing the amount of optical feedback to the laser diode, implementing a polarization-selective element to the external laser cavity for cleaning the polarization, testing different collimation lenses, and trying to remove the protection cap of a laser diode. In spite of all attempts, no reliable laser operation with the Thorlabs laser diodes was achieved. For this reason, the laser diode was changed to that of Nichia.

The best performance of the violet diode laser in terms of stability, single-mode operation, and output power was obtained with the laser diode from Nichia. The laser that is described in this Thesis therefore refers to the realization with that specific laser diode. The Nichia laser diode has a center wavelength of $405\,\mathrm{nm}$, is specified to run single-mode, and is capable of de-

---

[1] Thorlabs, L405P20.

[2] Thorlabs, DL5146-101S.

[3] Nichia, Single-Mode Laser Diode NDV4316.

livering up to $120\,\mathrm{mW}$ output power. To collimate the emitted elliptical laser beam, a molded, aspheric lens[4] is used. The grating is a holographic diffraction grating[5] that is placed at a distance of about $56\,\mathrm{mm}$ in front of the laser diode. The grooves of the grating are oriented vertically such that the output laser beam is reflected within the horizontal plane. The linear polarization axis of the laser light coincides with the minor axis of the elliptical laser beam and is oriented parallel to the direction of the grating grooves. For this orientation, the optical feedback of the grating is specified to be $\sim 22\,\%$ according to the grating's data sheet. The temperatures for the inner housing of the laser and the laser diode are set to $25.5\,°\mathrm{C}$ and $30.3\,°\mathrm{C}$, respectively.

From the beginning of working with the violet diode laser it was rather difficult to get the Nichia laser diode to run single-mode at the desired wavelength of $404.4\,\mathrm{nm}$. It was even harder to stably operate the diode over a longer time than $\sim 20\,\mathrm{min}$ without multi-mode operation. Judging from the experiences with the Nichia laser diode, two reasons contributed to the aggravated single-mode operation: first, the Nichia laser diode exhibited rather narrow plateaus in the diode current, at which the diode would run single-mode. Typically, a change ΔI_diode in diode current with $\Delta I_\mathrm{diode} \ll 1\,\mathrm{mA}$ brought the laser already to multi-moding even with manual feed-forward of the piezo voltage. Attempts to operate the diode laser at different temperatures of the laser housing and laser diode did not improve the stability. Since the single-mode plateaus of laser diodes are generally observed to be broader in diode current at lower diode currents, it was also tried to benefit from operating the laser diode at lower diode currents. Also shifting the operating point of the laser diode to higher diode currents did not help in that respect. A general rule of thumb says that the mode-hop free tuning range of a laser diode decreases for shorter laser wavelengths and vice versa. In that respect, it could be that the behavior of the purchased Nichia laser diode is rather common than uncommon for violet laser diodes and that the instability issue is hence not a matter of malfunction. A similar mode instability was observed when scanning the laser frequency by means of the piezo voltage.

A second aspect that led to complications with the violet diode laser was some sort of uncontrollable drift that regularly appeared and gradually deteriorated the single-mode performance of the diode laser. A quick adjustment of the laser parameters such as piezo voltage and diode current could sometimes recover the spectroscopy signal but ended as often in the total loss of signal. In the latter case, the drifts entailed a time-consuming realignment of the laser. Despite all efforts, the cause of that drift remained unknown to us.

10.3. Optical Setup

To shield the laser setup from external disturbances, a wooden, soundproofed box was built around the diode laser and the surrounding optical setup. Figure 10.2 depicts the optical setup for the violet diode laser. The output beam of the diode laser first passes through an anamorphic prism pair to make the elliptical beam nearly radially symmetric. An optical isolator placed after the prism pair blocks back reflections of subsequent optical elements and thus avoids undesired optical feedback to the laser diode. Following this, a half-wave plate together with a polarising beam splitter (PBS) splits the laser beam into two beams. One beam gets reflected towards a section that is needed to frequency-lock the diode laser (*frequency sta-*

---

[4] Thorlabs, C340TMD-A.

[5] Thorlabs, GH13-18U.

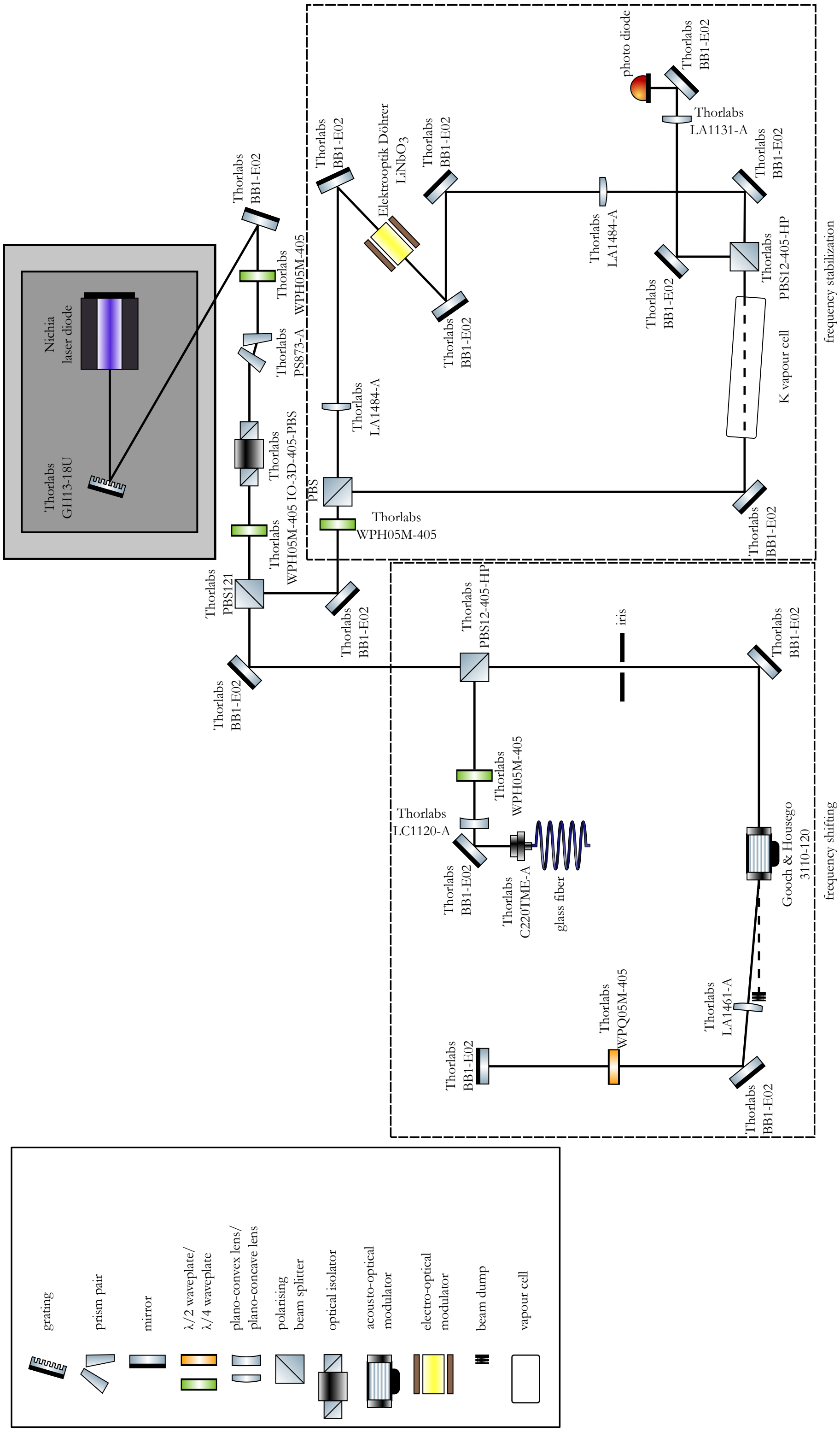

Figure 10.2.: Optical setup. Schematical overview of the optical setup for frequency locking and frequency shifting of the violet laser light. The legend on the lower side of this Figure assigns an optical element to each symbol.

bilization section). The second beam travels towards a section that is required to shift the laser frequency of the light portion that is sent to the main chamber and that couples that light into a glass fiber (*frequency shifting section*).

The frequency stabilization section uses the technique of modulation transfer saturation spectroscopy (MTSS) for frequency stabilization. Modulation transfer saturation spectroscopy is a pump-probe scheme with sub-Doppler resolution [McC08]. In this scheme, two counter-propagating laser beams are overlapped with each other within a gaseous medium of a vapour cell. One beam, the *pump beam*, is frequency modulated at a frequency ν_{m}. The frequency modulation creates sidebands around the carrier frequency ν_{c} of the pump beam with frequencies $\nu_{\mathrm{c}} \pm n\nu_{\mathrm{m}}$ with $n \in \mathbb{Z}$. The frequency sidebands are transfered from the pump beam to the counter-propagating beam (*probe beam*) via four-wave mixing through the third-order susceptibility of the gaseous medium. The sidebands cause an interference-induced intensity oscillation of the probe beam, which can be detected by a photo diode. Through down-conversion of the photo diode signal with the modulation frequency ν_{m} and low-pass filtering, a frequency error signal is generated and can be used for frequency locking.

Frequency stabilization via MTSS is similar to the Pound-Drever-Hall technique [Bla01] and superior to other schemes [McC08]: it offers sub-Doppler resolution and therefore leads to steeper error signals with augmented frequency discrimination compared to other locking techniques. It produces a zero offset line and ergo the error signal zero crossings are centered on the atomic transitions. Furthermore, the zero crossing in MTSS remains largely unaffected from fluctuations in laser intensity, laser polarization, and temperature [McC08]. Modulation transfer saturation spectroscopy has been the standard technique in the laboratories of the Nägerl group since 2000 for locking diode lasers.

Modulation transfer saturation spectroscopy is realized within the optical setup of the violet diode laser as follows. A $\lambda/2-$waveplate in combination with a PBS splits the laser beam that is sent to the frequency stabilization section into a probe and a pump beam. Rotation of the waveplate allows for the controlled distribution of the laser power between the probe and pump beam. The pump beam is frequency modulated through an electronically driven crystal that serves as an electro-optical modulator at a frequency of $\nu_{\mathrm{m}} = 1.2\,\mathrm{MHz}$. This frequency is chosen in view of the condition $2\pi\nu_{\mathrm{m}} \simeq 0.7\Gamma$ (here Γ is the line width of the $4\mathrm{S}_{1/2} \rightarrow 5\mathrm{P}_{3/2}$ transition), which maximizes the slope of the error signal [McC08, Ebl07, Ma90]. In order to avoid truncation of the pump beam through the limited aperture of the electro-optical crystal, the laser beam is focused onto the crystal with a plano-convex lens. A second lens after the crystal recollimates the diverging pump beam. The pump beam is overlapped with the probe beam inside a $\sim 100\,\mathrm{mm}$-long potassium vapour cell. To control the potassium vapour pressure within the vapour cell, the cell is wrapped with heating wires. The cell is heated to a temperature of $84\,^{\circ}\mathrm{C}$. The probe beam is directed to the vapour cell without any optical manipulation. After having passed through the vapour cell, the probe beam is focused onto a photo diode. To generate a frequency error signal that is suitable to frequency lock the violet diode laser, it was necessary to forward most of the laser power of the diode laser towards the frequency stabilization section. The violet laser is locked on the ^{39}K ground-state cross-over resonance.

The frequency shifting section is used to tune the frequency of the laser beam that is sent to the experiment into resonance with the $4\mathrm{S}_{1/2}\ F = 1 \rightarrow 5\mathrm{P}_{3/2}$ transition of ^{39}K. It comprises an acousto-optical modulator[6] (AOM) in double-pass configuration. Since the laser light is locked to the ground-state cross-over resonance of ^{39}K, the AOM must be driven at a frequency

---

[6] Gooch & Housego, 3110-120.

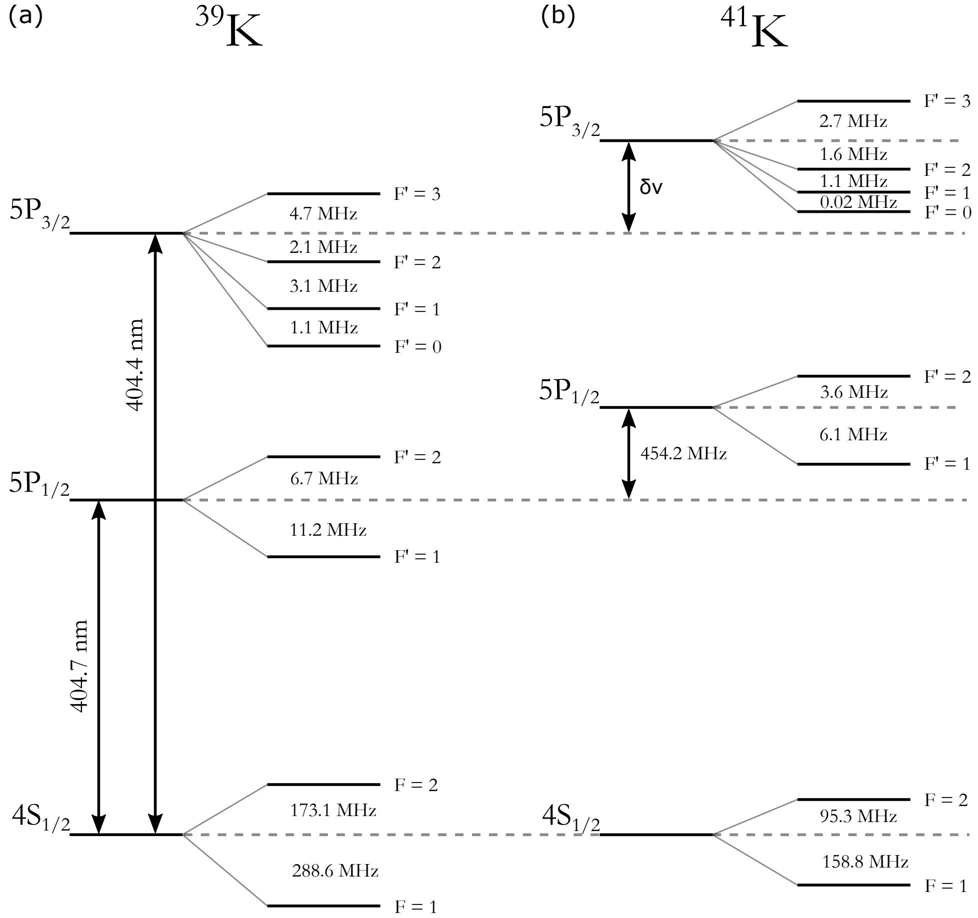

Figure 10.3.: Hyperfine structure in potassium isotopes. Hyperfine structure of the $4S_{1/2}$ ground state and the excited $5P_{1/2}$ and $5P_{3/2}$ levels of the potassium isotopes (a) ^{39}K and (b) ^{41}K. The isotope shift of the $4S_{1/2} \rightarrow 5P_{3/2}$ transition between the two mentioned isotopes is unknown to us and therefore denoted with $\delta\nu$. Data for ^{39}K is taken from Ref. [San08] and for ^{41}K from Ref. [Ari77, Ney69, Sin12, Jia13, Beh11]. Based on figure in Ref. [Han15].

that corresponds to a quarter (115.4 MHz) of the ground-state hyperfine splitting of ^{39}K to bring the laser into resonance with that transition. Figure 10.3 (a) shows the hyperfine structure of the $4S_{1/2}$ and $5P_{1/2,3/2}$ levels of ^{39}K. The efficiency of the AOM double pass was measured to be 53 %. The frequency-shifted laser light is sent to the main chamber through a glass fiber[7]. The coupling efficiency into the fiber was determined to be 48 % of the incident laser power.

10.4. Experimental Results

To characterize the violet diode laser, the laser output power P_{laser} is recorded as a function of the laser diode drive current I_{diode}. The laser output power is measured with a commercial power meter[8], which has a measurement uncertainty of ± 5 % in the spectral region between 400 nm and 439 nm. At first, the power dependency of the laser diode is determined when

---

[7] Thorlabs, PM-S405-XP.

[8] Thorlabs, S121C.

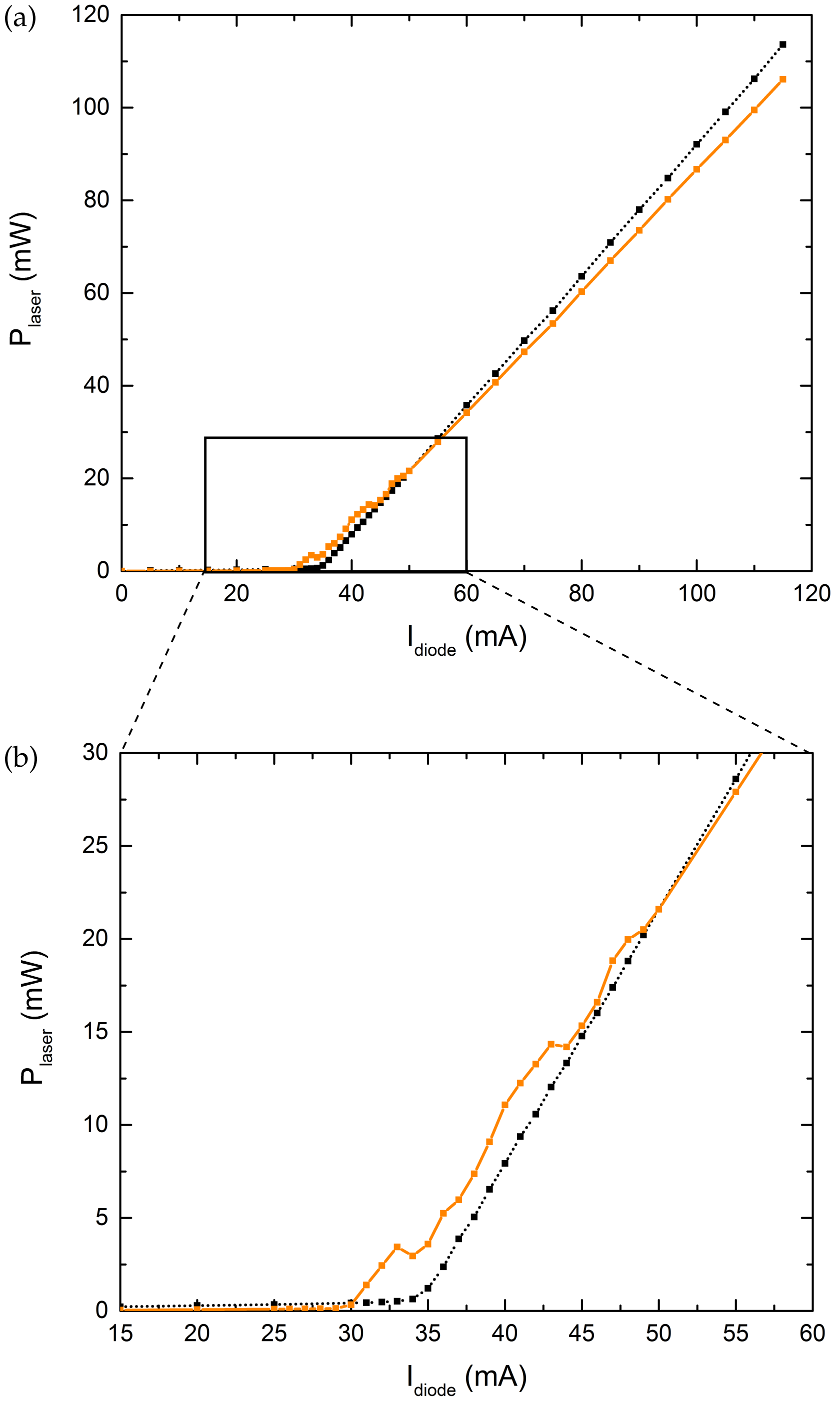

Figure 10.4.: Laser output power versus diode current. (a) Experimental data for the dependence of the optical output power P_{laser} of the violet diode laser on the diode current I_{diode}. The black squares show the data for the bare laser diode without optical feedback. The orange squares show the data for optimized optical feedback to the laser diode. The depicted curves are guides for the eye. (b) Zoom into (a).

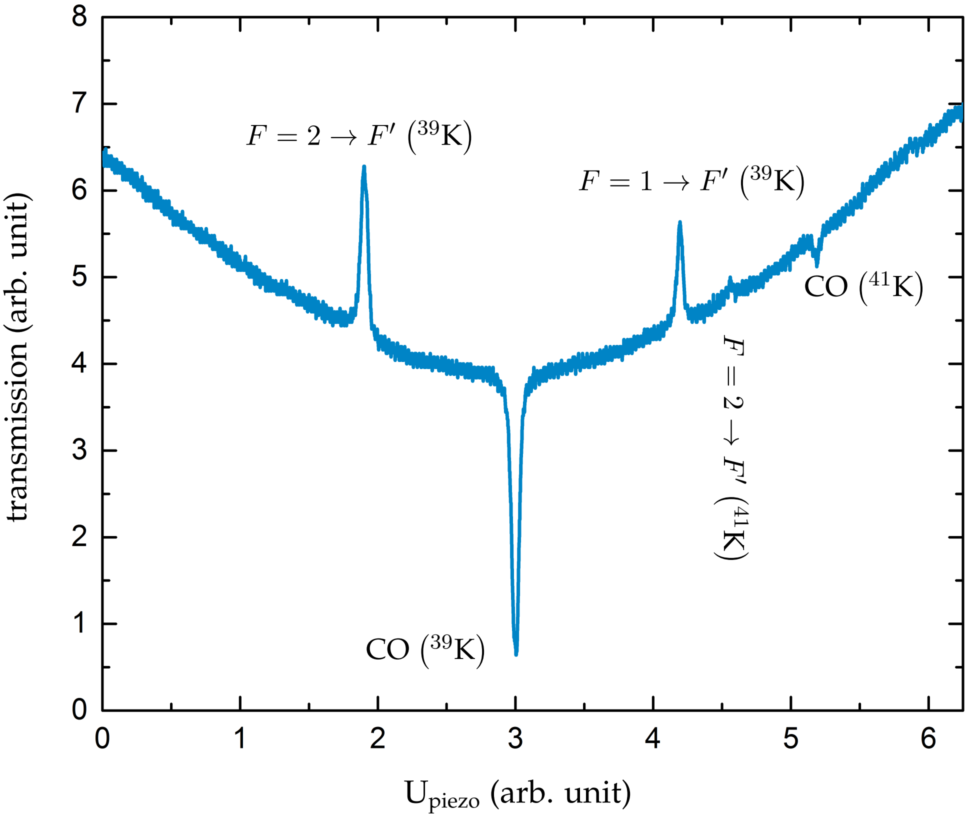

Figure 10.5.: Saturated absorption spectroscopy signal. Transmission spectrum obtained from saturated absorption spectroscopy on potassium vapour. The transmission peaks and dips occur because of absorption on atomic transitions and cross-over (CO) resonances, which are indicated in the Figure and discussed in the main text. The piezo voltage U_{piezo} and the transmission of the probe laser are both given in arbitrary units.

no optical feedback is sent back to the laser diode. Figure 10.4 (a) shows the experimentally obtained $P_{\text{laser}} - I_{\text{diode}}$ curve. The laser output power P_{laser} is constant and nearly zero below a certain threshold current $I_{\text{th}}^{\text{bare}}$ and increases linearly for $I_{\text{diode}} > I_{\text{th}}^{\text{bare}}$. The resulting curve thus shows the expected qualitative behavior of an ideal laser diode. By fitting a linear function to the data for laser diode currents between $36\,\text{mA}$ and $115\,\text{mA}$ the threshold current $I_{\text{th}}^{\text{bare}}$ is determined. The linear fit yields an intersection with the I_{diode}−axis at $I_{\text{th}}^{\text{bare}} = 34.5(2)\,\text{mA}$.

As a next step, the measurement of the $P_{\text{laser}} - I_{\text{diode}}$ curve is repeated now for optimized optical feedback to the laser diode. The results for this measurement are also given in Fig. 10.4 (a). The data for the optically stabilized diode laser exhibits a threshold behavior that is similar to the curve for the bare laser diode. When comparing the two $P_{\text{laser}} - I_{\text{diode}}$ curves, one notices that the slope of the stabilized laser diode is smaller and the threshold current appears at a lower current. The ascending branch of the data for the laser diode with optical feedback segments into two sections. For currents I_{diode} between $30\,\text{mA}$ and $50\,\text{mA}$, the data exhibits kinks in laser power. Figure 10.4 (b) shows a zoom into Fig. 10.4 (a) and reveals the kinks in laser power. These kinks are most likely a result of mode-hops and multi-mode operation. For $I_{\text{diode}} \geq 50\,\text{mA}$, the data is smooth and displays a clearly linear increase. The two sections have different slopes as can be verified by independent fits of linear functions to the two sections.

To determine the laser threshold current $I_{\text{th}}^{\text{fb}}$ for the stabilized diode laser, linear functions are fitted to the two regions $[31\,\text{mA}, 50\,\text{mA}]$ and $[50\,\text{mA}, 115\,\text{mA}]$. As intersection points of the linear functions with the $I_{\text{diode}}-$axis the values $I_{\text{th},1}^{\text{fb}} = 30.7(1.4)\,\text{mA}$ and $I_{\text{th},2}^{\text{fb}} =$ and $33.7(2)\,\text{mA}$ are obtained, respectively. A comparison of $I_{\text{th}}^{\text{bare}}$ and the two values for $I_{\text{th}}^{\text{fb}}$ shows that the optical feedback lowered the threshold current as expected independently of which value for $I_{\text{th}}^{\text{fb}}$ is considered as threshold current. Up to $27\,\text{mW}$ of single-mode laser light were achieved with the violet laser setup.

Finally, the optical setup of the frequency stabilization section is utilized to record an absorption spectrum of the potassium vapour within the heated vapour cell. To that end, the modulation of the pump beam is switched off. As the piezo voltage U_{piezo} of the laser is scanned the intensity of the probe beam after transmission through the vapour cell is detected with the photo diode. The unmodulated pump beam transfers K atoms from the $4\text{S}_{1/2}$ ground state into higher excited states and thereby modifies the absorption of the atomic vapour. The counter-propagating probe beam detects the modified absorption only when both beams act on atoms in the same velocity class. Since pump and probe beam have the same laser frequency, the latter is the case for atoms that move in some velocity class $v = 0$ perpendicular to the pump and probe beam. Absorption then takes place only when the frequency of the diode laser fulfills the sub-Doppler resonance condition of an optical transition [Smi04] (*Doppler-free saturation absorption spectroscopy*). The transmission spectrum that is recorded by the photo diode therefore exhibits the hyperfine structure of the K atoms that is otherwise masked by the Doppler broadened overall absorption profile.

To scan the frequency of the violet diode laser, a time-varying voltage U_{piezo} with a triangular waveform is applied to the piezo crystal within the laser housing. Figure 10.5 shows the obtained transmission spectrum. Because it was not possible to probe the absorption spectrum across the Doppler profile without mode-hopping, the transmission spectrum shown in Fig. 10.5 consists of three images that were combined to one spectrum. The spectrum exhibits a Doppler- and collision broadened profile with sub-Doppler dips and peaks. Near the center of the transmission spectrum at about $U_{\text{piezo}} \approx 3$ in Fig. 10.5, a prominent dip marks enhanced absorption while the peaks to both sides of the central dip indicate enhanced transmission. The transmission peaks occur due to hyperfine ground-state transitions that are driven by the pump beam.

In order to identify the atomic transitions that are responsible for the occurence of the transmission peaks in the recorded transmission spectrum, the experimental results are compared with the theoretical predictions given in Ref. [Han15]. According to these theoretical predictions, the left and right central peaks are caused due to the atomic transitions $4\text{S}_{1/2}$ $F = 2 \to F'$ and $4\text{S}_{1/2}$ $F = 1 \to F'$ of ^{39}K. The central transmission dip thus corresponds to the ^{39}K cross-over resonance. The additional (smaller) features to the right side of the transmission spectrum in Fig. 10.5 come presumably from a residual amount of ^{41}K atoms in the vapour cell. From left to right, the transmission features are assumed to arise due to the atomic transition $4\text{S}_{1/2}$ $F = 2 \to F'$ and the ^{41}K cross-over resonance. Figure 10.3 (b) shows a reduced level scheme of ^{41}K with the hyperfine structure of the $4\text{S}_{1/2}$, $5\text{P}_{1/2}$, and $5\text{P}_{3/2}$ levels.

When the pump beam of the frequency stabilization section is frequency-modulated, the error signal for frequency stabilization is obtained. Figure 10.6 depicts a typical error signal that is generated by the MTSS setup. For this measurement, the laser frequency is tuned across the ground-state cross-over resonance of ^{39}K.

After a long time of testing, optimizing, and rebuilding the violet laser setup, violet laser light was sent to the potassium atoms within the main chamber. At that time, the instability

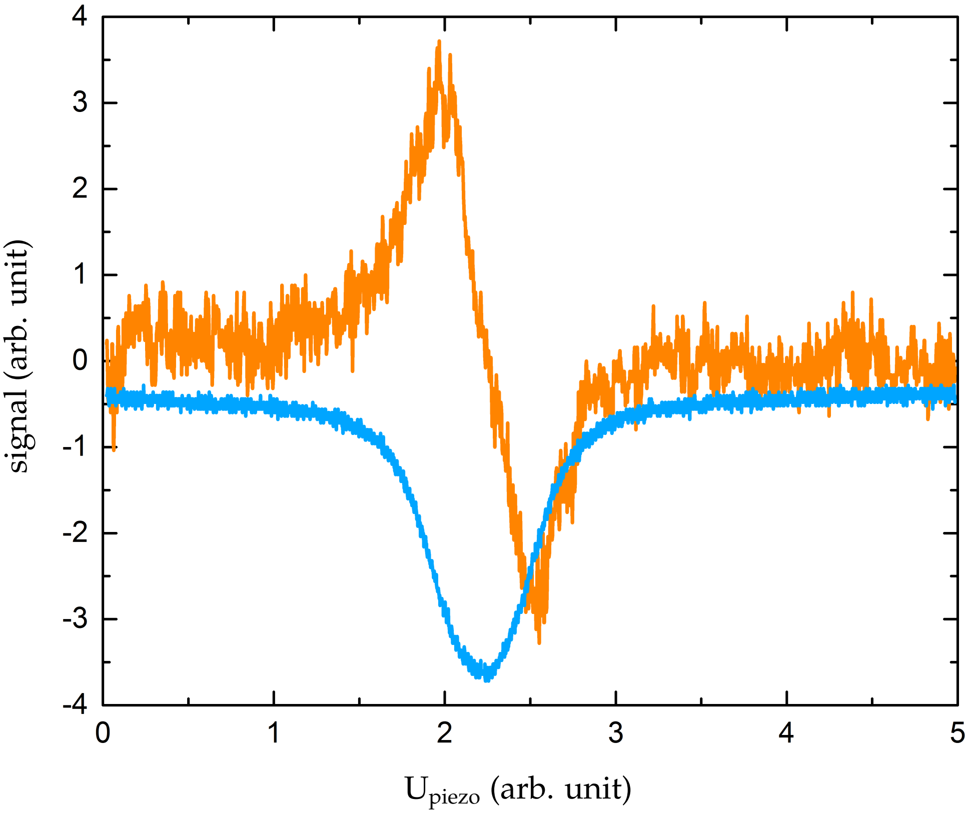

Figure 10.6.: Frequency error signal. A typical error signal (orange curve) for frequency locking of the violet laser obtained with the laser setup. The laser frequency is scanned across the ground-state cross-over resonance of ^{39}K by modulating the piezo voltage U_{piezo}. The error signal is derived from the photo diode signal (blue curve) of MTSS. The piezo voltage U_{piezo} and the error signal as well as the photo diode signal are given in arbitrary units.

of the diode laser was not solved and re-locking of the laser was necessary several times per hour. To align the violet laser beam to the ^{39}K atoms within the main chamber, a ^{39}K 3D-MOT was repeatedly loaded and transfered into a compressed MOT. While the atoms were cooled in the compressed MOT the atoms were exposed to violet laser light. After the compressed MOT phase, the remaining ^{39}K atoms were imaged via absorption imaging on the D_2 line transition. Figure 10.7 shows two absorption images of ^{39}K atoms taken after the compressed MOT phase and during the alignment of the violet laser beam. The images demonstrate the influence of the resonant violet laser light on the ^{39}K atom cloud for two different positions of the violet laser beam. In both cases atoms were removed from the atom cloud and leave behind a gap, which is clearly visible in the Figure. The images show that the violet laser addresses the ^{39}K atoms.

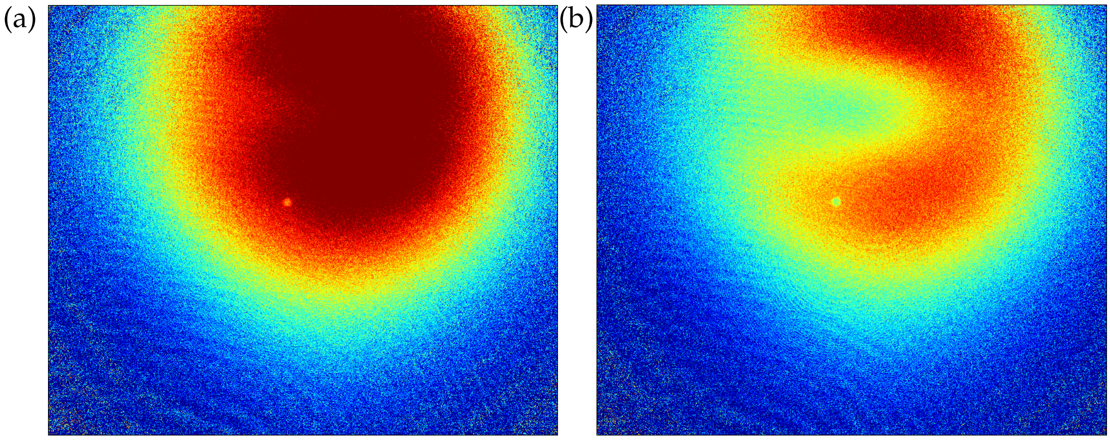

Figure 10.7.: Absorption images of potassium atoms. The two absorption images (taken at $766\,\mathrm{nm}$) show the influence of the resonant violet laser beam during its alignment to the atoms. The violet laser beam (a) slightly grazes and (b) clearly strikes the ^{39}K compressed MOT. In both cases, atoms are removed from the cloud and leave behind a gap, which is clearly visible in (b).

11. Summary and Outlook

This Thesis reports on the technical design and experimental realization of an entirely new quantum gas apparatus that will be used for quantum simulation of condensed matter systems using a fluorescence quantum gas microscope. To build this apparatus, a formerly unused room was renovated and converted into a new laboratory by ourselves. The laboratory now accomodates an operating quantum gas apparatus, with which first experimental studies have been published already.

The new quantum gas apparatus is a dual-species apparatus that is designed for the production and investigation of ultracold mixtures of K, Cs, and KCs ground-state molecules. It centers around a compact UHV system that has been designed and realized from scratch. The vacuum system consists of a main vacuum system and a science chamber setup, both of which have been put successfully into operation during this Thesis. The main vacuum system is constructed mostly out of stainless steel components and primarily serves as a production site for atomic condensates. It comprises two $2D^+$-MOT atom beam sources, two differential pumping sections, a main chamber, and a pumping section. A detailed description of the main vacuum system was given in this Thesis. The main chamber is furnished with magnetic compensation coils that have been realized partially in Helmholtz-like configuration and partially in birdcage-coil configuration. The design of the compensation coils was detailed in this Thesis and magnetic field simulations were performed to characterize the generated magnetic field at the position of the atoms.

The science chamber of the K$-$Cs apparatus will be employed to study ultracold atomic and molecular samples within optical lattices with single-site and single-atom resolution. For this purpose, it incorporates a high-resolution imaging system. In the course of this Thesis, two science chamber setups have been designed and experimentally realized. The first setup centers around a stainless steel science chamber with home-built vacuum viewports. It was replaced by a new glass cell science chamber setup. The glass cell houses the front lens of the imaging system as well as titanium rod electrodes. Both, lens and electrodes, are held within the glass cell by an elaborate mechanical construction. A precise explanation of the glass cell science chamber setup as well as its internal mounting construction was presented in this Thesis and technical aspects have been addressed in depth. A simulation of the deformation of the upper glass cell window due to the atmospheric pressure led to the conclusion that the optical performance of the high-resolution imaging system will not be impaired.

The K$-$Cs apparatus will use the rod electrodes within the glass cell to polarize KCs molecules. For this reason, the electric field dependence of the (transition) dipole moments of the energetically lowest lying rotational states of the electronic and vibrational ground state of polarized ^{39}KCs molecules was computed. Furthermore, different electric field distributions that can be generated with the rod electrodes were simulated. Their expected homogeneity was analyzed and numerically evaluated. A study of the influence of the found residual field inhomogeneities on the optical trapping of deeply bound ^{39}KCs molecules within a $532\,\mathrm{nm}$$-$square lattice showed that no relevant impairment of the on-site confinement is expected. Additionally, the effect of the residual electric field inhomogeneities of the vertical electric field configuration on spin exchange between ^{39}KCs molecules were numerically examined. The study demonstrated that the vertical electric field configuration is homogeneous enough to observe nearest-neighbor spin exchange between ^{39}KCs molecules within a $532\,\mathrm{nm}$-lattice spacing 2D square optical lattice across the entire field of view of the K$-$Cs imaging system. As part of this computation, the parameter regime of the spin-coupling constants of the Heisenberg XXZ spin lattice model that will be accessible within the K$-$Cs apparatus was determined.

A further goal of this Thesis was to start and advance the project of violet fluorescence quantum gas microscopy of ^{39}K atoms within the K$-$Cs apparatus using the $4S_{1/2} \rightarrow 5P_{3/2}$ transition. As a first step into this direction, a preliminary theoretical study on the feasibility of violet fluorescence imaging of trapped ^{39}K atoms with simultaneous EIT cooling was conducted in this Thesis. The results of the simulation suggest that lattice-confined ^{39}K atoms that are exposed to resonant $404.4\,\mathrm{nm}$ laser light and simultaneous EIT cooling emit enough violet photons within a $1\,\mathrm{s}$ exposure time to perform fluorescence quantum gas microscopy. For the simulation it was necessary to calculate the frequency-dependent valence scalar and valence tensor polarizabilities for all atomic states between the $4S_{1/2}$ and $5P_{3/2}$ level of ^{39}K for $1064\,\mathrm{nm}$ laser light. The numerical results for the atomic polarizabilities and their uncertainties were tabulated and discussed. The program that was developed to determine the atomic polarizabilities of ^{39}K can be furthermore used to compute the atomic polarizabilities at other desired laser wavelengths. For testing and studying violet fluorescence imaging of ^{39}K atoms in experiments, a home-built diode laser system for $404.4\,\mathrm{nm}$ laser light was set up. The diode laser is frequency-stabilized with modulation transfer saturation spectroscopy and achieves up to $27\,\mathrm{mW}$ of single-mode laser light. Absorption images of laser cooled ^{39}K atoms within the main chamber demonstrated the effect of the violet laser beam on the atoms.

Within this Thesis work three peer-reviewed journal publications appeared: in a first publication, we described the experimental capabilities of the new K$-$Cs apparatus and reported on the independent production of atomic ^{39}K and ^{133}Cs BECs in one experimental apparatus. In particular we outlined the experimental sequence that is required to achieve ^{39}K and ^{133}Cs condensates within the K$-$Cs apparatus. In a second publication, interspecies Feshbach resonances in mixtures of ^{39}K and ^{133}Cs atoms were studied. The observed Feshbach resonances allowed the refinement of the K$-$Cs interaction potentials and lead to an improved characterization of the scattering and bound-state properties of the isotopes ^{39}K, ^{40}K, and ^{41}K interacting with ^{133}Cs. In a third publication, sub-Doppler laser cooling of ^{39}K atoms using degenerate 3D Raman sideband cooling on the D_1 optical transition was investigated. The implementation of this new laser cooling scheme to our experimental sequence lead to a fourfold temperature reduction and a tenfold phase-space density increase of the laser cooled ^{39}K atoms compared to our previous cooling scheme.

In near future, the main experimental focus of the K$-$Cs apparatus will be twofold: one primary goal will be the investigation of K and Cs atoms in optical lattices with the high-resolution imaging system. This project is currently pursued and mechanical and optical infrastructure around the glass cell is mounted. The part of the high-resolution imaging system outside the glass cell is all set and ready for implementation. The first step towards fluorescence quantum gas microscopy within the K$-$Cs apparatus will be the reliable transport of atomic potassium and cesium samples from the main chamber to the glass cell. To minimize three-body losses during the transport, it will be crucial to control the scattering length of the K and Cs atoms over the entire transportation distance. For this reason, it is planned to mount additional magnetic offset coils along the transportation axis.

The second short-term goal of the K−Cs apparatus will be the formation of ultracold ^{39}KCs ground-state molecules. In that respect, we envision to first create a Bose-Bose double-species Mott insulator state of ^{39}K and Cs atoms within an optical lattice and then use magneto-association and subsequent STIRAP to create ^{39}KCs molecules in their absolute ground state [Rei17]. For the last step, it will be necessary to first experimentally identify the absolute rovibrational ground state of the electronic ground state of ^{39}KCs via molecular spectroscopy.

Violet fluorescence quantum gas microscopy of trapped ^{39}K atoms within the K−Cs apparatus after all is a long-term project. It will come to the fore after experience with conventional fluorescence quantum gas microscopy on the principal D line optical transitions of potassium will have been gained.

Appendices

A. List of Publications

Journal publications discussed in this Thesis

1. M. Gröbner, **P. Weinmann**, F. Meinert, K. Lauber, E. Kirilov, and H.-C. Nägerl
   "A new quantum gas apparatus for ultracold mixtures of K and Cs and KCs ground-state molecules"
   In: *Journal of Modern Optics* **63**, 1829-1839 (2016)

2. M. Gröbner, **P. Weinmann**, E. Kirilov, H.-C. Nägerl, P. S. Julienne, C. R. Le Sueur, and J. M. Hutson
   "Observation of interspecies Feshbach resonances in an ultracold ^{39}K$-^{133}$Cs mixture and refinement of interaction potentials"
   In: *Phys. Rev. A* **95**, 022715 (2017)

3. M. Gröbner, **P. Weinmann**, E. Kirilov, and H.-C. Nägerl
   "Degenerate Raman sideband cooling of ^{39}K"
   In: *Phys. Rev. A* **95**, 033412 (2017)

Further publications

4. F. Meinert, M. J. Mark, E. Kirilov, K. Lauber, **P. Weinmann**, A. J. Daley, and H.-C. Nägerl
   "Quantum Quench in an Atomic One-Dimensional Ising Chain"
   In: *Phys. Rev. Lett.* **111**, 053003 (2013)

5. F. Meinert, M. J. Mark, E. Kirilov, K. Lauber, **P. Weinmann**, M. Gröbner, A. J. Daley, and H.-C. Nägerl
   "Observation of many-body dynamics in long-range tunneling after a quantum quench"
   In: *Science* **344**, 1259-1262 (2014)

B. Anti-Reflection Coating Charts for the Main Chamber Viewports

B.1. Coating A (750−1500 nm)

Figure B.1.: Rest reflectivity. Measured reflectivity of the anti-reflection coating given in percentage per side for perpendicular incidence. Figure reprinted with permission from Larson Electronic Glass.

B.2. Coating B (400−532 nm & 1064 nm)

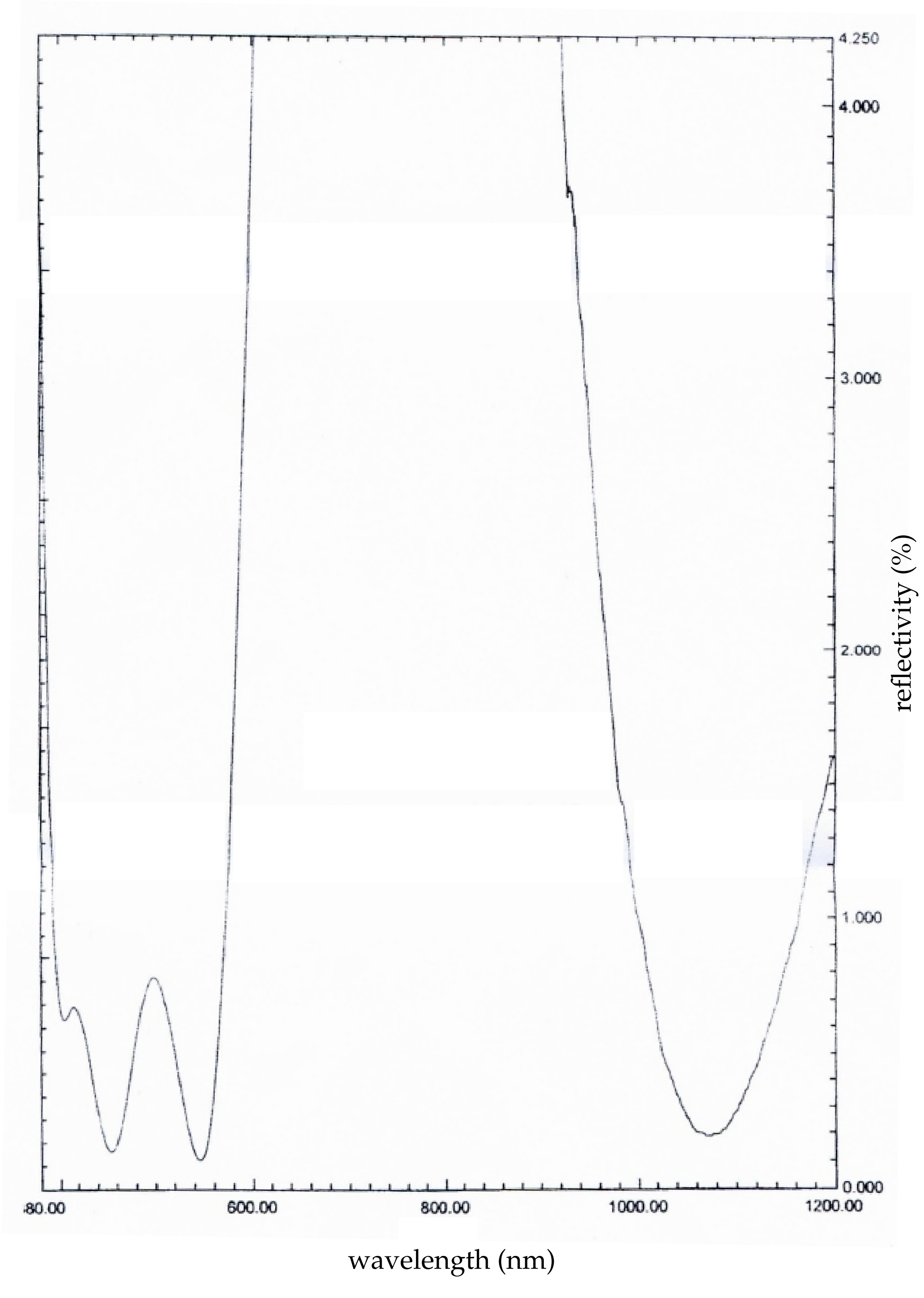

Figure B.2.: Rest reflectivity. Measured reflectivity of the anti-reflection coating given in percentage per side for perpendicular incidence. Figure reprinted with permission from Larson Electronic Glass.

C. Technical Drawings of the Main Vacuum System

C.1. CF40 Re-Entrant Viewport

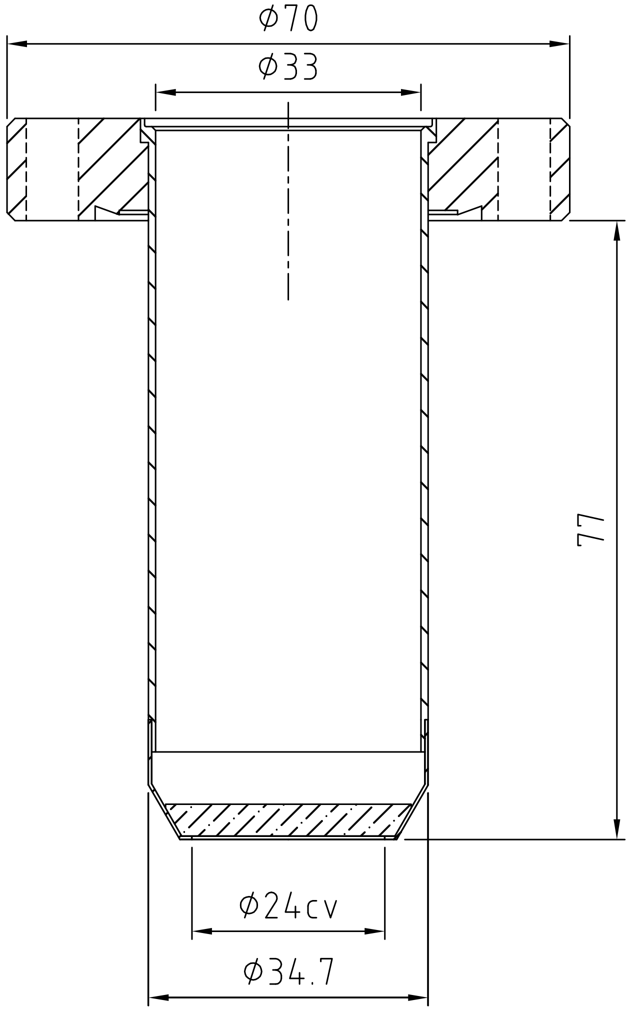

Figure C.1.: Technical drawing of the inverted CF40 viewport located at the main chamber. Dimensions are given in millimeter. Figure reprinted with permission from UKAEA, United Kingdom.

C.2. CF200 Re-Entrant Viewport

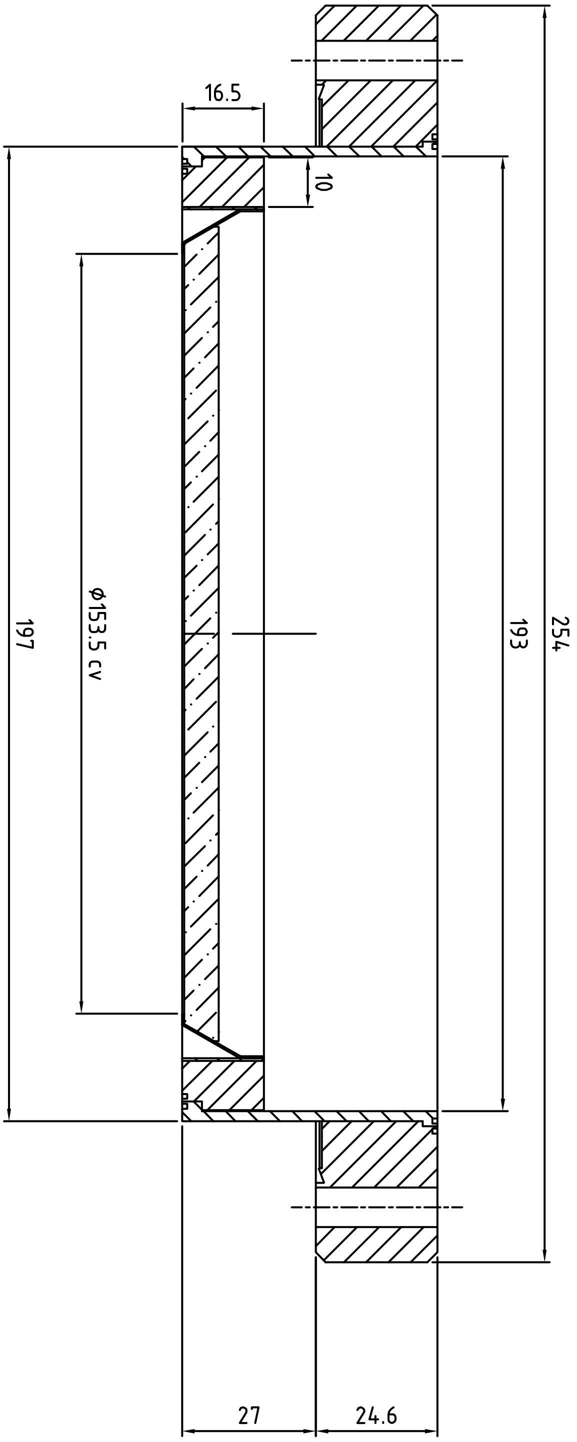

Figure C.2.: Technical drawing of the inverted CF200 viewport located at the main chamber. Dimensions are given in millimeter. Figure reprinted with permission from UKAEA, United Kingdom.

C.3. Stainless Steel Mirror

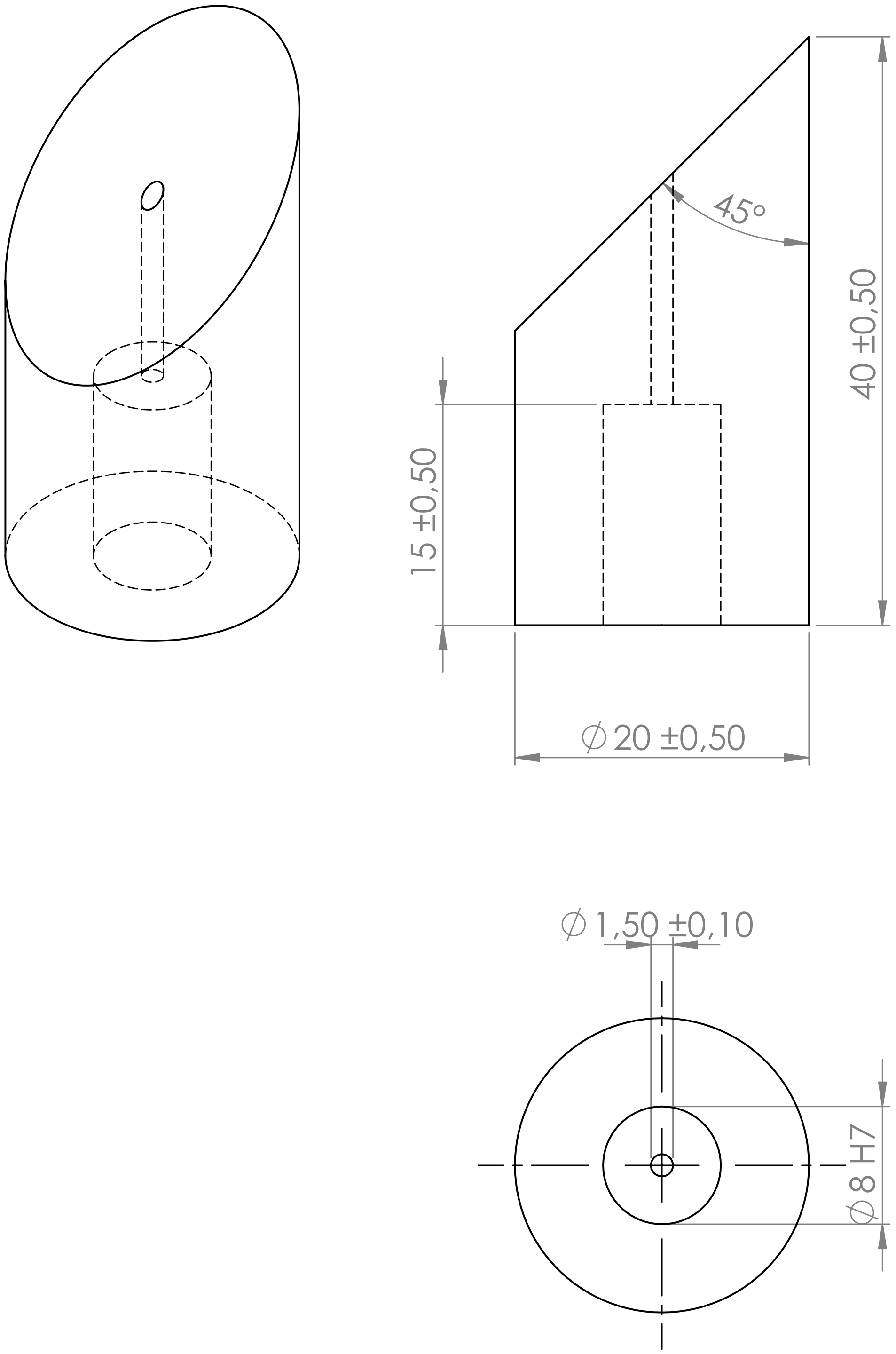

Figure C.3.: Technical drawing of the stainless steel mirrors used in the 2D-MOT chambers. Dimensions are given in millimeter. Material: 1.4432.

C.4. 2D-MOT Glass Cell

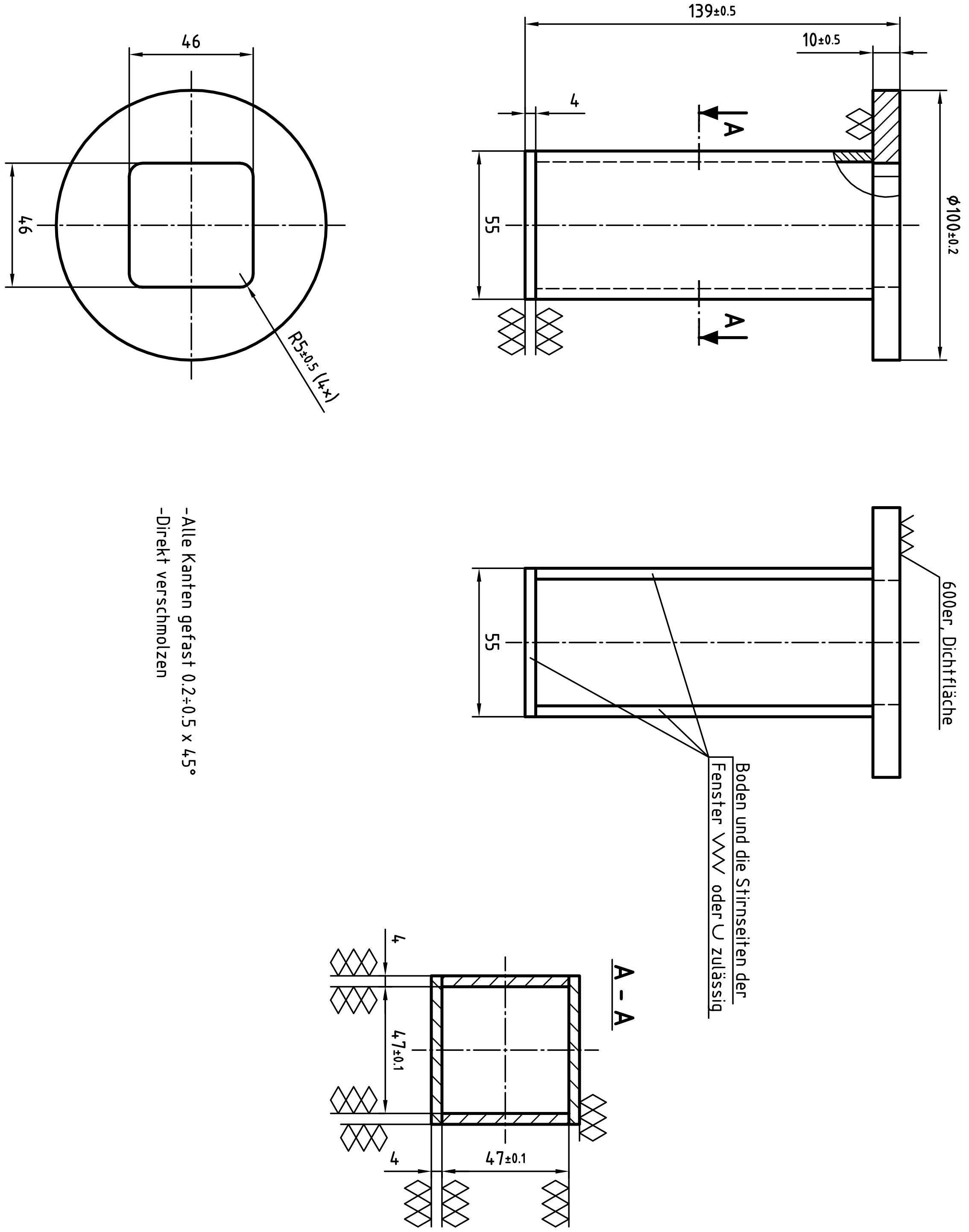

Figure C.4.: Technical drawing of the 2D-MOT glass cell. Dimensions are given in millimeter. Figure reprinted with permission from Hellma, Germany.

C.5. Stainless Steel Rod

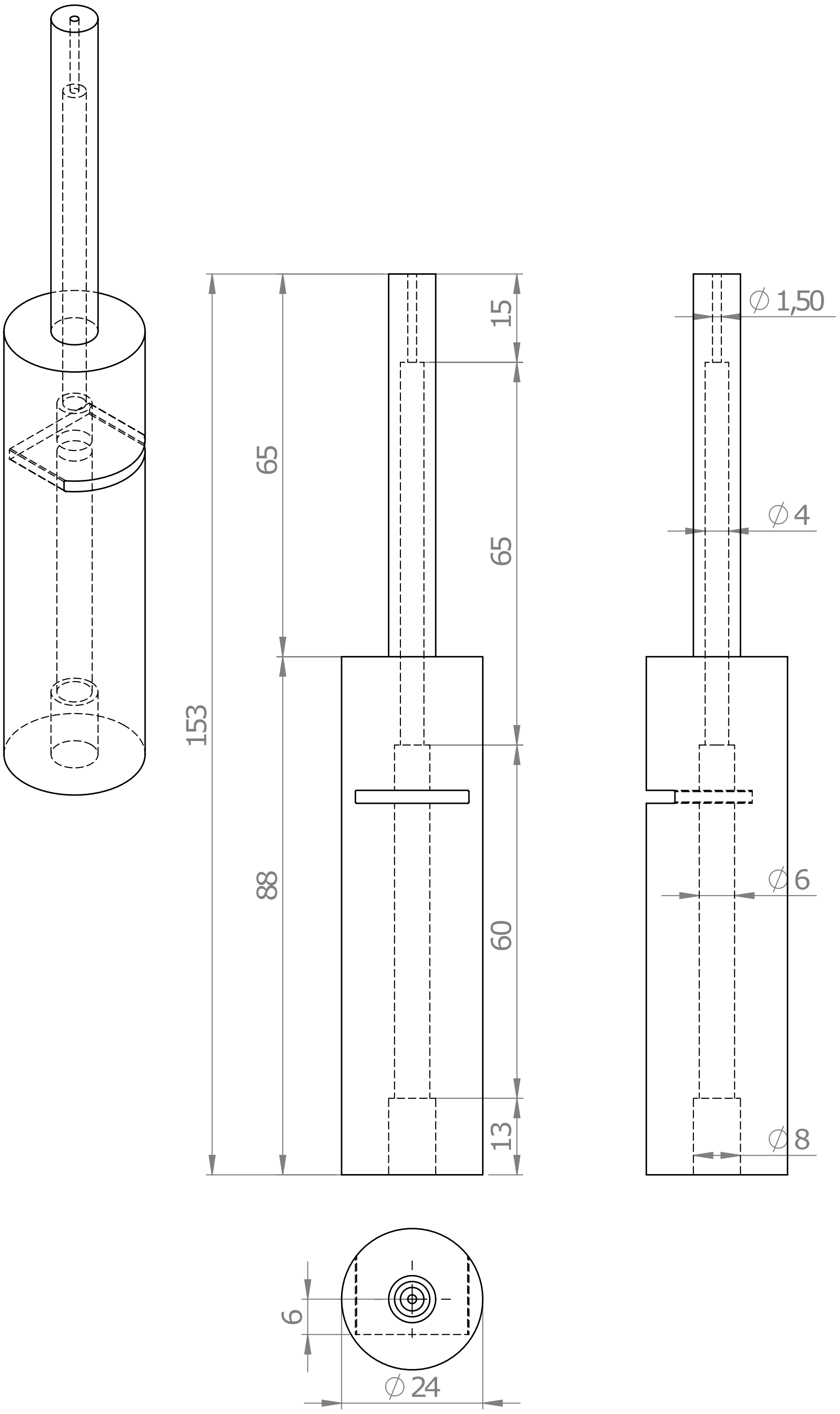

Figure C.5.: Technical drawing of the stainless steel rod of the differential pumping section. Dimensions are given in millimeter. Material: 1.4301.

C.6. CF50-to-CF16 Straight Reducer

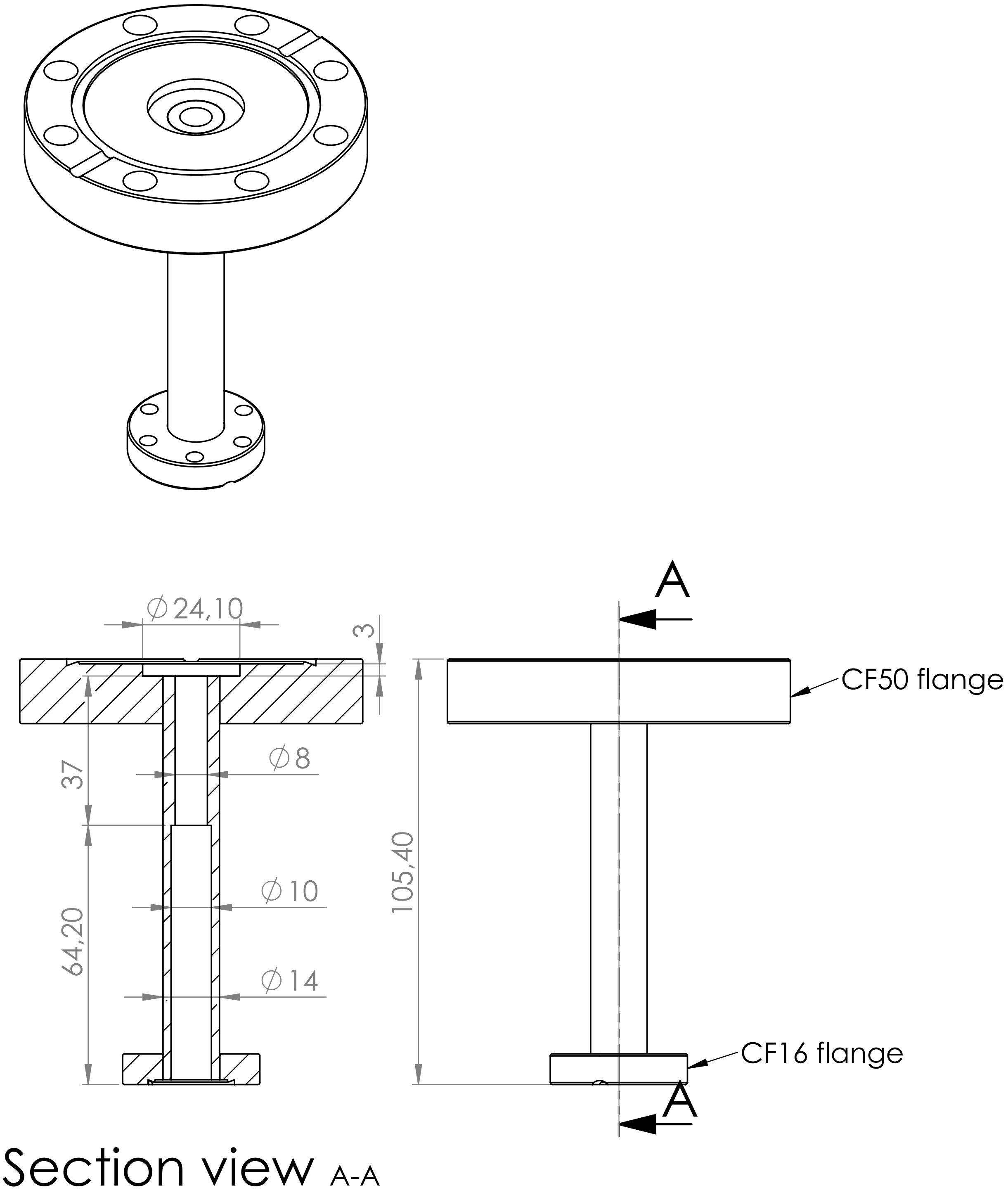

Figure C.6.: Technical drawing of the CF50-to-CF16 straight reducer of the differential pumping section. Dimensions are given in millimeter. Material: 1.4301.

D. Technical Drawing of the Stainless Steel Science Chamber Setup

D.1. Home-Built CF63 Viewport

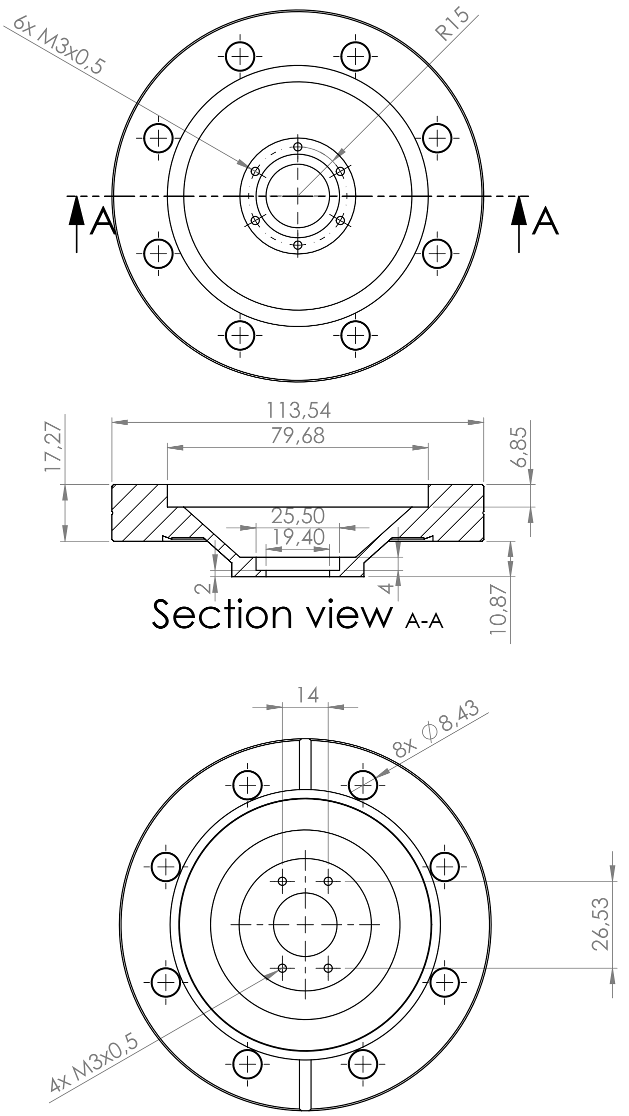

Figure D.1.: Technical drawing of the home-built CF63 viewports at the stainless steel science chamber. Dimensions are given in millimeter. Material: 1.4435/BN2.

E. Technical Drawings of the Glass Cell Science Chamber Setup

E.1. Glass Cell Science Chamber

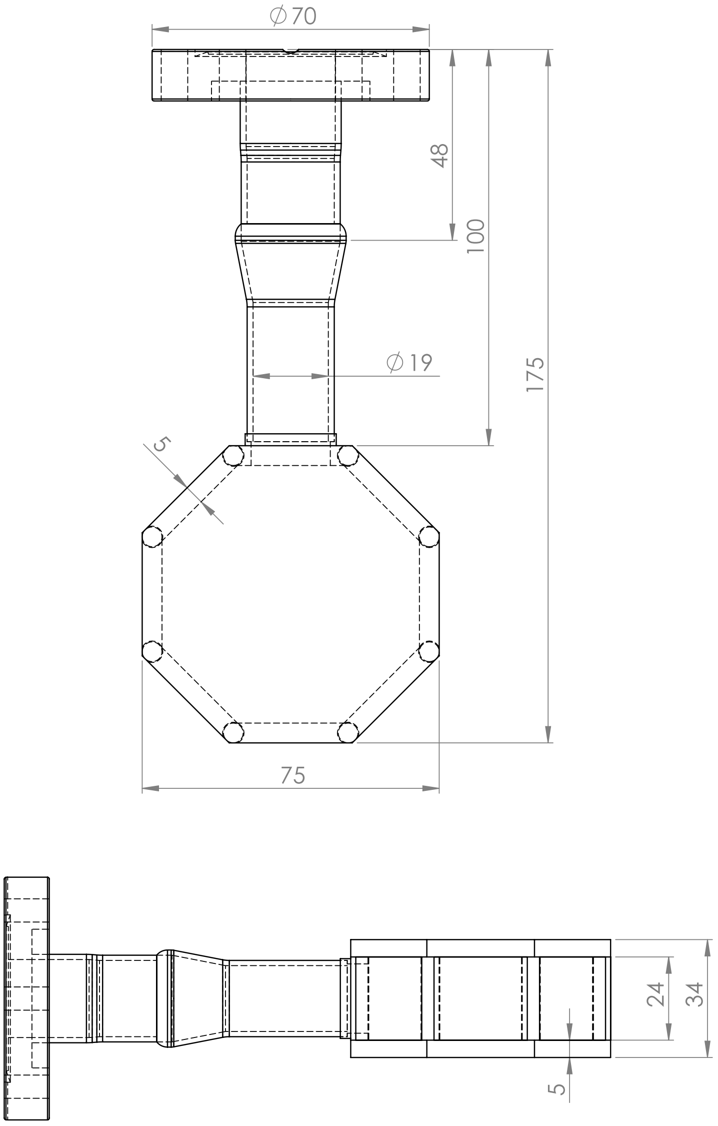

Figure E.1.: Technical drawing of the glass cell science chamber. Dimensions are given in millimeter.

E.2. Titanium Rod Electrodes

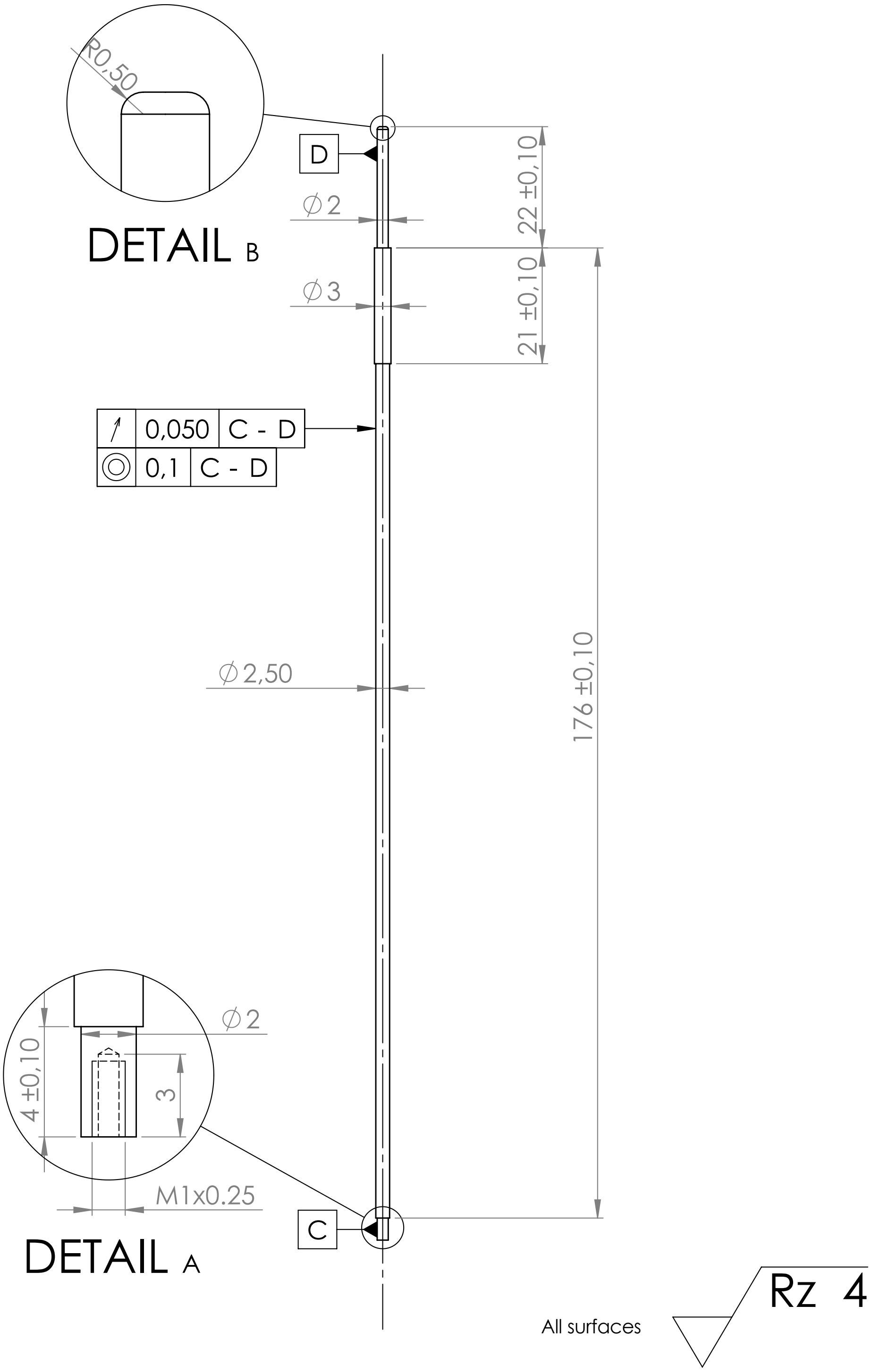

Figure E.2.: Technical drawing of the titanium rod electrodes within the glass cell science chamber. Dimensions are given in millimeter. Material: 3.7035

E.3. Lens Holder

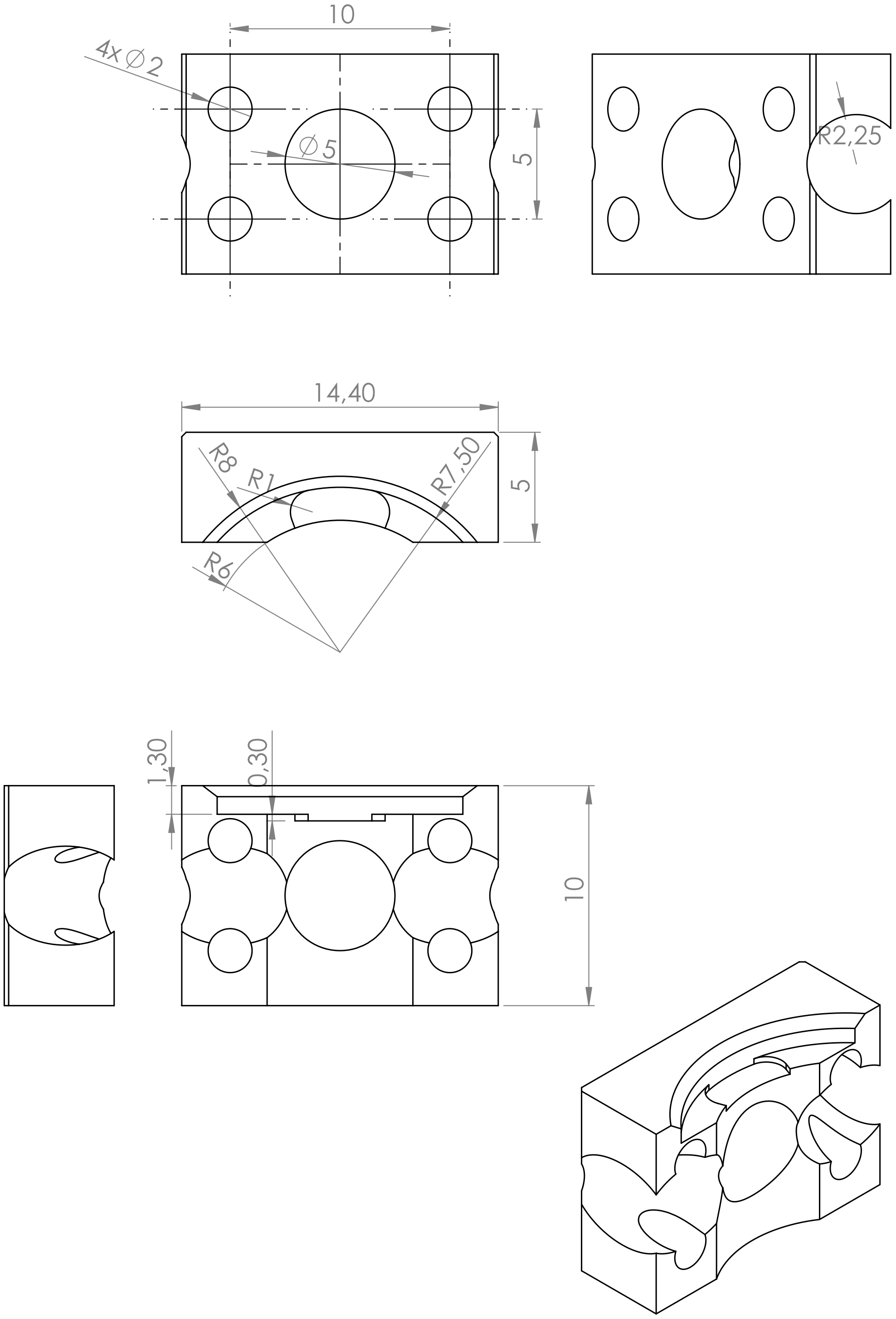

Figure E.3.: Technical drawing of the lens holders in the glass cell science chamber. Dimensions are given in millimeter. Material: Macor®.

E.4. Electrodes Holder

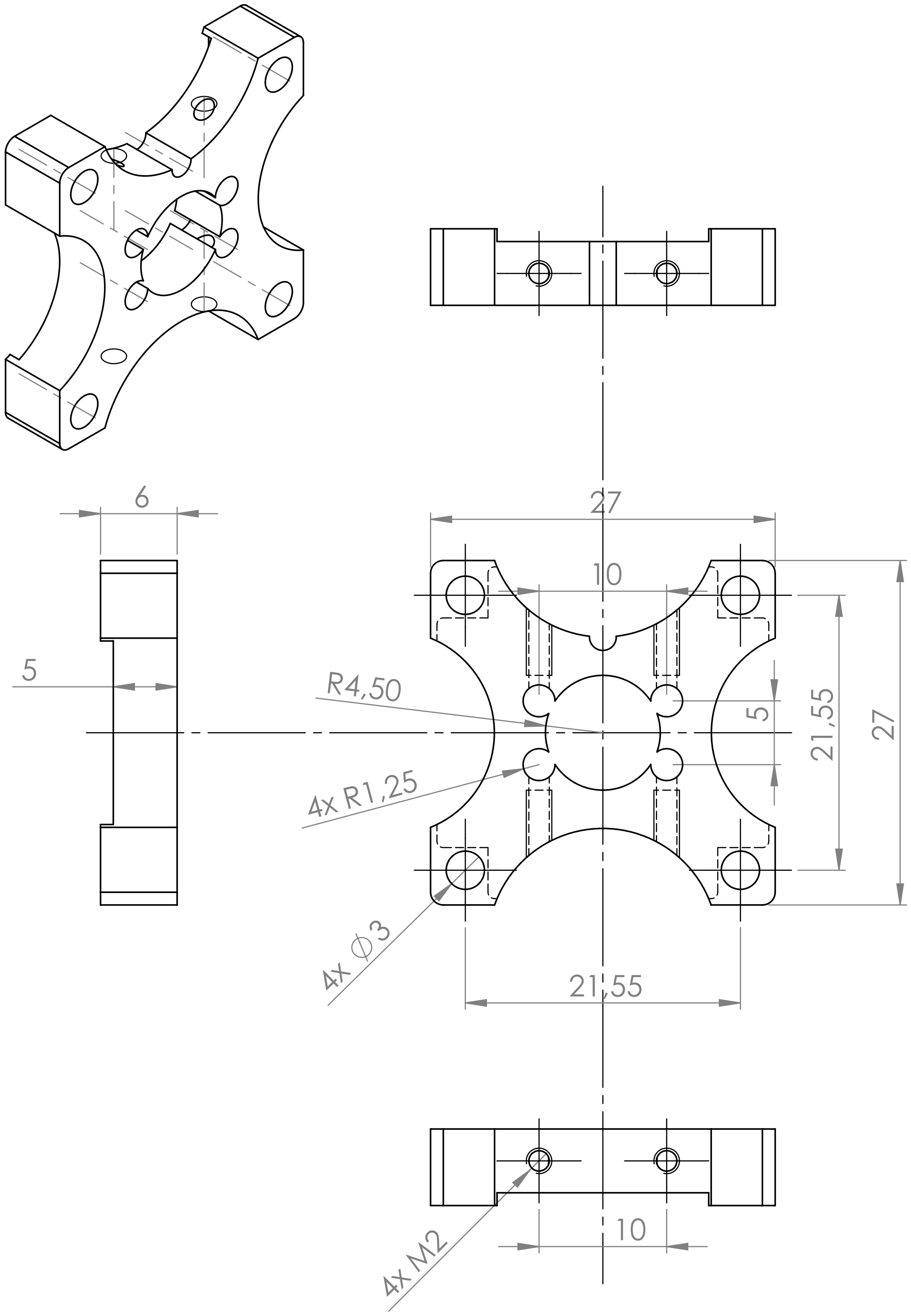

Figure E.4.: Technical drawing of the electrodes holder in the glass cell science chamber. Dimensions are given in millimeter. Material: Macor®.

E.5. Sphere Holder

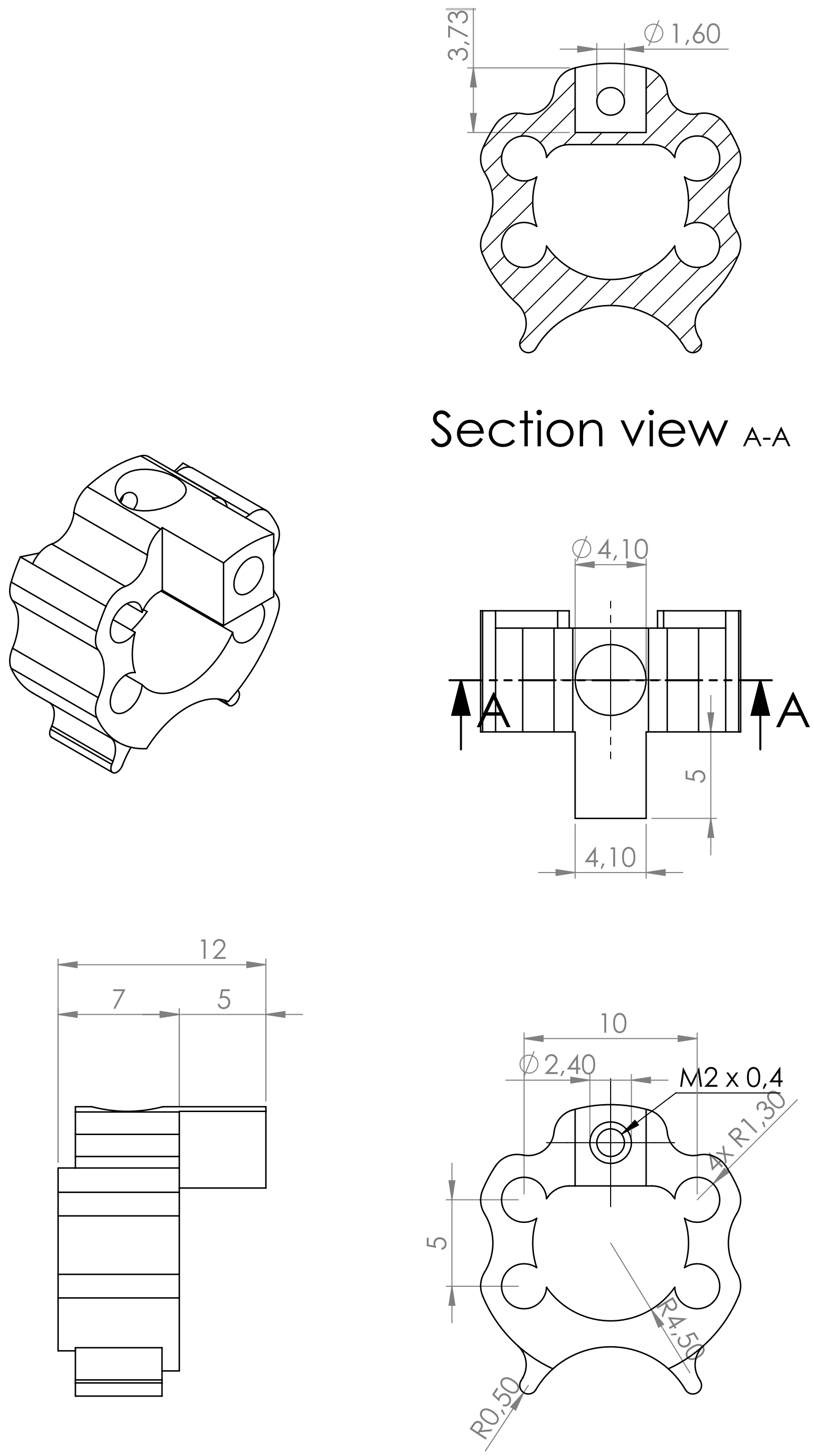

Figure E.5.: Technical drawing of the sphere holder in the glass cell science chamber. Dimensions are given in millimeter. Material: Macor®.

F. Anti-Reflection Coating Charts for the Glass Cell Science Chamber

F.1. Coating Type 1 (766 nm, 852 nm, and 1064 nm)

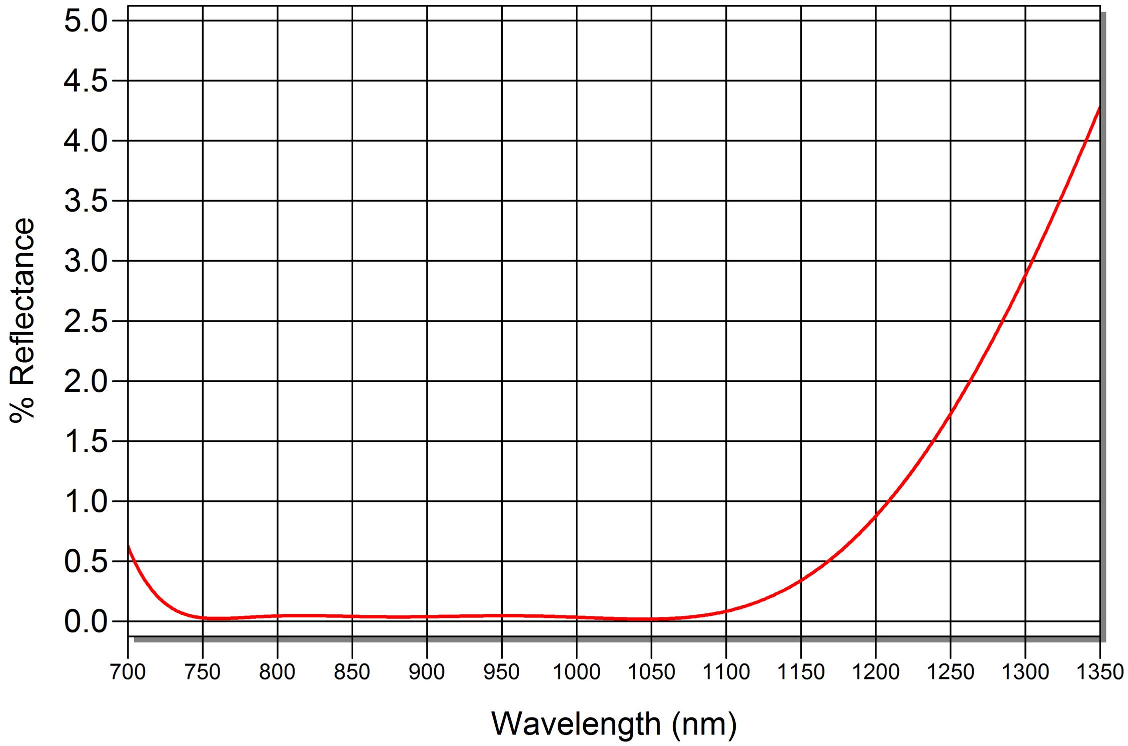

Figure F.1.: Simulation of the anti-reflection coating of type 1 for the glass cell substrates for perpendicular incidence and a single surface. The coating was calculated by Dr. Ding (email: fpding@gmail.com). Figure reprinted with permission from Japan Cell.

F.2. Coating Type 2 (1064 nm−1500 nm)

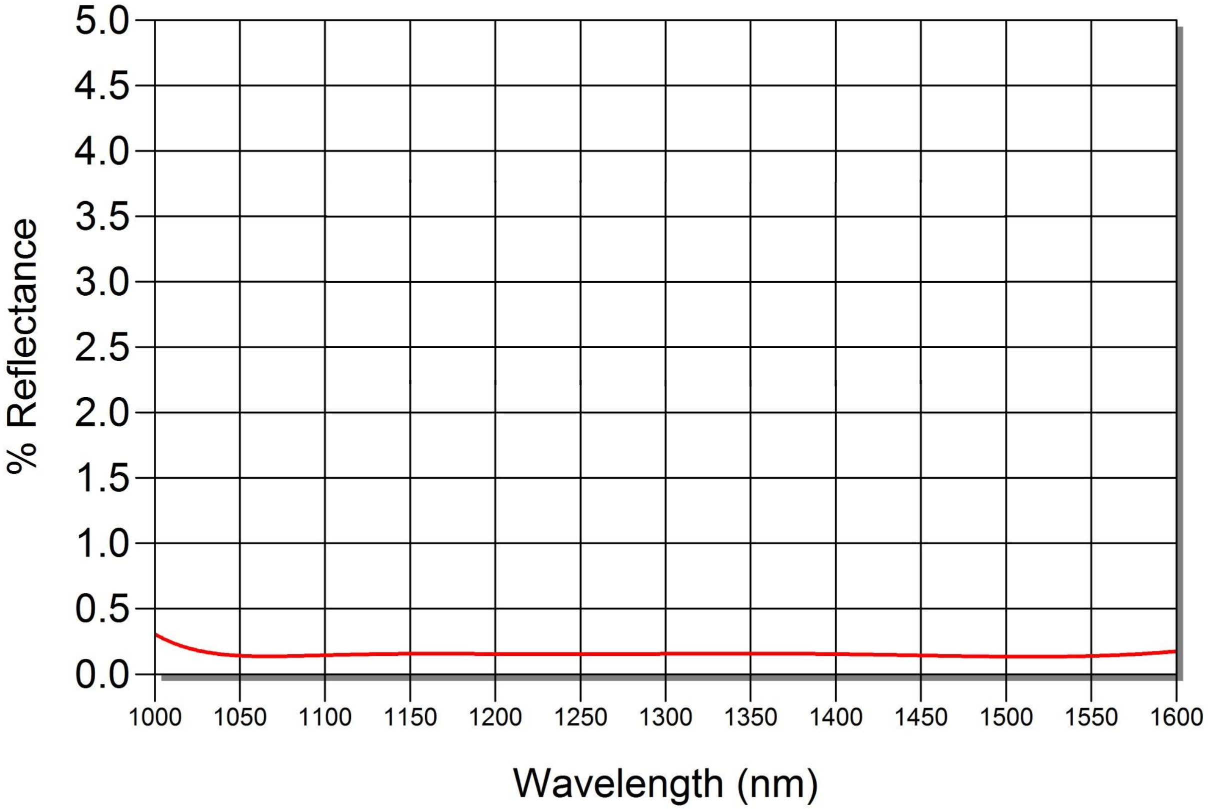

Figure F.2.: Simulation of the anti-reflection coating of type 2 for the glass cell substrates for perpendicular incidence and a single surface. The coating was calculated by Dr. Ding (email: fpding@gmail.com). Figure reprinted with permission from Japan Cell.

Bibliography

[Agi] Agilent Technologies. *Agilent Ion Pumps*. Retrieved December 11, 2018. URL: `https://www.agilent.com/cs/library/catalogs/public/06_Ion_Pumps.pdf` (cit. on p. 100).

[Al 04] M. Al Hajj, N. Guihéry, J.-P. Malrieu, and P. Wind. "Theoretical studies of the phase transition in the anisotropic two-dimensional square spin lattice", *Phys. Rev. B* **70**, 094415 (2004) (cit. on p. 19).

[And95] M. H. Anderson, J. R. Ensher, M. R. Matthews, C. E. Wieman, and E. A. Cornell. "Observation of Bose-Einstein Condensation in a Dilute Atomic Vapor", *Science* **269**, 198–201 (1995) (cit. on p. 22).

[Ari77] E. Arimondo, M. Inguscio, and P. Violino. "Experimental determinations of the hyperfine structure in the alkali atoms", *Rev. Mod. Phys.* **49**, 31–75 (1977) (cit. on pp. 55, 153, 186).

[Aro07] B. Arora, M. S. Safronova, and C. W. Clark. "Magic wavelengths for the np-ns transitions in alkali-metal atoms", *Phys. Rev. A* **76**, 052509 (2007) (cit. on pp. 52, 54).

[Ash76] N. W. Ashcroft and N. D. Mermin. *Solid State Physics*. Holt, Rinehart and Winston. Printed in Japan, 1981 (1976) (cit. on pp. 9–15).

[Atk17] P. Atkins and J. De Paula. *Elements of Physical Chemistry*. 7th ed. Oxford University Press, Oxford (2017) (cit. on pp. 3, 4, 153, 169).

[Atl] Atlas Technologies, Washington (USA). *Aluminum's Extreme Vacuum Performance*. Retrieved November 24, 2017. URL: `https://www.atlasuhv.com/aluminums-extreme-vacuum-performance/` (cit. on p. 84).

[Aue94] A. Auerbach. *Interacting Electrons and Quantum Magnetism*. 1st ed. Springer-Verlag, New York (1994) (cit. on pp. 17, 18).

[Axn04] O. Axner, J. Gustafsson, N. Omenetto, and J. D. Winefordner. "Line strengths, A-factors and absorption cross-sections for fine structure lines in multiplets and hyperfine structure components in lines in atomic spectrometry—a user's guide", *Spectrochimica Acta Part B: Atomic Spectroscopy* **59**, 1–39 (2004) (cit. on p. 72).

[Aym05] M. Aymar and O. Dulieu. "Calculation of accurate permanent dipole moments of the lowest ${}^{1,3}\Sigma^{+}$ states of heteronuclear alkali dimers using extended basis sets", *The Journal of Chemical Physics* **122**, 204302 (2005) (cit. on p. 157).

[Bak11] W. S. Bakr. *Microscopic Studies of Quantum Phase Transitions in Optical Lattices*. PhD thesis, Harvard University (2011) (cit. on pp. 43, 44).

[Bak09] W. S. Bakr, J. I. Gillen, A. Peng, S. Fölling, and M. Greiner. "A quantum gas microscope for detecting single atoms in a Hubbard-regime optical lattice", *Nature* **462**, 74–77 (2009) (cit. on pp. 5, 33, 35, 37–41, 43, 44).

[Bec10] C. Becker, P. Soltan-Panahi, J. Kronjäger, S. Dörscher, K. Bongs, and K. Sengstock. "Ultracold quantum gases in triangular optical lattices", *New Journal of Physics* **12**, 065025 (2010) (cit. on p. 27).

[Bed86] J. G. Bednorz and K. A. Müller. "Possible High T_c Superconductivity in the Ba−La−Cu−O System", *Zeitschrift für Physik B Condensed Matter* **64**, 189–193 (1986) (cit. on p. 2).

[Beh11] A. Behrle, M. Koschorreck, and M. Köhl. "Isotope shift and hyperfine splitting of the $4s \to 5p$ transition in potassium", *Phys. Rev. A* **83**, 052507 (2011) (cit. on p. 186).

[Ber98] K. Bergmann, H. Theuer, and B. W. Shore. "Coherent population transfer among quantum states of atoms and molecules", *Rev. Mod. Phys.* **70**, 1003–1025 (1998) (cit. on p. 119).

[Bid05] C. Bidinosti, I. Kravchuk, and M. Hayden. "Active shielding of cylindrical saddle-shaped coils: Application to wire-wound RF coils for very low field NMR and MRI", *Journal of Magnetic Resonance* **177**, 31–43 (2005) (cit. on p. 105).

[Bis98] R. F. Bishop and D. J. J. Farnell. "A microscopic theory of magnetic order in strongly correlated quantum spin lattices". In: *Many-Body Theory of Correlated Fermion Systems*. Ed. by J. M. Arias, M. I. Gallardo, and M. Lozano. Retrieved from `https://personalpages.manchester.ac.uk/staff/raymond.bishop/RFB_papers/[137]MBTCorrFermiSys(1998)1` on November 10 2018. World Scientific Publishing, Singapore (1998), 1–24 (cit. on p. 19).

[Bis17] R. F. Bishop, P. H. Y. Li, R. Zinke, R. Darradi, J. Richter, D. J. J. Farnell, and J. Schulenburg. "The spin-half XXZ antiferromagnet on the square lattice revisited: A high-order coupled cluster treatment", *Journal of Magnetism and Magnetic Materials* **428**, 178–188 (2017) (cit. on pp. 15, 19).

[Bla01] E. D. Black. "An introduction to Pound–Drever–Hall laser frequency stabilization", *American Journal of Physics* **69**, 79–87 (2001) (cit. on p. 185).

[Blo13] I. Bloch. “Ultracold atoms in optical lattices”. In: *Les Houches 2010 Session XCIV, Many-Body Physics with Ultracold Gases*. Ed. by C. Salomon, G. Shlyapnikov, and L. F. Cugliandolo. 1st ed. Oxford University Press (United Kingdom) (2013), 71–108 (cit. on pp. 5, 28, 34, 35).

[Blo08] I. Bloch, J. Dalibard, and W. Zwerger. “Many-body physics with ultracold gases”, *Rev. Mod. Phys.* **80**, 885–964 (2008) (cit. on pp. 3, 21, 27, 30, 31).

[Boh09] J. L. Bohn. “Electric Dipoles at Ultralow Temperatures”. In: *Cold Molecules: Theory, Experiment, Applications*. Ed. by R. V. Krems, W. C. Stwalley, and B. Friedrich. 1st ed. CRC Press, Taylor & Francis Group, Boca Raton (2009) (cit. on pp. 153, 155, 157).

[Bol88] L. Bolinger, M. G. Prammer, and J. S. Leigh, Jr. “A Multiple-Frequency Coil with a Highly Uniform B_1 Field”, *Journal of Magnetic Resonance (1969)* **81**, 162–166 (1988) (cit. on p. 105).

[Bon97] K. D. Bonin and V. V. Kresin. *Electric-Dipole Polarizabilities of Atoms, Molecules, And Clusters*. World Scientific Publishing Co. Pte. Ltd., Singapore (1997) (cit. on pp. 49, 50, 52–54, 61, 82, 167).

[Boy94] R. Boyer, G. Welsch, and E. W. Collings, eds. *Materials Properties Handbook: Titanium Alloys*. ASM International, Materials Park, OH (1994) (cit. on pp. 84, 143).

[Bra15] S. Brakhane, W. Alt, D. Meschede, C. Robens, G. Moon, and A. Alberti. “Note: Ultra-low birefringence dodecagonal vacuum glass cell”, *Review of Scientific Instruments* **86**, 126108 (2015) (cit. on p. 142).

[Bri] British Stainless Steel Association. *Is stainless steel non-magnetic?* Retrieved November 26, 2017. URL: `https://www.bssa.org.uk/faq.php?id=24` (cit. on p. 84).

[Bro03] J. Brown and A. Carrington. *Rotational Spectroscopy of Diatomic Molecules*. Cambridge University Press, Cambridge (2003) (cit. on pp. 153–155).

[Bro86] L. S. Brown and G. Gabrielse. “Geonium theory: Physics of a single electron or ion in a Penning trap”, *Rev. Mod. Phys.* **58**, 233–311 (1986) (cit. on pp. 70, 71).

[Cah69] K. E. Cahill and R. J. Glauber. “Ordered Expansions in Boson Amplitude Operators”, *Phys. Rev.* **177**, 1857–1881 (1969) (cit. on p. 73).

[Car09] L. D. Carr, D. DeMille, R. V. Krems, and J. Ye. “Cold and ultracold molecules: science, technology and applications”, *New Journal of Physics* **11**, 055049 (2009) (cit. on pp. 4, 6, 153).

[Cat06] J. Catani. *A new apparatus for ultracold K-Rb Bose-Bose atomic mixtures*. PhD thesis, University of Florence (2006) (cit. on pp. 96, 98).

[Che17] L. W. Cheuk. *Quantum Gas Microscopy of Strongly Correlated Fermions*. PhD thesis, Massachusetts Institute of Technology (2017) (cit. on pp. 43, 44).

[Che15] L. W. Cheuk, M. A. Nichols, M. Okan, T. Gersdorf, V. V. Ramasesh, W. S. Bakr, T. Lompe, and M. W. Zwierlein. "Quantum-Gas Microscope for Fermionic Atoms", *Phys. Rev. Lett.* **114**, 193001 (2015) (cit. on pp. 39, 41, 43, 44, 49, 81).

[Chi10] C. Chin, R. Grimm, P. Julienne, and E. Tiesinga. "Feshbach resonances in ultracold gases", *Rev. Mod. Phys.* **82**, 1225–1286 (2010) (cit. on pp. 3, 22).

[COM] COMSOL 5.2a. *AC/DC Module User's Guide* (cit. on p. 158).

[Cor02] E. A. Cornell and C. E. Wieman. "Nobel Lecture: Bose-Einstein condensation in a dilute gas, the first 70 years and some recent experiments", *Rev. Mod. Phys.* **74**, 875–893 (2002) (cit. on p. 22).

[Cora] Corning Incorporated, Corning, NY (U.S.A.) *Corning® HPFS® 7979, 7980, 8655 Fused Silica (Datasheet).* Retrieved on April 21, 2017. URL: `https://www.corning.com/media/worldwide/csm/documents/5bf092438c5546dfa9b08e423348317b.pdf` (cit. on p. 149).

[Corb] Corning Incorporated, Corning, NY (U.S.A.) *MACOR® Machinable Glass Ceramic For Industrial Applications (Datasheet).* Retrieved on April 21, 2017. URL: `https://www.corning.com/worldwide/en/products/advanced-optics/product-materials/specialty-glass-and-glass-ceramics/glass-ceramics/macor.html` (cit. on pp. 145, 149, 166).

[Cov18] J. P. Covey, S. A. Moses, J. Ye, and D. S. Jin. "Chapter 11: Controlling a Quantum Gas of Polar Molecules in an Optical Lattice". In: *Cold Chemistry: Molecular Scattering and Reactivity Near Absolute Zero*. Ed. by O. Dulieu and A. Osterwalder. The Royal Society of Chemistry (2018), 537–578 (cit. on p. 157).

[Dan10] J. G. Danzl, M. J. Mark, E. Haller, M. Gustavsson, R. Hart, J. Aldegunde, J. M. Hutson, and H.-C. Nägerl. "An ultracold high-density sample of rovibronic ground-state molecules in an optical lattice", *Nature Physics* **6**, 265 (2010) (cit. on p. 5).

[DeM99] B. DeMarco and D. S. Jin. "Onset of Fermi Degeneracy in a Trapped Atomic Gas", *Science* **285**, 1703–1706 (1999) (cit. on p. 22).

[Dem08] W. Demtröder. *Laser Spectroscopy Volume 1: Basic Principles*. 4th ed. Springer-Verlag Berlin Heidelberg (2008) (cit. on pp. 72, 73).

[DeP99] M. T. DePue, C. McCormick, S. L. Winoto, S. Oliver, and D. S. Weiss. "Unity Occupation of Sites in a 3D Optical Lattice", *Phys. Rev. Lett.* **82**, 2262–2265 (1999) (cit. on p. 40).

[Der99] A. Derevianko, W. R. Johnson, M. S. Safronova, and J. F. Babb. “High-Precision Calculations of Dispersion Coefficients, Static Dipole Polarizabilities, and Atom-Wall Interaction Constants for Alkali-Metal Atoms”, *Phys. Rev. Lett.* **82**, 3589–3592 (1999) (cit. on pp. 51, 57).

[Die98] K. Dieckmann, R. J. C. Spreeuw, M. Weidemüller, and J. T. M. Walraven. “Two-dimensional magneto-optical trap as a source of slow atoms”, *Phys. Rev. A* **58**, 3891–3895 (1998) (cit. on p. 95).

[Dua11] P. M. Duarte, R. A. Hart, J. M. Hitchcock, T. A. Corcovilos, T.-L. Yang, A. Reed, and R. G. Hulet. “All-optical production of a lithium quantum gas using narrow-line laser cooling”, *Phys. Rev. A* **84**, 061406 (2011) (cit. on p. 180).

[Dut15a] N. N. Dutta, S. Roy, and P. C. Deshmukh. “Dynamic polarizabilities and hyperfine-structure constants for Sc^{2+}”, *Phys. Rev. A* **92**, 052510 (2015) (cit. on pp. 51, 54).

[Dut15b] O. Dutta, M. Gajda, P. Hauke, M. Lewenstein, D.-S. Lühmann, B. A. Malomed, T. Sowiński, and J. Zakrzewski. “Non-standard Hubbard models in optical lattices: a review”, *Reports on Progress in Physics* **78**, 066001 (2015) (cit. on p. 29).

[Ebl07] J. F. Eble and F. Schmidt-Kaler. “Optimization of frequency modulation transfer spectroscopy on the calcium $4^1\mathrm{S}_0$ to $4^1\mathrm{P}_1$ transition”, *Applied Physics B* **88**, 563–568 (2007) (cit. on p. 185).

[Edg17] G. Edge. *Imaging fermionic atoms in a quantum gas microscope*. PhD thesis, University of Toronto (2017) (cit. on pp. 43, 44, 82, 180).

[Edg15] G. J. A. Edge, R. Anderson, D. Jervis, D. C. McKay, R. Day, S. Trotzky, and J. H. Thywissen. “Imaging and addressing of individual fermionic atoms in an optical lattice”, *Phys. Rev. A* **92**, 063406 (2015) (cit. on pp. 37, 39, 41, 43, 44, 49, 65, 78, 81).

[Esc03] J. Eschner, G. Morigi, F. Schmidt-Kaler, and R. Blatt. “Laser cooling of trapped ions”, *J. Opt. Soc. Am. B* **20**, 1003–1015 (2003) (cit. on p. 70).

[ESP] ESPI Metals, Oregon, U.S.A. *Sealing With Indium (Technical Data)*. Retrieved on March 28, 2017. URL: `http://www.espimetals.com/index.php/technical-data/95-Indium-%20Sealing%20With` (cit. on p. 96).

[Fed96] P. O. Fedichev, M. W. Reynolds, and G. V. Shlyapnikov. “Three-Body Recombination of Ultracold Atoms to a Weakly Bound s Level”, *Phys. Rev. Lett.* **77**, 2921–2924 (1996) (cit. on p. 22).

[Fer08] R. Ferber, I. Klincare, O. Nikolayeva, M. Tamanis, H. Knöckel, E. Tiemann, and A. Pashov. “The ground electronic state of KCs studied by Fourier transform spectroscopy”, *The Journal of Chemical Physics* **128**, 244316 (2008) (cit. on p. 157).

[Fer13] R. Ferber, O. Nikolayeva, M. Tamanis, H. Knöckel, and E. Tiemann. "Long-range coupling of $X\,^1\Sigma^+$ and $a\,^3\Sigma^+$ states of the atom pair K + Cs", *Phys. Rev. A* **88**, 012516 (2013) (cit. on pp. 114, 117, 118).

[Fey82] R. P. Feynman. "Simulating physics with computers", *International Journal of Theoretical Physics* **21**, 467–488 (1982) (cit. on p. 2).

[Fle05] M. Fleischhauer, A. Imamoglu, and J. P. Marangos. "Electromagnetically induced transparency: Optics in coherent media", *Rev. Mod. Phys.* **77**, 633–673 (2005) (cit. on p. 74).

[Fuh12] A. Fuhrmanek, R. Bourgain, Y. R. P. Sortais, and A. Browaeys. "Light-assisted collisions between a few cold atoms in a microscopic dipole trap", *Phys. Rev. A* **85**, 062708 (2012) (cit. on pp. 39, 40).

[Ful12] P. Fulde. *Correlated Electrons in Quantum Matter*. World Scientific Publishing, Singapore (2012) (cit. on p. 9).

[Gad16] B. Gadway and B. Yan. "Strongly interacting ultracold polar molecules", *Journal of Physics B: Atomic, Molecular and Optical Physics* **49**, 152002 (2016) (cit. on p. 4).

[Gal78] T. F. Gallagher and W. E. Cooke. "Fine-structure intervals and polarizabilities of highly excited d states of K", *Phys. Rev. A* **18**, 2510–2516 (1978) (cit. on p. 55).

[Gem09] N. Gemelke, X. Zhang, C.-L. Hung, and C. Chin. "*In situ* observation of incompressible Mott-insulating domains in ultracold atomic gases", *Nature* **460**, 995–998 (2009) (cit. on p. 35).

[Gem16] M. W. Gempel, T. Hartmann, T. A. Schulze, K. K. Voges, A. Zenesini, and S. Ospelkaus. "Versatile electric fields for the manipulation of ultracold NaK molecules", *New Journal of Physics* **18**, 045017 (2016) (cit. on p. 168).

[Geo13] A. Georges and T. Giamarchi. "Strongly correlated bosons and fermions in optical lattices". In: *Les Houches 2010 Session XCIV, Many-Body Physics with Ultracold Gases*. Ed. by C. Salomon, G. V. Shlyapnikov, and L. F. Cugliandolo. 1st ed. Oxford University Press (United Kingdom) (2013), 1–70 (cit. on pp. 29–31).

[Geo14] I. M. Georgescu, S. Ashhab, and F. Nori. "Quantum simulation", *Rev. Mod. Phys.* **86**, 153–185 (2014) (cit. on p. 2).

[Ger08] F. Gerbier, S. Trotzky, S. Fölling, U. Schnorrberger, J. D. Thompson, A. Widera, I. Bloch, L. Pollet, M. Troyer, B. Capogrosso-Sansone, N. V. Prokof'ev, and B. V. Svistunov. "Expansion of a Quantum Gas Released from an Optical Lattice", *Phys. Rev. Lett.* **101**, 155303 (2008) (cit. on p. 34).

[Gol04] J. Goldwin, S. Inouye, M. L. Olsen, B. Newman, B. D. DePaola, and D. S. Jin. "Measurement of the interaction strength in a Bose-Fermi mixture with ^{87}Rb and ^{40}K", *Phys. Rev. A* **70**, 021601 (2004) (cit. on p. 128).

[Gre02] M. Greiner, O. Mandel, T. Esslinger, T. W. Hänsch, and I. Bloch. "Quantum phase transition from a superfluid to a Mott insulator in a gas of ultracold atoms", *Nature* **415**, 39–44 (2002) (cit. on pp. 3, 32).

[Gri00] R. Grimm, M. Weidemüller, and Y. B. Ovchinnikov. "Optical Dipole Traps for Neutral Atoms". In: ed. by B. Bederson and H. Walther. Vol. 42. Advances In Atomic, Molecular, and Optical Physics. Academic Press (2000), 95–170 (cit. on pp. 3, 23, 24, 38).

[Grö17a] M. Gröbner. *A quantum gas apparatus for ultracold mixtures of K and Cs*. PhD thesis, University of Innsbruck (2017) (cit. on pp. 45, 93, 109, 110, 113).

[Grö16] M. Gröbner, P. Weinmann, F. Meinert, K. Lauber, E. Kirilov, and H.-C. Nägerl. "A new quantum gas apparatus for ultracold mixtures of K and Cs and KCs ground-state molecules", *Journal of Modern Optics* **63**, 1829–1839 (2016) (cit. on pp. 7, 86, 93, 109, 112, 115, 122).

[Grö17b] M. Gröbner, P. Weinmann, E. Kirilov, and H.-C. Nägerl. "Degenerate Raman sideband cooling of ^{39}K", *Phys. Rev. A* **95**, 033412 (2017) (cit. on pp. 7, 86, 109, 119–125).

[Grö17c] M. Gröbner, P. Weinmann, E. Kirilov, H.-C. Nägerl, P. S. Julienne, C. R. Le Sueur, and J. M. Hutson. "Observation of interspecies Feshbach resonances in an ultracold $^{39}\mathrm{K} - ^{133}\mathrm{Cs}$ mixture and refinement of interaction potentials", *Phys. Rev. A* **95**, 022715 (2017) (cit. on pp. 7, 86, 109, 115–118).

[Gro17] C. Gross and I. Bloch. "Quantum simulations with ultracold atoms in optical lattices", *Science* **357**, 995–1001 (2017) (cit. on pp. 2, 3).

[Gro14] R. Gross and A. Marx. *Festkörperphysik*. 2nd ed. De Gruyter Oldenburg, Berlin/ Boston (2014) (cit. on pp. 9–12, 14).

[Guo16] M. Guo, B. Zhu, B. Lu, X. Ye, F. Wang, R. Vexiau, N. Bouloufa-Maafa, G. Quéméner, O. Dulieu, and D. Wang. "Creation of an Ultracold Gas of Ground-State Dipolar ^{23}Na^{87}Rb Molecules", *Phys. Rev. Lett.* **116**, 205303 (2016) (cit. on p. 119).

[Gus01] T. L. Gustavson, A. P. Chikkatur, A. E. Leanhardt, A. Görlitz, S. Gupta, D. E. Pritchard, and W. Ketterle. "Transport of Bose-Einstein Condensates with Optical Tweezers", *Phys. Rev. Lett.* **88**, 020401 (2001) (cit. on p. 45).

[Gus08] M. Gustavsson. *A quantum gas with tunable interactions in an optical lattice*. Dissertation, University of Innsbruck (2008) (cit. on p. 89).

[Hak06] H. Haken and H. C. Wolf. *Molekülphysik und Quantenchemie*. 5th ed. Springer-Verlag Berlin Heidelberg (2006) (cit. on pp. 154, 155, 157, 169).

[Hal15] E. Haller, J. Hudson, A. Kelly, D. A. Cotta, B. Peaudecerf, G. D. Bruce, and S. Kuhr. "Single-atom imaging of fermions in a quantum-gas microscope", *Nature Physics* **11**, 738–742 (2015) (cit. on pp. 39, 43, 44, 49, 65, 78).

[Ham98] S. E. Hamann, D. L. Haycock, G. Klose, P. H. Pax, I. H. Deutsch, and P. S. Jessen. "Resolved-Sideband Raman Cooling to the Ground State of an Optical Lattice", *Phys. Rev. Lett.* **80**, 4149–4152 (1998) (cit. on p. 121).

[Han00] D.-J. Han, S. Wolf, S. Oliver, C. McCormick, M. T. DePue, and D. S. Weiss. "3D Raman Sideband Cooling of Cesium Atoms at High Density", *Phys. Rev. Lett.* **85**, 724–727 (2000) (cit. on p. 121).

[Han15] R. K. Hanley, P. D. Gregory, I. G. Hughes, and S. L. Cornish. "Absolute absorption on the potassium D lines: theory and experiment", *Journal of Physics B: Atomic, Molecular and Optical Physics* **48**, 195004 (2015) (cit. on pp. 65, 186, 189).

[Han94] K. Hanzawa. "Anisotropic Exchange Interactions in Cuprates", *Journal of the Physical Society of Japan* **63**, 264–270 (1994) (cit. on pp. 4, 6).

[Hay85] C. E. Hayes, W. A. Edelstein, J. F. Schenck, O. M. Mueller, and M. Eash. "An efficient, highly homogeneous radiofrequency coil for whole-body NMR imaging at 1.5 T", *Journal of Magnetic Resonance (1969)* **63**, 622–628 (1985) (cit. on p. 106).

[Hec09] E. Hecht. *Optik*. 5th ed. Oldenbourg Wissenschaftsverlag GmbH, München (2009) (cit. on p. 37).

[Her] Heraeus Quartzglas GmbH & Co. KG. *Base Materials Heraeus Quartzglas*. Retrieved on June 03, 2019. URL: `https://www.heraeus.com/media/media/hqs/doc_hqs/products_and_solutions_8/BaseMaterials_Image_EN.pdf` (cit. on p. 85).

[Her15] I. V. Hertel and C.-P. Schulz. *Atoms, Molecules and Optical Physics 1 Atoms and Spectroscopy*. Springer-Verlag Berlin Heidelberg (2015) (cit. on p. 61).

[Hil82] R. C. Hilborn. "Einstein coefficients, cross sections, f values, dipole moments, and all that", *American Journal of Physics* **50**, 982–986 (1982) (cit. on pp. 71, 72).

[Hof18] W. Hofstetter and T. Qin. "Quantum simulation of strongly correlated condensed matter systems", *Journal of Physics B: Atomic, Molecular and Optical Physics* **51**, 082001 (2018) (cit. on p. 3).

[Hol76] L. Holmgren, I. Lindgren, J. Morrison, and A.-M. Mårtensson. “Fine-Structure Intervals in Alkali-Like Spectra Obtained from Many-Body Theory”, *Z. Physik A* **276**, 179–185 (1976) (cit. on p. 55).

[Hub63] J. Hubbard. “Electron correlations in narrow energy bands”, *Proceedings of the Royal Society of London A: Mathematical, Physical and Engineering Sciences* **276**, 238–257 (1963) (cit. on pp. 3, 15, 16).

[Hub64a] J. Hubbard. “Electron correlations in narrow energy bands II. The degenerate band case”, *Proceedings of the Royal Society of London A: Mathematical, Physical and Engineering Sciences* **277**, 237–259 (1964) (cit. on p. 16).

[Hub64b] J. Hubbard. “Electron correlations in narrow energy bands III. An improved solution”, *Proceedings of the Royal Society of London A: Mathematical, Physical and Engineering Sciences* **281**, 401–419 (1964) (cit. on p. 16).

[Ilz18] P. Ilzhöfer, G. Durastante, A. Patscheider, A. Trautmann, M. J. Mark, and F. Ferlaino. “Two-species five-beam magneto-optical trap for erbium and dysprosium”, *Phys. Rev. A* **97**, 023633 (2018) (cit. on p. 180).

[Inf] Informationsstelle Edelstahl Rostfrei. *Merkblatt 821 Edelstahl Rostfrei - Eigenschaften*. Retrieved Dezember 04, 2018. URL: `https://www.edelstahl-rostfrei.de/downloads/iser/MB_821.pdf` (cit. on p. 84).

[Ing07] M. Inguscio, W. Ketterle, and C. Salomon, eds. *Proceedings of the International School of Physics «Enrico Fermi »Course CLXIV*. IOS Press Netherlands (2007) (cit. on p. 22).

[Jac05] M. W. Jack and M. Yamashita. “Bose-Hubbard model with attractive interactions”, *Phys. Rev. A* **71**, 023610 (2005) (cit. on p. 30).

[Jac99a] J. D. Jackson. *Classical Electrodynamics*. 3rd ed. JOHN WILEY & SONS, INC. (1999) (cit. on p. 50).

[Jac99b] J. D. Jackson. *Classical Electrodynamics*. 3rd ed. , Problem 5.30. JOHN WILEY & SONS, INC. (1999) (cit. on pp. 103, 105).

[Jak98] D. Jaksch, C. Bruder, J. I. Cirac, C. W. Gardiner, and P. Zoller. “Cold Bosonic Atoms in Optical Lattices”, *Phys. Rev. Lett.* **81**, 3108–3111 (1998) (cit. on pp. 29, 30, 32).

[Jer14] D. Jervis and J. H. Thywissen. “Making an Ultracold Gas”. In: *Quantum Gas Experiments*. Ed. by P. Törmä and K. Sengstock (2014), 5–32 (cit. on pp. 22, 34, 35, 50).

[Jia13] J. Jiang and J. Mitroy. “Hyperfine effects on potassium tune-out wavelengths and polarizabilities”, *Phys. Rev. A* **88**, 032505 (2013) (cit. on p. 186).

[Jo12] G.-B. Jo, J. Guzman, C. K. Thomas, P. Hosur, A. Vishwanath, and D. M. Stamper-Kurn. "Ultracold Atoms in a Tunable Optical Kagome Lattice", *Phys. Rev. Lett.* **108**, 045305 (2012) (cit. on p. 27).

[Jou13] K. Jousten, ed. *Wutz Handbuch Vakuumtechnik*. 11th ed. Springer Vieweg, Wiesbaden (2013) (cit. on p. 98).

[Jud77] B. R. Judd. *Operator Techniques In Atomic Spectroscopy*. Authorized facsimile by University Microfilms International. Originally published by McGraw-Hill Book Company, Inc. (1977) (cit. on p. 73).

[Jul11] P. S. Julienne, T. M. Hanna, and Z. Idziaszek. "Universal ultracold collision rates for polar molecules of two alkali-metal atoms", *Phys. Chem. Chem. Phys.* **13**, 19114–19124 (2011) (cit. on pp. 4, 6).

[Ker00] A. J. Kerman, V. Vuletić, C. Chin, and S. Chu. "Beyond Optical Molasses: 3D Raman Sideband Cooling of Atomic Cesium to High Phase-Space Density", *Phys. Rev. Lett.* **84**, 439–442 (2000) (cit. on p. 121).

[Ket99] W. Ketterle, D. S. Durfee, and D. M. Stamper-Kurn. "Making, probing and understanding Bose-Einstein condensates". In: *Proceedings of the International School of Physics «Enrico Fermi »Course CXL*. Ed. by M. Inguscio, S. Stringari, and C. E. Wieman. IOS Press Netherlands (1999) (cit. on pp. 4, 21, 22, 33, 34, 113).

[Kha68] A. Khadjavi, A. Lurio, and W. Happer. "Stark Effect in the Excited States of Rb, Cs, Cd, and Hg", *Phys. Rev.* **167**, 128–135 (1968) (cit. on p. 54).

[Kir] E. Kirilov. Private communication (cit. on p. 150).

[Koc08] T. Koch, T. Lahaye, J. Metz, B. Fröhlich, A. Griesmaier, and T. Pfau. "Stabilization of a purely dipolar quantum gas against collapse", *Nature Physics* **4**, 218 (2008) (cit. on p. 4).

[Köh06] T. Köhler, K. Góral, and P. S. Julienne. "Production of cold molecules via magnetically tunable Feshbach resonances", *Rev. Mod. Phys.* **78**, 1311–1361 (2006) (cit. on p. 119).

[Kop07] K. Kopitzki and P. Herzog. *Einführung in die Festkörperphysik*. 6th ed. Reprinted in 2009. Vieweg+Teubner (2007) (cit. on pp. 9, 12).

[Kot04] G. Kotliar and D. Vollhardt. "Strongly Correlated Materials: Insights From Dynamical Mean-Field Theory", *Physics Today* **57**, 53–59 (2004) (cit. on p. 2).

[Kraa] A. Kramida, Y. Ralchenko, J. Reader, and NIST ASD Team. *NIST Atomic Spectra Database (ver. 5.5.6), [Online]*. Retrieved on April 28, 2018. National Institute of Standards and Technology, Gaithersburg, MD. URL: `https://physics.nist.gov/asd` (cit. on pp. 36, 37, 49, 66, 180).

[Krab] A. Kramida, Y. Ralchenko, J. Reader, and NIST ASD Team. *NIST Atomic Spectra Database (ver. 5.5.6), [Online].* Retrieved on April 23, 2018. National Institute of Standards and Technology, Gaithersburg, MD. URL: `https://physics.nist.gov/asd` (cit. on pp. 56, 57).

[Kra49] H. R. Kratz. "The Principal Series of Potassium, Rubidium, and Cesium in Absorption", *Phys. Rev.* **75**, 1844–1850 (1949) (cit. on pp. 36, 37, 180).

[Küc09] A. Küchler. *Hochspannungstechnik: Grundlagen – Technologie – Anwendungen*. 3rd ed. Springer-Verlag Berlin Heidelberg (2009) (cit. on p. 166).

[Kuh01] S. Kuhr, W. Alt, D. Schrader, M. Müller, V. Gomer, and D. Meschede. "Deterministic Delivery of a Single Atom", *Science* **293**, 278–280 (2001) (cit. on p. 45).

[Kur] Kurt J. Lesker Company. *CF Flanges (Aluminum A2219)*. Retrieved on June 03, 2019. URL: `https://www.lesker.com/newweb/flanges/flanges_cf_aluminum.cfm?pgid=0` (cit. on p. 84).

[Lah09] T. Lahaye, C. Menotti, L. Santos, M. Lewenstein, and T. Pfau. "The physics of dipolar bosonic quantum gases", *Reports on Progress in Physics* **72**, 126401 (2009) (cit. on pp. 4, 22, 170).

[Lan12] M. Landini, S. Roy, G. Roati, A. Simoni, M. Inguscio, G. Modugno, and M. Fattori. "Direct evaporative cooling of ^{39}K atoms to Bose-Einstein condensation", *Phys. Rev. A* **86**, 033421 (2012) (cit. on p. 114).

[Lei03] D. Leibfried, R. Blatt, C. Monroe, and D. Wineland. "Quantum dynamics of single trapped ions", *Rev. Mod. Phys.* **75**, 281–324 (2003) (cit. on pp. 70, 74).

[Lem13] M. Lemeshko, R. V. Krems, J. M. Doyle, and S. Kais. "Manipulation of molecules with electromagnetic fields", *Molecular Physics* **111**, 1648–1682 (2013) (cit. on p. 156).

[Léo14] J. Léonard, M. Lee, A. Morales, T. M. Karg, T. Esslinger, and T. Donner. "Optical transport and manipulation of an ultracold atomic cloud using focus-tunable lenses", *New Journal of Physics* **16**, 093028 (2014) (cit. on p. 45).

[Lew07] M. Lewenstein, A. Sanpera, V. Ahufinger, B. Damski, A. Sen(De), and U. Sen. "Ultracold atomic gases in optical lattices: mimicking condensed matter physics and beyond", *Advances in Physics* **56**, 243–379 (2007) (cit. on pp. 3, 27).

[Lie68] E. H. Lieb and F. Y. Wu. "Absence of Mott Transition in an Exact Solution of the Short-Range, One-Band Model in One Dimension", *Phys. Rev. Lett.* **20**, 1445–1448 (1968) (cit. on p. 16).

[Lu11] M. Lu, N. Q. Burdick, S. H. Youn, and B. L. Lev. "Strongly Dipolar Bose-Einstein Condensate of Dysprosium", *Phys. Rev. Lett.* **107**, 190401 (2011) (cit. on p. 4).

[Luc76] E. Luc-Koenig. "Doublet inversions in alkali-metal spectra: Relativistic and correlation effects", *Phys. Rev. A* **13**, 2114–2122 (1976) (cit. on p. 55).

[Ma90] L.-S. Ma and J. L. Hall. "Optical heterodyne spectroscopy enhanced by an external optical cavity: toward improved working standards", *IEEE Journal of Quantum Electronics* **26**, 2006–2012 (1990) (cit. on p. 185).

[Man91] E. Manousakis. "The spin-½ Heisenberg antiferromagnet on a square lattice and its application to the cuprous oxides", *Rev. Mod. Phys.* **63**, 1–62 (1991) (cit. on pp. 4, 6, 19).

[Mar17] M. Marszałek. *Assembly and testing of an objective lens designed for imaging ultracold quantum gases*. Master thesis, University of Innsbruck (2017) (cit. on pp. 46, 47).

[Mar12] N. Marzari, A. A. Mostofi, J. R. Yates, I. Souza, and D. Vanderbilt. "Maximally localized Wannier functions: Theory and applications", *Rev. Mod. Phys.* **84**, 1419–1475 (2012) (cit. on p. 12).

[McC08] D. J. McCarron, S. A. King, and S. L. Cornish. "Modulation transfer spectroscopy in atomic rubidium", *Measurement Science and Technology* **19**, 105601 (2008) (cit. on p. 185).

[McK11] D. C. McKay, D. Jervis, D. J. Fine, J. W. Simpson-Porco, G. J. A. Edge, and J. H. Thywissen. "Low-temperature high-density magneto-optical trapping of potassium using the open $4S \rightarrow 5P$ transition at 405 nm", *Phys. Rev. A* **84**, 063420 (2011) (cit. on p. 180).

[Mer66] N. D. Mermin and H. Wagner. "Absence of Ferromagnetism or Antiferromagnetism in One- or Two-Dimensional Isotropic Heisenberg Models", *Phys. Rev. Lett.* **17**, 1133–1136 (1966) (cit. on p. 18).

[Mes65a] A. Messiah. *Quantum Mechanics Volume I*. North-Holland Publishing Company, Amsterdam (1965) (cit. on p. 28).

[Mes65b] A. Messiah. *Quantum Mechanics Volume II*. North-Holland Publishing Company, Amsterdam (1965) (cit. on pp. 18, 19, 54, 68, 69, 73, 156).

[Met99] H. J. Metcalf and P. van der Straten. *Laser Cooling and Trapping*. 3rd reprint. Springer Verlag, New York (1999) (cit. on pp. 21, 22, 24, 38, 73).

[Mil93] J. D. Miller, R. A. Cline, and D. J. Heinzen. "Far-off-resonance optical trapping of atoms", *Phys. Rev. A* **47**, R4567–R4570 (1993) (cit. on p. 24).

[Mil78] T. M. Miller and B. Bederson. "Atomic and Molecular Polarizabilities-A Review of Recent Advances", *Advances in Atomic and Molecular Physics* **13**, 1–55 (1978) (cit. on pp. 50, 51).

[Mir15] M. Miranda, R. Inoue, Y. Okuyama, A. Nakamoto, and M. Kozuma. “Site-resolved imaging of ytterbium atoms in a two-dimensional optical lattice”, *Phys. Rev. A* **91**, 063414 (2015) (cit. on pp. 37–39, 41, 43, 44).

[Mit10] J. Mitroy, M. S. Safronova, and C. W. Clark. “Theory and applications of atomic and ionic polarizabilities”, *Journal of Physics B: Atomic, Molecular and Optical Physics* **43**, 202001 (2010) (cit. on pp. 51, 52, 54, 57).

[Mol14] P. K. Molony, P. D. Gregory, Z. Ji, B. Lu, M. P. Köppinger, C. R. Le Sueur, C. L. Blackley, J. M. Hutson, and S. L. Cornish. “Creation of Ultracold ^{87}Rb^{133}Cs Molecules in the Rovibrational Ground State”, *Phys. Rev. Lett.* **113**, 255301 (2014) (cit. on p. 119).

[Mor03] G. Morigi. “Cooling atomic motion with quantum interference”, *Phys. Rev. A* **67**, 033402 (2003) (cit. on pp. 65, 74).

[Mor00] G. Morigi, J. Eschner, and C. H. Keitel. “Ground State Laser Cooling Using Electromagnetically Induced Transparency”, *Phys. Rev. Lett.* **85**, 4458–4461 (2000) (cit. on pp. 65, 74–77, 81).

[Mor07] H. Moritz, T. Stöferle, K. Günter, M. Köhl, and T. Esslinger. “A lab in a trap: Fermionic quantum gases, Bose-Fermi mixtures and molecules in optical lattices”. In: *Proceedings of the International School of Physics «Enrico Fermi »Course CLXIV*. Ed. by M. Inguscio, W. Ketterle, and C. Salomon. IOS Press Netherlands (2007) (cit. on p. 29).

[Mor12] E. Morosan, D. Natelson, A. H. Nevidomskyy, and Q. Si. “Strongly Correlated Materials”, *Advanced Materials* **24**, 4896–4923 (2012) (cit. on p. 2).

[Mor06] O. Morsch and M. Oberthaler. “Dynamics of Bose-Einstein condensates in optical lattices”, *Rev. Mod. Phys.* **78**, 179–215 (2006) (cit. on pp. 21, 34).

[Mos16] S. A. Moses. *A quantum gas of polar molecules in an optical lattice*. PhD thesis, University of Colorado (2016) (cit. on p. 178).

[Mos15] S. A. Moses, J. P. Covey, M. T. Miecnikowski, B. Yan, B. Gadway, J. Ye, and D. S. Jin. “Creation of a low-entropy quantum gas of polar molecules in an optical lattice”, *Science* **350**, 659–662 (2015) (cit. on p. 119).

[Mot64] N. F. Mott. “Electrons in transition metals”, *Advances in Physics* **13**, 325–422 (1964) (cit. on p. 15).

[Nan12] D. K. Nandy, Y. Singh, B. P. Shah, and B. K. Sahoo. “Transition properties of a potassium atom”, *Phys. Rev. A* **86**, 052517 (2012) (cit. on pp. 50, 57).

[Nat] National Science and Technology Council. *Materials Genome Initiative for Global Competitiveness*. Retrieved August 11, 2018 (cit. on p. 1).

[Nel07] K. D. Nelson, X. Li, and D. S. Weiss. "Imaging single atoms in a three-dimensional array", *Nature Physics* **3**, 556–560 (2007) (cit. on pp. 35, 39, 40).

[Nen83] G. Nenciu. "Existence of the exponentially localised Wannier functions", *Comm. Math. Phys.* **91**, 81–85 (1983) (cit. on p. 13).

[Ney69] J. Ney. "Hyperfeinstrukturuntersuchung der 4p und $5p^2P3/2$-Terme im K I-Spektrum durch Resonanzstreuung von Licht zur Bestimmung der Kernquadrupolmomente von K^{39} und K^{41}", *Zeitschrift für Physik A Hadrons and nuclei* **223**, 126–138 (1969) (cit. on p. 186).

[Ni08] K.-K. Ni, S. Ospelkaus, M. H. G. de Miranda, A. Pe'er, B. Neyenhuis, J. J. Zirbel, S. Kotochigova, P. S. Julienne, D. S. Jin, and J. Ye. "A High Phase-Space-Density Gas of Polar Molecules", *Science* **322**, 231–235 (2008) (cit. on p. 119).

[Nou13] N. Nouri and B. Plaster. "Comparison of magnetic field uniformities for discretized and finite-sized standard $\cos\theta$, solenoidal, and spherical coils", *Nucl. Instrum. Methods Phys. Res. A* **723**, 30–35 (2013) (cit. on pp. 103, 105).

[Omr16] A. Omran. *A Microscope for Fermi Gases*. Dissertation, Ludwig-Maximilians-Universität München (2016) (cit. on p. 44).

[Omr15] A. Omran, M. Boll, T. A. Hilker, K. Kleinlein, G. Salomon, I. Bloch, and C. Gross. "Microscopic Observation of Pauli Blocking in Degenerate Fermionic Lattice Gases", *Phys. Rev. Lett.* **115**, 263001 (2015) (cit. on pp. 39, 43, 44).

[Par15] M. F. Parsons, F. Huber, A. Mazurenko, C. S. Chiu, W. Setiawan, K. Wooley-Brown, S. Blatt, and M. Greiner. "Site-Resolved Imaging of Fermionic ^{6}Li in an Optical Lattice", *Phys. Rev. Lett.* **114**, 213002 (2015) (cit. on pp. 39, 41, 43, 44).

[Pat14] H. J. Patel, C. L. Blackley, S. L. Cornish, and J. M. Hutson. "Feshbach resonances, molecular bound states, and prospects of ultracold-molecule formation in mixtures of ultracold K and Cs", *Phys. Rev. A* **90**, 032716 (2014) (cit. on p. 114).

[Pet08] C. J. Pethick and H. Smith. *Bose-Einstein Condensation in Dilute Gases*. 2nd ed. Retrieved November 19, 2018. Cambridge University Press (2008) (cit. on p. 22).

[Pet94] K. I. Petsas, A. B. Coates, and G. Grynberg. "Crystallography of optical lattices", *Phys. Rev. A* **50**, 5173–5189 (1994) (cit. on p. 27).

[Pil09] K. Pilch. *Optical trapping and Feshbach spectroscopy of an ultracold Rb-Cs mixture*. Dissertation, University of Innsbruck (2009) (cit. on p. 89).

[Pyy18] P. Pyykkö. "Year-2017 nuclear quadrupole moments", *Molecular Physics* **116**, 1328–1338 (2018) (cit. on p. 154).

[Rad95] L. J. Radziemski, R. Engleman, and J. W. Brault. "Fourier-transform-spectroscopy measurements in the spectra of neutral lithium, ^{6}I and ^{7}I (Li I)", *Phys. Rev. A* **52**, 4462–4470 (1995) (cit. on pp. 36, 180).

[Raj05] K. Rajan. "Materials informatics", *Materials Today* **8**, 38–45 (2005) (cit. on p. 1).

[Rav18] C. Ravensbergen, V. Corre, E. Soave, M. Kreyer, E. Kirilov, and R. Grimm. "Production of a degenerate Fermi-Fermi mixture of dysprosium and potassium atoms", *Phys. Rev. A* **98**, 063624 (2018) (cit. on p. 180).

[Rei17] L. Reichsöllner, A. Schindewolf, T. Takekoshi, R. Grimm, and H.-C. Nägerl. "Quantum Engineering of a Low-Entropy Gas of Heteronuclear Bosonic Molecules in an Optical Lattice", *Phys. Rev. Lett.* **118**, 073201 (2017) (cit. on pp. 5, 119, 195).

[Ric95] L. Ricci, M. Weidemüller, T. Esslinger, A. Hemmerich, C. Zimmermann, V. Vuletic, W. König, and T. W. Hänsch. "A compact grating-stabilized diode laser system for atomic physics", *Optics Communications* **117**, 541–549 (1995) (cit. on p. 182).

[Rid11a] A. Ridinger, S. Chaudhuri, T. Salez, U. Eismann, D. Fernandes, K. Magalhães, D. Wilkowski, C. Salomon, and F. Chevy. "Large atom number dual-species magneto-optical trap for fermionic ^{6}Li and ^{40}K atoms", *Eur. Phys. J. D* **65**, 223–242 (2011) (cit. on pp. 89, 95).

[Rid11b] A. Ridinger. *Towards quantum degenerate Fermi mixtures: Photoassociation of weakly bound 6Li40K molecules*. PhD thesis, Ecole Normale Supérieure de Paris (2011) (cit. on pp. 96, 180).

[Roo00] C. F. Roos, D. Leibfried, A. Mundt, F. Schmidt-Kaler, J. Eschner, and R. Blatt. "Experimental Demonstration of Ground State Laser Cooling with Electromagnetically Induced Transparency", *Phys. Rev. Lett.* **85**, 5547–5550 (2000) (cit. on p. 65).

[Ryc04] D. Rychtařik. *Two-dimensional Bose-Einstein Condensate in an optical surface trap*. Dissertation, University of Innsbruck (2004) (cit. on p. 89).

[Sac06] S. Sachdev. "Quantum phase transitions". In: *The New Physics: For the Twenty-First Century*. Ed. by G. Fraser. Cambridge University Press (Cambridge) (2006), 229–254 (cit. on p. 2).

[Sac11] S. Sachdev. *Quantum Phase Transitions*. 2nd ed. Cambridge University Press (2011) (cit. on p. 2).

[Saf15] M. S. Safronova. Personal communication. (2015) (cit. on pp. 59, 60).

[Saf06] M. S. Safronova, B. Arora, and C. W. Clark. "Frequency-dependent polarizabilities of alkali-metal atoms from ultraviolet through infrared spectral regions", *Phys. Rev. A* **73**, 022505 (2006) (cit. on p. 57).

[Saf13] M. S. Safronova, U. I. Safronova, and C. W. Clark. “Magic wavelengths for optical cooling and trapping of potassium”, *Phys. Rev. A* **87**, 052504 (2013) (cit. on pp. 50, 51, 57–60).

[Sal13] G. Salomon, L. Fouché, P. Wang, A. Aspect, P. Bouyer, and T. Bourdel. “Gray-molasses cooling of 39K to a high phase-space density”, *EPL* **104**, 63002 (2013) (cit. on pp. 113, 122).

[San08] J. E. Sansonetti. “Wavelengths, Transition Probabilities, and Energy Levels for the Spectra of Potassium (KI through KXIX)”, *Journal of Physical and Chemical Reference Data* **37**, 7–96 (2008) (cit. on pp. 5, 56, 57, 67, 186).

[San09] J. E. Sansonetti. “Wavelengths, Transition Probabilities, and Energy Levels for the Spectra of Cesium (CsI–CsLV)”, *Journal of Physical and Chemical Reference Data* **38**, 761–923 (2009) (cit. on pp. 5, 110).

[San14] L. Santos. “Dipolar Gases – Theory”. In: *Quantum Gas Experiments*. Ed. by P. Törmä and K. Sengstock (2014), 293–309 (cit. on p. 113).

[Sch06] S. Schmid, G. Thalhammer, K. Winkler, F. Lang, and J. Hecker Denschlag. “Long distance transport of ultracold atoms using a 1D optical lattice”, *New Journal of Physics* **8**, 159 (2006) (cit. on pp. 25, 45).

[See] See Supplemental Material at `http://link.aps.org/supplemental/10.1103/PhysRevA.95.022715` (cit. on p. 118).

[Sen11] M. S. Senn, J. P. Wright, and J. P. Attfield. “Charge order and three-site distortions in the Verwey structure of magnetite”, *Nature* **481**, 173 (2011) (cit. on p. 2).

[She10] J. F. Sherson, C. Weitenberg, M. Endres, M. Cheneau, I. Bloch, and S. Kuhr. “Single-atom-resolved fluorescence imaging of an atomic Mott insulator”, *Nature* **467**, 68–71 (2010) (cit. on pp. 5, 33, 35–40, 43, 44, 81).

[Sie86] A. E. Siegman. *Lasers*. University Science Books, Mill Valley, California (1986) (cit. on p. 23).

[Sin12] Y. Singh, D. K. Nandy, and B. K. Sahoo. “Reexamination of nuclear quadrupole moments in $^{39-41}$K isotopes”, *Phys. Rev. A* **86**, 032509 (2012) (cit. on p. 186).

[Sin01] J. Singleton. *Band theory and electronic properties of solids*. 1st ed. Reprinted in 2010. Oxford University Press, New York (2001) (cit. on p. 11).

[Smi04] D. A. Smith and I. G. Hughes. “The role of hyperfine pumping in multilevel systems exhibiting saturated absorption”, *American Journal of Physics* **72**, 631–637 (2004) (cit. on p. 189).

[Smi66] W. J. Smith. *Modern Optical Engineering*. McGraw-Hill, Inc. (1966) (cit. on p. 41).

[Sob79] I. I. Sobelman. *Atomic Spectra and Radiative Transitions*. Springer-Verlag, Berlin, Heidelberg (1979) (cit. on pp. 52, 60).

[Ste86] S. Stenholm. "The semiclassical theory of laser cooling", *Rev. Mod. Phys.* **58**, 699–739 (1986) (cit. on p. 73).

[Tak96] T. Takekoshi and R. J. Knize. "CO2 laser trap for cesium atoms", *Opt. Lett.* **21**, 77–79 (1996) (cit. on p. 24).

[Tak19] T. Takekoshi. Personal communication. (2019) (cit. on p. 127).

[Tak14] T. Takekoshi, L. Reichsöllner, A. Schindewolf, J. M. Hutson, C. R. Le Sueur, O. Dulieu, F. Ferlaino, R. Grimm, and H.-C. Nägerl. "Ultracold Dense Samples of Dipolar RbCs Molecules in the Rovibrational and Hyperfine Ground State", *Phys. Rev. Lett.* **113**, 205301 (2014) (cit. on pp. 119, 127).

[Tar12] L. Tarruell, D. Greif, T. Uehlinger, G. Jotzu, and T. Esslinger. "Creating, moving and merging Dirac points with a Fermi gas in a tunable honeycomb lattice", *Nature* **483**, 302–305 (2012) (cit. on p. 27).

[Tar18] L. Tarruell and L. Sanchez-Palencia. "Quantum simulation of the Hubbard model with ultracold fermions in optical lattices", *Comptes Rendus Physique* **19**, 365–393 (2018) (cit. on pp. 6, 16–18).

[Tre01] P. Treutlein, K. Y. Chung, and S. Chu. "High-brightness atom source for atomic fountains", *Phys. Rev. A* **63**, 051401 (2001) (cit. on p. 111).

[Ueh08] T. Uehlinger. *A 2D Magneto-Optical Trap as a High-Flux Source of Cold Potassium Atoms*. Diploma thesis, Swiss Federal Institute of Technology Zurich (2008) (cit. on p. 96).

[Vaca] Vacom Vakuum Komponenten & Messtechnik GmbH. *Materials*. Retrieved May 14, 2018. URL: `https://www.vacom.de/en/products/standard-components/materials` (cit. on p. 93).

[Vacb] Vacom Vakuum Komponenten & Messtechnik GmbH. *Stainless steel 1.4429-ESU (316 LN-ESR)*. Retrieved May 6, 2018. URL: `www.vacom-vacuum.com` (cit. on p. 89).

[Vol12] D. Vollhardt. "Dynamical mean-field theory for correlated electrons", *Annalen der Physik* **524**, 1–19 (2012) (cit. on p. 15).

[Vul98] V. Vuletić, C. Chin, A. J. Kerman, and S. Chu. "Degenerate Raman Sideband Cooling of Trapped Cesium Atoms at Very High Atomic Densities", *Phys. Rev. Lett.* **81**, 5768–5771 (1998) (cit. on p. 121).

[Wal15] M. L. Wall, K. R. A. Hazzard, and A. M. Rey. "Quantum Magnetism with Ultracold Molecules". In: *From Atomic to Mesoscale: The Role of Quantum Coherence in Systems of Various Complexities*. Ed. by S. A. Malinovskaya and I. Novikova. World Scientific Publishing, Singapore (2015) (cit. on pp. 4, 19, 155, 157, 169–171, 174).

[Wan10] D. Wang, B. Neyenhuis, M. H. G. de Miranda, K.-K. Ni, S. Ospelkaus, D. S. Jin, and J. Ye. "Direct absorption imaging of ultracold polar molecules", *Phys. Rev. A* **81**, 061404 (2010) (cit. on p. 4).

[Wan62] G. H. Wannier. "Dynamics of Band Electrons in Electric and Magnetic Fields", *Rev. Mod. Phys.* **34**, 645–655 (1962) (cit. on p. 12).

[Web03a] T. Weber. *Bose-Einstein Condensation of Optically Trapped Cesium*. Dissertation, University of Innsbruck (2003) (cit. on p. 89).

[Web03b] T. Weber, J. Herbig, M. Mark, H.-C. Nägerl, and R. Grimm. "Bose-Einstein Condensation of Cesium", *Science* **299**, 232–235 (2003) (cit. on pp. 5, 110, 111).

[Wei11] C. Weitenberg. *Single-Atom Resolved Imaging and Manipulation in an Atomic Mott Insulator*. Dissertation, Ludwig-Maximilians-Universität München (2011) (cit. on pp. 38, 39, 44).

[Wei14] C. Weitenberg. "Fluorescence Imaging of Quantum Gases". In: *Quantum Gas Experiments*. Ed. by P. Törmä and K. Sengstock (2014), 121–143 (cit. on pp. 35, 39).

[Wie91] C. E. Wieman and L. Hollberg. "Using diode lasers for atomic physics", *Review of Scientific Instruments* **62**, 1–20 (1991) (cit. on p. 182).

[Wil96] R. N. Wilson. *Reflecting Telescope Optics I*. Springer-Verlag Berlin Heidelberg (1996) (cit. on p. 41).

[Win13] P. Windpassinger and K. Sengstock. "Engineering novel optical lattices", *Reports on Progress in Physics* **76**, 086401 (2013) (cit. on pp. 27, 30, 31).

[Win79] D. J. Wineland and W. M. Itano. "Laser cooling of atoms", *Phys. Rev. A* **20**, 1521–1540 (1979) (cit. on pp. 73, 74).

[Wir10] G. Wirth, M. Ölschläger, and A. Hemmerich. "Evidence for orbital superfluidity in the P-band of a bipartite optical square lattice", *Nature Physics* **7**, 147 (2010) (cit. on p. 27).

[Yam16] R. Yamamoto, J. Kobayashi, T. Kuno, K. Kato, and Y. Takahashi. "An ytterbium quantum gas microscope with narrow-line laser cooling", *New Journal of Physics* **18**, 023016 (2016) (cit. on pp. 37, 39, 43, 44).

[Yan13] B. Yan, S. A. Moses, B. Gadway, J. P. Covey, K. R. A. Hazzard, A. M. Rey, D. S. Jin, and J. Ye. "Observation of dipolar spin-exchange interactions with lattice-confined polar molecules", *Nature* **501**, 521 (2013) (cit. on pp. 157, 171, 173, 177).

[Yuc06] C. Yuce, A. Kilic, and A. Coruh. "Inverted oscillator", *Physica Scripta* **74**, 114 (2006) (cit. on p. 70).

[Zha05] G.-F. Zhang and S.-S. Li. "Thermal entanglement in a two-qubit Heisenberg XXZ spin chain under an inhomogeneous magnetic field", *Phys. Rev. A* **72**, 034302 (2005) (cit. on p. 174).

[Żuc10] P. S. Żuchowski and J. M. Hutson. "Reactions of ultracold alkali-metal dimers", *Phys. Rev. A* **81**, 060703 (2010) (cit. on p. 4).

Acknowledgments

I would like to close my Thesis by acknowledging support and guidance that I have received from many people during my dissertation. Given the time pressure of a dissertation, I unfortunately might not always have had the time to let these people know that they − in one way or another − helped me to complete my Thesis. This is why it is all the more important to me to use the last page of my Thesis to say thank you to those.

I am most grateful to Rainer Blatt for being the co-advisor of my Thesis. His assistance and determination constituted the backbone of my dissertation. Without his constructive feedback I would not have gotten to the point where I am today. I also would like to acknowledge my advisor Hanns-Christoph Nägerl for funding me and giving me access to the laboratory.

I owe special thanks to Patricia Moser, Karin Köhle, and Michaela Palz for support in administrative and personal matters. I always enjoyed their sense of humor, their constant positive attitude, and will miss the flying visits in their offices as well as their good advice. I also thank Thomas Monz and Philipp Schindler for giving straight answers and helping me to make the right decisions.

I should also thank the Nägerl group, especially Emil Kirilov, Tetsu Takekoshi (now with the Blatt group), Katharina Jag-Lauber, and Florian Meinert, for sharing their knowledge. I greatly benefited from the members of the Blatt-, Ferlaino-, and Grimm-group in Innsbruck. Their generosity in lending optics and other lab equipment often allowed me to proceed with my work. In particular, I thank Rudi Grimm for employing me for one year at the Institute for Quantum Optics and Quantum Information.

I very much appreciated the collaboration with Toni Schönherr, Christoph Wegscheider, Armin Sailer, and Helli Jordan from the mechanical workshop. Their commitment and expertise contributed to the successful realization of the K−Cs apparatus and enabled me to learn many lessons in engineering. My sincere thanks also goes to Christine Götsch-Obmascher, Sabine Hofer-Brigo, and Carina Oberhöler for handling administrative work.

I am indebted to my dear friends and colleagues Rianne Lous, Stefanie Unterguggenberger, Cornee Ravensbergen, Slava and Lukas Reichsöllner, Albert and Sabine Frisch, Andreas Schindewolf, Regina Lechner, Sara Khorsand, Lea Münch, Jan Kucharcik, and Verena Minsch for proofreading my Thesis, cooking Kasspatzln, computational help, climbing via ferratas, common mountain hikes, long phone calls, joint kitchen time, elderflower syrup, going bouldering, first aid, assistance with vector images, and much more.

I had epic times with my fellows Markus Teller, Verena Podlesnic, Lukas Tiefenthaler, Benjamin Wilhelm, Peter Sandbichler, Patrick Hangl, Dominic Jäger, and Bill Limerick during sunday night football, ice climbing, trash talking at its finest, nights, and joint activities. Many of them had a big impact on me and contributed to many unforgettable memories.

Last, and certainly not least, I am profoundly grateful to Nina, Florian, and my parents for their empathy, relentless support, and constant believe in me.

Philipp
Innsbruck, July 2019